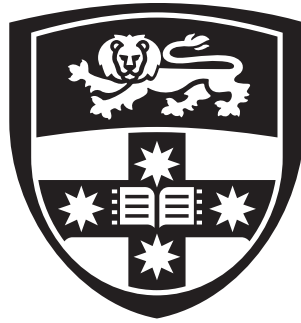


Symmetry-Protected Topological Phases for Robust Quantum Computation



Sam Roberts

School of Physics
The University of Sydney

This dissertation is submitted to the
Faculty of Science, School of Physics of The University of Sydney
in partial fulfillment of the requirements for the degree of
Doctor of Philosophy (Physics)

February 2019

Acknowledgements

I would first like to thank my supervisor Stephen Bartlett for being an incredible supervisor and mentor, and for introducing me to the exciting world of quantum physics. You have always been available to discuss research, share your enthusiasm for physics, or to give guidance on topics beyond physics. I have always looked forward to our meetings and left them with a feeling of positivity and inspiration, even when deeply stuck on a problem. I am very grateful for you looking out for me and caring about my growth as a scientist.

I would also like to express my appreciation to Robert Raussendorf, Beni Yoshida, Andrew Doherty, Steve Flammia, David Poulin, and Terry Rudolph for being inspiring physicists, for sharing interesting discussions, and for their guidance.

I am very grateful to everybody in the USYD group for creating an amazing and unique workplace. I would like to especially thank Russ Evans, Billy Smith, Hakop Pashayan, Angela Karanjai, Harrison Ball, Chris Chubb, Jacob Bridgeman, Kamil Korzekwa, Donnie Elman, Arne Grimsmo, Ziggy Cristina, Paul Webster, Wei-Wei Zhang, Robin Harper, Natasha Gabay, Riddhi Gupta, Jen Wakulicz, Parth Girdhar, Alan Robertson, David Tucket, Prahlad Warszawski for many great memories.

I am also very grateful for having met many uplifting people in the community, for sharing fascinating discussions or a crisp VB. I thank Tomas Jochym-O'Connor, Richard Kueng, Aleksander Kubica, Dominic Williamson, Courtney Brell, Andrew Darmawan, Benji Brown, Cihan Okay, Markus Frembs, Nicolas Delfosse, Michael Beverland, Juani Bermejo-Vega, Nikolas Breuckmann, David Stephen, Naomi Nickerson, Fernando Pastawski, and Nadish de Silva.

Of course, I can't thank my parents and brother enough, for endless help, for encouraging me and for making countless sacrifices for me. And to my friends who mean everything to me, I am endlessly thankful for the amazing memories and support over the past few years.

Finally, I would like to give my deepest gratitude to Leanna Haines, for everything.

Statement of Originality

I hereby declare that except where specific reference is made to the work of others, the contents of this dissertation are original and have not been submitted in whole or in part for consideration for any other degree or qualification in this, or any other university. I certify that the intellectual content of this thesis is the product of my own work and that any the assistance received in preparing this thesis and sources have been acknowledged, either in the text or as outlined in the Statement of Student Contribution. This dissertation contains fewer than 100,000 words, excluding appendices and bibliography.

Sam Roberts
February 2019

Statement of Student Contribution

This thesis consists of an introduction, three body chapters, and a summary and outlook. The three body chapters are based on three separate research articles with small additional edits. These research articles are either published or under review. The Introduction and Conclusion are written by me. A statement of research contribution for each of these body chapters is listed below.

Chapter 2: Symmetry-protected topological order at nonzero temperature.

Published in: Physical Review A **96**, 022306 (2017).

Author list: S Roberts, B Yoshida, A Kubica, SD Bartlett.

Student contribution: I am lead author on this publication. I was primarily responsible for the initial research, analytical calculations and drafting. The development of the main results was undertaken by me with extensive discussions with all authors. All authors are responsible for further edits, proofreading and corrections to calculations.

Chapter 3: Symmetry-protected self-correcting quantum memories.

Published in: arXiv preprint arXiv:1805.01474 (2018).

Author list: S Roberts, SD Bartlett.

Student contribution: I am lead author on this article. I am responsible for the research, writing and calculations of this article, under the supervision of Stephen Bartlett.

Chapter 4: Universal fault-tolerant measurement-based quantum computation.

Published in: arXiv preprint arXiv:1811.11780 (2018).

Author list: B Brown, S Roberts.

Student contribution: I am joint author of this paper, together with postdoctoral fellow Benjamin Brown. The research reported in this paper originated through independently-developed ideas by both myself and Dr Brown. These ideas were further developed, and calculations were carried out, by both authors working collaboratively, roughly in equal proportions. Dr Brown is responsible for the first drafting of the article, while further input and editing was undertaken by both authors.

Supervisor signature: _____

Sam Roberts
February 2019

Abstract

In recent years, topological phases of matter have presented exciting new avenues to achieve scalable quantum computation. In this thesis, we investigate a class of quantum many-body spin models known as symmetry-protected topological (SPT) phases for use in quantum information processing and storage. We explore the fault-tolerant properties of SPT phases, and how they can be utilized in the design of a quantum computer. Of central importance in this thesis is the concept of quantum error-correction, which in addition to its importance in fault-tolerant quantum computation, is used to characterise the stability of topological phases at finite temperature.

We begin with an introduction to quantum computation, quantum error correction, and topological phases of matter. We then focus on the fundamental question of whether symmetry-protected topological phases of matter can exist in thermal equilibrium; we prove that systems protected by global onsite symmetries cannot be ordered at nonzero temperature. Subsequently, we show that certain three-dimensional models with generalised higher-form symmetries can be thermally SPT ordered, and we relate this order to the ability to perform fault-tolerant measurement-based quantum computation. Following this, we assess feasibility of these phases as quantum memories, motivated by the fact that SPT phases in three dimensions can possess protected topological degrees of freedom on their boundary. We find that certain SPT ordered systems can be self-correcting, allowing quantum information to be stored for arbitrarily long times without requiring active error correction. Finally, we develop a framework to construct new schemes of fault-tolerant measurement-based quantum computation. As a notable example, we develop a cluster-state scheme that simulates the braiding and fusion of surface-code defects, offering novel alternative methods to achieve fault-tolerant universal quantum computation.

Contents

1	Introduction	1
1.1	Introduction	1
1.2	Quantum computing	2
1.3	Topological phases of matter	15
1.4	Computational phases of matter	21
1.5	Organisation of the thesis	22
2	Symmetry-protected topological order at nonzero temperature	25
2.1	Introduction	25
2.2	Thermal SPT-order	28
2.3	A model with a thermal SPT phase	47
2.4	Localizable entanglement	66
2.5	Outlook	72
3	Symmetry-protected self-correcting quantum memories	75
3.1	Introduction	75
3.2	Background	78
3.3	Self correction with a 1-form SPT phase	88
3.4	The gauge color code protected by 1-form symmetry	113
3.5	Emergent 1-form symmetries	123
3.6	Discussion	133
3.7	Davies Formalism	135

3.8	Thermal instability of 0-form SPT ordered memories	137
3.9	Energy barrier is sufficient	138
4	Universal fault-tolerant measurement-based quantum computation	141
4.1	Introduction	141
4.2	Quantum error correction	143
4.3	Foliation	145
4.4	Foliated qubits	148
4.5	The foliated system	161
4.6	The twisted surface code	167
4.7	Quantum computation with the foliated surface code	170
4.8	Concluding remarks	180
4.9	Proofs and generalisations	180
5	Conclusion	197
	Bibliography	201

1 | Introduction

1.1 Introduction

One of the most remarkable applications of quantum information is the theoretical development of quantum computing. Quantum computers are devices that exploit the unique quantum mechanical phenomena of coherent quantum systems to solve difficult computational problems, including many that are intractable using current approaches. Originally proposed by Richard Feynmann in the 80s [1] as a way to overcome the notorious difficulty of simulating quantum systems, the theory of quantum computing has since flourished into a rich multidisciplinary field with many important applications. Perhaps the most famous example of this is Shor's discovery of an integer factoring algorithm [2], which has a runtime exponentially faster than the best known classical algorithm. This profound discovery has propelled the field forward, as Shor's algorithm along with others [3–5] presents a radical paradigm shift for computing and the broader face of technology.

With the promise of quantum computing also comes a unique challenge – coherent quantum systems are fragile, and the information stored in a quantum system can decohere easily. As such, the design and construction of a quantum computer requires exceptional control, in order to preserve the delicate quantum information from the effects of noise. This challenge has led to the development of the beautiful theory of quantum fault-tolerance and quantum error correction, which provide novel approaches to tackle decoherence. At the core of fault-tolerance is the threshold theorem [6–10], which guarantees that arbitrary sized quantum computations are possible, provided the noise experienced by each qubit and component is below a threshold value. For systems with below-threshold noise, arbitrary size quantum computations can be performed fault-tolerantly with only modest resource overheads. Estimates of the noise threshold value vary greatly and are constantly changing, as error modelling becomes more sophisticated, and fault-tolerant techniques and error-correcting codes are being rapidly improved. It is becoming clear that scalable quantum computation is no longer a pipe-dream, as current experimental progress places near term quantum devices within tantalising reach.

As the quantum information has matured, its domain has expanded and it has developed deep connections with many areas of mathematics, physics, computer science and chemistry.

Notably, the confluence of condensed matter and fault-tolerant quantum computation has led to many profound insights in recent years. For example, new quantum error-correcting codes and even radically different approaches to computing (such as through the manipulation of quasiparticles called anyons [11]) have been inspired by the discoveries of the condensed matter community. Conversely, the discovery of new types of topological codes (such as fractal codes [12]) has led to new paradigms in the classification of phases of matter.

It is the goal of this thesis to leverage this symbiotic relationship between condensed matter and quantum information further, to develop and understand fault-tolerant methods for quantum computing using the unique capabilities of topological phases of matter. By now, topological phases – such as Kitaev’s toric code [11] – are ubiquitous in fault-tolerant quantum computing. While it is clear at a coarse level that the natural robustness of these phases to noise offers great potential, how to precisely translate these features into useful, fault-tolerant computational structures can be a nontrivial task. We will be focussing on a family of ordered, many-body spin models called symmetry-protected topological phases for their use in quantum information storage and processing. We discuss how thermally stable SPT phases can be used as resources for fault-tolerant measurement-based quantum computation, as well as for quantum memories with macroscopic lifetimes. In the remainder of this introduction chapter, we review some of the basic concepts of quantum computation and topological phases of matter.

1.2 Quantum computing

There are many radically different approaches to quantum computing, varying greatly in both the method of computation as well as physical realisation. The most prominent models of computation are the circuit model [13], adiabatic quantum computation [14], topological quantum computation [11, 15], and measurement-based quantum computation [16]. While the models are all very distinctive, the computational content of each approach is the same [17–20]. In developing physical architectures, it is beneficial to have a variety of approaches, as some architectures are more suited to a particular model. For example, measurement-based quantum computation is an attractive model for architectures based on linear optics [21, 22] or trapped ions [23, 24].

The benefit of having a variety of approaches is the additional flexibility that is offered in the development of physical architectures, as physical manifestations of some models may be preferable in some architecture over others (for example, measurement-based quantum computation is an attractive model for architectures based on linear optics [21, 22] or trapped ions [23, 24]). In the remainder of this section, we will outline some models of computation that will be used throughout the thesis, introduce quantum-error correction, and outline some methods of fault-tolerance.

1.2.1 Preliminary notation

The central ingredient common to all of these approaches is the qubit – the elementary unit of quantum information. A qubit is the smallest quantum degree of freedom, and its statespace is given by the two-dimensional vector space \mathbb{C}^2 . With n -qubits, the statespace is given by the n -fold tensor product

$$\mathcal{H}_n = \underbrace{\mathbb{C}^2 \otimes \dots \otimes \mathbb{C}^2}_{n \text{ times}} \cong \mathbb{C}^{2^n}. \quad (1.1)$$

A standard basis for the n -qubits is the computational basis

$$\mathcal{B} = \{|a_1, a_2, \dots, a_n\rangle \mid a_i \in \mathbb{Z}_2\}. \quad (1.2)$$

An important set of operations is given by the Pauli operators on one qubit

$$I = \begin{pmatrix} 1 & 0 \\ 0 & 1 \end{pmatrix}, \quad X = \begin{pmatrix} 0 & 1 \\ 1 & 0 \end{pmatrix}, \quad Y = \begin{pmatrix} 0 & -i \\ i & 0 \end{pmatrix}, \quad Z = \begin{pmatrix} 1 & 0 \\ 0 & -1 \end{pmatrix}. \quad (1.3)$$

The group generated by these operators is the Pauli group on one qubit $\mathcal{P}_1 = \langle X, Y, Z \rangle$. On n -qubits the Pauli group is given by the n -fold tensor product

$$\mathcal{P}_n = \underbrace{\mathcal{P}_1 \otimes \mathcal{P}_1 \otimes \dots \otimes \mathcal{P}_1}_{n \text{ times}} \quad (1.4)$$

The Pauli group provides a basis for linear operators, and an important set to describe many quantum operations. Unless stated otherwise, we leave n implicit and just refer to the Pauli group on n qubits as \mathcal{P} .

The Clifford group \mathcal{C} is the normaliser of the Pauli group \mathcal{P} ,

$$\mathcal{C} := \mathcal{N}(\mathcal{P}) = \{u \in U(2^n) \mid uPu^\dagger \in \mathcal{P} \quad \forall P \in \mathcal{P}\}. \quad (1.5)$$

It is generated by the Hadamard gate H , the Phase gate S , and the two qubit controlled-not gate CX , acting on all possible qubits or pairs of qubits:

$$H = \frac{1}{\sqrt{2}} \begin{pmatrix} 1 & 1 \\ 1 & -1 \end{pmatrix}, \quad S = \begin{pmatrix} 1 & 0 \\ 0 & i \end{pmatrix}, \quad CX = \begin{pmatrix} 1 & 0 & 0 & 0 \\ 0 & 1 & 0 & 0 \\ 0 & 0 & 0 & 1 \\ 0 & 0 & 1 & 0 \end{pmatrix}. \quad (1.6)$$

For a fixed number of qubits n , the Clifford hierarchy is defined by setting $C_1 = \mathcal{P}$, and sequentially defining

$$C_D = \{u \in U(2^n) : uPu^\dagger \in C_{D-1}, \forall P \in \mathcal{P}\} \quad (1.7)$$

for $D \geq 2$. In particular, we have that C_2 is the Clifford group on n -qubits, while important non-Clifford operations are the T gate and the three qubit controlled-controlled- Z gate CCZ ,

$$T = \begin{pmatrix} 1 & 0 \\ 0 & \sqrt{i} \end{pmatrix}, \quad CCZ = \text{diag}(1, 1, 1, 1, 1, 1, 1, -1), \quad (1.8)$$

which both belong to C_3 . Important to note is that for $D > 2$, C_D is no longer a group, but is a finite set.

1.2.2 The circuit model

A particularly useful way of thinking about computation (while ignoring details of the exact physical implementation) is through the circuit model. In the circuit model, states are prepared, undergo unitary evolution, and finally, are measured. The unitary evolution depends on the specific algorithm that is to be implemented, and is realised through a sequence of *gates* acting on the Hilbert space of some number of qubits. Typically, it is assumed that preparations and final measurements are in the computational basis. The output of the computation is encoded in the final state and must be reliably deducible from the measurement outcomes. Since measurements are probabilistic in nature, we only require that the correct solution is acquired with a success probability of strictly greater than $1/2$; the circuit can then be repeatedly run to gain an arbitrarily high probability of success.

Quantum circuits are typically represented by a number of wires and boxes. Wires represent a qubit evolving in time (with time running from left to right), and boxes represent either gates or measurements acting on qubits at a particular time. An example of a quantum circuit is depicted in Fig. 1.1.

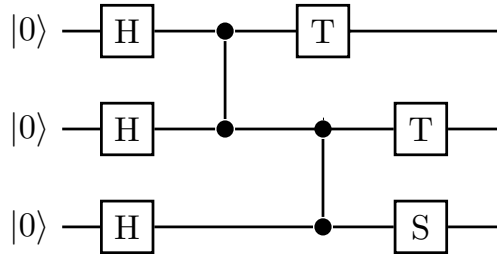


Fig. 1.1 An example quantum circuit. Qubits are initialised on the left, and a number of gates are applied, in order from left to right.

The gates that of a quantum circuit must be drawn from some gate-set. Critically, if arbitrary quantum computations are to be possible, then the gate set must be *universal*. We say

a set of gates \mathcal{G} is universal for quantum computation if any unitary operation can be arbitrarily well approximated by a quantum circuit using gates from \mathcal{G} . In other words, the unitary circuits on n qubits with gates from \mathcal{G} are dense in $U(2^n)$ (with metric described below). It turns out that discrete sets of universal gates exist, a standard choice is given by $\mathcal{G}_{st} = \{H, S, CX, T\}$. Note that we have redundantly included $S = T^2$, as it is often the case that T gates are costly to implement compared to the Clifford gate S . Many other universal gate sets exist, for example, $\{H, S, CX, A\}$ is universal for any non-Clifford A , and $\{CCZ, H\}$ is also universal [25].

While circuits generated from a discrete gate set can not synthesise general unitaries exactly, in practice we are only interested in approximations thereof. In particular, we can determine the approximation error between an ideal unitary V and one generated by a finite set of gates U by the operator norm

$$d(U, V) = \|U - V\|_{op} = \sup_{|\psi\rangle} \|(U - V)|\psi\rangle\|. \quad (1.9)$$

Universality of \mathcal{G}_{st} means that for any given target unitary V on n qubits, there exist sequences of n qubit circuits C_i , $i = 1, 2, \dots$ of increasing depth, comprised of gates from $\{H, S, CX, T\}$ such that $d(C_i, V) \rightarrow 0$. Closeness of unitaries in this metric means that the corresponding probability distributions upon measurement (for any POVM) are also close. The Solvay-Kitaev algorithm provides a way to produce an approximation of any unitary, given a universal gate set. While the algorithm is efficient in inverse error and Hilbert space dimension in terms of run-time and number of gates required, it is **not** efficient in number of qubits. In fact, approximating an arbitrary n -qubit unitary is very hard, requiring, in general, exponentially many gates (for a fixed error).

1.2.3 Measurement-based quantum computation

The approach of measurement-based quantum computation (MBQC) is starkly different to that of the circuit model. In contrast to the circuit model – where computation is specified by a sequence of unitary gates on an initial product state, followed by a computational basis measurement – MBQC proceeds by performing single qubit measurements on a fixed, highly entangled resource state. The choice of measurements determines the algorithm to be implemented, and with the right resource state, arbitrary quantum computations are possible. These single qubit measurements drive the computation, consuming entanglement in the process. In addition to being a useful framework for certain architectures (such as linear optical architectures [21, 22] and trapped ion architectures [23, 24]), MBQC is also a powerful theoretical framework which allows us to investigate computational usefulness of phases of matter. We discuss this idea in more detail in Sec. 1.4.

Crucially, since measurements are in general random, to ensure deterministic computation one must adapt measurement bases depending upon previous measurement outcomes. This complexity of deciding these future measurement outcomes is often very tame, and can be performed with a small amount of classical side processing (for most models only mod-2 addition is required) [26, 27]. As such, entanglement in the resource state alone is not enough; we must also be able to extract correlations in the classical data returned from measurements. Indeed, too much entanglement can result in the resource state being useless for MBQC [28].

In order to perform longer computations or computations involving more qubits, only the size of the resource state needs to be increased. For certain families of resource states, adaptive single qubit measurements are sufficient to perform universal quantum computation, and such families are known as universal resource states. There are in fact many known families of universal resource states. The most well known are the square lattice graph states (which we will describe further below) [26, 20], other graph states [29, 30], various AKLT states [31–34], Hypergraph states [35, 36] and more [37–40].

Graph states

For MBQC, an important class of resource states are the cluster states, also known as graph states. These states can be defined for any graph, and universality of the state depends heavily upon the underlying graph. Let $G = (V, E)$ be a graph, where V is a set of vertices and E a set of edges. Then a graph state $|\psi_G\rangle$ corresponding to the graph G can be defined as follows:

1. For each vertex $v \in V$, place a qubit prepared in the $|+\rangle = \frac{1}{\sqrt{2}}(|0\rangle_v + |1\rangle_v)$ state.
2. For each edge $e = (v, w)$ apply the controlled- Z gate

$$CZ_e = \exp\left(\frac{i\pi}{4}(1 - Z_v)(1 - Z_w)\right). \quad (1.10)$$

The circuit $U_E = \prod_{e \in E} CZ_e$ is called the entangling circuit. As the state prior to application of U_E is a $+1$ eigenstate of X_v for $v \in V$, we can find new $+1$ -eigenoperators for the resource state by conjugating X_v by U_E :

$$K_v := U_E X_v U_E^\dagger = X_v \prod_{w \in \mathcal{N}(v)} Z_w, \quad (1.11)$$

where $\mathcal{N}(v)$ is the neighbourhood of v , consisting of all vertices sharing an edge with v . The operators K_v are called graph stabilizers or cluster stabilizers, since the graph state satisfies

$$K_v |\psi_G\rangle = |\psi_G\rangle \quad \forall v \in V. \quad (1.12)$$

In general, graph states can be highly entangled [29]. Universality depends on the underlying family of graphs used. The canonical example is the square lattice cluster state [26]. On this lattice measurements in the X , Y , Z , and $\frac{1}{\sqrt{2}}(X \pm Y)$ basis are sufficient to perform universal quantum computation. One can view measurements on the square lattice cluster state as simulating the circuit model: Pauli Z measurements are used to print out computational wires, X and Y are used to enact Clifford gates, and $\frac{1}{\sqrt{2}}(X \pm Y)$ measurements are used to perform T gates. Adaptivity amounts to determining the sign in the measurement $\frac{1}{\sqrt{2}}(X \pm Y)$, and can be done by evaluating the parity of certain previous measurement outcomes. Schematically, this is represented in Fig. 1.2.

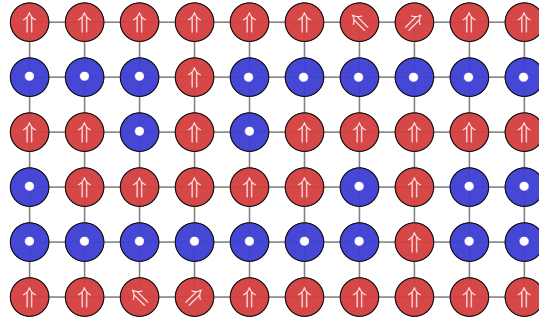


Fig. 1.2 Schematic for measurement-based quantum computation on a square lattice graph state. Simulated time runs from left to right. Qubits live on the vertices of a square lattice. Measurements in the Z -basis are depicted by blue nodes, measurements in the X -basis are depicted by red nodes with upward facing arrows. Measurements in the $\frac{1}{\sqrt{2}}(X \pm Y)$ -basis are depicted by red nodes with rotated arrows.

1.2.4 Quantum error correction

One of the primary underlying challenges of quantum information science is that coherent quantum systems are fragile, and the information stored in a quantum system can decohere easily. Since all of the operations discussed in the previous section (state preparations, unitary gates, measurements) are all prone to error in any physical realisation, we must ensure that the computation is performed in a way that errors can be tolerated. In order to protect information, we must use error-correcting codes. Quantum error correction is the fundamental ingredient that allows fault-tolerant quantum computing to be possible.

The simplest example of a classical error-correcting code is the repetition code. In this code, the goal is to protect one bit of information. To achieve this, the information is stored redundantly

$$0 \mapsto \underbrace{00 \dots 0}_n \quad 1 \mapsto \underbrace{11 \dots 1}_n. \quad (1.13)$$

Provided that errors occur to less than half of the bits, then we can successfully recover the encoded information using a majority vote. Therefore, if the probability of an error that flips a bit is sufficiently low, then the repetition code provides enhanced protection of classical information.

The philosophy behind quantum error correction is similar: we redundantly encode quantum information by embedding it in a larger Hilbert space. The added difficulty in finding quantum error-correcting codes comes from: (1) sources of error can come in multiple bases, (2) measurements can in general collapse the state, destroying the quantum information, (3) the no-cloning theorem [41] prevents us from copying arbitrary states. Fortunately, these challenges only serve as inspiration, and the field of quantum error correction is rich with interesting examples.

Stabilizer codes

One of the most well-known and rich frameworks to construct quantum error-correcting codes is the stabilizer formalism, introduced by Gottesman [42]. This formalism provides an efficient way of expressing a large class of quantum error-correcting codes, codestates, the effect of errors, and the measurements used to diagnose these errors.

A stabilizer code on n qubits is specified by an abelian subgroup \mathcal{S} of the Pauli group $\mathcal{P} = \mathcal{P}_n$, not containing $-\mathbf{1}$. The codespace \mathcal{C} is specified by the mutual $+1$ -eigenspace of all operators in \mathcal{S} :

$$\mathcal{C} = \{|\psi\rangle \in \mathbb{C}^{2^n} \mid g|\psi\rangle = |\psi\rangle \ \forall g \in \mathcal{S}\}. \quad (1.14)$$

States in \mathcal{C} are referred to as codestates, and elements of \mathcal{S} are called stabilizers. Codestates can be mapped between each other by means of logical operators. The logical Pauli operators are given by elements

$$\mathcal{L} = \mathcal{Z}_{\mathcal{P}}(\mathcal{S}), \quad (1.15)$$

where $\mathcal{Z}_{\mathcal{P}}(\mathcal{S})$ is the centraliser of \mathcal{S} in \mathcal{P} , consisting of all Pauli operators that commute with all stabilizers. Logical operators include stabilizers, which act trivially on codestates, along with nontrivial Pauli operators which are elements of $\mathcal{Z}_{\mathcal{P}}(\mathcal{S}) - \mathcal{S}$. Since logical operators have equivalent action on \mathcal{C} up to multiplication of stabilizers, we can group them into equivalence classes given by $\mathcal{Z}_{\mathcal{P}}(\mathcal{S})/\mathcal{S}$.

For a stabilizer code on n qubits with $n - k$ independent stabilizer generators, we have $\dim(\mathcal{C}) = 2^k$, as well as $\mathcal{Z}_{\mathcal{P}}(\mathcal{S})/\mathcal{S} \cong \mathcal{P}_k$. This means that for a stabilizer group with $n - k$ independent generators, we can encode k logical qubits. Here, a set of stabilizers $\mathcal{S} =$

$\langle g_1, \dots, g_{n-k} \rangle$ are independent if for some binary numbers $\alpha_j \in \mathbb{Z}_2$, we have

$$\prod_{i=1}^{n-k} g_j^{\alpha_j} = \mathbf{1} \implies \alpha_j = 0 \quad \forall j. \quad (1.16)$$

We have already seen an example of a stabilizer code; the graph state of Eq. (1.12) which has a stabilizer group given by the operators in Eq. (1.11) and encodes no logical qubits (the codespace consists of a unique state – the cluster state). Other important classes of stabilizer codes include the Shor code [43], Reed-Muller codes [44, 45], CSS codes [46] which allows us to construct quantum codes based on certain pairs of classical codes, and topological codes, which we discuss in the next section.

Errors and decoding

Errors are detected by performing stabilizer measurements. These measurements produce no information about the logical state, but only about the location of errors. If we write the stabilizer group in terms of a set of independent generators $\mathcal{S} = \langle g_1, \dots, g_{n-k} \rangle$, the Hilbert space decomposes as

$$\mathcal{H} = \bigoplus_{\mathbf{s}} C_{\mathbf{s}}, \quad (1.17)$$

where each choice of $\mathbf{s} \in \mathbb{Z}_2^{n-k}$ labels a set of eigenspaces of $\mathbf{g} = (g_1, \dots, g_{n-k})$. Namely, for each $\mathbf{s} = (s_1, \dots, s_{n-k})$, the subspace $C_{\mathbf{s}}$ is defined by

$$C_{\mathbf{s}} = \{|\psi\rangle \in \mathbb{C}^{2^n} \mid g_i |\psi\rangle = (-1)^{s_i} |\psi\rangle, \forall i\}. \quad (1.18)$$

The codespace is given by $C_{\mathbf{0}}$, where $\mathbf{0} = (0, \dots, 0)$.

For any state within the codespace, measurement of a stabilizer produces a +1 outcome. Upon measurement of a (perhaps overcomplete) generating set of stabilizers, a syndrome is obtained: a list of measurement outcomes. Any −1 outcomes indicate the presence of errors. A syndrome of \mathbf{s} means the post measured state belongs to the syndrome space $C_{\mathbf{s}}$. Error correction consists of choosing a Pauli operator R that returns the erred state to $C_{\mathbf{0}}$. Error correction is successful if no logical fault has been implemented in the process, that is, if $RE \in \mathcal{S}$. The algorithm that determines the correction operator is the decoder. It receives a syndrome (corresponding to some error) and returns a recovery operator R .

A stabilizer code can correct a set of errors $\mathcal{E} = \{E_a \mid a \in A\} \subset \mathcal{P}_n$ (for some index set A), if and only if $E_a E_b \notin \langle i \rangle \mathcal{S}$, $\forall E_a, E_b \in \mathcal{E}$. For any Pauli operator P , we define $\text{wt}(P)$ to be the number of nontrivial Pauli factors of P (for example $\text{wt}(X \otimes \mathbf{1} \otimes Z \otimes \mathbf{1}) = 2$). The distance of the code d is defined to be the smallest weight of any nontrivial logical Pauli

operator. That is

$$d = \min_{P \in \mathcal{Z}_{\mathcal{P}}(\mathcal{S}) - \mathcal{S}} \text{wt}(P). \quad (1.19)$$

The distance is used as useful tool in assessing how tolerant a code is to Pauli errors. A code with distance d can detect Pauli errors of weight up to $d - 1$, and can correct any Pauli errors of weight up to $\lfloor \frac{d-1}{2} \rfloor$. We refer to a stabilizer code on n qubits which encodes k logical qubits with distance d , as an $[[n, k, d]]$ code.

In general, measurements can be faulty and therefore stabilizers must be repeatedly measured to obtain reliable information about the location of errors [47]. Remarkably, some codes admit single-shot error correction, whereby only a single round of stabilizer measurements is required to obtain reliable information about the location of errors. Examples of single-shot codes are the gauge color code in three-dimensions [48] and the self-dual four-dimensional toric code [47]. As error correction is in general resource intensive and complex, single shot codes offer a competitive advantage.

Subsystem codes

An important generalisation of stabilizer codes are subsystem codes [49–52]. A subsystem code can be constructed by declaring some logical qubits as gauge degrees of freedom that are not used to encode logical information. Logical information is therefore encoded in a subsystem of the stabilizer codespace. A prominent advantage of such codes is that the measurement of stabilizers can sometimes be replaced by the measurement of simpler, lower weight operators (known as gauge operators). We will see examples of such codes in Chapters 3 and 4.

1.2.5 Topological codes

Perhaps one of the most important classes of stabilizer codes are topological codes. Topological codes are stabilizer codes that encode qubits in global or topological degrees of freedom and detect errors using only local stabilizer measurements. Assuming that errors act locally, they cannot corrupt the logical information if encoded in global degrees of freedom.

We first note that a topological code is really a family of codes, $\{\mathcal{S}_i \mid i = 1, 2, \dots\}$, where $(\mathcal{S}_i)_i$ constitutes a sequence of codes of increasing size. A D -dimensional topological code family consists of:

1. Qubits arranged with a finite density on a D -dimensional manifold M^D . For example, they may be on the sites of a D -dimensional lattice.
2. A stabilizer group that can be locally generated. Namely, there exists a generating set $\mathcal{S} = \langle g_1, \dots, g_{n-k} \rangle$ such that $\text{Supp}(g_i)$ is contained within a ball of finite radius. We also

require that each qubit is in the support of only a constant number of stabilizers in the generating set.

For a topological code to be nontrivial, we also require that the distance of the code scales with increasing system size.

Two-dimensional topological codes are widely pursued for a variety of reasons. Firstly, no long range interactions are required for syndrome extraction, which is a desirable feature for architectures with locality constraints. Secondly, the degree of protection they offer is readily tunable, as the distance can be scaled to achieve a target logical error-rate. The most important families of topological stabilizer codes are the two dimensional surface codes (including the toric code and planar code), originally due to Kitaev [7, 11] their higher dimension versions [47, 53], and the color codes in two dimensions [54] and higher [55, 56].

Toric codes perhaps best exemplify the beautiful concept behind topological codes; they can be defined on any cellulation of a D -dimensional manifold. After choosing a cellulation, the surface code is uniquely defined by an integer $k \in \{1, \dots, D-1\}$. To each k -cell we place a qubit, to each $(k+1)$ -cell p we define a Z -stabilizer Z_p , and to each $(k-1)$ cell v we define an X stabilizer X_v . The Z_p stabilizers are given by a product of Pauli- Z on all qubits on the boundary of the $(k+1)$ cell p , while X_v stabilizers are given by a product of Pauli- X on all qubits incident to the $(k-1)$ cell v . These operators always commute, and the stabilizer group \mathcal{S} is generated by all such stabilizers. Logical operators are associated with homologically nontrivial cycles of the cellulation. To each nontrivial k -cycle, a logical Z operator is defined by a product of Z operators along the cycle. Similarly, we can define a logical X operator for each nontrivial k -cocycle. As nontrivial (co)cycles are global features of the manifold, the logical information is topologically encoded.

The information storage capabilities of topological codes in 2D have been well characterised. In particular, topological codes with n qubits, encoding k logical qubits with distance d must satisfy the bound $kd^2 \leq O(n)$ [57]. The toric code saturates this bound. For subsystem codes with local generators this can be relaxed to $kd \leq O(n)$ [58] (and is known to be tight [58, 59]), however they must also satisfy $d^2 \leq O(n)$ [60, 61]. This motivates further study of two-dimensional topological subsystem codes for their improved coding properties [59].

Self-correcting quantum memories

Performing error correction is resource intensive and a complex process. A potential solution is to find memories that are self-correcting. A self-correcting quantum memory is the quantum analogue of a classical hard-drive, that allows information to be robustly stored for long periods of time. Such a memory does not require active error correction, and instead naturally dissipates errors that build up over time. By constructing larger systems, the memory time can grow

without bound. Self-correction is known to be possible in 4D (for sufficiently low temperatures), with the first known example being the 4D toric code [47, 62]. Whether such models can exist in three-dimensions or less is one of the major unsolved problems in quantum information, and one with important implications to the future of quantum computing. We will discuss self-correction in much greater detail in Chapter 3.

1.2.6 Fault-tolerant logic

In order to perform fault-tolerant quantum computation, we must also be able to perform logic gates in a protected way. In order to do so, we must make sure we do not spread errors by too much. In this way, any additional errors that are introduced during the logical gates can be handled by error correction, provided the error-rate is sufficiently low. In the following, we outline some methods of performing fault-tolerant logical gates in topological codes.

Locality-preserving logical gates

One of the popular methods for achieving fault-tolerant logic in topological codes is to find transversal implementation of logical gates. For a code on n -qubits, a single qubit logical gate U is transversal if it can be implemented in the form

$$U = \bigotimes_{i=1}^n U_i, \quad (1.20)$$

for some single qubit gates U_i . The reason such an implementation is desirable, is that single qubit operations do not spread errors. If \mathcal{E} is some set of errors on the code, and U is transversal as above, then $\text{Supp}(U\mathcal{E}U^\dagger) \subseteq \text{Supp}(\mathcal{E})$, meaning the set of support of the error has not grown by mapping the logical state $|\psi\rangle$ to $U|\psi\rangle$ (of course the local gates U_i may themselves be faulty). More generally, one can consider logical gates that are transversal with respect to some partition of qubits, meaning that the logical gate factors (with respect to the tensor product) across the partition. Notable examples of codes with transversal gates are the 2D color codes [54] which admit all Cliffords transversally, and the 3D color codes, which have a transversal logical T gate.

It is known that no single code admits a universal set of transversal gates due to a theorem of Eastin and Knill [63]. In an effort to circumvent this theorem, one often considers generalisations of transversality, such as constant-depth quantum circuits or locality-preserving quantum circuits. Constant-depth quantum circuits provide a similar degree of protection, as the propagation of errors is limited to a bounded light cone. For a lattice in D -dimensions, a constant-depth

quantum circuit U takes the form

$$U = \prod_{j=1}^d C_j, \quad C_j = \bigotimes_{i=1}^{n_j} U_i^{(j)}, \quad (1.21)$$

where d is constant (independent of the system size) called the depth, and each of the unitaries U_i is supported on a ball of constant radius. Logical gates of this form are examples of *locality-preserving gates*, as errors can only spread by a constant amount, in this case, by a distance dr , where r is the maximum range of any gate U_i .

However, the group of logical gates that can be implemented by constant-depth quantum circuits is also constrained by dimension. Namely, Bravyi and König have shown that for a D -dimensional topological code, gates implementable by constant-depth quantum circuits must belong to the D -th level of the Clifford Hierarchy C_D [64]. This means in particular that 2D topological codes cannot implement non-Clifford gates by constant-depth quantum circuits, and that topological codes in any dimension only admit a finite set of constant-depth logical gates. The Bravyi König result has been extended to subsystem codes by Pastawski and Yoshida [65], where they also demonstrate several other trade-offs between desirable code-properties – such as code-distance or loss-tolerance – with fault-tolerant implementability of logical gates [65].

Topological defect based quantum computation

Looking beyond transversal gates and locality-preserving logical gates there are a variety of alternatives. A popular approach is to encode into global degrees of freedom corresponding to topological defects. Such defects are regions of inhomogeneity in the code, and can take for example the form of punctures in the surface code [66], or lattice dislocations called twist defects [67]. Topological defects are physical defects in the lattice or underlying manifold that the code resides on, and can be considered as modifications of the original code.

These topological defects can carry charge, and therefore be used to encode quantum information. By making the defects large or well separated, the information is immune to local errors and operations; only operations that enclose a defect or connect two defects can access the quantum information. Topological defects can have rich interplay with each other, and one can perform logical gates by braiding and fusing them. For example, in the surface code, the braiding of punctures and twists can be used to realise encoded Clifford gates. These operations can be realised by adiabatically varying the code, for instance through a sequence of measurements that alter the defect locations [68, 69]. Such a sequence of measurements can be viewed as a series of modifications to the code, and are commonly referred to as code deformation.

1.2.7 Lattice surgery

Lattice surgery is an alternate approach for surface codes to realise encoded gates [70–72]. The idea is that multi-qubit logical Pauli measurements between different logical qubits can be used to achieve logical Clifford gates. In many topological codes, multi-qubit logical Pauli measurements can be performed locally and in a fault-tolerant way, and this is called lattice surgery. In the case of surface codes, if arranged appropriately, logical Pauli measurements can be implemented by measuring local Pauli operators between neighbouring surface codes. The operators measured can be viewed as the stabilizers of a larger code and therefore have an interpretation of modifying the underlying lattice structure (hence the name). Lattice surgery has been extended to more general topological codes, such as color codes [73].

Gauge fixing

Gauge-fixing is a procedure where Pauli measurements and subsequent Pauli corrections are performed to map between different stabilizer codes. Gauge fixing is particularly advantageous when used to switch between two codes with transversal operations that combined are universal. Best described using the language of subsystem codes [49, 51], one can interpret the measurement as projecting certain (gauge) degrees of freedom into a fixed state (up to a potential Pauli correction). In particular, a subsystem code is a stabilizer code where some of the logical qubits are not used to protect information and are referred to as gauge qubits. Measurements and operations on these gauge qubits do not disturb the encoded information, and as such we are free to modify them as we please. By fixing them in different states we can map between different stabilizer codes

Prominent examples of universal fault-tolerant logic by gauge fixing include the Paetznick and Reichardt scheme based on triorthogonal codes [74], and dimensional jumping between the 3D color code (admitting transversal T) and the 2D color code (admitting transversal Cliffords) due to Bombin [75, 76].

Fault-tolerant MBQC

Finally, we comment on fault-tolerance protocols for MBQC. Due to the equivalence of the circuit model and MBQC, one can in principle construct MBQC variants of the aforementioned fault-tolerant protocols. Code deformation within the surface code is naturally expressed within the MBQC framework, as originally proposed by Raussendorf *et. al.* [66]. The idea is to use a three-dimensional cluster state, upon which measurements simulate the manipulation of punctures within the surface code. In this setup, two of the lattice dimensions correspond to the surface code dimensions, and the third corresponds to simulated time. Defects in the

surface code can be introduced and braided by single qubit Z measurements, and local X measurements used to propagate the code through time. These measurements can be used to reconstruct stabilizer check operators to detect errors, as the resource state is constructed such that $\mathcal{M} \cap \mathcal{S} \neq \emptyset$, where \mathcal{M} is the group generated by single qubit measurements, and \mathcal{S} is the cluster state stabilizers of Eq. (1.11). The existence of these check operators is essential for fault-tolerant computation.

In Chapter 4 we will explore this concept in much greater depth, discussing generalisations and modifications to this approach. In particular, we will show how to construct graph states and measurement patterns that simulate general gauge-fixing, code deformation and lattice surgery approaches on arbitrary stabilizer (and subsystem) codes.

1.3 Topological phases of matter

One of the fundamental questions of condensed matter is to classify what phases can exist and what are their properties. One of the most successful theories in this direction is Landau's symmetry breaking paradigm [77]. Landau classified systems according to the types of symmetries they break, describing ordered states in terms of local order parameters. Crystals and ferromagnets are prominent examples of the types of systems captured by this framework. However it was realised that certain quantum phases of matter did not fit into this paradigm, for example spin liquids and certain quantum hall systems [78–83]. Such systems are known as topological phases of matter, and their existence is fascinating not only from the perspective of fundamental physics, but for their application to quantum information too.

In this section we will outline what topological phases are and several ways of characterising them. We emphasise that the field is still rapidly changing and definitions are in flux, as new classes of models are being discovered.

1.3.1 Many-body spin models

With the abundance of exotic new materials being discovered, the tools used to model and understand them have become more sophisticated. Quantum many-body models have had a variety of success in elucidating properties of existing systems and predicting new materials. Examples include quantum spin liquids, topological insulators, integer and fractional quantum Hall materials, and many more [84–86, 82, 87]. We focus on many-body models where the constituent degrees of freedom are hard-core bosons, and such models can be described by tensor products of finite dimensional spins.

The models that we consider in this thesis describe strongly interacting, gapped, local spin systems. The Hilbert space of such systems consist of tensor products of finite dimensional spins,

which we will often refer to as qubits (for spin half particles) or qudits (for higher dimensional spins). These spins can be arranged with some finite density in D -dimensional space, and most commonly are assumed to live on the sites of a finite degree graph or lattice. The Hamiltonians that describe these systems are given by sums over local terms, where a term is local if it is supported on a ball of finite radius and is of bounded strength (one can consider nonlocal interactions, provided the strength of the term decays rapidly with the support radius).

Importantly, we do not consider a single system, but a sequence of systems of increasing size, and we are most concerned with the ground space properties after taking the thermodynamic limit. One can coarsely distinguish between two very different types of systems depending on whether the energy gap remains open or if it closes. Here, the energy gap, or more simply the gap, is the difference between the ground space energy and the first excited space energy (where any exponentially small splitting between approximately degenerate ground states is ignored). If the gap remains uniformly bounded away from zero, we say the system is gapped, otherwise it is gapless. We will primarily be concerned with gapped systems in this thesis.

1.3.2 Topological order

Topologically ordered systems are states that realise interesting global patterns of entanglement. There are many ways of characterising and defining topological order. Thus far, there is no universally agreed upon definition that is applicable to systems in all dimensions. The central idea common to all definitions is that topologically ordered systems should be distinct from trivial non-interacting spin systems. The term topological order can apply to either a state or a Hamiltonian, and we will describe both situations.

Closely related is the idea of a topological phase, which is an equivalence class of topologically ordered states sharing the same global features. Two Hamiltonians are said to belong to the same phase, if there exists a gapped path of local Hamiltonians that connects them. Here, a path is defined by smoothly varying parameters in the Hamiltonian. This allows us to define the trivial phase, which is that of a non-interacting, gapped local Hamiltonian that has a product state as its ground state. Any phase that is not the trivial phase is a topological phase, and any Hamiltonian that does not belong to the trivial phase is said to be topologically ordered. Quantum phase transitions occur when parameters in the system are tuned such that the gap closes. Quantum phase transitions correspond to non-analytic behaviour in the ground space and can result in changes in the macroscopic features of a system.

The topological stability theorems [88–90] give a precise definition for topological order. The definitions of topological order presented in Refs. [88–90] are, roughly speaking, that a system possesses a ground space containing global degrees of freedom that are inaccessible to local operations. For instance, degenerate ground states of a topologically ordered system must be

locally indistinguishable, meaning the expectation value of any local observable is the same for any ground state. They prove that for gapped, local commuting projector models meeting their definition, local perturbations can only modify the energy spectrum in a controlled way, and that the gap of the system remains open, provided the local perturbation strength is sufficiently small. Thus the essential feature of a topological phase in this sense, is that it is robust to all local perturbations.

In terms of states, topological order is characterised by long-range entanglement that can not be removed by local unitaries [91, 92]. A state (that is a ground state of a gapped local Hamiltonian) is said to be topologically ordered if it cannot be approximately mapped to a product state, using a local unitary. Here a local unitary can take many different forms, depending on the application or framework of interest. For instance, a local unitary may be considered a constant-depth quantum circuit, where all of the gates are local. Alternatively, it may take the form of evolution under a gapped, local Hamiltonian with bounded strength terms, for a bounded amount of time [92]. The fact that topological order can be characterised by quantum circuit complexity is a remarkable discovery.

One can similarly define topological phases as equivalence classes of ground states. We say two ground states belong to the same phase if they can be related by a local unitary (again, the local unitary may take the form of, for example, a constant-depth quantum circuit, or evolution under a local Hamiltonian). Here, the trivial phase is the one containing all product states, and states within this phase are said to be short range entangled. States that do not belong to the trivial phase are called long range entangled, or topologically ordered. The Hamiltonian-based definition and the state-based definitions of phases are related. Gap-preserving deformations of a Hamiltonian induce local unitary evolution in the ground space by means of (quasi-)adiabatic evolution [93, 94, 91]. Conversely, any two states equivalent under local unitary evolutions also have path connected parent Hamiltonians (conjugating a gapped local Hamiltonian by a local unitary gives another gapped local Hamiltonian).

Properties of topologically ordered phases

One of the hallmarks of topologically ordered systems, and often used as the defining feature, is the existence of anyonic excitations. Anyons are particles that can exist in 2D systems that have exchange statistics that are neither fermionic nor bosonic, and are perhaps one of the most fascinating features of topologically ordered systems. The presence of anyonic excitations is closely related to the existence of topological degeneracy, where the ground space degeneracy depends on the topology of the manifold it is defined on. The toric code provides an illustrative example, when defined on a closed 2D surface, the ground space degeneracy is given by 4^g where g is the genus of the surface. These degenerate ground states are locally indistinguishable, in that the expectation value of any local observable is the same. This rules out the possibility of

having any local order parameter, and also implies that the ground space degeneracy is stable, in that it cannot be lifted by any local perturbation, provided it is sufficiently small.

Another important way of characterising topologically ordered systems is to define topological invariants: quantities that do not change under smooth deformations of the ground space (for example, ground space degeneracy). An important topological invariant is the topological entanglement entropy, first introduced by Kitaev and Preskill [95]. Groundstates of gapped many-body systems generically obey an area law for entanglement [96, 97], meaning the von Neumann entropy of a reduced state on some region is expected to scale in proportion to the boundary of that region. However, for topologically ordered systems such as the toric code, it was discovered that there can be additive corrections to this law [98]. For a 2D system, the topological entanglement entropy (TEE) arises as a constant additive correction to the entanglement area law, and a nonzero value signifies topological order. The TEE is closely related to the existence of anyonic excitations, its value can be expressed in terms of the total quantum dimension of the system (a quantity determined by the number of anyonic excitations and their fusion channels). Thus, except in spurious cases [99–101], the topological entanglement entropy provides a way of diagnosing nontrivial topological order.

Due to the robustness to local errors, topologically ordered systems are promising candidates for quantum memories. In particular, the degenerate ground space of a topologically ordered system can be used as a codespace, where local errors do not corrupt the information. Kitaev’s toric code [11] – an example of a topologically ordered spin model – provides the most well-known instantiation of this idea, as it is currently one of the most actively pursued error-correcting codes in both theory and experiment.

We finally remark that defining topological phases in the presence of measurements is an interesting problem. Measurements are somewhat pathological in that they can enable transfigurations between states with very different amounts of entanglement. For example, a depth-1 circuit of single qubit measurements can be used to drive between a 2D cluster state (topologically trivial) and a toric code state (topologically nontrivial) [102]. If however, we model the measurements as being implemented by an adiabatic evolution [103], then one recovers the expected circuit depth that is required to transform between these states. Further investigation in this direction is an interesting problem.

1.3.3 Symmetry-protected topological order

Symmetries are ubiquitous in nature, and it turns out that the types of topological phases that can exist are much richer when symmetry is taken into account. A recent breakthrough in condensed matter physics is the discovery of new types of ordered short-ranged entangled systems that preserve certain symmetries, and such systems are said to exhibit symmetry

protected topological (SPT) order. The first discovery of such a system was a new type of 2D time reversal invariant band insulator, now known as a topological insulator [104–106]. Since then, there has been many newly predicted and discovered SPT ordered models, including in strongly many body spin models, where for example, SPT ordered systems can exist in one-dimension [107] while intrinsically topologically ordered systems (i.e. without symmetry) require at least two-dimensions.

In terms of Hamiltonians, a gapped many-body system is said to be SPT ordered if the following conditions are met. Firstly, the Hamiltonian must be invariant under a set of symmetries, and these symmetries are not spontaneously broken. Secondly, there is no gapped, symmetry-preserving path of local Hamiltonians that connects to a trivial model. Thirdly, if the symmetry is broken, it is possible to find a gapped path connecting to a trivial model. Here, a trivial model is any symmetry respecting Hamiltonian whose terms are non-interacting. So in other words, SPT ordered systems belong to the trivial phase in the absence of symmetry, but a distinct phase in the presence of symmetry. In terms of the states, the third condition implies that the ground state is unique and short range entangled. While the second condition implies that this state cannot be mapped to a product state using a local unitary, if the local unitary respects the symmetry.

Because these systems belong to the trivial phase if the symmetry is broken, they do not exhibit any of the exotic features of (intrinsic) topologically ordered phases. Namely, they do not possess long range entanglement, topology dependent ground space degeneracies, nor anyonic excitations in the bulk. The exotic features of SPT ordered systems manifest when they have boundaries; SPT ordered systems always have protected boundary modes. The meaning of protected boundary modes depends on dimension. In 1D, it means the boundaries of a spin chain support degeneracies that are inaccessible to local symmetry-preserving operations. For 2D, the boundaries must always be gapless or break the symmetry (either explicitly or spontaneously) [108, 109]. While for 3D, a new possibility opens: if the 2D boundary is gapped and symmetry-preserving, then it must be topologically ordered [110–112].

1.3.4 Symmetry-enriched topological order

As the theory of SPT phases became better understood, research was undertaken on the interplay between symmetry and topologically ordered systems. Systems that have unbroken symmetries and host anyonic excitations are known as symmetry-enriched topological (SET) phases, and it was soon realised that the symmetry can interact in highly nontrivial ways with anyonic excitations of such systems. For example, anyons can gain fractional charge under the symmetry, or the symmetry can even act as a permutation on the set of anyons [113–115]. These symmetries can be used to define domain walls and symmetry defects [113], that enact nontrivial permutations on the anyons upon their crossing or braiding.

The theory of SET phases of matter is closely related to the theory of SPT phases. For instance, some SET phases can only be realised on the boundary of a higher dimensional SPT phase: It was found that certain anyon permuting symmetries are *anomalous* [116], meaning they cannot be physically realised in a standalone 2D system, but that the anomaly can be ‘cancelled’ by a matching 3D SPT phase [117]. Additionally, many SPT and SET phases can be related by a duality mapping known as gauging. One can partially or fully gauge symmetries of SPT phases to obtain SET or topologically ordered models [109, 113, 118]. Finally, the domain walls that appear in SET phases are closely related to the theory of SPT phases [119].

Symmetry?	Yes	SPT phases	SET phases
	No	Trivial	Topological phases
		No	Yes
		Long range entanglement?	

Fig. 1.3 The types of phases are characterised by whether they are long range entangled or not, and whether they have unbroken symmetries or not. One could replace the bottom row with whether the system hosts anyonic excitations or not.

1.3.5 Thermal stability of quantum phases

Up until now, we have considered quantum phases at zero temperature. An important problem that is emerging in recent years is to classify what types of topological phases can exist in equilibrium at nonzero temperature. Much of the difficulty lies in first defining topological order for states beyond the zero temperature limit (and more generally mixed states), as many of the Hallmarks of topological order are specific to the ground space.

Broadly speaking, there have been three main approaches to defining topological order at nonzero temperature. The first is to employ order parameters such as the topological entanglement entropy (TEE) or topological mutual information to probe nontriviality of thermal states [120–122]. Secondly, circuit complexity has been used as a metric of nontriviality. One defines a thermal state as being topologically nontrivial if it requires a large-depth circuit to prepare it from a classical ensemble [123]. The third type is to define a topologically ordered

system as thermally stable if it has a long lifetime (and therefore long thermalisation time) when viewed as a quantum memory [124]. Essentially, this last approach states that a phase is thermally stable if it is self-correcting.

Many of these definitions have been shown to agree in many cases. For example, under all definitions, 2D commuting models are thermally trivial, while the 4D toric code is topologically ordered at nonzero temperature under all definitions [47, 124, 123, 120]. However, not all definitions are the same. The 3D toric code is circuit trivial at nonzero temperature [123], has a constant lifetime for quantum information (but a macroscopic lifetime for classical information), however it retains a nonvanishing TEE for low enough temperatures [121]. Finding models that maintain topological order in 3D or less is an important problem, and such examples may lead to the discovery of a physically realistic self-correcting quantum memory.

1.4 Computational phases of matter

An exciting paradigm in recent years is the concept of a computational phase of matter. One can ask the question: what are the properties of a Hamiltonian that allow for universality of measurement-based quantum computation when cooled to its ground state? The question of whether one can have a universal phase of matter, where all states within the phase are universal resources for MBQC was first proposed by Doherty and Bartlett [125]. The hope was that phases of matter could exist where the computational power does not depend on the precise state within the phase, but rather is a property of the phase itself, insensitive to microscopic imperfections and perturbations.

A fascinating discovery is that such phases can exist. That is, there are phases of matter where one can perform computation without an exact description of the underlying resource state, relying only more coarse features. A prevailing view in recent years is that SPT order is a computational resource for MBQC, and that SPT phases are natural candidates for computational phases. This paradigm was first shown for a variety of 1D SPT ordered models [126–128], where the classification of 1D phases is heavily utilized [129–131]. However, 1D models are incapable of universal quantum computation, and instead can only be used as computational wires, capable only of single qubit (qudit) operations. Later it was proven that neighbourhoods of an SPT phase around the square lattice cluster point can be used for universal quantum computation [132], along with numerical simulations demonstrating that certain SPT phase boundaries coincide with computational universality [34, 133]. Recently it was proved that the entire phase of the square lattice cluster model is universal, if rigid-line like symmetries are imposed [134]. Additionally, cluster models with rigid fractal symmetries [135] have also shown to support universal phases.

While several examples of such phases now exist, questions of general classification schemes, whether rigid subsystem symmetries are necessary (as opposed to global onsite symmetries), and whether they can be made fault-tolerant are now becoming important. One question of interest, that we will approach more precisely in the next chapter, is whether one can extend computational phases of matter to nonzero temperature. A first pressing question is how to define SPT order at nonzero temperature.

1.5 Organisation of the thesis

The goal of this thesis is to study the utility of symmetry-protected topological phases in the design of a quantum computer. The remainder of the thesis consists of three chapters and a conclusion. These chapters are organised as follows:

Chapter 2: Symmetry-protected topological order at nonzero temperature

In this chapter, we ask the question of whether symmetry-protected topological phases can persist at nonzero temperature. At zero temperature, it has previously been shown that such phases are enabling resources for universal MBQC. This chapter is concerned with moving beyond the zero temperature limit and answering the question of whether these quantum phases and their computational properties are robust at nonzero temperature.

We begin this chapter by introducing the setting of SPT phases we are interested in. We then define carefully what it means for a model to have SPT order at nonzero temperature using an appropriate notion of circuit complexity for Gibbs ensembles. We then prove that all of the currently known SPT phases with onsite symmetries (that are represented by commuting projector models), namely the group cohomology models, are SPT-trivial at any nonzero temperature. In other words, the SPT order in these models is present only at zero temperature (in the exact ground space).

Moving beyond onsite symmetries, we show that thermal SPT phases can exist at nonzero temperature, using the three-dimensional cluster state model of Raussendorf, Bravyi and Harrington [136]. We introduce this model and the symmetries it possesses – a particular kind of symmetry known as a 1-form symmetry. We demonstrate that this model is SPT ordered at nonzero temperature using two arguments: (i) by gauging the model to produce a nontrivial domain wall in the four-dimensional toric code, and (ii) by constructing nonlocal order parameters which distinguish the model from the trivial phase. We then discuss the operational interpretation of these order parameters as quantifying the entanglement that can be localized between distant regions in the thermal state through measurements in the bulk. This provides a direct link between thermal SPT phases and fault-tolerant measurement-based quantum computation.

Chapter 3: Symmetry-protected self-correcting quantum memories

This chapter concerns the feasibility of self-correction in models that have symmetries present. We ask whether self-correction is possible in three dimensional spin models protected by symmetry. We propose symmetry-protected topological phases as candidates for self-correcting quantum memories. This class of models are natural to consider for self-correcting quantum memories due to their ‘protected’ boundary modes, and the fact that they can form thermally stable phases of matter in 3D. We find that certain 3D models, protected by 1-form symmetries, are self-correcting. Throughout this chapter we focus on the relationship between thermal stability of bulk SPT order and self-correction, arguing that the two notions are fundamentally linked within the class of models we examine.

We begin this chapter with a review of self-correction and the relevant energetic quantities that determine the memory time. We then formalise what it means for a model to be self-correcting in the presence of symmetry; noting that one can always trivially obtain self-correction by imposing arbitrarily strong symmetries, we first formalise the conditions that must be satisfied for a model to meet the conditions of a nontrivial symmetry-protected self-correcting quantum memory. Following this, we then argue that the more conventional SPT models that are protected by onsite (0-form) symmetries cannot be self-correcting in 3D. We then present two models, one based on a three-dimensional cluster model, the other based on the gauge-color code, that are self-correcting under 1-form symmetries. The self correcting properties of these models arise from a bulk-boundary correspondence for SPT phases at nonzero temperature. In particular, this correspondence places a polynomial lower bound to the circuit depth required to prepare approximate Gibbs states for these systems. We conclude this chapter by investigating under what conditions 1-form symmetries can become emergent.

Chapter 4: Universal fault-tolerant measurement-based quantum computation

In this chapter we focus on the model of measurement-based quantum computation, and develop new techniques to achieve fault-tolerant quantum computation in this setting. This chapter is concerned with developing a framework for fault-tolerant MBQC – based on single qubit measurements on a cluster state – to employ protocols designed for the more conventional circuit-based model of quantum computation. The framework provides a wealth of new protocols for fault-tolerant quantum computation within the measurement-based framework, offering more resource efficient and noise-tolerant alternatives to conventional approaches. Additionally, we show how MBQC can be understood as a specific case of gauge fixing of a particular subsystem code.

We begin this chapter by reviewing measurement-based quantum computation on cluster states. After recalling how measurements on a 1D cluster state can propagate a qubit through time, we build up the framework by showing how to construct a foliated channel – a system capable of propagating an encoded qubit (of a quantum error-correcting code) through time. We then show how logical information can be manipulated by concatenating different foliated channels. We illustrate the utility of this framework by demonstrating how to simulate the manipulation of certain symmetry-defects in the surface code – called twist defects – with single qubit measurements on a three-dimensional cluster state. These twist defects behave like quasiparticles known as Majorana fermions, and schemes based on their braiding and fusion have been shown to be among the best approaches to realise low-overhead quantum computation in the circuit-based model.

While the focus of this Chapter is on quantum computation (over topological phases), we emphasise that the models we develop can be viewed as examples of SPT phases with higher-form symmetries. In particular, the models can be seen as generalisations of the cluster model of Raussendorf, Bravyi and Harrington discussed in Chapter 2, where fault-tolerance arises from employing error correction to effectively enforce these higher-form symmetries. Using the techniques in Chapter 2 one can demonstrate SPT-nontriviality at nonzero temperature for many of these models. We also remark that the theory of domain walls and symmetry defects is intimately related to the theory of SPT phases (see for example Ref. [119] and Chapter 2, Sec. 2.3.2).

2 | Symmetry-protected topological order at nonzero temperature

Abstract

We address the question of whether symmetry-protected topological (SPT) order can persist at nonzero temperature, with a focus on understanding the thermal stability of several models studied in the theory of quantum computation. We present three results in this direction. First, we prove that nontrivial SPT-order protected by a global onsite symmetry cannot persist at nonzero temperature, demonstrating that several quantum computational structures protected by such onsite symmetries are not thermally stable. Second, we prove that the 3D cluster state model used in the formulation of topological measurement-based quantum computation possesses a nontrivial SPT-ordered thermal phase when protected by a generalized (1-form) symmetry. The SPT-order in this model is detected by long-range localizable entanglement in the thermal state, which compares with related results characterizing SPT-order at zero temperature in spin chains using localizable entanglement as an order parameter. Our third result is to demonstrate that the high error tolerance of this 3D cluster state model for quantum computation, even without a protecting symmetry, can be understood as an application of quantum error correction to effectively enforce a 1-form symmetry.

2.1 Introduction

Topological phases are not only fascinating from the perspective of fundamental physics but are also well-suited for the design of quantum computers, for two essential reasons. First, such phases possess topology-dependent ground-state degeneracies, into which quantum information can be encoded and which can manifest themselves through boundary degrees of freedom. That is, qubits arranged on a spin lattice in a topologically-ordered phase are an instance of a quantum error correcting code: information is encoded in nonlocal degrees of freedom, offering robustness to local errors that can be detected through the measurement of local syndromes.

Second, these desirable properties are robust against perturbations that act locally on the system [88], making them ideal for quantum information processing with faulty devices without the requirement of precise control over all microscopic degrees of freedom.

Although much of the existing work on the study of topological phases is devoted to studying ground state (zero temperature) properties, identifying systems that can maintain their quantum coherence in equilibrium at some nonzero temperature would be highly desirable for quantum computing applications. Most of the well-studied exactly-solvable models in two or three dimensions (such as Kitaev's toric code) do not maintain their topological order except at zero temperature [123, 137]. The full range of phenomena of topological models in three or more dimensions has yet to be fully explored, though, so there is plenty of room for optimism.

A promising new direction in recent years is to add a symmetry to the mix. Symmetries have historically proven to be a powerful tool for understanding the structure and thermal stability of many-body phases of matter, for example, Landau's paradigm of symmetry breaking, the Mermin-Wagner theorem [138], and Elitzur's theorem [139]. More recently, symmetries have been used to characterise the order in systems away from equilibrium, such as periodically driven (Floquet) systems, where the thermalization time can be long [140, 141]. Even at zero temperature, a rich set of ordered phases can appear even in trivial models when a symmetry is enforced; such symmetry-protected topological (SPT) phases are described by short-range entangled states that cannot be adiabatically connected to a trivial product state while preserving the symmetry [129–131]. Like topological phases, these SPT phases can possess ground-state degeneracies manifested through boundary degrees of freedom, and these degeneracies are robust against local symmetry-respecting perturbations. With symmetry, new avenues open up. For example, SPT-nontrivial phases can be identified even in spin chains with only one spatial dimension; nontrivial topological phases require at least 2D.

Nontrivial SPT phases are not likely to be useful for defining good quantum codes, mainly because this would require a very strong assumption about the error model (i.e., that it respects the symmetry). Nonetheless, SPT phases have found several applications in our understanding of other features of quantum computation. First, the model for measurement-based quantum computation (MBQC) [26] can be understood in terms of performing computations on fractionalized edge modes associated with the boundaries of symmetry-protected phases of spin chains [142, 126, 143]; a very precise relationship between the computational properties of a spin chain and its SPT-order was developed by Else *et al.* [127, 132] and Miller *et al.* [144]. Second, a direct relationship between the set of fault-tolerant gates for a topological code, the classification of gapped boundaries of this code, and SPT phases for which these gapped boundaries serve as ground states has been shown [119, 145]. This relationship is useful for the construction of fault-tolerant non-Clifford gates and may have applications in magic state

distillation. These results hint at a new relationship between such gapped domain walls and SPT-ordered phases on the boundary, in particular in higher dimensions.

Very little is known about the thermal stability of SPT-ordered systems, and the possibility is left open that some of the robust properties of SPT-ordered phases for quantum computing may survive at nonzero temperature when the local symmetry is enforced. The presence of SPT-order in thermal systems is deeply connected to survival of the aforementioned gapped boundaries in a topological code and their associated fault-tolerant non-Clifford gates at nonzero temperature. The survival of SPT-order for systems excited out of the ground state has been investigated in the context of many-body localization [146, 147].

Our first result is a proof that a nontrivial SPT phase protected by a global onsite (zero-form) symmetry cannot exist for any nonzero temperature. This proof requires us to formulate a definition of nontrivial SPT-order for thermal states, which we do through an appropriate definition of a symmetric Gibbs state together with a definition of nontrivial SPT-order for mixed states based on circuit complexity following a similar approach by Hastings for topological order [123]. We prove this result for the broad class of models described by group cohomology [111].

As SPT-order has been shown to be an enabling feature of measurement-based quantum computation, this no-go result would suggest that thermal states at nonzero temperature cannot be used as resource states for such schemes. Surprisingly, though, we know this to be false, through the existence of several counterexamples. The topological cluster state scheme of Raussendorf *et al.* [66] is the basis for essentially all currently-pursued high-error-threshold architectures for quantum computing (its circuit-model implementation gives the well-studied ‘surface code’ architecture [148]). Using a cluster state Hamiltonian in three dimensions, the results of Ref. [136] show that the thermal state of this model is a resource for quantum computation below some critical temperature. This is despite the fact that this cluster model Hamiltonian does not undergo any thermodynamic phase transition, even when protected by an onsite symmetry, and so the physical origin of its thermal stability remains elusive. Other 3D Hamiltonians have been proposed that are universal for MBQC at nonzero temperature [149, 40, 150], but there is currently no guiding principle explaining the thermal robustness of MBQC.

As our second result, we present and analyse the 3D cluster state model from the perspective of SPT-order, and show that this model possesses a nontrivial SPT phase at nonzero temperature when protected by a 1-form symmetry. Higher-form symmetries are a natural generalization of the 0-form global symmetry for which the group action is onsite. A q -form symmetry can be imposed by an operator acting on a closed codimension- q manifold \mathcal{M} . When $q > 0$, the symmetry imposes much stronger constraints than the onsite, $q = 0$ case. Several recent works have investigated SPT phases with higher-form symmetries [151–156]. By enforcing

a 1-form symmetry on the 3D cluster state model, we prove that SPT-ordering in 1-form symmetric models can be maintained at nonzero temperature. We explicitly construct types of nonlocal order parameters that characterize this SPT-ordering in the thermal state. These order parameters consist of pairs of membranes, and when equipped with local error-correcting operations on the boundaries serve as a witness of the long-range localizable entanglement that is present in the thermal state.

Our third result is to provide an operational interpretation of this SPT-ordering under the 1-form symmetry, using the concept of localizable entanglement in the thermal state. This interpretation provides an explanation of the thermal stability of the topological cluster state model for quantum computation, even for the case where symmetries are not enforced. In one dimension, the SPT-ordering at zero temperature of the cluster state model protected by a global 0-form $\mathbb{Z}_2 \times \mathbb{Z}_2$ symmetry is characterised by the ability to localize entanglement in the ground state between the fractionalized edge modes via symmetry-adapted measurements in the bulk [127, 132]. By analogy, in the 3D cluster state model, we demonstrate that our order parameter takes near-maximal values for the nontrivial SPT phase at low temperature, which guarantees robustness of the localizable entanglement between two boundary surface codes of this model via symmetry-adapted measurements in the bulk. In addition to localizing entanglement, the measurements provide complete information about the 1-form symmetry operators. Therefore, even when the 1-form symmetry is not enforced, measurement of these symmetry operators allows for error correction of the resulting thermal state to the corresponding thermal SPT-ordered state for which entanglement is ensured. Therefore, the scheme can offer thermal stability even without enforcing the symmetry.

The Chapter is organised as follows. In section 2.2 we formulate and define the types of models and relevant notions of SPT-order for thermal states. We then provide a proof that SPT-order protected by an onsite symmetry cannot exist at nonzero temperature. We prove this first for a well known SPT model in 2D, and then for the more general group cohomology models. In section 2.3 we show that the 3D cluster model possesses SPT-order at nonzero temperature, protected by a 1-form symmetry. We show this firstly through an argument based on gauging and secondly through a nonlocal order parameter. In section 2.4 we discuss the nontrivial SPT protected by 1-form symmetry in the context of measurement-based quantum computation. We conclude with a discussion and outlook in section 2.5.

2.2 Thermal SPT-order

In this section we introduce the types of models we will be treating and the relevant definitions of SPT-order. We then develop a toolset to analyse SPT-order in a thermal setting, making use of the well-known framework of simulating thermalization of quantum many-body systems

based on the Davies map [157, 158]. Our main result in this section is a proof of the instability of SPT-order at nonzero temperature for models in arbitrary dimension protected by an onsite symmetry.

2.2.1 The setting

Consider a discrete lattice Λ embedded in a D -dimensional manifold M^D . Spins with local Hilbert space \mathcal{H}_i are placed at each site $i \in \Lambda$ ('sites' can be chosen to be at vertices, edges, etc., of the lattice), with total Hilbert space $\mathcal{H} = \otimes_{i \in \Lambda} \mathcal{H}_i$. The types of models that we are considering can be represented by local, commuting projector Hamiltonians $H = \sum_X h_X$, where each local term h_X is supported on a subset $X \subseteq \Lambda$ with $\text{diam}(X) \leq \text{const}$. We assume that the system has some symmetry described by a group G , with unitary representation S . The symmetries we consider can be onsite symmetries, as well as more general higher-form symmetries, which we now define. An onsite symmetry takes the form

$$S(g) = \bigotimes_{i \in \Lambda} u_i(g), \quad (2.1)$$

where $u_i(g)$ is the representation of G on a single site $i \in \Lambda$. A q -form symmetry (for some $q \in \{0, 1, \dots, D-1\}$) consists of operators $S_{\mathcal{M}}(g)$, supported on codimension- q submanifolds \mathcal{M} in M^D , with $g \in G$ [151–156]. In this language, an onsite symmetry may also be referred to as a 0-form symmetry. In such a theory, charged excitations are q -dimensional objects and symmetry operators impose conservation laws on higher-dimensional charged objects.

A useful way to classify phases of matter at zero temperature is to use circuit complexity [92]. A quantum circuit may be represented as

$$U_{\text{circ}} = \prod_{j=1}^d \mathcal{D}_j \quad \text{where} \quad \mathcal{D}_j = u_1^{(j)} \otimes u_2^{(j)} \otimes \dots \otimes u_{k_j}^{(j)}, \quad (2.2)$$

where each geometrically local gate $u_k^{(j)}$ is supported on a region of radius at most r , and d is the number of layers. The depth of such a circuit is defined to be the product rd , and a circuit is known as *low-depth* if rd is constant in the system size¹. We say a ground state of a gapped Hamiltonian H is *short-range entangled*, if it can be transformed into a product state using a low-depth circuit [92]. In the context of SPT phases, the local gates $u_k^{(j)}$ of a quantum circuit are constrained to commute with the symmetry $S(g)$.

¹Note that it is common to refer to r and d as the *range* and the *depth* of the circuit U_{circ} , respectively, but we do not make this distinction.

Namely, SPT-order at zero temperature is defined in the following way. Let $|\psi\rangle$ be the unique ground state of a gapped Hamiltonian H on a closed (without boundary) lattice, with symmetry G . Then $|\psi\rangle$ belongs to a nontrivial SPT phase if:

1. it is short-range entangled,
2. any low-depth circuit connecting $|\psi\rangle$ to a product state has gates that break the symmetry.

We emphasize that while there may exist a low-depth symmetric unitary map that connects a state with nontrivial SPT-order to a product state, the local gates composing it cannot be symmetric. SPT models have trivial bulk properties in the sense that they have no exotic excitations or degeneracies dependent on the topology of the underlying manifold. Despite this absence, interesting protected surface states are known to appear at the boundary of an SPT phase. For example, in 1D, nontrivial SPT chains can exhibit fractionalized edge modes at their endpoints, such as with spin-1 antiferromagnets in the Haldane phase or Majorana nanowires. In general, in higher dimensions, it is believed that the 1D surface of a 2D SPT must be gapless or break the symmetry [108, 109], while in three or more dimensions it is believed that the surface must be gapless, break the symmetry or be topologically ordered [110, 159].

A large and well-known class of SPT models are the group cohomology models protected by onsite symmetries [111]. In terms of circuit depth, using gates of constant range, these wavefunctions require a circuit of depth $\mathcal{O}(N)$ to symmetrically disentangle, where N is the number of spins (for example, the one-dimensional case is proven in [160]). While this class captures a large number of SPT phases, there are known models beyond group cohomology, including 3D models that are protected by time reversal symmetry [161–164]. More recently, looking beyond onsite symmetries has led to generalised SPT models protected by higher-form symmetries, both in the continuum and on the lattice [153, 155, 156].

2.2.2 Defining SPT-order for thermal states

As defined above, SPT-order is manifestly a pattern of entanglement in the gapped ground state of a Hamiltonian. In this section we extend this definition to systems at nonzero temperature after briefly reviewing thermalization via the Davies map [157, 158]. We will argue that in the presence of symmetry, a natural notion of a thermal state at temperature T is the *symmetric* Gibbs ensemble

$$\rho(\beta) = \lim_{\lambda \rightarrow \infty} \rho_\lambda(\beta), \quad (2.3)$$

where $\beta = T^{-1}$, and $\rho_\lambda(\beta)$ is the (usual) Gibbs ensemble of a modified Hamiltonian $H(\lambda)$

$$\rho_\lambda(\beta) = \mathcal{Z}(\lambda)^{-1} e^{-\beta H(\lambda)}, \quad H(\lambda) = H - \lambda \sum_{g \in G} S(g), \quad (2.4)$$

where $\mathcal{Z}(\lambda) = \text{Tr} e^{-\beta H(\lambda)}$. Note that in the case of a higher-form symmetry, the sum in Eq. (2.4) is over all symmetry operators. The symmetric ensemble arises naturally in two different contexts: (i) the fixed point of a system thermalizing in the presence of a symmetry, (ii) the post error corrected state of a thermal ensemble. We will overview the first point (i) in this section, before returning to error correction in detail in section 2.4.2.

To motivate this notion of a symmetric thermal state, consider thermalization as modelled by weakly coupling the system to a bosonic bath

$$H' = H_S \otimes I_B + I_S \otimes H_B + H_{int}, \quad (2.5)$$

where H_S is the system Hamiltonian describing the SPT phase, H_B is the bath Hamiltonian, and $H_{int} = \sum_{\alpha} s_{\alpha} \otimes b_{\alpha}$ is the interaction Hamiltonian comprised of the system and bath operators s_{α} and b_{α} respectively. The interaction Hamiltonian is constrained by the symmetry in that it must commute with the symmetry on the joint system $U(g) = S(g) \otimes I_B$. Note that we require no other symmetry of the bath, other than that the couplings respect the system symmetry $S(g)$. (If instead we required $U(g) = S(g) \otimes S(g)_B$, for a suitable extension of the symmetry $S(g)_B$ to the bath, then we can always trivialise the SPT system due to the invertibility of SPT phases. We will explain this subtle point following the definition below.)

In order to realise the usual Gibbs ensemble as the fixed point of the reduced system dynamics, we require the dynamics to be ergodic. This is usually achieved by choosing bath couplings that are as simple as possible while ensuring the system operators address all energy levels of the system Hamiltonian H_S . The necessary and sufficient condition for ergodicity is that no nontrivial operators commute with all of the Hamiltonian and system operators [165, 166]. In the presence of symmetry, such a choice in general will not be possible, since the system operators s_{α} must respect the symmetry. Therefore ergodicity can only be achieved on a given sector, and for the sake of concreteness we focus our attention on the symmetric sector (the +1-eigenspace of $U(g)$).

We assume that the coupling is chosen such that the only operators that commute with H_S and all of the system operators s_{α} are symmetry operators, and additionally that the initial state belongs to the symmetric sector. Then, following the Davies prescription, the unique fixed point of the dynamics generated by the above interaction will be the *symmetric* Gibbs ensemble of Eq. (2.3). We will return to the assumption of the initial state belonging to the symmetric sector in section 2.4, specifically in the context of error correction.

Given this ensemble, let us now define what it means to have SPT-order at nonzero temperature by modifying a definition due to Hastings [123]. The notion of a *trivial state* is replaced by a *classical symmetric ensemble*, which is the symmetric Gibbs ensemble of a classical Hamiltonian H_{cl} . Here a classical Hamiltonian refers to a Hamiltonian expressible by

a sum of terms diagonal in a local product basis. To define SPT at nonzero temperature, we follow Hastings [123] and ask what is the circuit depth required to approximate the symmetric Gibbs ensemble, beginning with a classical Gibbs ensemble.

Definition 1. Let ρ be the symmetric Gibbs state of a Hamiltonian H that has symmetry $S(g)$, $g \in G$ and a SRE, unique ground state. We say ρ is (r, ϵ) SPT-trivial if there exists:

1. An enlarged Hilbert space $\mathcal{H}' = \mathcal{H} \otimes \mathcal{K}$.
2. A classical, nondegenerate Hamiltonian H_{cl} defined on \mathcal{H}' with symmetry

$$U(g) = S(g) \otimes I_{\mathcal{K}}. \quad (2.6)$$

3. A circuit \mathcal{U} with depth r acting on the enlarged space \mathcal{H}' , composed of symmetric gates, such that

$$\left\| \rho - \text{Tr}_{\mathcal{K}} \left(\mathcal{U} \rho_{cl} \mathcal{U}^\dagger \right) \right\|_1 < \epsilon, \quad (2.7)$$

where ρ_{cl} is the symmetric Gibbs ensemble of H_{cl} , and $\|\cdot\|_1$ denotes the trace norm.

We make a few remarks on this definition. Firstly, we require H_{cl} in the definition to be non-degenerate to exclude spontaneous symmetry breaking, since the symmetric Gibbs state of such a system can be highly nontrivial in terms of circuit depth. Secondly, we make the choice of symmetry in Eq. (2.6) to avoid the following situation. Suppose the choice of symmetry was given by $U(g) = S(g) \otimes S(g)$. For any SPT-ordered state $|\psi\rangle$ with symmetry $S(g)$, there exists a state $|\psi^{-1}\rangle$ with symmetry $S(g)$ such that $|\psi\rangle \otimes |\psi^{-1}\rangle$ can be prepared from a product state by a constant-depth circuit that is symmetric under $U(g)$. This property is referred to as the invertibility of SPT phases [167]. After tracing out the second subsystem, this choice of symmetry would imply that $|\psi\rangle$ is $(r, 0)$ trivial (even at $T = 0$) for some constant r .

Operationally, the above definition asserts that an SPT-trivial state is one that can be prepared from a classical ensemble using a low-depth symmetric quantum circuit (potentially with ancillas). An important consequence of this definition is that if a (symmetric) Gibbs ensemble can be expressed (up to error ϵ) as a mixture of $(r, 0)$ SPT-trivial states, then it is an (r, ϵ) SPT-trivial state [123]. Indeed our strategy in the following section will be to show that the symmetric Gibbs ensemble of SPTs protected by onsite symmetries can be approximated by a convex combination of states, each of which is symmetrically low-depth equivalent to a product state.

2.2.3 Onsite symmetric models have no SPT-order at nonzero temperature

We now show that any SPT-ordered Hamiltonian H with an *onsite* symmetry is trivial at any $T > 0$ according to the above definition. For concreteness, we focus on a particular 2D

example with \mathbb{Z}_2 onsite symmetry and defer the more general result to the next subsection. The proof proceeds by first constructing a new Hamiltonian H' from H whose Gibbs ensemble approximates that of H and is obtained by removing terms from H . By dividing the lattice into disjoint regions of small size (i.e. logarithmic in the system size), the missing terms present within each region allow us to define a circuit with small-depth that transforms H' into a trivial Hamiltonian describing a paramagnet. We find that many tools used to prove that two-dimensional, commuting projector Hamiltonians have trivial (intrinsic) topological order at nonzero temperature (in the absence of symmetry) in Ref. [123] apply in this context.

Our proof method has the following physical interpretation. In the SPT-ordered Hamiltonian H , excitations are point-like objects and the \mathbb{Z}_2 onsite symmetry imposes a conservation law on H that the number of point-like excitations must be even. By removing terms in H' , we create sinks where single point-like excitations can be created and destroyed, circumventing the above conservation law. Using these sinks, one can construct a symmetric disentangler out of operators that move point-like excitations into the sinks. This construction leaves open the possibility of thermal SPT-order in the presence of higher-form symmetries, as the removed terms do not act as sinks for the higher-dimensional excitations of these models, as we investigate in the next section.

The example 2D model we consider was first discussed in [109] (although it appeared, previously in a different guise in [108]), and will capture the key ingredients used to prove the general case. Consider a triangular lattice whose set of vertices, edges and faces is labelled by Δ_0 , Δ_1 , and Δ_2 respectively. On each vertex $v \in \Delta_0$ resides a qubit as in Fig. 2.1a, and let $N = |\Delta_0|$ be the number of qubits. Consider first the trivial paramagnet

$$H_0 = - \sum_{v \in \Delta_0} X_v, \quad (2.8)$$

where X_v is the Pauli X operator acting on the qubit at vertex v . The unique, gapped ground state of this model is the trivial product state $|\psi_0\rangle = |+\rangle^{\otimes N}$, where $|+\rangle = \frac{1}{\sqrt{2}}(|0\rangle + |1\rangle)$. The Hamiltonian, and thus the unique ground state, possess an onsite \mathbb{Z}_2 symmetry generated by

$$S = \bigotimes_{v \in \Delta_0} X_v. \quad (2.9)$$

We would like to construct a model with the same symmetry, but belonging to a nontrivial SPT phase. We first define the controlled- Z unitary acting on two qubits sharing an edge $e = (v_1, v_2)$ to be

$$CZ_{(v_1, v_2)} = \exp\left(\frac{i\pi}{4}(I - Z_{v_1})(I - Z_{v_2})\right). \quad (2.10)$$

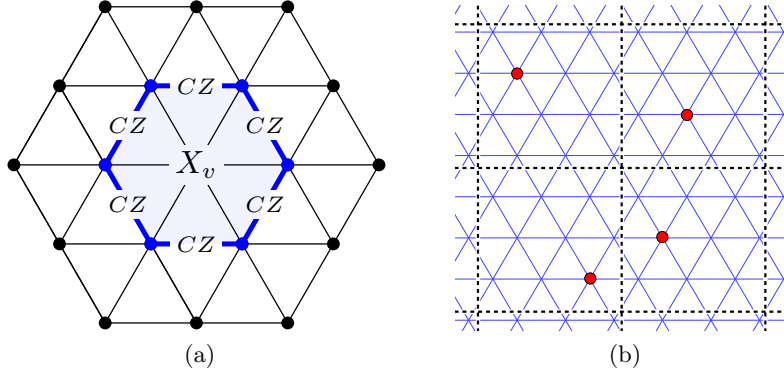


Fig. 2.1 (Color online) (a) The triangular lattice and one of the terms h_v belonging to H_1 . The 1-link of the vertex v is the set of blue (thick line) edges. (b) A valid configuration has sinks (large dots) for each square region in \mathcal{P}_l , where a sink is a vertex v with $k_v = 0$.

The nontrivial model can be constructed from these operators as a sum of local terms

$$H_1 = - \sum_{v \in \Delta_0} h_v, \quad h_v = X_v \prod_{e \in \text{Link}_1(v)} CZ_e, \quad (2.11)$$

where the $\text{Link}_1(v)$ consists of the neighbouring edges of v that do not contain v , as depicted by thick blue edges in Fig. 2.1a. We note that H_1 is slightly different to the model presented in [109], but they are equivalent up to a constant-depth quantum circuit comprised of symmetric gates. Each of the terms h_v are commuting and satisfy $h_v^2 = I$, and therefore have eigenvalues ± 1 . One can confirm that this model shares the same \mathbb{Z}_2 symmetry as the trivial paramagnetic model H_0 .

The unique ground state $|\psi_1\rangle$ is the +1-eigenstate of each of the terms h_v . Additionally, one can show that this model is short-range entangled, as it can be connected to the trivial ground state via the following unitary $U_1 = \prod_{t \in \Delta_2} C^{\otimes 2} Z_t$, where $C^{\otimes 2} Z_t$ the 3-qubit controlled- Z unitary acting on qubits in a triangle $t = (v_1, v_2, v_3)$ as:

$$C^{\otimes 2} Z_t = \exp \left(\frac{i\pi}{8} (I - Z_{v_1})(I - Z_{v_2})(I - Z_{v_3}) \right). \quad (2.12)$$

The unitary U_1 given by the whole circuit commutes with the symmetry, $[U_1, S] = 0$, provided the lattice has no boundary. But importantly, each gate in the circuit is not symmetric on its own, $[C^{\otimes 2} Z_t, S] \neq 0$. It is shown in [109] that H_1 cannot be adiabatically connected to the trivial paramagnet H_0 without closing the gap or breaking the symmetry, so it is impossible to approximate U_1 by a constant-depth circuit comprised of symmetric gates. Therefore, H_1 has nontrivial SPT-order at zero temperature.

Now let us show that the model H_1 becomes SPT-trivial at nonzero temperature. Similarly to Refs. [123, 168], we associate a binary value $k_v \in \{0, 1\}$ to each site $v \in \Delta_0$ to indicate the presence or absence of a term in an *imperfect* Hamiltonian:

$$H(\mathbf{k}) = - \sum_{v \in \Delta_0} k_v h_v, \quad (2.13)$$

where $\mathbf{k} \in \{0, 1\}^N$. For a given imperfect Hamiltonian $H(\mathbf{k})$ we say a site v is a *sink* if $k_v = 0$, corresponding to a missing term. We now wish to express the Gibbs ensemble in terms of a convex sum of the ground spaces of imperfect Hamiltonians. Let $\bar{\rho}(\mathbf{k})$ be the uniform mixture of symmetric ground states of $H(\mathbf{k})$. Then following [168], we define the free symmetric ensemble at $\beta = T^{-1}$ as

$$\rho_f(\beta) = \sum_{\mathbf{k} \in \{0, 1\}^N} \text{Pr}(\mathbf{k}) \bar{\rho}(\mathbf{k}), \quad (2.14)$$

where $\text{Pr}(\mathbf{k})$ is a probability distribution

$$\text{Pr}(\mathbf{k}) = (1 - p_\beta)^{w(\mathbf{k})} p_\beta^{N - w(\mathbf{k})}, \quad p_\beta = \frac{2}{e^{2\beta} + 1}, \quad (2.15)$$

and $w(\mathbf{k})$ is the Hamming weight of the vector \mathbf{k} (the number of nonzero entries).

Lemma 1. *Let $\rho(\beta)$ be the symmetric Gibbs ensemble of H_1 with $T > 0$, then*

$$\|\rho(\beta) - \rho_f(\beta)\|_1 \leq \mathcal{O}(e^{-\eta N}) \quad (2.16)$$

for some constant $\eta > 0$ (independent of system size).

Proof. The proof is similar to that in Ref. [168]. Consider first the usual Gibbs ensemble $\rho'(\beta)$ of H_1 (without enforcing the symmetry). Because H_1 is a sum of commuting terms, we have

$$\rho'(\beta) = \frac{1}{\mathcal{Z}'} \prod_{v \in \Delta_0} e^{\beta h_v}. \quad (2.17)$$

Since each term satisfies $h_v^2 = I$, we have $\exp(\beta h_v) = \cosh(\beta)I + \sinh(\beta)h_v$. Introducing a new normalization factor $\tilde{\mathcal{Z}} = (e^\beta + e^{-\beta})^N \mathcal{Z}'$ we have

$$\rho'(\beta) = \frac{1}{\tilde{\mathcal{Z}}} \prod_{v \in \Delta_0} \left((1 - p) \frac{I + h_v}{2} + p \frac{I}{2} \right), \quad (2.18)$$

where we have set $p = 2/(e^{2\beta} + 1)$. Expanding this out and introducing a dummy binary variable k_v for each vertex $v \in \Delta_0$, we have

$$\rho'(\beta) = \frac{1}{\tilde{Z}} \sum_{\mathbf{k} \in \{0,1\}^N} \left(\prod_{v \in \Delta_0} (1-p)^{k_v} p^{1-k_v} \left(\frac{I + k_v h_v}{2} \right) \right), \quad (2.19)$$

which we can rewrite as

$$\rho'(\beta) = \frac{1}{\tilde{Z}} \sum_{\mathbf{k} \in \{0,1\}^N} \text{Pr}(\mathbf{k}) \rho(\mathbf{k}), \quad (2.20)$$

where

$$\rho(\mathbf{k}) = \frac{1}{2^N} \prod_{v \in \Delta_0} (I + k_v h_v), \quad (2.21)$$

and $\text{Pr}(\mathbf{k})$ is given by Eq. (2.15). Note that $\rho(\mathbf{k})$ is a uniform mixture of all ground states of the imperfect Hamiltonian $H(\mathbf{k})$. Let us confirm that the normalization of $\rho(\mathbf{k})$ is correct. For any subset $M \subseteq \Delta_0$, we have

$$\text{Tr} \left(\prod_{v \in M} h_v \right) = \text{Tr} \left(\prod_{v \in M} U_1 X_v U_1^\dagger \right) = \text{Tr} \left(\prod_{v \in M} X_v \right) = 0, \quad (2.22)$$

and therefore $\text{Tr}(\rho(\mathbf{k})) = 1$. Now notice that

$$\sum_{\mathbf{k} \in \{0,1\}^N} \text{Pr}(\mathbf{k}) = \sum_{l=0}^N \binom{N}{l} (1-p)^l p^{N-l} = 1, \quad (2.23)$$

and therefore $\tilde{Z} = 1$, which means we have

$$\rho'(\beta) = \sum_{\mathbf{k} \in \{0,1\}^N} \text{Pr}(\mathbf{k}) \rho(\mathbf{k}). \quad (2.24)$$

Having considered the usual Gibbs ensemble without symmetries, we now consider the Gibbs ensemble with the symmetry enforced. Let $P = (I + S)/2$ be the projector onto the +1-eigenspace of S (recall, S is the symmetry operator defined in Eq. (2.9)). The symmetric Gibbs ensemble $\rho(\beta)$ can be obtained by projecting $\rho'(\beta)$ into the symmetric sector and renormalizing

$$\rho(\beta) = \frac{P \rho'(\beta) P}{\text{Tr}(P \rho'(\beta) P)}. \quad (2.25)$$

For $\mathbf{k}_1 := (1, \dots, 1)$, the Hamiltonian $H(\mathbf{k}_1)$ has a unique and symmetric ground state and therefore $\bar{\rho}(\mathbf{k}_1) = \rho(\mathbf{k}_1)$. For $\mathbf{k} \neq \mathbf{k}_1$, the imperfect Hamiltonian $H(\mathbf{k})$ has a $2^{N-w(\mathbf{k})}$ -dimensional ground space, which is partitioned equally into the +1- and -1-eigenspaces of S . Therefore we have

$$\text{Tr}(P \rho(\mathbf{k}) P) = \frac{1}{2} \text{Tr}(\rho(\mathbf{k})) = \frac{1}{2} \quad \forall \mathbf{k} \neq \mathbf{k}_1. \quad (2.26)$$

The symmetric ground space projectors of the imperfect Hamiltonian $H(\mathbf{k})$ can be written

$$\bar{\rho}(\mathbf{k}) = \begin{cases} \rho(\mathbf{k}) & \text{if } \mathbf{k} = \mathbf{k}_1, \\ 2P\rho(\mathbf{k})P & \text{otherwise} \end{cases} \quad (2.27)$$

Let us evaluate the normalization factor $\mathcal{Z} = \text{Tr}(P\rho'(\beta)P)$. We obtain

$$\mathcal{Z} = \sum_{\mathbf{k} \in \{0,1\}^N} \text{Pr}(\mathbf{k}) \text{Tr}(P\rho(\mathbf{k})P) = \sum_{\mathbf{k} \neq \mathbf{k}_1} \frac{1}{2} \text{Pr}(\mathbf{k}) + \text{Pr}(\mathbf{k}_1) = \frac{1}{2}(1 + \text{Pr}(\mathbf{k}_1)). \quad (2.28)$$

In particular, notice that $\mathcal{Z} \in [\frac{1}{2}, 1]$. Then the trace distance between $\rho_f(\beta)$ and $\rho(\beta)$ is given by

$$\|\rho(\beta) - \rho_f(\beta)\|_1 = \left\| \mathcal{Z}^{-1} \sum_{\mathbf{k} \in \{0,1\}^N} \text{Pr}(\mathbf{k}) P\rho(\mathbf{k})P - \sum_{\mathbf{k} \in \{0,1\}^N} \text{Pr}(\mathbf{k}) \bar{\rho}(\mathbf{k}) \right\|_1 \quad (2.29)$$

Using Eq. (2.27), and the triangle inequality, we get

$$\|\rho(\beta) - \rho_f(\beta)\|_1 \leq \left(2 - \mathcal{Z}^{-1}\right) \sum_{\mathbf{k} \neq \mathbf{k}_1} \text{Pr}(\mathbf{k}) \|P\rho(\mathbf{k})P\|_1 + (1 - \mathcal{Z}^{-1}) \text{Pr}(\mathbf{k}_1) \|\rho(\mathbf{k}_1)\|_1 \quad (2.30)$$

$$= \left(2 - \mathcal{Z}^{-1}\right) \sum_{\mathbf{k} \neq \mathbf{k}_1} \text{Pr}(\mathbf{k}) \frac{1}{2} + (\mathcal{Z}^{-1} - 1) \text{Pr}(\mathbf{k}_1), \quad (2.31)$$

where we have used Eq. (2.26) in the second line. Then making use of Eqs. (2.23) and (2.28), we get

$$\|\rho(\beta) - \rho_f(\beta)\|_1 \leq \frac{1}{2} \left(2 - \mathcal{Z}^{-1}\right) (1 - \text{Pr}(\mathbf{k}_1)) + \left(\mathcal{Z}^{-1} - 1\right) \text{Pr}(\mathbf{k}_1) \quad (2.32)$$

$$\leq \frac{2 \text{Pr}(\mathbf{k}_1)}{1 + \text{Pr}(\mathbf{k}_1)}. \quad (2.33)$$

Since $\text{Pr}(\mathbf{k}_1) = (1 - p_\beta)^N$ and $p_\beta \in (0, 1]$ for $T > 0$, we therefore have

$$\|\rho(\beta) - \rho_f(\beta)\|_1 \leq 2e^{-N \log(1-p_\beta)}. \quad (2.34)$$

Setting $\eta = -\log(1 - p_\beta) > 0$, the claim follows. \square

We now divide up the lattice into a square grid \mathcal{P}_l as in Fig. 2.1b, with each square region having side-length $l = (c \log(L))^{\frac{1}{2}}$ for some constant c . We will choose c to be sufficiently large to ensure that, with high probability, there will be at least one sink within each square region. A configuration \mathbf{k} is called *l-valid* if there is a sink in every square region and invalid otherwise. We want to show that the Gibbs state $\rho(\beta)$ at inverse temperature β is well approximated by a distribution over *l-valid* configurations.

Lemma 2. For a given grid \mathcal{P}_l , let $\mathcal{V} \subseteq \{0, 1\}^N$ be the set of l -valid configurations, and let

$$\rho_{\mathcal{V}}(\beta) = \sum_{\mathbf{k} \in \mathcal{V}} \Pr(\mathbf{k}) \bar{\rho}(\mathbf{k}). \quad (2.35)$$

For any $T > 0$, there exists a constant $\delta > 0$ (independent of system size) such that $\rho_{\mathcal{V}}(\beta)$ satisfies

$$\|\rho_{\mathcal{V}}(\beta) - \rho(\beta)\|_1 \leq \mathcal{O}(L^{-\delta}). \quad (2.36)$$

Proof. Recall that $\Pr(\mathbf{k}) = \prod_{v \in \Delta_0} (1-p)^{k_v} p^{1-k_v}$, such that $1-p$ is the probability of having a sink at a given vertex. Let $P_{\mathcal{V}} := \sum_{\mathbf{k} \in \mathcal{V}} \Pr(\mathbf{k})$, then from Lemma 1, we have the following

$$\|\rho_{\mathcal{V}}(\beta) - \rho(\beta)\|_1 = \left\| \sum_{\mathbf{k} \notin \mathcal{V}} \Pr(\mathbf{k}) \bar{\rho}(\mathbf{k}) \right\|_1 \quad (2.37)$$

$$\leq \sum_{\mathbf{k} \notin \mathcal{V}} \Pr(\mathbf{k}) \quad (2.38)$$

$$= 1 - P_{\mathcal{V}} \quad (2.39)$$

Let B be the set of vertices within a square region of the grid \mathcal{P}_l . The contribution of configurations containing at least one sink in each square region is given by

$$P_{\mathcal{V}} = \prod_{\text{squares } B} (1 - q_B), \quad (2.40)$$

where $q_B = (1-p)^{|B|}$ is the probability that square region B contains no sink. Since the probability of each square having a sink is independent, and there are $n = L^2/c \log(L)$ squares in the grid \mathcal{P}_l , using Bernoulli's inequality, we have

$$P_{\mathcal{V}} = (1 - q_B)^n \geq 1 - nq_B. \quad (2.41)$$

Since $|B| = c \log(L)$, we have $q_B = L^{c \log(1-p)}$, and Eq. (2.39) becomes

$$\|\rho_{\mathcal{V}}(\beta) - \rho(\beta)\|_1 \leq \frac{L^{2+c \log(1-p)}}{c \log(L)} \quad (2.42)$$

$$\leq \frac{1}{c} L^{-\delta}, \quad (2.43)$$

where we have defined $\delta = -2 - c \log(1-p)$. Notice that for $T > 0$, we have $\log(1-p) < 0$. Therefore, choosing $c > -2/\log(1-p)$ gives $\delta > 0$. \square

We can now show that the symmetric Gibbs ensemble $\rho(\beta)$ is SPT-trivial by constructing a symmetric disentangling circuit that maps $\bar{\rho}(\mathbf{k})$ to a product state, for each valid configuration

\mathbf{k} . Then since $\rho(\beta)$ is approximated by a sum of SPT-trivial states, it follows that $\rho(\beta)$ is SPT-trivial. We note that the following theorem also applies if we replace the symmetric Gibbs ensemble by the usual Gibbs ensemble.

Theorem 1. *For any $T > 0$, the symmetric Gibbs ensemble $\rho(\beta)$ of H_1 is (r, ϵ) SPT-trivial, where $r = \mathcal{O}(\log^{\frac{1}{2}}(L))$, and $\epsilon = \mathcal{O}(L^{-\delta})$.*

Proof. Let \mathbf{k} be a valid configuration. To construct a disentangling circuit $\mathcal{D}_{\mathbf{k}}$ for $\bar{\rho}(\mathbf{k})$ we define the elementary gates of the circuit

$$U_{(v,w)} = \exp\left(\frac{\pi}{4} h_v Z_v Z_w\right), \quad W_{(v,w)} = \exp\left(\frac{\pi}{4} X_v Z_v Z_w\right), \quad v, w \in \Delta_0. \quad (2.44)$$

Notice that both $U_{(v,w)}$ and $W_{(v,w)}$ are symmetric. Moreover, for any vertex v , and any sink h , the operator $Z_v Z_h$ has the following commutation and anti-commutation relations

$$\{h_v, Z_v Z_h\} = 0, \quad [h_w, Z_v Z_h] = 0 \quad \forall w \neq v. \quad (2.45)$$

Because of the above relations, we can interpret $Z_v Z_h$ as an operator which creates an excitation at vertex v in the imperfect Hamiltonian $H(\mathbf{k})$.

The disentangling circuit $\mathcal{D}_{\mathbf{k}}$ is composed of a number of layers $\mathcal{D}_{\mathbf{k}} = \prod_{j=1}^d \mathcal{D}_j$, such that each \mathcal{D}_j is comprised of gates with constant range, and $d = (c' \log(L))^{\frac{1}{2}}$ for some constant c' . The goal is to first disentangle terms near each sink, and then inductively the next nearest neighbours, moving outwards as depicted in Fig. 2.2. We define sets of vertices which determine the order that we perform the gates. Let the initial set of vertices $V(0)$ contain exactly one sink in each square region (if there are many in each square region, choose any of them). Then for $j \geq 1$, let

$$V(j) = \{v \in \Delta_0 \mid \text{dist}(v, w) \leq j \text{ for some } w \in V(0)\}, \quad (2.46)$$

be the union of balls of radius j around each sink, where $\text{dist}(v, w)$ is the shortest path between vertices v and w . We also define

$$\bar{V}(j) = V(j) \setminus V(j-1), \quad (2.47)$$

to be the set of vertices in $V(j)$ that are not in $V(j-1)$. Notice that for increasing j , $V(j)$ defines neighbourhoods of increasing size around each of the sinks, and that $\bar{V}(j)$ can be considered the boundary set of vertices of $V(j)$.

For any vertex v , let $h_j(v) \in V(j)$ be the nearest vertex to v that belongs to $V(j)$ (if there are multiple, choose any of them). Then the j 'th layer of the circuit is defined by

$$\mathcal{D}'_j = \prod_{v \in \bar{V}(j)} U_{(v, h_{j-1}(v))}. \quad (2.48)$$

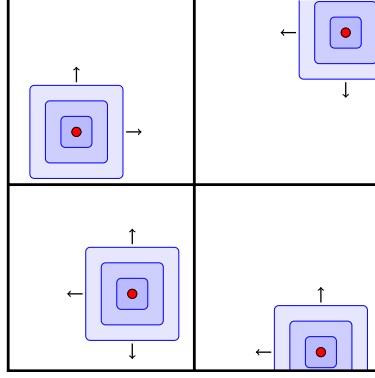


Fig. 2.2 (Color online) The disentangler acts first on terms in $H(\mathbf{k})$ neighbouring the sinks (large dots), then moves outward. The set $V(0)$ consists of the sinks, depicted as large dots, and the successive shaded (blue) discs represent the sets $V(1)$, $V(2)$ and $V(3)$.

Now \mathcal{D}'_j has constant depth for each j , because it is comprised of gates supported on a small neighbourhood of $\bar{V}(j)$. The gates can be divided into non-overlapping sets, each of which can be performed simultaneously (for example, the lattice is 3-colorable, and all gates $U_{(v, h_{j-1}(v))}$ with v a fixed colour can be performed in parallel).

Each gate $U_{(v,w)}$ has the following action under conjugation:

$$h_v \mapsto -Z_v Z_w, \quad (2.49)$$

and commutes with h_l for all $l \neq v, w$, and $Z_x Z_y$ for all $x, y \neq v$. Notice that for the first layer, \mathcal{D}_1 conjugates all the terms h_v sharing an edge with a sink into terms $-Z_v Z_{h_0(v)}$, where $h_0(v)$ is the sink adjacent to the vertex v . Subsequent layers \mathcal{D}_j map all the terms h_v inside $V(j)$ to terms of the form $Z_v Z_w$. Let the constant c' be chosen such that $d = (c' \log(L))^{\frac{1}{2}}$ is the diameter of each square region. Since each square region has a sink in it, we have $V(d) = \Delta_0$. Therefore, after at most d layers, the circuit $\mathcal{D}'_k = \prod_{j=1}^d \mathcal{D}'_j$ conjugates the imperfect Hamiltonian $H(\mathbf{k})$ into a sum of terms of the form $Z_v Z_w$.

Next, we make use of the gates $W_{(v,w)}$. In a similar way, we define the j 'th layer of a second circuit by

$$\mathcal{D}''_j = \prod_{v \in \bar{V}(j)} W_{(v, h_{j-1}(v))}. \quad (2.50)$$

The circuit $\mathcal{D}''_k = \prod_{j=1}^d \mathcal{D}''_j$ has depth d , as can be shown by the same argument given for \mathcal{D}'_k . Each gate $W_{(v,w)}$ has the following action under conjugation:

$$Z_v Z_w \mapsto X_v, \quad (2.51)$$

and commutes with $Z_l Z_m$ for all $l, m \neq v$. Defining $\mathcal{D}_k = \mathcal{D}_k'' \circ \mathcal{D}_k'$, the circuit \mathcal{D}_k applied to the imperfect Hamiltonian has the following action

$$\mathcal{D}_k H(\mathbf{k}) \mathcal{D}_k^\dagger = \sum_{v \in \Delta_0} k_v X_v := H_0(\mathbf{k}). \quad (2.52)$$

Therefore the circuit \mathcal{D}_k maps $\bar{\rho}(\mathbf{k}) \mapsto \bar{\rho}_0(\mathbf{k})$, where $\bar{\rho}_0(\mathbf{k})$ is the (normalised) symmetric ground space projector of $H_0(\mathbf{k})$, which is a product state. This holds for each valid configuration $\mathbf{k} \in \mathcal{V}$ and therefore each $\bar{\rho}(\mathbf{k})$ is a $(2d, 0)$ -trivial state, where $d = (c' \log(L))^{\frac{1}{2}}$ for some constant c' .

A state $\rho(\beta)$ is (r, ϵ) SPT-trivial if and only if it can be approximated up to error ϵ (in trace norm) by a convex combination of $(r, 0)$ SPT-trivial states. Since from Lemma 2 we have that $\rho(\beta)$ is approximated to within $\epsilon = \mathcal{O}(L^{-\delta})$ error by the imperfect state in Eq. (2.35), and the imperfect state is a convex combination of $(2d, 0)$ SPT-trivial states, the result then follows. \square

The existence of a symmetric unitary \mathcal{D} that disentangles terms is closely related to the existence of sinks at some sites $k_v = 0$, where point-like excitations can be locally created and destroyed. The existence of such excitations is a generic feature of Hamiltonians describing SRE phases, which suggests how the proof can be generalized to arbitrary dimension. In the next subsection, we sketch the more general proof for any SPT models based on group cohomology, using the tools developed in this section.

2.2.4 Thermal instability of SPT for group cohomology models

We now prove the more general formulation of Theorem 1: that SPTs in arbitrary dimension, protected by onsite symmetries are trivial at nonzero temperature. We prove this statement for a class of models based on the group cohomology formalism [111]. This class captures many of the known SPT phases protected by onsite symmetries, and we believe the arguments presented here can be generalised to models with onsite symmetries outside of the formalism. The construction of these models involves some technical details which we briefly review.

The models are constructed in terms of special functions known as cocycles of the group G . A d -cochain of the group G over $U(1)$ is a function $\nu_d : G^{d+1} \rightarrow U(1)$ that satisfies

$$\nu_d(g_0, g_1, \dots, g_d) = \nu_d(gg_0, gg_1, \dots, gg_d) \quad \forall g, g_k \in G. \quad (2.53)$$

An important set of d -cochains are the d -cocycles, which satisfy the additional cocycle condition for any $d + 2$ elements g_0, \dots, g_{d+1} of G , namely

$$\prod_{j=0}^{d+1} \nu_d(g_0, \dots, g_{j-1}, g_{j+1}, \dots, g_{d+1})^{(-1)^j} = 1 \quad \forall g_k \in G. \quad (2.54)$$

An equivalence relation on the set of d -cocycles is given by multiplication by a d -coboundary. A d -coboundary λ_d is a d -cochain that can be expressed as

$$\lambda_d(g_0, g_1, \dots, g_d) = \prod_{j=0}^d \mu_{d-1}(g_0, \dots, g_{j-1}, g_{j+1}, \dots, g_d)^{(-1)^j}, \quad (2.55)$$

for some $(d - 1)$ -cochain μ_{d-1} . Note that every d -coboundary is a d -cocycle, but not necessarily the other way around. The equivalence classes of d -cocycles are labelled by elements of the d -cohomology group $\mathcal{H}^d(G, U(1))$.

For a system with symmetry group G in d spatial dimensions, consider a triangulation T^Δ of a d -dimensional manifold. We label the k -simplexes of the triangulation by σ_k , and the set of all k -simplexes by Δ_k . We assume that T^Δ has a bounded degree (the number of edges containing any given vertex must be constant). Additionally, we require that the triangulation has a branching structure (an orientation on each edge such that there is no oriented loop on any triangle) which allows us to give a parity $P(\sigma_d) = \pm 1$ to each d -simplex. To each vertex $v \in \Delta_0$, we associate a $|G|$ -dimensional Hilbert space, a basis for which is given by $\{|g\rangle, g \in G\}$. Let $N = |\Delta_0|$ be the number of spins. The symmetry action is given by the left regular representation

$$S(g) |g_1, \dots, g_N\rangle = |gg_1, \dots, gg_N\rangle. \quad (2.56)$$

Consider first the trivial product state

$$|\psi_0\rangle = |+\rangle^{\otimes N}, \quad \text{where} \quad |+\rangle = \frac{1}{\sqrt{|G|}} \sum_{g \in G} |g\rangle, \quad (2.57)$$

which is the ground state of the trivial Hamiltonian

$$H_0 = \sum_{v \in \Delta_0} (I - 2|+\rangle\langle +|_v), \quad (2.58)$$

where the notation $|+\rangle\langle +|_v$ means the projector $|+\rangle\langle +|$ at site v , and identity elsewhere. Notice that $(I - 2|+\rangle\langle +|_v)^2 = I$. For any $(d + 1)$ -cocycle ν_{d+1} , one can construct the unitary

$$U = \prod_{\sigma_d \in \Delta_d} (U_{\nu_{d+1}}^{\sigma_d})^{P(\sigma_d)}, \quad P(\sigma_d) = \pm 1, \quad (2.59)$$

where $U_{\nu_{d+1}}^{\sigma_d}$ acts on spins that are vertices of σ_d and $P(\sigma_d)$ represents the orientation of σ_d . Here $U_{\nu_{d+1}}$ is a $(d+1)$ -body diagonal phase operator that acts as

$$U_{\nu_{d+1}}|g_1, \dots, g_{d+1}\rangle = \nu_{d+1}(1, g_1, \dots, g_{d+1})|g_1, \dots, g_{d+1}\rangle. \quad (2.60)$$

Consider the Hamiltonian $H(\nu_{d+1}) = UH_0U^\dagger$ with ground state $|\psi(\nu_{d+1})\rangle = U|\psi_0\rangle$. Two important results in Ref. [111] are the following:

1. The unitary U , Hamiltonian $H(\nu_{d+1})$, and state $|\psi(\nu_{d+1})\rangle$ are symmetric under the onsite symmetry of G .
2. If ν_{d+1} is nontrivial (i.e. it is not equivalent to the constant $\nu'_{d+1} = 1$), then $|\psi(\nu_{d+1})\rangle$ belongs to a nontrivial SPT phase.

An important consequence of the cocycle functions that will be used in our proof, is their invariance under the so-called Pachner moves. Pachner moves are local operations that convert one triangulation into another one. Any two triangulations of a (piecewise linear) manifold can be related by a sequence of Pachner moves. In two-dimensions, the two basic Pachner moves are shown in Fig. 2.3. If two triangulations are related by a sequence of Pachner moves, then the SPT wavefunctions on these triangulations are related by a symmetric unitary combined with the addition/removal of ancillas in the $|+\rangle$ state. Since a sequence of Pachner moves corresponds to a symmetric unitary, we can define the depth of this sequence. Namely, we define a parallel Pachner move as any sequence of Pachner moves performed on disjoint d -simplexes. Then the depth of a Pachner sequence is the number of parallel Pachner moves, multiplied by the (max) diameter of the d -simplexes that are acted upon (this equals the depth of the corresponding symmetric unitary).

We now prove that for any group G and in any dimension d , the above Hamiltonian must have trivial SPT-order at nonzero temperature. The proof proceeds in a similar way to Theorem 1, where we first approximate the Gibbs ensemble $\rho(\beta)$ by a convex combination of valid configurations, and then show that each valid configuration is low-depth equivalent to a classical ensemble. Since a combination of trivial ensembles is trivial, the result follows.

Theorem 2. *For any $T > 0$, the symmetric Gibbs state $\rho(\beta)$ of $H(\nu_{d+1})$ is (r, ϵ) SPT-trivial, where $r = \mathcal{O}(\log(L) \log \log(L))$, and $\epsilon = 1/\text{poly}(L)$, where $\text{poly}(L)$ is a polynomial in the lattice linear size L .*

Proof sketch. Let T^Δ be the triangulation upon which $H(\nu_{d+1})$ is defined. For simplicity of presentation, we assume the triangulation is translationally invariant on some scale (although non-essential, this allows us to use a lattice renormalization argument). We assume that for each hypercubic region of side-length l , there is a constant number $N_c = \mathcal{O}(l^d)$ of vertices in

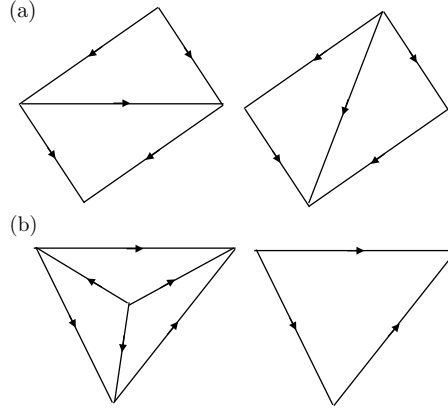


Fig. 2.3 In two dimensions, there are two distinct Pachner moves: (a) two triangles are replaced by two triangles and (b) three triangles are replaced by one triangle and the number of vertices changes by 1. The arrows represent the orientation of each edge. Notice that there are no oriented loops on any triangle.

T^Δ . Since T^Δ has bounded degree (by assumption), we have that each vertex belongs to a constant number of d -simplexes.

Similarly to the two-dimensional case, we divide up the lattice into a hypercubic grid \mathcal{P}_l such that each hypercubic region has side-length $l = (c \log(L))^{\frac{1}{d}}$ for some constant c . For each $\mathbf{k} \in \{0, 1\}^N$, we can define an imperfect Hamiltonian $H(\mathbf{k})$. Let $\bar{\rho}(\mathbf{k})$ be the normalized, symmetric ground-space projector of $H(\mathbf{k})$. Any configuration that has at least one sink in every hypercubic region is called valid. By a straightforward generalization of Lemma 2, we can approximate $\rho(\beta)$, up to an error that is an inverse polynomial in the system size L by a weighted combination of valid configurations $\bar{\rho}(\mathbf{k})$.

Fix a valid configuration \mathbf{k} , and let S be a subset of vertices containing precisely one sink in each hypercubic region. The goal is to find a sequence of Pachner moves taking T^Δ to a different triangulation T^S , whose vertex set is the chosen set of sinks S (note that T^S is not uniquely determined, but any choice will suffice). This sequence of Pachner moves gives a corresponding symmetric unitary $\mathcal{D}_{\mathbf{k}}$, taking the imperfect Hamiltonian to a trivial Hamiltonian. In particular, let T^S be any triangulation with vertices that are sinks and whose set of k -simplexes is labelled by Δ_k^S (see Fig. 2.4c). Then

$$U_{\mathbf{k}}^{(S)} = \prod_{\sigma_d \in \Delta_d^S} (U_{\nu_{d+1}}^{\sigma_d})^{P(\sigma_d)} \quad (2.61)$$

is a symmetric unitary that is supported entirely on the set of sinks and therefore the imperfect Hamiltonian $H_0(\mathbf{k})$ of the trivial model H_0 in Eq. (2.58) is invariant under U_S . Then since T^S and T^Δ are Pachner equivalent, there exists a symmetric unitary $\mathcal{D}_{\mathbf{k}}$ such that

$$\mathcal{D}_{\mathbf{k}} H(\mathbf{k}) \mathcal{D}_{\mathbf{k}}^\dagger = U_{\mathbf{k}}^{(S)} H_0(\mathbf{k}) U_{\mathbf{k}}^{(S)\dagger} = H_0(\mathbf{k}), \quad (2.62)$$

from which it follows that $\mathcal{D}_{\mathbf{k}}\bar{\rho}(\mathbf{k})\mathcal{D}_{\mathbf{k}}^\dagger$ is a trivial product state.

Now it only remains to determine an upper bound on the depth of the circuit $\mathcal{D}_{\mathbf{k}}$ corresponding to this sequence of Pachner moves. We now describe a sequence of Pachner moves taking T^Δ to T^S that upper bounds the depth of $\mathcal{D}_{\mathbf{k}}$ by $\mathcal{O}(\log(L) \log \log(L))$.

The sequence of Pachner moves taking T^Δ to T^S can be divided into two steps: a renormalization sequence, followed by a small vertex shifting. We present the argument in 2 dimensions, as the case for higher dimensions works analogously, where the 2 dimensional Pachner moves are replaced with the corresponding higher dimensional Pachner moves. The steps are depicted in Fig. 2.4. Note that we will keep track of the original vertices throughout, which we refer to as *ambient vertices* (as they correspond to the original degrees of freedom). Any ambient vertices that are not part of new triangulations correspond to spins in the $|+\rangle$ state.

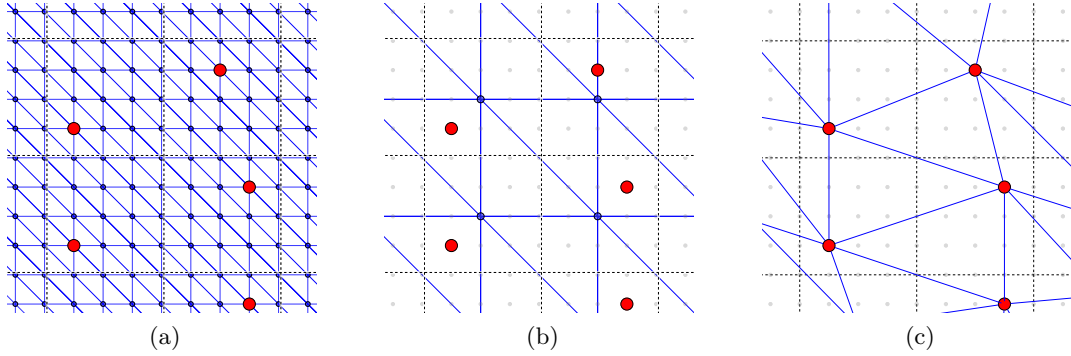


Fig. 2.4 (Color online) The two principle steps to take the original triangulation T^Δ in (a) to the triangulation T^S in (c), whose vertices are all sinks (large dots). The first step is to renormalize the T^Δ , resulting in the triangulation in (b). The second step is a vertex shifting, resulting in the triangulation in (c). The grid \mathcal{P}_l with side-lengths $(c \log(L))^{\frac{1}{d}}$ is displayed by the dashed lines. Faded grey nodes denote ambient vertices no longer part of the triangulation, which correspond to decoupled spins in the $|+\rangle$ state after the circuit \mathcal{D} has been applied.

Firstly, we perform a sequence of renormalization steps, which increases the original length of the edges in T^Δ from $\mathcal{O}(1)$ to l , and in doing so reduces the number of vertices down to one per cubic region. Firstly, we claim that to renormalize the length of all edges by a factor of 2 takes a constant number of parallel Pachner moves. Indeed for a triangular lattice, it takes 12 parallel Pachner moves to scale the lattice by a factor of 2, as depicted in Fig. 2.5. In general, the number of moves will be proportional to the maximum degree of a vertex. Since we wish to rescale the edge length to $l = (c \log(L))^{\frac{1}{d}}$, we need to do $\mathcal{O}(\log \log(L))$ renormalization steps. Each Pachner move acts on a simplex of size at most $l^d = c \log(L)$, and therefore the depth of this Pachner sequence is $\mathcal{O}(\log(L) \log \log(L))$.

Secondly, we need to transform the renormalized triangulation (depicted in Fig. 2.4b) to T^S . Since there is only one vertex per cubic region in the renormalized triangulation, this process can

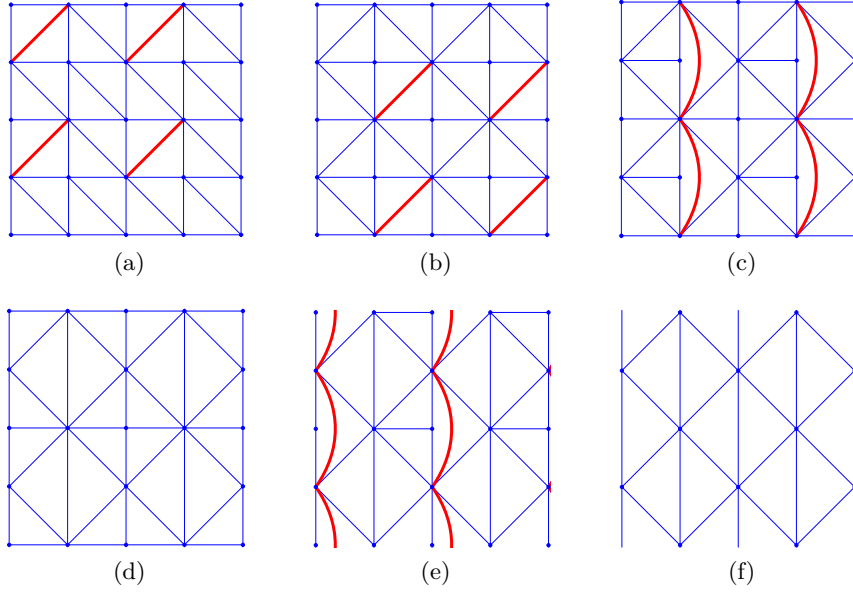


Fig. 2.5 (Color online) The first six parallel Pachner moves for a single renormalization step that scales the edge lengths of the triangular lattice by a factor of two. New edges arising from Pachner moves are depicted by thick (red) lines. Notice that some of the edges are unchanged (namely the diagonal ones), but this process can be repeated to rescale them too. Sinks are not displayed in this figure as they do not yet play a role. This process can be repeated $\mathcal{O}(\log \log(L))$ times to rescale T^Δ to the renormalized triangulation in Fig. 2.4b.

be considered as a shifting of the vertices. This can be achieved by firstly reintroducing the sinks as vertices using the second Pachner move in Fig. 2.3, then removing the remaining ambient vertices using a combination of Pachner moves². Since Pachner moves in disjoint simplexes can be performed in parallel, the depth of this sequence is proportional to the degree which (by assumption) is bounded in the original triangulation, and therefore also the renormalized triangulation. Then as each move acts on a simplex of size $l^d = c \log(L)$ the depth of this sequence is $\mathcal{O}(\log(L))$.

Putting these two steps together we have the depth of the sequence of Pachner moves taking T^Δ to T^S is $\mathcal{O}(\log(L) \log \log(L))$. This sequence of Pachner moves gives rise to a symmetric circuit \mathcal{D}_k taking $\bar{\rho}(k)$ to a trivial state. Since this argument works for every valid configuration, we have that $\rho(\beta)$ is polynomially approximated by a sum of $(\mathcal{O}(\log(L) \log \log(L)), 0)$ SPT-trivial states, and therefore $\rho(\beta)$ is (r, ϵ) SPT-trivial, with $r = \mathcal{O}(\log(L) \log \log(L))$, and $\epsilon = 1/\text{poly}(L)$. Note that the key ingredient in this sequence of Pachner moves is that the degree remains bounded at all stages, and therefore to disentangle any spins requires only a constant number

²Note that we assume that we have a sufficiently large system such that there exists enough sinks to perform the required Pachner moves. This is without loss of generality as we are concerned with the scaling rather than small system details.

of Pachner moves. The exponent of the log may be improved for example by keeping the sinks in the triangulation during the renormalization steps. \square

2.3 A model with a thermal SPT phase

Despite proving that a thermal SPT phase is impossible in models with only onsite symmetries, we now provide an example of a model with thermal SPT-order by enforcing a stronger, higher-form symmetry. The model we consider is the cluster model on a particular three-dimensional lattice, first introduced by Raussendorf, Bravyi and Harrington (RBH) [136], protected by a $\mathbb{Z}_2 \times \mathbb{Z}_2$ 1-form symmetry. While the discussion here is specific to the RBH model, the tools developed and the analysis is quite general, and can be extended to other higher-form models.

Cluster states are well known within the quantum information community for their importance as a resource for measurement-based quantum computation (MBQC) [20]. They can be defined on any graph or lattice, and their usefulness for computation is strongly dependent upon the underlying graph or lattice dimension [169, 20]. In the context of SPT phases, the 1D cluster model is known to belong to a nontrivial phase with a $\mathbb{Z}_2 \times \mathbb{Z}_2$ onsite symmetry [170], and states within this phase have been shown to be useful as quantum computational wires [132]. Additionally, certain states in 2D possessing SPT-order protected by onsite symmetries have been shown to be universal resources for MBQC [35, 171].

From an information processing standpoint, the RBH model is very compelling. The model forms a basis for the topological MBQC scheme, a universal model of quantum computation with a very high threshold arising from topological considerations [66, 172]. We wish to understand the physical origin and underlying quantum order that underpins the high threshold of this scheme. We begin by reviewing the RBH model.

2.3.1 The RBH model

In order to present the RBH model, it will be helpful to review some homological terminology, which will allow us to specify all relevant operators and make the following analysis simpler. The lattice we consider is a cubic lattice \mathcal{C} of linear size d . For simplicity, we consider periodic boundary conditions in each direction such that \mathcal{C} has topology of a 3-torus. We label by Δ_3 , Δ_2 , Δ_1 , and Δ_0 the set of all cubes, faces, edges, and vertices of \mathcal{C} , respectively. Elements of Δ_k are called k -cells and denoted by σ_k for $k \in \{0, 1, 2, 3\}$.

Some homological notation

The lattice \mathcal{C} naturally gives rise to a chain complex

$$C_3 \xrightarrow{\partial_3} C_2 \xrightarrow{\partial_2} C_1 \xrightarrow{\partial_1} C_0, \quad (2.63)$$

which is a set of vector spaces C_k and linear maps $\partial_k : C_k \rightarrow C_{k-1}$ between them called boundary maps, which we now define. Each vector space $C_k \equiv C_k(\mathcal{C}; \mathbb{Z}_2)$ has elements consisting of formal sums of the basis elements $\sigma_k \in \Delta_k$ with coefficients from the field \mathbb{Z}_2 . A general vector c_k in C_k is called a k -chain, and can be uniquely written as $c_k = \sum_{\sigma_k \in \Delta_k} a(\sigma_k) \sigma_k$, with $a(\sigma_k) \in \mathbb{Z}_2$. Intuitively, a k -chain can be one-to-one identified with a subset of k -cells of Δ_k , so a 3-chain $c_3 \in C_3$ represents a subset of volumes (i.e. $c_3 \subset \Delta_3$), a 2-chain represents a subset of surfaces, and so on. Between vector spaces C_k we have the boundary map $\partial_k : C_k \rightarrow C_{k-1}$, defined on each basis element as

$$\partial_k(\sigma_k) = \sum_{\substack{\sigma_{k-1} \in \Delta_k \\ \sigma_{k-1} \subset \sigma_k}} \sigma_{k-1} \quad (2.64)$$

and extended to an arbitrary k -chain by linearity. Here, the sum is over all $(k-1)$ -cells σ_{k-1} that are contained in σ_k .

There are two important classes of chains known as cycles and boundaries. The k -cycle group $Z_k = \ker(\partial_k)$ is the vector space (which can be regarded as a group) consisting of k -chains that have no boundary. Elements of Z_k are known as k -cycles. Similarly, the k -boundary group $B_k = \text{im}(\partial_{k+1})$ is the vector space consisting of k -chains that are the boundary of a $(k+1)$ -chain. Elements of B_k are known as k -boundaries. Importantly, the boundary maps satisfy $\partial_{k-1} \circ \partial_k = 0$, which implies that every boundary is a cycle, but in general not every cycle is a boundary. A cycle that is not a boundary is referred to as nontrivial or noncontractible.

One can define the dual lattice \mathcal{C}^* of the cubic lattice \mathcal{C} , which is obtained by replacing volumes by vertices, faces by edges, edges by faces, and vertices by volumes. The dual lattice \mathcal{C}^* is also a cubic lattice, but shifted with respect to the primal (initial) lattice. We can define a chain complex associated with the dual lattice in a similar way to Eq. (2.63), where C_k^* are vector spaces with k -cells of the dual lattice as basis vectors, and corresponding boundary maps ∂_k^* . We denote the dual cycle groups by Z_k^* , and dual boundary groups by B_k^* .

Since each k -chain corresponds to a unique dual- $(3-k)$ -chain, the dual boundary map $\partial_k^* : C_k^* \rightarrow C_{k-1}^*$ can be thought of as a map $\partial_k^* : C_{3-k} \rightarrow C_{4-k}$. Namely, since any $(3-k)$ -chain c_{3-k} is dual to a unique dual- k -chain c_k' , we define $\partial_k^* c_{3-k}$ to be the unique $(4-k)$ -chain dual to $\partial_k^* c_k'$. In the following, we suppress the subscript on the boundary and dual boundary maps, and we will freely apply the dual boundary map on both chains and dual chains using the previous correspondence. This allows us to regard 1-cycles and dual-1-cycles as closed loop-like

subsets of the lattice \mathcal{C} , and 2-cycles and dual-2-cycles as closed surface-like subsets of the lattice \mathcal{C} .

The RBH Hamiltonian

With this terminology, we can now present the RBH model in a useful homological formulation. The Hilbert space can be constructed by placing a qubit on every 2-cell $\sigma_2 \in \Delta_2$ and every 1-cell $\sigma_1 \in \Delta_1$, which we will refer to as the primal and dual qubits respectively (we think of dual qubits as residing on the 2-cells of the dual lattice). The Hilbert space is given by $\mathcal{H} = \mathcal{H}_1 \otimes \mathcal{H}_2$, where \mathcal{H}_1 is the Hilbert space of the dual qubits, and \mathcal{H}_2 is the Hilbert space of the primal qubits.

For a given 2-chain $c_2 = \sum_{\sigma_2 \in \Delta_2} a(\sigma_2) \sigma_2$, with $a(\sigma_2) \in \mathbb{Z}_2$, define the Pauli operator

$$X(c_2) = \prod_{\sigma_2 \in c_2} X_{\sigma_2}, \quad (2.65)$$

where X_{σ_2} is the Pauli X supported on the qubit at σ_2 . One can similarly define operators for Pauli Z as well as for the dual qubits. A general Pauli operator P then has the following decomposition

$$P = i^\alpha X(c_2) Z(c'_2) X(c_1) Z(c'_1), \quad (2.66)$$

for some $\alpha \in \{0, 1, 2, 3\}$, 2-chains c_2, c'_2 and 1-chains c_1 and c'_1 . One could equivalently decompose the operator P in terms of dual chains.

In this notation we can now describe the RBH Hamiltonian on this lattice. The Hamiltonian is given by a sum of local, commuting (5-body) terms

$$H_{\mathcal{C}} = - \sum_{\sigma_1 \in \Delta_1} K(\sigma_1) - \sum_{\sigma_2 \in \Delta_2} K(\sigma_2), \quad (2.67)$$

where

$$K(\sigma_1) = X(\sigma_1) Z(\partial^* \sigma_1), \quad \text{and} \quad K(\sigma_2) = X(\sigma_2) Z(\partial \sigma_2), \quad (2.68)$$

as depicted in Fig. 2.6a. We note that $K(\sigma_1)$ and $K(\sigma_2)$ are the standard cluster state stabilizer generators. The *cluster state* $|\psi_{\mathcal{C}}\rangle$ is the unique ground state of $H_{\mathcal{C}}$ which is the +1-eigenstate of each of the cluster terms $K(\sigma_1)$ and $K(\sigma_2)$.

An alternative description in terms of a circuit description shows that the cluster state is short-range entangled. Consider the circuit \mathcal{U}_{CZ} comprised of controlled- Z gates between every

neighbouring primal and dual qubit

$$\mathcal{U}_{CZ} = \prod_{\substack{\sigma_1 \in \Delta_1 \\ \sigma_2 \in \Delta_2}} \left(\prod_{\sigma'_1 \in \partial \sigma_2} CZ_{(\sigma_2, \sigma'_1)} \right) \left(\prod_{\sigma'_2 \in \partial^* \sigma_1} CZ_{(\sigma_1, \sigma'_2)} \right), \quad (2.69)$$

where the controlled- Z operator is defined in Eq. (2.10). One can confirm that

$$\mathcal{U}_{CZ}^\dagger H_C \mathcal{U}_{CZ} = - \sum_{\sigma_1 \in \Delta_1} X(\sigma_1) - \sum_{\sigma_2 \in \Delta_2} X(\sigma_2) =: H_X. \quad (2.70)$$

From this relation we see that the cluster state can be prepared from a product state by the circuit \mathcal{U}_{CZ} , as

$$|\psi_C\rangle = \mathcal{U}_{CZ} |+\rangle^{\otimes |\Delta_2 \cup \Delta_1|}, \quad (2.71)$$

where $|+\rangle$ is the $+1$ -eigenstate of Pauli X . Since \mathcal{U}_{CZ} can be represented by a constant-depth quantum circuit, the cluster state is short-range entangled. We now proceed to identify a 1 -form $\mathbb{Z}_2 \times \mathbb{Z}_2$ symmetry of the model and show that $|\psi_C\rangle$ resides in a nontrivial SPT phase at zero temperature when this symmetry is enforced.

1-form symmetry

The cluster state is a short-range entangled state and so in the absence of a symmetry it belongs to the SPT-trivial phase. One can show that with only an onsite symmetry, this model remains in the SPT-trivial phase³. We introduce a $\mathbb{Z}_2 \times \mathbb{Z}_2$ 1-form symmetry of the model and show that the cluster state is in a nontrivial SPT phase when this symmetry is enforced. Formally, we have two copies of a \mathbb{Z}_2 1-form symmetry: one for each lattice (primal and dual). The symmetry actions are given by a unitary representation S of the 2-boundary and dual-2-boundary groups as

$$S(b_2) := X(b_2), \quad S(b'_2) := X(b'_2), \quad (2.72)$$

for any 2-boundary $b_2 \in B_2$ and dual-2-boundary $b'_2 \in B_2^*$. Any 2-boundary or dual-2-boundary corresponds to a closed, two-dimensional surface \mathcal{M} of the primal or dual lattice, respectively. The 1-form symmetry can therefore be viewed as being imposed by symmetry operators supported on qubits residing on closed, contractible two-dimensional submanifolds of \mathcal{C} .

³Indeed, for a cluster state in any dimension $D \geq 2$, with onsite symmetry, one can generalise the two-dimensional result of [35] and construct a disentangling circuit involving symmetric gates comprised of controlled- Z operations.

A local, generating set of symmetry operators is given by the following elementary operators

$$\tilde{G} = \{S(\partial\sigma_3), S(\partial^*\sigma_0) \mid \sigma_3 \in \Delta_3, \sigma_0 \in \Delta_0\}, \quad (2.73)$$

which are all 6-body. For example, an elementary 1-form operator $S(\partial\sigma_3)$ is supported on the surface of a single cube as depicted in Fig. 2.6b. Multiplying two neighbouring symmetry operators $S(b_2)S(\bar{b}_2) = S(b_2 + \bar{b}_2)$ can be viewed as gluing together the pair of surfaces that they correspond to. We conclude that the symmetry is a representation of the boundary groups $B_2 \times B_2^*$.

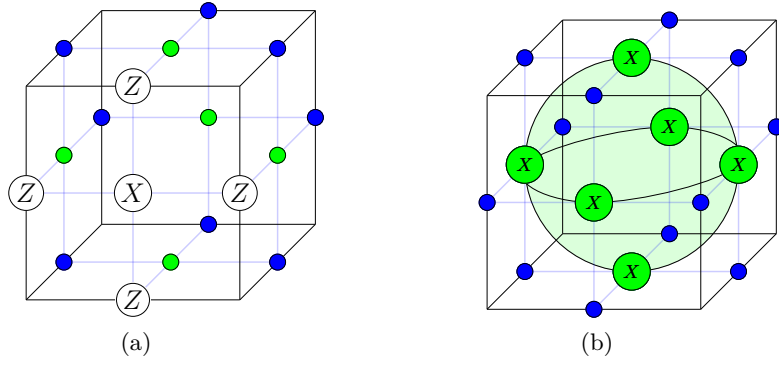


Fig. 2.6 (Color online) (a) A unit cell of the cluster lattice \mathcal{C} with a single cluster term $K(\sigma_2)$. (b) An elementary 1-form operator $S(\partial\sigma_3)$. The primal qubits are depicted as light (green) circles and the dual qubits are depicted in dark (blue) circles.

An important feature of the 1-form symmetry operators is that they can be expressed as products of cluster terms

$$S(b_2) = \prod_{\sigma_2 \in b_2} K(\sigma_2) \quad \text{and} \quad S(b'_2) = \prod_{\sigma_1^* \in b'_2} K(\sigma_1), \quad (2.74)$$

where the second product is over all 1-cells σ_1 whose dual belong to b'_2 . For example, this is easily verified for the elementary 1-form operator in Fig. 2.6. It follows that these operators commute with $H_{\mathcal{C}}$, and thus are symmetries of the cluster model. Additionally, the cluster state is a +1-eigenstate of these symmetry operators. Interestingly, such operators arise naturally in the context of topological MBQC and error correction [172, 136] and we will return to this connection in the following section.

Thermal state of the 1-form symmetric RBH model

We now consider the symmetric Gibbs state of the RBH model Hamiltonian $H_{\mathcal{C}}$. In the presence of the 1-form symmetry, excitations in the RBH model take the form of one-dimensional, loop-like objects, which can be seen as follows. Excitation operators can be constructed out of

Pauli- Z operators, but the 1-form symmetry demands they form closed loops in the following way. Consider the operator $Z(c_1)$ for any 1-chain $c_1 \in C_1$. This operator anti-commutes with cluster terms along the cycle

$$\{K(\sigma_1), Z(c_1)\} = 0 \iff \sigma_1 \in c_1, \quad (2.75)$$

and will commute with the 1-form symmetry operators if and only if it has no boundary $\partial c_1 = 0$. Therefore excitation operators on the dual lattice are given by $Z(\gamma)$ where $\gamma \in Z_1$ is a 1-cycle. Similarly, excitation operators on the primal lattice are given by $Z(c'_1)$, for any dual-1-cycle $c'_1 \in Z_1^*$. Recall, 1-cycles and dual-1-cycles look like loop-like objects, and example excitation operators are shown in Fig. 2.7.

A general symmetric excitation is given by $|\psi(\gamma, \gamma')\rangle = Z(\gamma)Z(\gamma')|\psi_{\mathcal{C}}\rangle$ with $\gamma \in Z_1$, $\gamma' \in Z_1^*$, and the energy cost of introducing this excitation is $E(\gamma, \gamma') = 2(|\gamma| + |\gamma'|)$. Notice that excitations created by Pauli X operators can be converted into the above form, since they are equivalent up to products of cluster terms (of which the cluster state is a $+1$ -eigenstate). As such, excited states are in one-to-one correspondence with elements of the 1-cycle and dual-1-cycle groups $Z_1 \times Z_1^*$.

The symmetric Gibbs state under this 1-form symmetry is given by a distribution over loop configurations

$$\rho_{\mathcal{C}}(\beta) = \sum_{(\gamma, \gamma') \in Z_1 \times Z_1^*} \Pr_{\beta}(\gamma, \gamma') |\psi(\gamma, \gamma')\rangle \langle \psi(\gamma, \gamma')|, \quad (2.76)$$

where the sum is over all primal and dual 1-cycles, and

$$\Pr_{\beta}(\gamma, \gamma') = \frac{1}{\mathcal{Z}} e^{-\beta E(\gamma, \gamma')}, \quad \text{where} \quad \mathcal{Z} = \sum_{(\gamma, \gamma') \in Z_1 \times Z_1^*} \Pr_{\beta}(\gamma, \gamma'). \quad (2.77)$$

Here, $\Pr_{\beta}(\gamma, \gamma')$ is a probability distribution over loop-like configurations. In the following subsection, we show that this ensemble has nontrivial SPT-order under the 1-form symmetry, using a duality map known as *gauging*. Then in the subsequent section, we will provide a proof of the nontrivial SPT-ordering of the thermal state using a set of non-local order parameters as witnesses of the SPT-order.

2.3.2 SPT-order of the RBH model

We now show that the RBH model possesses nontrivial SPT-order under the 1-form symmetry by means of a duality map known as *gauging*. Gauging is a procedure widely used throughout the study of many-body physics [109, 173–175], and has recently found application in the study of fault-tolerant logical gates in topological quantum codes [156, 145]. Gauging is the process of transforming a global symmetry G into a local symmetry by minimally coupling the system

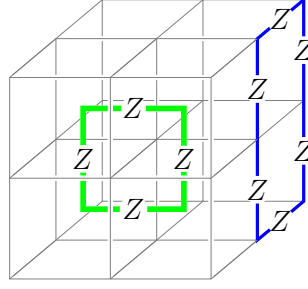


Fig. 2.7 (Color online) Examples of excitation operators. A 1-cycle is depicted by the thinner dark (blue) line, while a dual-1-cycle is depicted by the thicker light (green) line.

to gauge fields. We will use an argument originally proposed by Levin and Gu [109] that two Hamiltonians must belong to distinct SPT phases if the gauged versions belong to distinct topological phases.

We will take the approach of [156, 145] and view the gauging procedure as a duality map between SPT-ordered Hamiltonians and topologically ordered Hamiltonians, a correspondence known to hold for many models [173]. By showing that the gauged RBH model belongs to a different phase than the gauged trivial model, we can deduce that the RBH model belongs to a nontrivial SPT phase. Furthermore, thermal stability of the SPT-order can be demonstrated by showing that the RBH cluster state corresponds to a nontrivial gapped domain wall in the 4D toric code, which is known to have thermally stable topological order [47].

Gauging the 1-form symmetry

We now outline the procedure of gauging the $\mathbb{Z}_2 \times \mathbb{Z}_2$ 1-form symmetry. More details of gauging models possessing higher-form symmetries can be found in [145]. We start with a basis for the primal and dual Hilbert spaces \mathcal{H}_1 and \mathcal{H}_2 given by vectors of the 1-chain and 2-chain groups respectively. For any 1-chain $c_1 \in C_1$, we can uniquely specify a computational basis state

$$c_1 = \sum_{\sigma_1 \in \Delta_1} a(\sigma_1) \sigma_1, \quad \implies \quad |c_1\rangle = |\{a(\sigma_1)\}\rangle, \quad (2.78)$$

where $a(\sigma_1) \in \mathbb{Z}_2$. A similar identification holds for the computational basis states in \mathcal{H}_2 and the 2-chain group. The gauging map \mathcal{G} on the level of states takes states in \mathcal{H}_1 to \mathcal{H}_2 , and states in \mathcal{H}_2 to \mathcal{H}_1 and can be concisely defined by the boundary and dual boundary maps, as follows. On the computational basis, the map $\mathcal{G} : \mathcal{H}_1 \otimes \mathcal{H}_2 \rightarrow \mathcal{H}_2 \otimes \mathcal{H}_1$ is defined by

$$\mathcal{G}(|c_1\rangle \otimes |c_2\rangle) = |\partial^* c_1\rangle \otimes |\partial c_2\rangle, \quad (2.79)$$

and extended to $\mathcal{H} = \mathcal{H}_1 \otimes \mathcal{H}_2$ by linearity. For example, on a computational basis state, \mathcal{G} is depicted in Fig. 2.8.

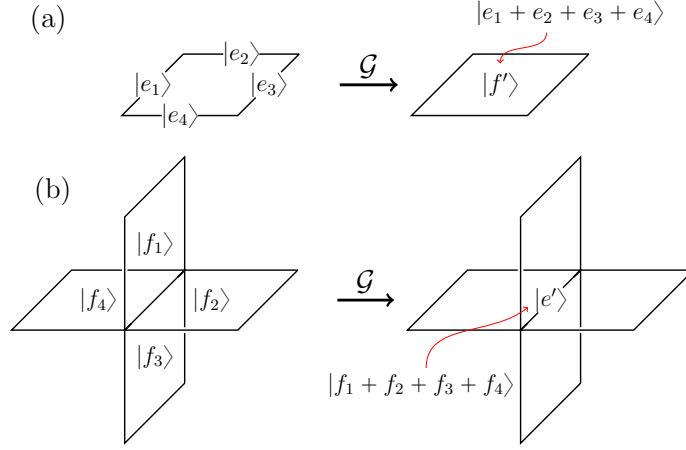


Fig. 2.8 (Color online) The gauging map on computational basis states. (a) States on the dual sublattice map to states on the primal sublattice. (b) States on the primal lattice map to states on the dual sublattice. The sums are performed mod 2.

Importantly, any state $|\psi_{\mathcal{G}}\rangle$ in the image of \mathcal{G} satisfies the gauge symmetry condition

$$Z(z_2)Z(z'_2)|\psi_{\mathcal{G}}\rangle = |\psi_{\mathcal{G}}\rangle, \quad (2.80)$$

for any 2-cycle z_2 and dual-2-cycle z'_2 . These gauge symmetry operators are similar to the 1-form operators in the RBH model, only they are now in the Pauli- Z basis, and there are additional gauge symmetry operators for nontrivial and 2-cycles dual-2-cycles. Since higher-form symmetries can be viewed as gauge symmetries in a dual description, the distinction between the two types of symmetries is not a definitive one. In this Chapter, we treat higher-form symmetries as symmetries which exist before the gauging map, and gauge symmetries as those which emerge after the gauging map.

The gauging map \mathcal{G} can be extended to a map on symmetry respecting operators. For any symmetric operator A , the gauged operator A' is defined implicitly by the following equation

$$\mathcal{G}(A|\psi\rangle) = A'\mathcal{G}(|\psi\rangle). \quad (2.81)$$

Importantly, the 1-form symmetry operators are mapped to the identity. Note that A' is only defined up to gauge symmetry operators in Eq. (2.80). One can use Eq. (2.81) to verify that gauging the trivial Hamiltonian H_X of Eq. (2.70) gives the following Hamiltonian

$$H_X^{(\mathcal{G})} = - \sum_{\sigma_1 \in \Delta_1} X(\partial^* \sigma_1) - \sum_{\sigma_2 \in \Delta_2} X(\partial \sigma_2). \quad (2.82)$$

Since the gauged Hilbert space satisfies the gauge symmetry condition in Eq. (2.80), one can add Z -type terms $Z(\partial\sigma_3)$ and $Z(\partial^*\sigma_0)$ to the gauged Hamiltonian $H_X^{(\mathcal{G})}$ to fix out the gauge invariant ground space. Therefore, gauging the trivial Hamiltonian gives rise to two decoupled three-dimensional toric code Hamiltonians with qubits on faces and edges, respectively. Each of the toric codes belong to a nontrivial (intrinsic) topologically ordered phase at zero temperature.

On the other hand, gauging the RBH Hamiltonian gives

$$H_C^{(\mathcal{G})} = - \sum_{\sigma_1 \in \Delta_1} K^{(\mathcal{G})}(\sigma_1) - \sum_{\sigma_2 \in \Delta_2} K^{(\mathcal{G})}(\sigma_2), \quad (2.83)$$

where

$$K^{(\mathcal{G})}(\sigma_1) = Z(\sigma_1)X(\partial^*\sigma_1), \quad K^{(\mathcal{G})}(\sigma_2) = Z(\sigma_2)X(\partial\sigma_2). \quad (2.84)$$

This is equivalent to the original RBH Hamiltonian up to a Hadamard transformation $H^{\otimes |\Delta_1 \cup \Delta_2|}$, where H is the Hadamard gate, exchanging the Pauli X and Z operators. Therefore the ground state of $H_C^{(\mathcal{G})}$ remains short-range entangled. As \mathcal{G} is locality preserving and gap preserving, the inequivalence of the two gauged models shows that the RBH model belongs to a nontrivial SPT phase under the 1-form symmetry.

Gapped domain wall at nonzero temperature

An interesting and perhaps surprising application of the classification of SPT-ordered phases is in the construction of gapped domain walls in topological models [145]. Here, we show that the RBH model with $\mathbb{Z}_2 \times \mathbb{Z}_2$ 1-form symmetry can be used to construct a nontrivial domain wall in two copies of the four-dimensional toric code. The fact that the domain wall implements a nontrivial automorphism of the excitation labels in the 4D toric codes demonstrates that the RBH model has nontrivial SPT-order at zero temperature [119, 156]. We will in addition use this argument to demonstrate that the RBH model with 1-form symmetry retains its SPT-order at nonzero temperature, by leveraging the thermal stability of the 4D toric code.

To illustrate this procedure, let us first consider the simpler case of a two-dimensional system with $\mathbb{Z}_2 \times \mathbb{Z}_2$ 0-form symmetry. Namely, consider a square lattice Λ with boundary and place qubits on vertices of Λ . Qubits can be labelled by one of two colors in such a way that neighbouring qubits are of different colors. We consider a system consisting of a trivial Hamiltonian in the bulk and the cluster state Hamiltonian on the boundary:

$$H_0 = - \sum_{u \in \text{bulk}(\Lambda)} X_u + H_{\text{cluster}}^{1D}, \quad (2.85)$$

where H_{cluster}^{1D} consists of terms supported on the boundary of Λ in the following way,

$$H_{\text{cluster}}^{1D} = - \sum_{j \in \partial(\Lambda)} Z_{j-1} X_j Z_{j+1}, \quad (2.86)$$

and the sum is over qubits on the boundary (which have been given a linear ordering).

The whole Hamiltonian has a $\mathbb{Z}_2 \times \mathbb{Z}_2$ 0-form symmetry, generated by tensor product of Pauli X on each sublattice of a given color. One can apply the gauging map to obtain a gauged Hamiltonian which possesses intrinsic topological order with gapped boundary. In this example, we will have two copies of the toric code with twisted gapped boundaries, where the two copies of the toric code are coupled by terms acting on the boundary. On this gapped boundary, pairs of point-like excitations $e_1 m_2$ and $e_2 m_1$ may condense, where e_i and m_i ($i = 1, 2$) represent electric charges and magnetic fluxes from each copy of the toric code. The e_i and m_i excitations correspond to violated X -type and Z -type stabilisers respectively, and occur at the end of strings of Z -type and X -type operators respectively.

By unfolding the lattice (see Fig. 2.9, also Ref. [176]) one can view this gapped boundary as a gapped domain wall connecting two copies of the toric code. Upon crossing this domain wall, anyonic excitations are exchanged in the following manner:

$$e_1 \leftrightarrow m_2, \quad m_1 \leftrightarrow e_2. \quad (2.87)$$

Since this is a nontrivial automorphism of excitation labels, the cluster state cannot be prepared by a low depth quantum circuit as detailed in [119]. Gapped domain walls in higher-dimensional topological phases of matter can be also constructed from 0-form SPT phases, leading to explicit construction of gapped domain walls in the higher-dimensional generalizations of the quantum double model.

Now let us turn to a construction of gapped domain walls from 1-form SPT phases. Consider a four-dimensional system with $\mathbb{Z}_2 \times \mathbb{Z}_2$ 1-form symmetry, defined on a lattice Λ' with the cubic lattice \mathcal{C} (described in the previous section) as its boundary. We will consider the following Hamiltonian:

$$H_1 = - \sum_{v \in \text{bulk}(\Lambda')} X_v - H_{\text{RBH}}^{\mathcal{C}}, \quad (2.88)$$

where $H_{\text{RBH}}^{\mathcal{C}}$ is the RBH Hamiltonian supported on qubits living on the three-dimensional boundary $\partial\Lambda' = \mathcal{C}$ of the lattice Λ' . We can gauge the above Hamiltonian to obtain two copies of the four-dimensional toric code with twisted gapped boundaries. On the boundary, loop-like excitations $e_1 m_2$ and $e_2 m_1$ may condense. Here, e_i and m_i ($i = 1, 2$) correspond to loop-like electric and magnetic excitations (i.e. violated X -type and Z -type stabilisers

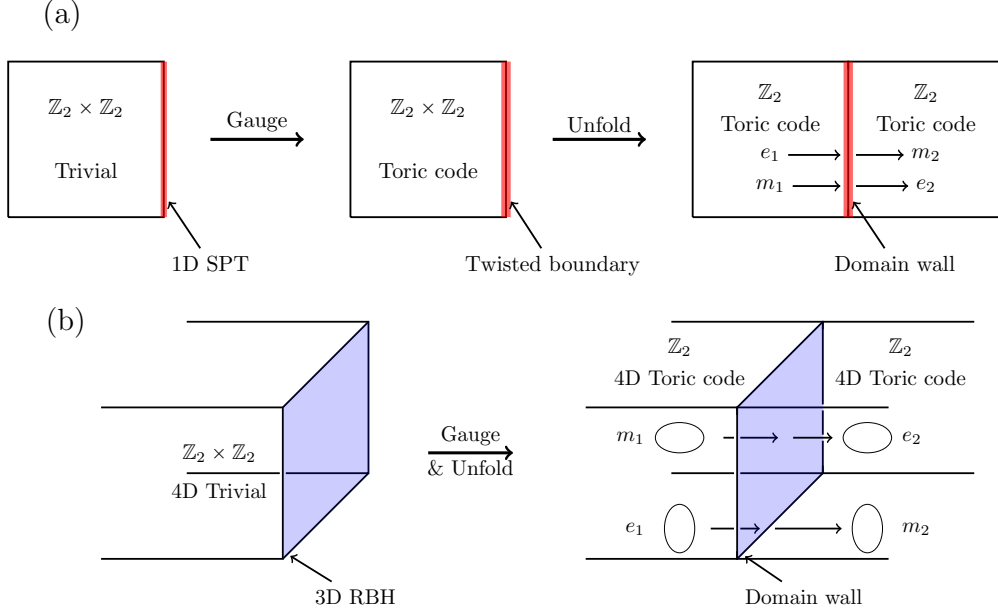


Fig. 2.9 (Color online) (a) Gauging $\mathbb{Z}_2 \times \mathbb{Z}_2$ symmetry of the two-dimensional model (which has the 1D cluster model on its boundary) leads to a twisted gapped boundary where point-like $e_1 m_2$ and $e_2 m_1$ particles may condense. This can be viewed as a nontrivial domain wall in the two-dimensional toric code. (b) Gauging the $\mathbb{Z}_2 \times \mathbb{Z}_2$ 1-form symmetry of the four-dimensional model (which has the three-dimensional RBH model on its boundary) leads to a nontrivial domain wall in the four-dimensional toric code, which exchanges electric and magnetic loop-like excitations.

of the four-dimensional toric code, respectively). The e_i and m_i excitations occur on the one-dimensional boundary of a two-dimensional membrane of Z -type and X -type operators, respectively. One can consider this gapped boundary as a gapped domain wall connecting the two copies of the four-dimensional toric code. Upon crossing the domain wall (see Fig. 2.9), the following exchange between electric and magnetic loop-like excitations is implemented

$$e_1 \leftrightarrow m_2, \quad m_1 \leftrightarrow e_2. \quad (2.89)$$

This observation already provides an argument that the RBH model is an example of a nontrivial 1-form SPT phase. To address the thermal stability of the SPT-order of the RBH model, one may appeal to the thermal stability of the four-dimensional toric code where the nontrivial braiding statistics between electric and magnetic loop-like excitations survive even at nonzero temperature. The fact that the gapped domain wall implements an exchange of loop-like excitations with nontrivial braiding properties at nonzero temperature is an indication that the underlying RBH Hamiltonian with 1-form symmetry is thermally stable.

2.3.3 Order parameters for detecting SPT-order of the thermal RBH model

We now give a direct proof of the nontrivial SPT-order of the thermal RBH model when the 1-form symmetry is enforced. The proof is based on a set of membrane operators that serve as order parameters. In addition to serving as witnesses of SPT-order, these membrane operators can be used to demonstrate the ability to perform gate teleportation in the MBQC scheme, as explored in section 2.4. These operators can be viewed as generalisations of the string order parameters used to detect SPT-order in one dimension [177–179] and similar constructions can be made for other higher-form SPT-ordered models. Such operators can be specified a two-dimensional surfaces as follows. For any dual-2-chain $\Gamma_1 \in C_2^*$ and any 2-chain $\Gamma_2 \in C_2$ (which will be thought of as surfaces in the primal and dual lattices respectively), we define a membrane operator

$$M(\Gamma_1) := \prod_{\sigma_1^* \in \Gamma_1} K(\sigma_1), \quad M(\Gamma_2) := \prod_{\sigma_2 \in \Gamma_2} K(\sigma_2), \quad (2.90)$$

where the first product is over all 1-cells σ_1 whose dual belongs to Γ_1 . By definition of the cluster terms in Eq. (2.68), the membrane operators can be written as follows

$$M(\Gamma_1) = X(\Gamma_1) \cdot Z(\partial^* \Gamma_1), \quad M(\Gamma_2) = X(\Gamma_2) \cdot Z(\partial \Gamma_2). \quad (2.91)$$

Since the cluster terms are commuting, the membrane operators for any 2-chain and dual-2-chain will also commute with each other and the cluster Hamiltonian. Additionally, at zero temperature the cluster state will be a +1-eigenstate of these operators for any choice of Γ_1 and Γ_2 (as the cluster state is a +1-eigenstate of the cluster terms).

We now specify a class of membrane operators that we will be interested in. First, let $(\hat{x}, \hat{y}, \hat{z})$ be a coordinate system of the cubic lattice \mathcal{C} (with opposite boundaries identified). We choose two two-dimensional slices $L \subseteq \mathcal{C}$ and $R \subseteq \mathcal{C}$ that are separated in the \hat{z} direction by a distance of at least $d/4$ (where d is the linear size of the lattice \mathcal{C}). These two regions are required to be extensive in both the \hat{x} and \hat{y} directions (i.e. each region has the topology of a torus) as depicted in Fig. 2.10.

We choose Γ_1 to be a nontrivial dual-2-cycle in the $\hat{x} - \hat{z}$ plane, which can be regarded as a noncontractible surface (see Fig. 2.10a). Let Γ_2 be a 2-chain in the $\hat{y} - \hat{z}$ plane, with boundary

$$\partial \Gamma_2 = S_2^L + S_2^R, \quad (2.92)$$

such that $S_2^L \subseteq L$ and $S_2^R \subseteq R$ are both nontrivial 1-cycles winding in the \hat{y} direction. The membrane operators corresponding to Γ_1 and Γ_2 are illustrated in Fig. 2.10. We note that the precise form of Γ_1 and Γ_2 is not important, any membranes that differ by a 2-boundary or a

dual-2-boundary may be considered equivalent. We note that the distance between the left and right boundaries S_2^L and S_2^R is lower bounded by $d/4$.

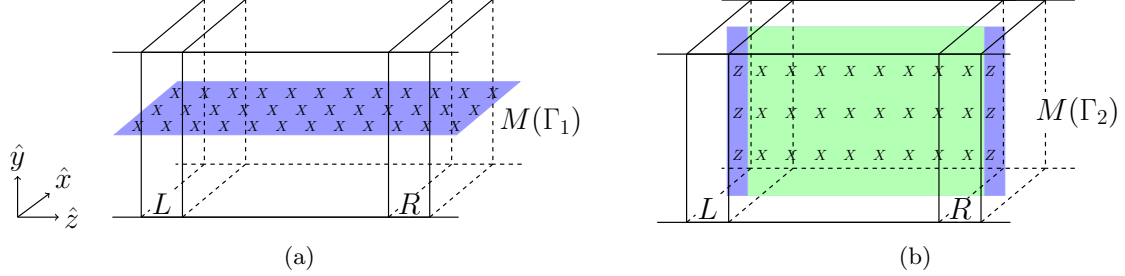


Fig. 2.10 (Color online) (a) The membrane operator $M(\Gamma_1)$ and (b) the membrane operator $M(\Gamma_2)$. The top and bottom boundaries are identified, as are the front and back boundaries. The primal qubits lie on the darker (blue) sheets, and the dual qubits on the lighter (green) sheet. The restrictions of these membrane operators to either L or R anti-commute. Note that length in the \hat{z} direction has been exaggerated.

These membrane operators are constructed to have nontrivial algebraic relations on the regions L and R . Namely, let $M^L(\Gamma_1)$ and $M^L(\Gamma_2)$ be the restriction of $M(\Gamma_1)$ and $M(\Gamma_2)$ to the region L , respectively. Then this restriction gives an anti-commuting pair of operators

$$\{M^L(\Gamma_1), M^L(\Gamma_2)\} = 0. \quad (2.93)$$

This is because the boundary of $M(\Gamma_2)$ consists of a string of Pauli Z operators, which intersects the sheet of Pauli X operators of $M(\Gamma_1)$ at a single site, as depicted in Fig. 2.10. Similarly, the restriction of the membrane operators to R gives a pair of anti-commuting operators. By analogy to one-dimensional SPT phases, the membrane operators $M(\Gamma_1)$ and $M(\Gamma_2)$ generate a $\mathbb{Z}_2 \times \mathbb{Z}_2$ group, while their restriction to the boundaries gives a nontrivial projective representation of the $\mathbb{Z}_2 \times \mathbb{Z}_2$ group [127, 132, 160].

For these choices, let $\Gamma = (\Gamma_1, \Gamma_2)$ denote the pair of membranes and let $M_1 = M(\Gamma_1)$ and $M_2 = M(\Gamma_2)$. To define the order parameter, we must also allow for the ability to perform local error correction within a neighbourhood of each region L and R . As we will see, this error correction will be a necessary ingredient to detect SPT-order in the RBH thermal state. In particular, let \bar{L} and \bar{R} be non-intersecting neighbourhoods of L and R respectively, and let $\mathcal{E}_{\bar{L}} \otimes \mathcal{E}_{\bar{R}}$ be any operation local to \bar{L} and \bar{R} . Namely, $\mathcal{E}_{\bar{L}} \otimes \mathcal{E}_{\bar{R}}$ consists of measurements, followed by an outcome dependent local unitary, which will be thought of as an error correction map. For a state ρ , the order parameter is defined as the expectation value of the membrane operators, maximized over all locally error corrected states $\bar{\rho} = \mathcal{E}_{\bar{L}} \otimes \mathcal{E}_{\bar{R}}(\rho)$,

$$O_\Gamma(\rho) := \max_{\bar{\rho} = \mathcal{E}_{\bar{L}} \otimes \mathcal{E}_{\bar{R}}(\rho)} \frac{1}{2} \text{Tr}(\bar{\rho}(M_1 + M_2)). \quad (2.94)$$

For our purposes it will be sufficient to consider error correction within neighbourhoods of L and R that have radius $\mathcal{O}(\log(d))$. One can impose the additional restriction that the measurements and unitaries of $\mathcal{E}_{\bar{L}} \otimes \mathcal{E}_{\bar{R}}$ be symmetric, although this is not required to distinguish phases.

In Lemma 3 we will derive an upper bound on the value of $O_\Gamma(\rho)$ for thermal states with trivial SPT-order. Then in Lemma 4 we show that there exists a nonzero critical temperature T_c , such that $O_\Gamma(\rho_C(\beta)) \approx 1$ for the symmetric thermal state of the RBH model at $0 \leq T \leq T_c$.

Lemma 3. *For any $\mathbb{Z}_2 \times \mathbb{Z}_2$ symmetric ensemble ρ_0 that is (r, ϵ) SPT-trivial with r sub-linear in the lattice size d , there exist sufficiently large d such that $O_\Gamma(\rho_0) \leq 1/2 + \epsilon$.*

Proof. Since ρ_0 is (r, ϵ) SPT-trivial, we can approximate it by $\rho' = \sum_a p(a) |\psi_a\rangle \langle \psi_a|$ up to error- ϵ in trace norm, where each state $|\psi_a\rangle$ is an $(r, 0)$ SPT-trivial state, and $p(a)$ is a probability distribution. For each $|\psi_a\rangle$, we have $\langle \psi_a | M_i | \psi_a \rangle = \langle \varphi | U_a^\dagger M_i U_a | \varphi \rangle$ for some symmetric circuit U_a of depth r , where $|\varphi\rangle$ is a product state.

Let w be the largest value out of $\mathcal{O}(\log(d))$ and r . Take enlarged regions \bar{L} of L and \bar{R} of R obtained by taking w -neighbourhoods around L and R respectively. Since r is sub-linear in d , then we can take d sufficiently large such that $\bar{L} \cap \bar{R} = \emptyset$. For a transversal operator A (meaning it is a tensor product of single-qubit operators), and a subregion χ of the lattice \mathcal{C} , let A^χ denote the restriction of A to χ . Since the membranes M_i are transversal, we can decompose them across the regions, $M_i = M_i^{\bar{L}} \otimes M_i^{\text{bulk}} \otimes M_i^{\bar{R}}$, where the bulk region is the complement of $\bar{L} \cup \bar{R}$. We now claim that the regions \bar{L} and \bar{R} are large enough so that $[M_i^{\text{bulk}}, U_a] = 0$ for $i = 1, 2$ and all a .

Firstly, we must have $[M_1, U_a] = 0$ for all a . This is because for any local region χ , there exists a dual-2-boundary b'_2 such that $M_1^\chi = S(b'_2)^\chi$. Since each gate in U_a has to be symmetric, it must commute with $S(b'_2)$ for any dual-2-boundary b'_2 . It follows that each gate must also commute with M_1 . Now consider M_2 , for any region χ away from the boundary of Γ_2 , similarly we can always find a 2-boundary b_2 such that $M_2^\chi = S(b_2)^\chi$. Similarly, each gate in U_a must commute with $S(b_2)$ for any 2-boundary b_2 and therefore also with M_2^{bulk} . This is not satisfied in general near the boundaries of Γ_2 . But provided M_2^{bulk} is supported a distance greater than the circuit depth r away from the boundaries S_2^L and S_2^R , then we have $[M_2^{\text{bulk}}, U_a] = 0, \forall a$.

We can therefore write $U_a^\dagger M_i U_a = M_{i,a}^{\bar{L}} \otimes M_i^{\text{bulk}} \otimes M_{i,a}^{\bar{R}}$, where $M_{i,a}^{\bar{L}} = U_a M_i^{\bar{L}} U_a^\dagger$ and similarly for $M_{i,a}^{\bar{R}}$. From Eq. (2.93), the restriction of membrane operators M_1 and M_2 to the either of the disjoint regions \bar{L} or \bar{R} , give rise to the following anti-commutation relations

$$\{M_1^{\bar{L}}, M_2^{\bar{L}}\} = \{M_1^{\bar{R}}, M_2^{\bar{R}}\} = 0. \quad (2.95)$$

Because of unitary equivalence between the operators, we also have

$$\{M_{1,a}^{\bar{L}}, M_{2,a}^{\bar{L}}\} = \{M_{1,a}^{\bar{R}}, M_{2,a}^{\bar{R}}\} = 0 \quad \forall a, \quad (2.96)$$

where these operators also have eigenvalues ± 1 . Since $|\varphi\rangle$ is a symmetric product state, it is a $+1$ -eigenstate of M_i^{bulk} . However, $|\varphi\rangle$ cannot be a simultaneous eigenstate of both $M_{1,a}^{\bar{L}}$ and $M_{2,a}^{\bar{L}}$, nor of $M_{1,a}^{\bar{R}}$ and $M_{2,a}^{\bar{R}}$ due to the anti-commutation relations of Eq. (2.96) and since \bar{L} and \bar{R} are disjoint. In particular, since $|\varphi\rangle$ is a tensor product $|\varphi\rangle = |\varphi\rangle_{\bar{L}} \otimes |\varphi\rangle_{bulk} \otimes |\varphi\rangle_{\bar{R}}$ then

$$\langle\psi_a|M_i|\psi_a\rangle = \langle\varphi|U_a^\dagger M_i U_a|\varphi\rangle \quad (2.97)$$

$$= \langle\varphi|_{\bar{L}} M_{i,a}^{\bar{L}} |\varphi\rangle_{\bar{L}} \cdot \langle\varphi|_{bulk} M_i^{bulk} |\varphi\rangle_{bulk} \cdot \langle\varphi|_{\bar{R}} M_{i,a}^{\bar{R}} |\varphi\rangle_{\bar{R}} \quad (2.98)$$

$$= \langle M_{i,a}^{\bar{L}} \rangle \cdot \langle M_{i,a}^{\bar{R}} \rangle \quad (2.99)$$

for $i = 1, 2$, where $\langle M_{i,a}^{\bar{L}} \rangle = \langle\varphi|_{\bar{L}} M_{i,a}^{\bar{L}} |\varphi\rangle_{\bar{L}}$ and $\langle M_{i,a}^{\bar{R}} \rangle = \langle\varphi|_{\bar{R}} M_{i,a}^{\bar{R}} |\varphi\rangle_{\bar{R}}$. It is shown in [180] that for k mutually anti-commuting operators $\{A_i\}$, each with eigenvalues ± 1 , any state $|\psi\rangle$ satisfies the following inequality

$$\sum_{i=1}^k \langle A_i \rangle_{|\psi\rangle} \leq \sum_{i=1}^k \langle A_i \rangle_{|\psi\rangle}^2 \leq 1, \quad (2.100)$$

where the expectation value is taken with respect to the state $|\psi\rangle$. Using Eq. (2.99), we have for the approximate state

$$\text{Tr}(\rho'(M_1 + M_2)) = \sum_a p(a) \left(\langle M_{1,a}^{\bar{L}} \rangle \cdot \langle M_{1,a}^{\bar{R}} \rangle + \langle M_{2,a}^{\bar{L}} \rangle \cdot \langle M_{2,a}^{\bar{R}} \rangle \right) \quad (2.101)$$

$$\leq \left(\langle M_{1,a}^{\bar{L}} \rangle^2 + \langle M_{2,a}^{\bar{L}} \rangle^2 \right)^{\frac{1}{2}} \left(\langle M_{1,a}^{\bar{R}} \rangle^2 + \langle M_{2,a}^{\bar{R}} \rangle^2 \right)^{\frac{1}{2}} \quad (2.102)$$

$$\leq 1, \quad (2.103)$$

where the first inequality is the Cauchy-Schwarz inequality and the second inequality is using Eq. (2.100). Now for any error correction map $\mathcal{E}_{\bar{L}} \otimes \mathcal{E}_{\bar{R}}$ that is localized to the non-intersecting neighbourhoods \bar{L} and \bar{R} of L and R respectively, we have by the same argument

$$\text{Tr}(\mathcal{E}_{\bar{L}} \otimes \mathcal{E}_{\bar{R}}(\rho')(M_1 + M_2)) \leq 1. \quad (2.104)$$

Then since ρ' and ρ_0 are close in trace norm, they have similar expectation values of bounded observables, in the following way. Assume $\mathcal{E} = \mathcal{E}_{\bar{L}} \otimes \mathcal{E}_{\bar{R}}$ is the map which maximizes $O_\Gamma(\rho_0)$,

then

$$|O_\Gamma(\rho_0) - \frac{1}{2} \text{Tr}(\mathcal{E}(\rho')(M_1 + M_2))| = \frac{1}{2} |\text{Tr}((M_1 + M_2)(\mathcal{E}(\rho_0) - \mathcal{E}(\rho')))| \quad (2.105)$$

$$\leq \frac{1}{2} \|(M_1 + M_2)(\mathcal{E}(\rho_0) - \mathcal{E}(\rho'))\|_1 \quad (2.106)$$

$$\leq \frac{1}{2} \|M_1 + M_2\|_\infty \cdot \|\mathcal{E}(\rho_0) - \mathcal{E}(\rho')\|_1 \quad (2.107)$$

$$\leq \|\rho_0 - \rho'\|_1 \quad (2.108)$$

$$\leq \epsilon, \quad (2.109)$$

where the second inequality follows from Hölder's inequality. The claim then follows. \square

One could define more complicated order parameters so that the bound on $O_\Gamma(\rho_0)$ in Lemma 3 can be made arbitrarily small. However, our choice and the above bound will be sufficient to show the RBH model has nontrivial SPT-order. Next we show that the thermal RBH model with 1-form symmetry has a high expectation value of the membrane operators provided the temperature is below some critical temperature T_c . We do this by showing that large loop excitations are confined in the low temperature phase. In subsection 2.3.4 we will show that T_c is the critical temperature of the three-dimensional \mathbb{Z}_2 Ising gauge model.

Lemma 4. *For the symmetric thermal Gibbs ensemble $\rho_C(\beta)$ of the RBH model with $\mathbb{Z}_2 \times \mathbb{Z}_2$ 1-form symmetry with $0 \leq T \leq 2/\log(5)$, there exists a constant $\delta > 0$ (independent of systems size) such that for sufficiently large d we have*

$$O_\Gamma(\rho_C(\beta)) \geq 1 - \mathcal{O}(d^{-\delta}). \quad (2.110)$$

Proof. Consider first the expectation value of M_2 . Since M_2 can be constructed from a product of cluster terms (as in Eq. (2.91)), we have at zero temperature $\text{Tr}(M_2\rho) = 1$. Using the symmetric Gibbs ensemble $\rho_C(\beta)$ in Eq. (2.76), the expectation value of a membrane operator is given by

$$\text{Tr}(\rho_C(\beta)M_2) = \sum_{(\gamma, \gamma') \in Z_1 \times Z_1^*} \text{Pr}_\beta((\gamma, \gamma')) \langle M_2 \rangle_{|\psi(\gamma, \gamma')\rangle}, \quad (2.111)$$

where the expectation value is with respect to the excited state $|\psi(\gamma, \gamma')\rangle = Z(\gamma)Z(\gamma')|\psi_C\rangle$. Let $|\Gamma_2 \cap \gamma'|$ denote the number of times γ' intersects Γ_2 . Since $|\psi(\gamma, \gamma')\rangle$ is a ± 1 eigenstate of $M(\Gamma_2)$, we have

$$\langle M(\Gamma_2) \rangle_{|\psi(\gamma, \gamma')\rangle} = \begin{cases} +1 & \text{if } |\Gamma_2 \cap \gamma'| = 0 \bmod 2 \\ -1 & \text{if } |\Gamma_2 \cap \gamma'| = 1 \bmod 2. \end{cases} \quad (2.112)$$

The right-hand side of Eq. (2.112) is independent of the 1-cycle γ since it is supported on the dual lattice and therefore $Z(\gamma)$ commutes with M_2 . Notice that a similar expression holds for M_1 . We call γ' an error cycle if $|\Gamma_2 \cap \gamma'| = 1 \bmod 2$ (and similarly for Γ_1). We will show that

there exists a critical temperature T_c , below which, large error cycles are suppressed and that error correction on the boundaries can account for the remaining errors. First we define an approximate state, where large loop-like excitations have been removed.

We say $\gamma \in Z_1$ is a *loop* if any proper subset $\gamma' \subsetneq \gamma$, is not a cycle. We can partition the set of 1-cycles according to the size of the largest loop they contain. Specifically, let $Z_1^\alpha \subseteq Z_1$ consist of the set of 1-cycles whose largest loops are of length smaller than α (a similar definition holds for $Z_1^{*\alpha} \subseteq Z_1^*$). Then define the approximate state

$$\rho_{\text{ap}}^\alpha(\beta) = \sum_{(\gamma, \gamma') \in Z_1^\alpha \times Z_1^{*\alpha}} \Pr_\beta(\gamma, \gamma') |\psi(\gamma, \gamma')\rangle \langle \psi(\gamma, \gamma')|. \quad (2.113)$$

We claim that for a fixed $0 \leq T < T_c = 2/\log(5)$, there exists a constant c such that for $\alpha = c \log(d)$, we have

$$\left\| \rho_{\text{ap}}^\alpha(\beta) - \rho(\beta) \right\|_1 \leq \mathcal{O}(d^{-\delta}), \quad (2.114)$$

for some constant $\delta > 0$. To see this, fix $\alpha = c \log(d)$ and let $V = (Z_1 \times Z_1^*) \setminus (Z_1^\alpha \times Z_1^{*\alpha})$, be set of (dual-)cycles containing a loop of size at least α (note that a loop may refer to a subset of a 1-cycle or a dual-1-cycle). Then we have

$$\left\| \rho_{\text{ap}}^\alpha(\beta) - \rho(\beta) \right\|_1 = \sum_{(\gamma, \gamma') \in V} \Pr_\beta(\gamma, \gamma'). \quad (2.115)$$

We can bound the above equation using the following relation

$$\sum_{(\gamma, \gamma') \in V} \Pr_\beta(\gamma, \gamma') \leq \sum_{\substack{\text{loops } l \in Z_1 \cup Z_1^* \\ |l| \geq \alpha}} \sum_{\substack{(c_1, c'_1) \in Z_1 \times Z_1^* \\ l \subseteq c_1 \text{ or } l \subseteq c'_1}} \Pr_\beta(c_1, c'_1), \quad (2.116)$$

$$\leq \sum_{\substack{\text{loops } l \in Z_1 \cup Z_1^* \\ |l| \geq \alpha}} e^{-2\beta|l|} \cdot \sum_{\substack{(c_1, c'_1) \in Z_1 \times Z_1^* \\ l \not\subseteq c_1 \text{ and } l \not\subseteq c'_1}} \Pr_\beta(c_1, c'_1), \quad (2.117)$$

$$\leq \sum_{\substack{\text{loops } l \in Z_1 \cup Z_1^* \\ |l| \geq \alpha}} e^{-2\beta|l|} \quad (2.118)$$

$$\leq \sum_{k \geq \alpha} N(k) e^{-2\beta k}, \quad (2.119)$$

where $N(k)$ is the number of loops in $Z_1 \cup Z_1^*$ of size k . For the cubic lattice \mathcal{C} , the number of loops $N(k)$ of size k can be bounded by $N(k) \leq 2^{\frac{6}{5}} |\Delta_0| 5^k$ (we can upper bound the number of possible loops by counting the number of non-backtracking walks: a non-backtracking walk can begin at any vertex and can move in at most 5 independent directions). Therefore, provided

$\beta > \log(5)/2$, we have

$$\sum_{(\gamma, \gamma') \in V} \Pr_\beta(\gamma, \gamma') \leq \frac{12}{5} |\Delta_0| \sum_{k=\alpha}^{\infty} e^{-k(2\beta - \log(5))} \quad (2.120)$$

$$= c' |\Delta_0| e^{-\alpha(2\beta - \log(5))}, \quad (2.121)$$

where $c' = 12/5(1 - e^{(\log(5) - 2\beta)})$ is independent of d . Since $|\Delta_0| = (d+1)^3$, the error in Eq. (2.114) is exponentially small in α , provided the temperature is below a critical temperature T_c . Here, we have given a lower bound on T_c by $2/\ln(5)$. In terms of the lattice size d we have

$$\sum_{(\gamma, \gamma') \in V} \Pr_\beta(\gamma, \gamma') \leq \mathcal{O}(d^{-c(2\beta - \log(5)) + 3}). \quad (2.122)$$

Choosing $c \geq 3/(2\beta - \log(5))$, we have $\delta = c(2\beta - \log(5)) - 3 > 0$ and the claim follows. Notice that this argument shows that large loop excitations in the RBH thermal state are suppressed, and is similar to Peierls' argument for spontaneous magnetization in the two-dimensional Ising model [181].

Now we show that for these values of T and α , there exists an error correction map \mathcal{E} such that

$$\text{Tr}(\mathcal{E}(\rho_{\text{ap}}^\alpha(\beta))(M_1 + M_2)) \geq 2 - \mathcal{O}(d^{-\delta}). \quad (2.123)$$

Indeed, notice that if d is large enough, the approximate state contains no homologically nontrivial excitations, as they must have length at least d . These are the only types of errors that reduce the expectation value of M_1 , and so the approximate state satisfies

$$\text{Tr}(\rho_{\text{ap}}^\alpha(\beta)M_1) = \text{Tr}(\rho_{\text{ap}}^\alpha) \quad (2.124)$$

$$= 1 - \sum_{(\gamma, \gamma') \in V} \Pr_\beta(\gamma, \gamma') \quad (2.125)$$

$$\geq 1 - \mathcal{O}(d^{-\delta}). \quad (2.126)$$

using Eq. (2.122). The only types of errors in the approximate state that reduce M_2 are dual-1-cycles containing a loop that wraps around a boundary component of $\partial\Gamma_2 = S_2^L \sqcup S_2^R$. Therefore any excitation in $\rho_{\text{ap}}^\alpha(\beta)$ that gives rise to an error is contained within an $\alpha/2$ neighbourhood of S_1^L and S_1^R . By measuring all cluster terms $K(\sigma_2)$ in an $\alpha/2$ neighbourhood of $\partial\Gamma_2$ one can determine the location of any possible error cycles (for sufficiently large d , these $\alpha/2$ neighbourhoods are non-intersecting). Then depending on the parity of the number of error loops, one can apply a correction operator $Z(\gamma')$ for some dual-1-cycle γ' wrapping around S_2^L or S_2^R , that returns $\rho_{\text{ap}}^\alpha(\beta)$ to the $+1$ eigenspace of M_2 . Letting \mathcal{E} denote the measurement and recovery steps (which in particular does not change the expectation value of the other

membrane operator M_1 since the recovery is a local unitary), the approximate state similarly satisfies $\text{Tr}(\mathcal{E}(\rho_{\text{ap}}^\alpha(\beta))M_2) \geq 1 - \mathcal{O}(d^{-\delta})$, and therefore Eq. (2.123) holds.

Finally, let \mathcal{E} be the aforementioned error correction map, using an argument similar to that in Lemma 3, we have

$$\left| \text{Tr} \left(\mathcal{E}(\rho_{\text{ap}}^\alpha(\beta))(M_1 + M_2) \right) - \text{Tr} \left(\mathcal{E}(\rho_{\mathcal{C}}(\beta))(M_1 + M_2) \right) \right| \leq 2 \left\| \mathcal{E}(\rho_{\text{ap}}^\alpha(\beta)) - \mathcal{E}(\rho_{\mathcal{C}}(\beta)) \right\|_1 \quad (2.127)$$

$$\leq 2 \left\| \rho_{\text{ap}}^\alpha(\beta) - \rho_{\mathcal{C}}(\beta) \right\|_1 \quad (2.128)$$

$$\leq \mathcal{O}(d^{-\delta}). \quad (2.129)$$

Then using Eq. (2.123) we have that

$$O_\Gamma(\rho_{\mathcal{C}}(\beta)) \geq 1 - \mathcal{O}(d^{-\delta}), \quad (2.130)$$

completing the proof. \square

Lemma 4 tells us that $O_\Gamma(\rho_{\mathcal{C}}(\beta)) \rightarrow 1$ in the limit of infinite system size. This, along with Lemma 3, shows that the RBH cluster model, protected by 1-form symmetry has nontrivial SPT-order for temperatures $0 \leq T \leq T_c$. The key ingredient in the proof is that large loop configurations are energetically suppressed in the low temperature phase, and this results in a type of *string tension*. This is the characteristic behaviour of the \mathbb{Z}_2 lattice gauge theory in three dimensions, and we make this connection precise in the next subsection. Above the critical temperature, the string tension disappears as large error cycles become entropically favourable [182, 183] and thus $O_\Gamma(\rho_{\mathcal{C}}(\beta))$ will approach 0. We correspondingly expect the SPT-order to disappear above T_c .

2.3.4 Comparison with a three-dimensional Ising gauge model

Having proved that the nontrivial SPT-order of the RBH model under the 1-form symmetry survives at nonzero temperature, we now compare it to a three-dimensional Ising gauge model [182, 184]. This comparison is natural because the 1-form symmetry of the RBH model and the gauge symmetry of the three-dimensional Ising gauge model are closely related. The model can be defined on the same lattice \mathcal{C} as the RBH model, and the Hamiltonian is given by a sum of plaquette terms

$$H_{IG} = - \sum_{\sigma_2 \in \Delta_2} Z(\partial\sigma_2) - \sum_{\sigma_1 \in \Delta_1} Z(\partial^*\sigma_1). \quad (2.131)$$

We notice that the first and second terms are supported on disjoint sublattices so that H_{IG} describes two decoupled copies of a three-dimensional Ising gauge model on the cubic lattice. This model has local gauge symmetries, which are the 1-form operators of Eq. (2.72).

Excitations of this model take the form of loop-like objects, and can be created by products of Pauli X operators. These loop-like excitations have an energy cost proportional to their length in the same way as the RBH model with 1-form symmetry. Indeed, the spectrum of H_{IG} is identical to that of the RBH model H_C with 1-form symmetry enforced, and one can construct a duality mapping between the 1-form symmetric model H_C and two copies of the three-dimensional Ising gauge model H_{IG} .

This Ising gauge model H_{IG} has a low-temperature ordered phase where the excitations have string tension, such that large loops excitations are suppressed. The suppression of large excitations was the necessary ingredient in the proof of Lemma 4 which we use to show the nontriviality of the 1-form symmetric RBH model at nonzero temperature. Therefore the lower bound of T_c in Lemma 4 of $2/\log(5) \approx 1.24$ can be increased to the critical temperature of the three-dimensional Ising gauge model, which has been estimated via numerical simulations [184], to be $T_{IG} \approx 1.31$.

It is worth noting that the model described by the Hamiltonian H_{IG} and the RBH model H_C belong to distinct phases at zero temperature under 1-form symmetries, since the three-dimensional Ising gauge model has long-range entangled (topologically ordered) ground states. This distinction persists to nonzero temperature T with $0 \leq T \leq T_c$, as the H_{IG} retains the same order as the three-dimensional toric code [121]. Indeed, the three models: the trivial paramagnet H_X , the RBH model H_C and the three-dimensional Ising gauge theory H_{IG} , all have the same spectrum under 1-form symmetries and belong to distinct symmetric phases for temperatures $0 \leq T \leq T_c$. From the viewpoint of quantum information processing tasks, each of these phases has distinct uses: H_{IG} can be used as a memory at nonzero temperature for the storage of classical bits [121], while the RBH model H_C is a universal resource for MBQC at nonzero temperature.

2.4 Localizable entanglement

In the previous section, we have shown that the RBH model possesses nontrivial SPT-order at nonzero temperature when protected by a 1-form symmetry, and we developed order parameters that detect this nontrivial SPT phase. In subsection 2.4.1 we provide an operational interpretation for these order parameters in terms of quantifying the entanglement that can be localized between distant regions in the thermal state through measurements in the bulk. This provides a connection with the zero-temperature results in 1D SPT models [127], where all nontrivial SPT-ordered ground states possess long-range localizable entanglement. These order

parameters are also relevant in the context of quantum computation, as localizable entanglement is the underlying mechanism through which—via gate teleportation—the RBH thermal state functions as a resource for measurement-based quantum computation.

In subsection 2.4.2 we then turn our attention back to the standard RBH model without symmetry, and reflect on the robustness of this model for measurement-based quantum computation even in the case where no symmetry is enforced. We find a novel perspective: that error correction can be used to restore an effective 1-form symmetry, and when the correction is successful, the model can be used to localize entanglement between distant regions. This provides a direct link between thermal SPT phase and fault-tolerant measurement-based quantum computation, or more generically, high error-threshold quantum computing architectures.

2.4.1 Localizable entanglement in the 1-form SPT model

A primitive form of computation is the ability to generate entanglement between distant regions. Localisable entanglement \tilde{L}_{LR} is the average entanglement (according to some entanglement measure E) of the post measured state between two regions L, R , maximized over all choices of single-site measurements M on the complement of $L \cup R$. Following [185], the localisable entanglement is defined as

$$\tilde{L}_{LR}(\rho) = \max_M \sum_s p_s E(\rho_s), \quad (2.132)$$

where $\rho_s = \Pi_s \rho \Pi_s / \text{Tr}(\Pi_s \rho)$ is the post-measurement state associated with a local measurement projector $\Pi_s = |s_1\rangle\langle s_1| \otimes \cdots \otimes |s_n\rangle\langle s_n|$ on $(L \cup R)^c$ and measurement outcome $s = (s_1, \dots, s_n)$, and $p_s = \text{Tr}(\Pi_s \rho)$ is the probability of outcome s .

In general, maximizing over all possible local measurements is difficult, but if the state ρ has a high degree of symmetry then the optimal measurement bases Π_s may be determined from symmetry arguments [186]. For the 3D cluster state with the 1-form symmetry, it is straightforward to show (following [125, 187]) that the optimal local measurement bases for localizing entanglement are always the X -basis; i.e., one should perform local X measurements on all spins in the bulk. The localizable entanglement of the state ρ can then be expressed as the average entanglement of the post-measurement state ρ_s across the L/R partition:

$$\tilde{L}_{LR}(\rho) = \sum_s p_s E(\rho_s). \quad (2.133)$$

This entanglement is also known as the *SPT-entanglement* [187], and shown to be an order parameter for SPT phases protected by onsite symmetries at zero temperature. We note that, in the presence of the 1-form symmetry, localizable entanglement and SPT-entanglement are identical.

We now show that the order parameters $O_\Gamma(\rho)$ developed in the previous section serve as a witness for localizable entanglement of the thermal SPT state. We note that the membrane operators $M(\Gamma_i)$ take the form

$$M(\Gamma_i) = M_i^L \otimes M_i^{bulk} \otimes M_i^R, \quad (2.134)$$

where the bulk region is the complement of $L \cup R$. Since L and R are 2-dimensional slices, the restrictions M_1^L and M_1^R are 1-dimensional strings of Pauli X operators, and M_2^L and M_2^R are 1-dimensional strings of Pauli Z operators. Consider measurement of Pauli X on all qubits that either do not belong to the two-dimensional slices L and R , or belong to 2-cells of L and R . Then the post measured state is an eigenstate of a pair of two-dimensional toric codes, each defined on the slices L and R (see Ref. [136] for details). The membrane operators restricted to these slices are equivalent to logical operators of the two-dimensional toric codes, and in particular may be written in terms of these logical operators as $M_1^{L \cup R} = \bar{X}_L \otimes \bar{X}_R$ and $M_2^{L \cup R} = \bar{Z}_L \otimes \bar{Z}_R$.

After performing the local X measurements on the bulk qubits, the measurement projector Π_s projects into eigenstates of M_i^{bulk} . Then the single qubit measurement outcomes can be multiplied to infer the outcome of each bulk operator M_i^{bulk} . This classical information is transmitted to L and R and we can infer the ± 1 outcomes of the logical operators $\bar{X}_L \otimes \bar{X}_R$ and $\bar{Z}_L \otimes \bar{Z}_R$ for the post measured state. Note that due to the anti-commutation relations of Eq. (2.93) these correlations are that of a maximally entangled state encoded within two two-dimensional toric codes. The order parameter of Eq. (2.94) after measurement, $\langle \bar{X}_L \otimes \bar{X}_R + \bar{Z}_L \otimes \bar{Z}_R \rangle / 2$, is therefore an entanglement witness for the entanglement between topological degrees of freedom. Note that measurement outcomes of $\bar{X}_L \otimes \bar{X}_R$ and $\bar{Z}_L \otimes \bar{Z}_R$ for the post measured state might potentially depend on the choice of membrane M_i^{bulk} , but as discussed in section 2.3.3, we can freely deform the membrane operators due to the 1-form symmetries, thus removing any ambiguity. This entanglement enables gate teleportation in the topological cluster state quantum computing scheme [66], using the thermal state as the resource state.

Having provided an operational interpretation of thermal SPT-order as localizable entanglement in measurement-based quantum computation, we now briefly consider the physical consequence of this localizable entanglement. Non-triviality of SPT-order manifests itself most dramatically through physical properties on the boundaries. For instance, 1D nontrivial SPT phases typically exhibit robust gapless boundary modes similar to those in topological insulators. The aforementioned localizable entanglement, or SPT-entanglement, for 1D SPT phases directly measures the boundary degeneracy that appear when the system has open edges [187]. For three-dimensional systems with symmetries, their two-dimensional boundaries may exhibit robust gapless modes, symmetry-breaking phases and/or 2D topological order

[110, 159]. With 1-form symmetries in the bulk, the boundary of the 3D cluster state at zero temperature supports the two-dimensional toric code on effective qubits localized near the boundary, and localizable entanglement, as quantified by membrane operators, measures the boundary degeneracy of the toric code on the boundaries. It is tempting to speculate that the presence of localizable entanglement at nonzero temperature in the 3D cluster state suggests that this boundary topological order persists even at nonzero temperature due to 1-form symmetries in the bulk.

2.4.2 Recovering effective 1-form symmetry with error correction

We have shown that the RBH model can retain its long-range localizable entanglement at nonzero temperature when a 1-form symmetry is enforced. The original results of Ref. [136] demonstrate, however, that this localizable entanglement persists in the thermal state even without any symmetry protection! This result is surprising because, as we have shown, the protection of a 1-form symmetry is necessary to define an SPT-ordered phase at nonzero temperature. To add to the confusion, the transition in localizable entanglement in the unprotected model, from long-range at low temperature to short-range at high temperature, does not correspond to any thermodynamic transition. Indeed, the Gibbs state of the RBH model without symmetry protection has no thermodynamic phase transition, and is equivalent to the Gibbs state of a non-interacting paramagnet. What is the underlying quantum order that persists up until this transition in localizable entanglement?

We offer a resolution to this confusing situation, by demonstrating that the persistence of localizable entanglement in the RBH model to nonzero temperature can be understood through imposing an effective 1-form symmetry in the unprotected model via error correction. The 1-form operators are not enforced *a priori*, but their eigenvalues are reconstructed via the outcomes of the local measurements, and the resulting state can be ‘restored’ to the SPT-ordered thermal state. We can therefore relax the symmetry requirement on the model, provided it can be effectively restored through error correction.

Consider the thermal state $\rho_0(\beta)$ of the RBH model H_C where no symmetry is enforced. In the absence of a symmetry, $\rho_0(\beta)$ is equivalent to the exact cluster state with local Z errors applied to each qubit with probability $p = (1 + \exp(2\beta))^{-1}$, as shown in Ref. [136]. In order to restore the 1-form symmetry, we follow the error correction scheme detailed in Ref. [136], which is based on the techniques of Ref. [47]. We now outline the steps involved with this procedure and we note that error correction proceeds on each sublattice independently.

Firstly, consider the measurement of all 1-form operators in the local generating set $\tilde{G} = \{S(\partial\sigma_3), S(\partial^*\sigma_0) \mid \sigma_3 \in \Delta_3, \sigma_0 \in \Delta_0\}$ given by Eq. (2.73), and let $\{s_b = \pm 1\}$ be the set of corresponding measurement outcomes. A syndrome is the set of all operators in \tilde{G} which return

measurement outcome -1 and can be found as the dual boundary $\partial^*(c'_1)$ of an error chain $Z(c'_1)$, and the boundary ∂c_1 of an error chain $Z(c_1)$, where $c_1 \in C_1$ and $c'_1 \in C_1^*$. To recover the 1-form symmetry, one can identify a recovery 1-chain $\gamma_1 \in C_1$ and dual-1-chain $\gamma'_1 \in C_1^*$ such that

$$\partial(\gamma_1 + c_1) = 0, \quad \text{and} \quad \partial^*(\gamma'_1 + c'_1) = 0. \quad (2.135)$$

The recovery operator $U_{\{s_b\}} = Z(\gamma_1)Z(\gamma'_1)$ is a product of Pauli Z operators, which is dependent on the measurement outcomes. The post-correction state is

$$\rho_{\text{sym}} = \sum_{\{s_b\}} U_{\{s_b\}} (\Pi_{\{s_b\}} \rho_{\text{in}} \Pi_{\{s_b\}}) U_{\{s_b\}}^\dagger \quad (2.136)$$

where $\Pi_{\{s_b\}}$ is the projection operator onto subspace with syndrome values $\{s_b\}$. Since this error-corrected state ρ_{sym} is 1-form symmetric by construction, its nontriviality under 1-form symmetries, in a sense of the circuit complexity, can be defined.

We have recovered the 1-form symmetry, but we have to determine when the error correction is successful, as the choice of recovery chains satisfying Eq. (2.135) is not arbitrary. The measure of success is determined by the usefulness of the post-correction state for localizing entanglement, as we will discuss. We say error correction is successful if the recovery chains γ_1 and γ'_1 satisfy

$$\gamma_1 + c_1 \in B_1, \quad \text{and} \quad \gamma'_1 + c'_1 \in B_1^* \quad (2.137)$$

meaning they are homologically trivial. This means we only need to find recovery chains that are equivalent to γ_1 and γ'_1 up to a 1-boundary and a dual-1-boundary, respectively. Optimal error correction finds the most probable equivalence class of chains satisfying Eqs. (2.135) and (2.137) for the given syndrome and is known as maximum-likelihood decoding [47].

The error correction succeeding is equivalent to the post-correction state ρ_{sym} having the same $+1$ expectation values of the operators $X(z_2)$ and $X(z'_2)$ as the cluster state, where $z_2 \in Z_2$ is a nontrivial 2-cycle, and $z'_2 \in Z_2^*$ is a nontrivial dual-2-cycle. In this case, the corrected state can be reliably used to localize entanglement between distant regions L and R , since the measurement outcomes of bulk of the membrane operators M_i^{bulk} in Eq. (2.134) can be accurately determined. In the case that $\gamma_1 + c_1$ or $\gamma'_1 + c'_1$ are homologically nontrivial, then we say a logical error has occurred, and there is no entanglement in the post measured state.

Throughout the above discussion, an important consequence of the localizable entanglement protocol is that one can defer the error correction procedure until after the single qubit measurements have been performed. In particular, rather than measure 1-form operators explicitly, one can perform all of the single qubit X measurements first and take products of measurement outcomes to infer the eigenvalues of the 1-form operators \tilde{G} . One can classically process the measurement outcomes to identify the post measured state, as pointed out in

Ref. [136]. This gives perspective on why the localisable entanglement persists in the thermal RBH model without symmetry protection, as the measurement outcomes used to localize entanglement also provide the potential for error correction.

A subtlety in this argument is the fact that the definition of ρ_{sym} depends on the error correction protocol, which determines the choice of recovery map $U_{\{s_b\}}$ in Eq. (2.136). In order to discuss the hidden SPT-order in an initial state $\rho_0(\beta)$, it is sensible to use the optimal quantum error correction protocol to construct the 1-form symmetric ensemble ρ_{sym} . The question of finding a threshold for this optimal error correction can be rephrased as a problem of finding a phase transition in a certain statistical mechanical model, the random-plaquette \mathbb{Z}_2 gauge theory in three-dimensions [47]. The random-plaquette \mathbb{Z}_2 gauge theory undergoes a phase transition between an low-temperature ordered and a high-temperature disordered phase [188]. The ordered phase corresponds to the ability to successfully perform error correction with a high success probability in the RBH model at low temperature. The threshold can be found at the critical point in the three-dimensional random-plaquette \mathbb{Z}_2 gauge theory along the Nishimori line (see Fig. 2.11). The critical point corresponds to a temperature of $T_0 \approx 0.6$, which lower bounds the transition in localizable entanglement [136]. It is thus natural to speculate that the thermal SPT-order in $\rho_0(\beta)$ persists up to T_0 .

So far we have considered the thermal state of the RBH model both with and without 1-form symmetries enforced. A natural family of models which interpolates between these two cases is the symmetric Hamiltonian of Eq. (2.4), with finite strength symmetry terms

$$H(\lambda) = H_C - \lambda \sum_{S_b \in \tilde{G}} S_b, \quad \lambda \geq 0. \quad (2.138)$$

In the limit of $\lambda \rightarrow \infty$, the thermal state is the 1-form symmetric state, for which measurement of the operators \tilde{G} always returns +1. As we have discussed, the related statistical model is the three-dimensional Ising gauge theory (or equivalently, the random-plaquette \mathbb{Z}_2 gauge theory with no randomness), which has a critical temperature at $T_\infty \approx 1.3$. Below this temperature we can always localize entanglement between distant boundaries.

For intermediate values of $\lambda \in (0, \infty)$, excitations also have an additional energy cost at their boundaries (proportional to λ), as there is a finite energy penalty to violating the symmetry. Increasing λ penalizes excitations which cannot be successfully corrected, leading to increased success rate if the same protocol is used. Finding the success rate appears difficult, as the corresponding statistical model is three-dimensional random-plaquette \mathbb{Z}_2 gauge theory, but with correlation between the plaquette random variables. If one neglects these correlations (which will be valid for small λ), then the transition temperature for finite λ would be approximated by the line separating the order and disorder phases in the phase diagram of the three-dimensional random plaquette \mathbb{Z}_2 gauge theory (see Fig. 2.11).

We remark that the protocol dependence of characterising topological order of thermal states is a generic challenge, both in the presence or absence of symmetries. It has been shown by Hastings, that the 4D toric code is topologically ordered at sufficiently small but finite temperature using the fact that quantum error correction protocol reliably works at low temperature [123].

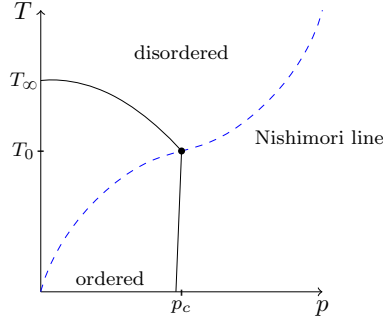


Fig. 2.11 (Color online) Sketch of the phase diagram of the three-dimensional random-plaquette \mathbb{Z}_2 gauge theory [47]. The random-plaquette \mathbb{Z}_2 gauge theory has ± 1 couplings, and the fraction of negative couplings is labelled p , the disorder strength. The disorder strength p is on the horizontal axis, and temperature T is on the vertical axis. The solid (black) line is the boundary between the ordered and disordered phase. The dashed (blue) curve is the Nishimori line $e^{-2\beta} = p/(1-p)$. The Nishimori point at (p_c, T_0) lies at the intersection of the phase boundary and the Nishimori line. The critical temperatures of $H(\lambda)$ in the limiting case of $\lambda = 0, \infty$ are depicted on the vertical axis. For intermediate values $\lambda \in (0, \infty)$, if correlation between plaquette random variables is ignored, the critical temperature is expected to interpolate between T_0 and T_∞ .

2.5 Outlook

Stability of thermal SPT-order provides a physical account for the surprisingly high error threshold attained in quantum computing architectures involving the 3D cluster state as well as a guiding principle to look for useful resource states for fault-tolerant quantum computation. Our work also opens new avenues for studies of higher-form SPT phases and their thermal properties with possible applications to quantum information processing as well as realizations of higher-form symmetries. Despite the theoretical beauty of higher-form SPT phases, the practical challenge was that physically realistic condensed matter systems do not naturally seem to possess higher-form symmetries. Our perspective on error correction in the 3D cluster state suggests that 1-form symmetries can emerge from error correction even if we do not impose them as physical symmetries. This raises an intriguing possibility of realizing higher-form symmetries in an emergent manner through quantum error correction. With this perspective, one can ask whether the three-dimensional models of Refs. [149, 40], which have thermal states

that are universal for MBQC, have underlying symmetries that give rise to SPT-order at nonzero temperature. In addition, our generalized definition of topological order at nonzero temperature in the presence of symmetries may be of independent interest as it provides insight into generalizing the Davies map formalism to simulate thermalization for quantum many-body systems with symmetries. This may be interesting in the context of symmetry-enriched topological phases, where the stability of a quantum memory may be enhanced by symmetry.

Thermal SPT phases are likely to find other applications in a broader context of fault-tolerant quantum computation. One particularly promising avenue is single-shot error correction [75], which can significantly reduce the computational overhead in quantum computation. Conventional error correction needs to take into account a possibility of faulty measurements, and thus repeated measurements are required to get reliable syndrome values. Single-shot error correction, where each syndrome is measured only once, is possible for topological stabilizer quantum codes which retain topological order at nonzero temperature [75]. While this observation relates thermal topological order to single-shot error correction, what remains as a puzzle is the fact that the 3D gauge color code [75, 189], an example of a subsystem quantum code, also admits single-shot error correction. This fact strongly suggests that the gauge color code retains some sort of order at nonzero temperature, but such thermal order would appear to be in conflict with the thermal instability of topological order at nonzero temperature in all the known three-dimensional models [137]. Our findings on thermal SPT-order hints that the 3D gauge color code may possess SPT-order protected by some set of symmetry operators that enable single-shot error correction.

Our perspective of the nontrivial 1-form SPT model as a gapped domain wall described in section 2.3 raises an interesting question concerning topological defects associated with such a 3D domain wall. In a two-dimensional toric code, defects associated with the endpoints of a gapped domain wall can be viewed as Majorana fermions [67]. This observation led to a huge body of work on characterizations of topological defects in two-dimensional topologically ordered systems [113, 190]. In our construction of a three-dimensional gapped domain wall associated with a nontrivial 1-form SPT model, its two-dimensional boundary may be viewed as some kind of topological defect in the 4D toric code. Characterization of such higher-dimensional defects and their thermal stability may be an interesting future question. We note also that the thermal stability of Majorana fermions in nanowires is also of interest [191, 192] and our characterisation of thermal SPT stability may contribute to this work.

3 | Symmetry-protected self-correcting quantum memories

Abstract

A self-correcting quantum memory can store and protect quantum information for a time that increases without bound with the system size, without the need for active error correction. We demonstrate that symmetry can lead to self-correction in 3D spin lattice models. In particular, we investigate codes given by 2D symmetry-enriched topological (SET) phases that appear naturally on the boundary of 3D symmetry-protected topological (SPT) phases. We find that while conventional onsite symmetries are not sufficient to allow for self-correction in commuting Hamiltonian models of this form, a generalized type of symmetry known as a 1-form symmetry is enough to guarantee self-correction. We illustrate this fact with the 3D ‘cluster state’ model from the theory of quantum computing. This model is a self-correcting memory, where information is encoded in a 2D SET ordered phase on the boundary that is protected by the thermally stable SPT ordering of the bulk. We also investigate the gauge color code in this context. Finally, noting that a 1-form symmetry is a very strong constraint, we argue that topologically ordered systems can possess *emergent* 1-form symmetries, i.e., models where the symmetry appears naturally, without needing to be enforced externally.

3.1 Introduction

Quantum error correcting codes can be used to protect information in a noisy quantum computer. While most quantum codes require complex active error correction procedures to be performed at regular intervals, it is theoretically possible for a code to be *self-correcting* [47, 62, 137]. That is, the energetics of a self-correcting quantum memory (SCQM) can suppress errors for a time that increases without bound in the system size, without the need for active control. Such a memory is typically envisioned as a many-body spin system with a degenerate ground space.

Quantum information can then be stored in its degenerate ground space for an arbitrarily long time provided that the system is large enough and the temperature is below some critical value.

In seeking candidate models for self-correction, inspiration has been drawn from recent advances in our understanding of topologically ordered spin lattice models. The simplest example of a two-dimensional topologically ordered model is Kitaev's toric code [193], one of the most studied and pursued quantum error correcting codes. With active error correction, the toric code has a lifetime that grows exponentially with the number of qubits. However it is not self-correcting, as without active error correction the lifetime of encoded information is independent of the number of qubits. On the other hand, the four-dimensional generalization of the toric code [47] provides a canonical example of a self-correcting quantum memory.

Encouraged by the capabilities of the 4D toric code, there has been a substantial effort to find self-correcting quantum memories that meet more physically realistic constraints and, in particular, exist in three or fewer spatial dimensions. A number of no-go results make this search very challenging [61, 65, 124, 194–197]. While there has been considerable progress with proposals that attempt to circumvent these constraints in various ways [12, 194, 196, 198–203], none have yet provided a complete answer to the problem.

Symmetry can provide new directions in the search for self-correcting quantum memories, as the landscape of ordered spin lattice models becomes even richer when one considers the interplay of symmetry and topology. If a global symmetry is imposed on a model, a system can develop new quantum phases under the protection of this symmetry. The properties that distinguish such symmetry-protected phases from more conventional phases persist only when these symmetries are not broken. This has led to new types of phases protected by symmetry, including symmetry-protected topological (SPT) phases [92, 111, 129–131, 204] (phases with no intrinsic topological order) and symmetry-enriched topological (SET) [112–115, 117, 163, 164, 190, 205–210] phases (those including both intrinsic topological order and symmetry). These phases have found many applications in quantum computing [34, 35, 67, 119, 125–127, 132, 134, 142–144, 156, 171, 211–218].

In this chapter, we show that such phases can support self-correcting quantum memories in three-dimensions, provided an appropriate symmetry is enforced. We argue that the generic presence of point-like excitations in commuting Hamiltonian models protected by an onsite symmetry precludes thermal stability (mirroring the instability of the 2D toric code), and so we are naturally led to consider higher-form symmetries. Models with higher-form symmetries have excitations that are higher-dimensional objects, such as strings or membranes, rather than point-like excitations that are typical in models with onsite symmetries. With such exotic excitations, we can seek models with the type of energetics believed to be needed for self-correction. Focussing on models with symmetries that are not spontaneously broken, we consider models that have an SPT ordered bulk. We then give two examples of 3D models

that are self-correcting when a 1-form symmetry is enforced. The first example is based on the 3D ‘cluster state’ model of Raussendorf, Bravyi and Harrington (RBH) [136]; this model with a 1-form symmetry has a bulk that remains SPT-ordered at non-zero temperature [216]. We show that a self-correcting quantum memory can be encoded in a 2D SET boundary of this 3D model, and is protected by the thermally-stable SPT ordering of the bulk. The second example is based on the 3D gauge color code [75], which is conjectured to be self-correcting; we show that a commuting variant of this model is self-correcting when subject to a 1-form symmetry.

Finally, we consider whether 1-form symmetries that lead to self-correction can be *emergent*, rather than enforced. A symmetry is emergent if it arises in the low-energy effective theory of a model, rather than one that is required explicitly in the microscopic model. The analogy here is to the charge-parity symmetry that emerges in the effective anyon theory that describes the low-energy theory of many topologically ordered models, such as the toric code; such symmetries need not be externally enforced, as they are intrinsic to the model and stable under perturbations. We give evidence that the 1-form symmetry used in the 3D gauge color code example may be emergent, arising as a result of emergent charge-parity symmetries on topologically-ordered codimension-1 submanifolds of the 3D bulk. In the gauge color code, this symmetry is the ‘color flux conservation’ identified by Bombin [48].

We would like to emphasise upfront an important subtlety in defining a symmetry-protected self-correcting quantum memory. Enforcing symmetries can be extremely powerful, and along with potentially providing protection against errors, a poor choice in symmetry may be so strong as to render the system useless as a quantum memory. In particular, one must be careful that the symmetry still allows for the implementation of logical operators using ‘local moves’, i.e., sequences of local, symmetric operators. This requirement of a symmetry-protected SCQM will rule out some choices of strong symmetries. For example, in the case of topological stabilizer codes, this removes the possibility of enforcing the entire stabilizer group as the symmetry (or for example, all of the vertex terms of a 3D toric code). We will revisit this subtle issue along with other rules in more detail in Sec. 3.2.3.

The chapter is structured as follows. In Sec. 3.2, we review self-correction and the conditions required for it, as well as phases of matter protected by symmetry. We analyse the effect of coupling symmetry-protected models to a thermal bath in Sec. 3.2.3, and argue that onsite symmetries are insufficient to offer thermal stability of a symmetry-protected phase. In Sec. 3.3 we present our first example of a self-correcting quantum memory protected by a higher (1-form) symmetry: a thermally-stable 3D SPT-ordered model with a protected 2D SET-ordered boundary. A second example, based on the 3D gauge color code, is analyzed in Sec. 3.4. We discuss the possibility of such 1-form symmetries being emergent in 3D topological models in Sec. 3.5, based around the gauge color code. We discuss some implications of these results and open questions in Sec. 3.6.

3.2 Background

In this section we briefly review self correcting quantum memories, as well topological phases with symmetry.

3.2.1 Self-correcting quantum memories

The requirements of a self-correcting quantum memory have been formalized in the so-called ‘Caltech rules’ [196, 202] (also see Ref. [137] for a review). Specifically, a self-correcting quantum memory (SCQM) in d spatial dimensions is a quantum many body spin system with the following four properties: (i) the Hilbert space consists of a finite density of finite-dimensional spins in d spatial dimensions; (ii) the Hamiltonian H has local terms with bounded strength and range, such that each spin is in the support of only a constant number of terms; (iii) the ground space of H is degenerate (in the large size limit) such that a qubit can be encoded in the ground space and that this ground space is perturbatively stable; (iv) the lifetime of the stored information after coupling the system to a thermal bath must grow without bound in the system size. Typically, it is required that the lifetime grow exponentially in the system size, however there are situations when polynomial growth may be sufficient. Another desirable feature for a practical SCQM is the existence of an efficient decoder: a classical algorithm that can correct for errors in the system that have accrued over time.

While the four-dimensional toric code meets all of the above requirements, there is currently no model that has been shown to meet these conditions in three-dimensions or fewer. The search for such a model has been encumbered by an assortment of no-go results for models consisting of commuting Pauli terms, known as stabilizer models [61, 65, 124, 194–196]. These no-go results are typically centered around the idea that a SCQM must have a macroscopic energy barrier, meaning any sequence of errors that are locally implemented must incur an energy cost that diverges with the size of the system. (Note we will define the energy barrier more concretely in the following subsection.) If a code has a macroscopic energy barrier then, naively, one may expect that logical faults can be (Boltzmann) suppressed by increasing the system size. This is indeed part of the puzzle, as it has been shown that a diverging energy barrier is necessary but not sufficient for self-correction for commuting Pauli Hamiltonians [219, 220] and abelian quantum doubles [197]. (In particular, this rules out any codes based on entropic error suppression such as that of Brown *et al.* [203].)

As such, any self-correcting quantum memory should be free of string-like (one-dimensional) logical operators, as these codes have a constant energy barrier. This holds since the restriction of a string-like logical to some region will commute with all terms in that region, and potentially only violate local terms near the boundary of the string. Therefore, to build up a logical fault (i.e., a logical string operator), one only needs to violate a constant number of terms, costing a

constant amount of energy. This immediately rules out all 2D stabilizer codes [61], and 3D stabilizer Hamiltonians that have translationally invariant terms and a ground space degeneracy that is independent of system size (the so-called STS models of Yoshida [124]). Quantum codes in 3D that are free of string-like logicals have been investigated by Haah [12, 194] and Michnicki [198, 199], however they do not achieve a memory time that is unbounded (with the size of the system) for a fixed temperature.

One class of proposals seeks to couple a 2D topologically ordered model, such as the toric code, to a 3D theory with long range interactions with the goal of confining the anyonic excitations. For example, excitations in the toric code can be coupled to the modes of a 3D bosonic bath [200, 201, 196] such that anyonic excitations experience long range interactions. This coupling can result in a strong suppression of anyon pair production via a diverging chemical potential, and a confinement in excitation pairs leading to self-correcting behaviour. A complication with this approach is that the bulk generically requires fine tuning, and the chemical potential can become finite upon a generic perturbation [196]. Such models are not self-correcting under generic perturbations.

Finally, while the search for self-correcting quantum memories has primarily focussed on stabilizer codes, *subsystem codes* [49, 51] are a promising direction because many of the no-go theorems described above do not directly apply. Briefly, a subsystem code is a stabilizer code where some of the logical qubits are chosen not to be used for encoding, and instead are left as redundant gauge degrees of freedom. For the purposes of quantum memories, the use of subsystem codes and gauge qubits offers much more flexibility in selecting a Hamiltonian for the code, and the spectral requirements of the model for self-correction are potentially more relaxed. The 3D gauge color code [75] is an example of a topological subsystem code with a variety of remarkable properties, including a fault-tolerant universal set of gates via a technique known as gauge fixing, and the ability to perform error-correction with only a single round of measurements. This later property is known as single-shot error correction [48] and arises from a special type of confinement of errors during the measurement step. It is conjectured in Ref. [75] that the 3D gauge color code is self-correcting.

Thermalization and memory time

The central question for a candidate self-correcting quantum memory is how long the encoded information can undergo thermal evolution while still being recoverable. For a self-correcting quantum memory, this time should grow with the system size provided the temperature is sufficiently low. In this section, we briefly review thermalization and motivate the energy barrier as a useful tool to diagnose the memory time.

The standard approach to modelling thermalization of a many body system is to couple the system to a thermal bosonic bath. Let H_{sys} be the Hamiltonian describing the quantum memory of interest, and let H_{bath} be a Hamiltonian for the bosonic bath. Thermalization is modelled by evolution under the following Hamiltonian

$$H_{\text{full}} = H_{\text{sys}} + H_{\text{bath}} + \lambda \sum_{\alpha} S_{\alpha} \otimes B_{\alpha}, \quad (3.1)$$

where $S_{\alpha} \otimes B_{\alpha}$ describe the system-bath interactions, S_{α} is a local operator acting on the system side, B_{α} is an operator acting on the bath side, and α is an arbitrary index. It is assumed that the coupling parameter is small, $|\lambda| \ll 1$.

Suppose that the state is initialized in a ground state $\rho(0)$ of H_{sys} . As the system is coupled to the thermal bath, after some time t the system evolves to a noisy state $\rho(t)$. Due to the nature of the coupling, described by local coupling operators $S_{\alpha} \otimes B_{\alpha}$, errors are introduced to the system in a local way, and so the time evolution of the state $\rho(t)$ must be described by a local sequence of operations. One can give a precise description of this process using a perturbation theory analysis, such as a master equation approach like the well-known Davies formalism [157, 158] which we review in Sec. 3.7.

For a self-correcting quantum memory, we wish to be able to recover the state $\rho(0)$ from $\rho(t)$ after some time t using a single final round of error correction. Error correction consists of two steps, firstly a sequence of measurements is performed on the noisy state $\rho(t)$ to obtain an error syndrome, then a recovery map is performed that depends on the syndrome (the measurement outcomes). The net action of the syndrome measurement and recovery map can be condensed into a map $\Phi_{\text{ec}} : \mathcal{H} \rightarrow \mathcal{H}$, where \mathcal{H} is the Hilbert space of the memory system. For a fixed error rate ϵ , we can define the memory time τ_{mem} as the maximum t for which the inequality

$$\|\Phi_{\text{ec}}(\rho(t)) - \rho(0)\|_1 \leq \epsilon \quad (3.2)$$

is satisfied.

An upper bound to the memory time, is the mixing time τ_{mix} , which is the time taken for $\rho(t)$ to be ϵ close to the Gibbs state (for some fixed ϵ). This bound holds since once the system has thermalized to the Gibbs state, the system retains no information about the initial state. However, the memory time can be substantially less than the mixing time (as, for example, with the 3D toric code) [219], and so this mixing time does not in general give us a tight bound on the memory time. Instead, a useful proxy for determining the memory lifetime of a SCQM is the energy barrier, since a growing energy barrier is necessary in many cases to achieve self-correction. In the following subsection we define this quantity.

Energy barrier

If we cannot recover the logical information after some time t , then we say that a logical fault has occurred. The coupling to the bath can lead to a logical fault if a sequence of local errors from the system-bath coupling results in a logical operator (or an operator near to a logical operator). Due to the locality of the coupling between the system and bath (in Eq. (3.1)), errors are introduced to the memory in a local way. There is an energy cost associated with any such process, which is directly related to the probability of such a process occurring when coupled to a bath at temperature T . We now define this *energy barrier* precisely.

We first define a local decomposition of a logical operator. In this chapter we restrict to stabilizer Hamiltonians, however the energy barrier can similarly be defined for any commuting projector Hamiltonian. Let $H_S = -\sum_i h_i$ be a stabilizer Hamiltonian (i.e., each local term is a Pauli operator, and all terms mutually commute), and \bar{l} a Pauli logical operator. A local decomposition of \bar{l} is a sequence of Pauli operators $\mathcal{D}(\bar{l}) = \{l^{(k)} \mid k = 1, \dots, N\}$ such that $l^{(1)} = I$ and $l^{(N)} = \bar{l}$, and $l^{(k)}$ and $l^{(k+1)}$ differ only by a local (constant range) operator.

For any ground state $|\psi_0\rangle$ of H_S , the state $l^{(k)}|\psi_0\rangle$ is also an eigenstate of H_S (for each k) with energy $E^{(k)}$. We can use this to define the energy barrier Δ for a logical fault. Namely, the energy barrier for the local decomposition $\mathcal{D}(\bar{l})$ is defined as

$$\Delta_{\mathcal{D}(\bar{l})} = \max_k (E^{(k)} - E_0), \quad (3.3)$$

where E_0 is the ground space energy. The energy barrier for a logical fault in H_S is defined as

$$\Delta = \min_{\bar{l}, \mathcal{D}(\bar{l})} \Delta_{\mathcal{D}(\bar{l})}. \quad (3.4)$$

In other words, the energy barrier for a logical fault is the smallest energy barrier of any logical operator, minimized over all local decompositions. Intuitively, the energy barrier should be large in order to suppress logical faults from occurring.

The expectation for many models is that below some critical temperature the memory time will grow exponentially in the energy barrier

$$\tau_{\text{mem}} \sim e^{\beta\Delta} \quad (3.5)$$

which is known as the *Arrhenius law*. This relationship is observed to hold for many models such as the classical 2D Ising model and 4D toric code, but does not hold in general, (for instance in models when entropic effects are significant [12, 194, 198, 199]). Indeed for stabilizer Hamiltonians, an energy barrier that grows with the size of the system is a necessary condition (although not sufficient) for self-correction [219, 220].

Dimensionality of excitations and self-correction

We conclude this subsection with a comment regarding the crucial role of the dimensionality of excitations in the feasibility of self-correction. The conventional wisdom is that deconfined point-like excitations are an obstruction to self-correction, as harmful errors can be introduced with a low energy cost due to excitations that are free to propagate. For models with higher dimensional excitations, the energy cost to growing and moving these excitations can be large, such that logical errors are suppressed.

The properties of excitations and their dimensions for a given system can often be understood in terms of its symmetries. As we will see in Sec. 3.2.3, systems with global onsite symmetries have point-like excitations that are free to propagate, and therefore such symmetries do not offer any extra stability. This motivates the consideration of more general subsystem symmetries beyond the global onsite case. Higher-form symmetries are a family of symmetries that generalise the conventional global onsite symmetry. Excitations in systems with higher-form symmetries form higher-dimensional objects, and so their importance in the context of self-correction becomes apparent.

3.2.2 Topological phases with symmetry

Quantum phases of matter are characterised by their ground state properties. Two gapped local Hamiltonians are said to belong to the same phase if they are connected by a one-parameter continuous family of local Hamiltonians without closing the gap. When symmetry is at play, the classification becomes richer, as all Hamiltonians in the family must respect the symmetry. In particular, it is possible that two Hamiltonians that are equivalent in the absence of symmetry, become inequivalent when the symmetry is enforced. This leads to the notion of SPT and SET phases, which we now briefly define (see Ref. [92] for a detailed discussion).

Consider a lattice Λ in d dimensions with a D -dimensional spin placed at each site $i \in \Lambda$. We consider systems described by a gapped, local Hamiltonian $H = \sum_{X \subset \Lambda} h_X$. Here, ‘local’ means that each term h_X is supported on a set of spins X with bounded diameter. We also assume the system has a symmetry described by a group G with a unitary representation S . We say two gapped Hamiltonians H_0 and H_1 with symmetry $S(g)$, $g \in G$ belong to the same phase if there exists a continuous path of gapped, local Hamiltonians $H(s)$ $s \in [0, 1]$ that all obey the symmetry $S(g)$ such that $H(0) = H_0$ and $H(1) = H_1$.

For SPT and SET ordered systems, one commonly considers global symmetries $S(g)$ that act via an onsite fashion on the underlying degrees of freedom. The global action of these onsite

symmetries $S(g)$ may be expressed as

$$S(g) = \bigotimes_{i \in \Lambda} u(g), \quad g \in G, \quad (3.6)$$

where $u(g)$ is a local, site-independent representation of G .

We will also consider a generalised class of global symmetries, known as higher-form symmetries, which have been recently of high interest in the condensed matter, high energy and quantum information communities [153, 155, 156, 216, 221, 222]. These higher-form symmetries form a family of increasingly stringent constraints that generalize the onsite case, and this will be central in the discussion of the interplay of symmetry and self-correction. We introduce these symmetries in Sec. 3.2.2, and for the present discussion and the definitions of SPT and SET phases, the action of the symmetry $S(g)$ is left general.

Symmetry protected topological phases

An SPT phase with symmetry $S(g)$ is defined as class of symmetric Hamiltonians which are equivalent under local symmetric transformations which do not close the gap and which are not in the same class as the trivial phase (a non-interacting spin model with a product ground state), but which *are* in the same phase as the trivial model if the symmetry were not enforced. Ground states of such models are short range entangled, meaning they can be mapped to a product state under a constant depth quantum circuit; however, such a circuit must break the symmetry. Key characteristics of such phases are the absence of anyonic excitations, and the absence of topology dependent ground space degeneracy. However, when defined on a lattice with boundary, these phases host protected modes localized on the boundary, meaning the boundary theory of an SPT phase must be either symmetry breaking, gapless, or topologically ordered (note that a topologically ordered boundary can only exist when the boundary has dimension $d \geq 2$). As such, these systems are typically regarded as having a trivial bulk, but exotic boundary theories. Some well known examples are the 1D cluster state and the spin-1 Haldane phase (with \mathbb{Z}_2^2 symmetry), both of which host degenerate boundary modes that transform as fractionalized versions of the symmetry. More generally the group cohomology models [111] provide a systematic way of constructing SPT ordered models.

Symmetry enriched topological phases

An SET phase with symmetry $S(g)$ is defined by a Hamiltonian that is distinct from the trivial phase, even without any symmetry constraint. These topological phases can form distinct equivalence classes under the symmetry $S(g)$, and are referred to as SET phases. The key characteristics of such phases are the presence of anyonic excitations, and topology-dependent

ground space degeneracy. These anyons can carry fractional numbers of the symmetry group, or may even be permuted under the symmetry action. Such anyon permuting symmetries can be used to define symmetry defects on the lattice, which can be thought of as localized and immobile quasiparticles that transform anyonic excitations when they are mutually braided. Some well known examples of SETs are found in Refs. [113, 190, 205–207], and a general framework is given by the symmetry-enriched string-nets of Refs. [114, 115]. These SET phases fall into two categories. The first category consists of non-anomalous SET phases. These are standalone topological phases in d -dimensions with onsite symmetry $S(g)$ as in Eq. (3.6). Anyons may undergo transformations under the symmetry action $S(g)$. The second category consists of anomalous SET phases. These are d -dimensional topological phases with a symmetry action that cannot be realised in an onsite way on the degrees of freedom on the d -dimensional boundary. These anomalous phases appear only on the boundary of $(d+1)$ -dimensional SPT phases.

It is conjectured that the topologically ordered boundary of an SPT phase with bulk onsite symmetry must always be anomalous. In particular, a wide class of 3-dimensional SPT phases can be classified by the group cohomology models [111], which are labelled by elements of the cohomology group $H^4(G, U(1))$. (See Refs. [161, 223–225] for examples of models outside this classification.) Moreover, in 2 dimensions, anyonic systems with discrete unitary symmetry G (that does not permute the anyons) also have a label in $H^4(G, U(1))$ that classifies the anomalies [226] (see also [113]). The case $\omega = 1$ (i.e., trivial) means that there is no anomaly, and $\omega \neq 1$ means the system is anomalous and cannot be realised in 2-dimensions in a standalone way with onsite symmetries [112, 117, 163, 164, 208, 209]. A conjecture of Ref. [209] is that the gapped boundary topological theory of a group cohomology model must always have an anomaly $\omega \in H^4(G, U(1))$ that agrees with the label specifying the bulk SPT order. This kind of bulk-boundary correspondence was proved in Ref. [210] in the case that the symmetry group G is abelian and does not permute the boundary anyons. Moreover, in Ref. [116], a general procedure to extract a boundary anomaly label from a bulk SPT has been given, in agreement with the conjecture.

Higher-form symmetries

We will make use of a family of symmetries called higher-form symmetries [153, 155, 156, 216, 221, 222], generalizing the onsite case. These symmetries have been of recent interest for several reasons, in particular, they provide a useful structure for error correction in quantum computation [216], have been used to construct new phases of matter [156], and to understand topological phases from the symmetry breaking paradigm [155, 222].

A q -form symmetry (for some $q \in \{0, 1, \dots, D-1\}$) is given by a symmetry operator associated with every closed codimension- q submanifold of the lattice; these operators are written as $S_{\mathcal{M}}(g)$

where \mathcal{M} is a closed codimension- q submanifold of Λ and $g \in G$. On these codimension- q submanifolds, the action of the symmetry operators takes an onsite form: for $g \in G$ and a codimension- q submanifold \mathcal{M} , the symmetry operator is

$$S_{\mathcal{M}}(g) = \prod_{i \in \mathcal{M}} u(g), \quad g \in G \quad (3.7)$$

where the product runs over all sites i of the submanifold \mathcal{M} , and $u(g)$ is a local, site-independent representation of G . That is, higher-form symmetries can be thought of as being onsite symmetries on lower dimensional submanifolds. For systems with boundary, the submanifolds that the higher-form symmetries are supported need only be closed relative the boundary of the lattice. In other words, the manifold \mathcal{M} on which the symmetry is supported may have a boundary on the boundary of the lattice Λ , i.e. $\partial\mathcal{M} \subset \partial\Lambda$.

A key feature of systems with q -form symmetries is that symmetric excitations must form q -dimensional objects. Of particular interest in this chapter will be 1-form symmetries in 3-dimensional systems, which are the next weakest generalization (within the family of higher-form symmetries) of the conventional global onsite symmetry. Symmetry operators in such systems are supported on closed 2-dimensional surfaces, and excitations form closed 1-dimensional loop-like objects. In Sec. 3.3 and Sec. 3.4 we will look at two examples of self-correcting quantum memories protected by \mathbb{Z}_2^2 1-form symmetries.

Self-correction and topological order

The relationship between self-correction and thermal stability is complex. Self-correction is a dynamic property of a system, whereas thermal stability is an equilibrium property. In many previous investigations, various quantities have been used as proxies or indicators of self-correction, for instance, the existence of a nonzero temperature phase transition [202, 227], the presence of topological entanglement entropy in the Gibbs state [121], or the nontriviality of Gibbs ensemble in terms of circuit depth [123]. Here, by ‘thermal stability’ we specifically mean the presence of topological order in the thermal state, as determined by the minimal circuit depth to prepare, following Refs. [123, 216]. While we do not yet have a general result connecting the thermal stability and memory time, we explore the connection between these two notions further through the example of the RBH model, by proving bulk thermal stability from the existence of a macroscopic energy barrier on the boundary. This type of bulk-boundary correspondence (at nonzero temperature) provides evidence in favour of a close relationship between thermal stability and self-correction.

3.2.3 Symmetry constraints and quantum memories

In this section, we consider what types of symmetric models may be worth investigating as potential self-correcting quantum memories.

An important condition that must be met by a symmetry-protected self-correcting quantum memory is that all logical operators can be implemented through a sequence of symmetric local moves. That is, all logical operators \bar{l} admit a local decomposition $\mathcal{D}(\bar{l}) = \{l^{(k)} \mid k = 1, \dots, N\}$, such that all $l^{(k)}$ are symmetric. This implies that even in the presence of symmetry, the bath is capable of implementing all logical faults, and the logical information will eventually be thermalized. If such a condition is not met, one can construct ‘trivial’ self-correcting models in which the symmetry is spontaneously broken, as explained below.

No spontaneous symmetry breaking

If we require our model to admit symmetric local decompositions of all logical operators, then the enforced symmetry $S(g)$ cannot be spontaneously broken. In a model where the symmetry is spontaneously broken, the ground space has less symmetry than the Hamiltonian, and this can render the model trivial as a memory by disallowing logical operator actions at all. Different ground states will in general be in different eigenspaces of the symmetry operator, and thus enforcing the symmetry would be prohibit transitions between ground states. In the case that the spontaneously broken symmetry is higher-form, enforcing it could remove some or all of the anyonic excitations from the model.

The 3D toric code provides an illustrative example, where one can trivially obtain a self-correcting quantum memory by enforcing a \mathbb{Z}_2 1-form symmetry that prevents any of the vertex terms from flipping. Enforcing the vertex and plaquette terms in a 2D toric code provides another trivial example of this phenomenon. These examples do not admit symmetric local decompositions of all logical operators. For this reason, we only consider models where the symmetry is not spontaneously broken, and SPT ordered systems provide a natural family of candidates.

Onsite symmetries are insufficient for stability

In this section we argue that onsite symmetries are insufficient to promote a 2D topological quantum memory to be self-correcting, even if such a phase lives on the boundary of a 3D SPT model. Our goal here is simply to motivate moving beyond onsite symmetries (to higher-form symmetries), not to rigorously rule out any role for onsite symmetries in the study of self-correction.

In particular, consider the case where the full system is given by a commuting Hamiltonian with boundary, and that the protecting symmetry is abelian and onsite (with possibly an anomalous boundary action). The excitations in such systems will be point-like, and their presence precludes the possibility of having thermally stable (symmetry-protected) topological order, as shown in Ref. [216]. This suggests that the boundary theory is also not thermally stable, and thus not self-correcting. Indeed, as we show in Sec. 3.8, this is the case for the class of models where the boundary is an abelian twisted quantum double with a potentially anomalous boundary symmetry. Specifically, we show that there is a constant (symmetric) energy barrier in this case. Therefore we see that in the case of onsite (0-form) symmetries, the SPT ordered bulk offers no additional stability to the boundary theory. This motivates us to consider the boundaries of SPTs protected by 1-form (or other higher-form) symmetries.

System-bath coupling with symmetry and the symmetric energy barrier

Consider the system bath coupling of Eq. (3.1) and a symmetry $S(g)$ (with $g \in G$ for some group G). If

$$[H_{\text{full}}, S(g)] = 0, \quad (3.8)$$

then all of the errors that are introduced due to interactions with the bath must be from symmetric processes that commute with $S(g)$. In particular, only excitations that can be created by symmetric thermal errors will be allowed and the symmetry is preserved throughout the dynamics.

Under symmetric dynamics, we should only consider local decompositions of logical operators that commute with the symmetry when defining the energy barrier Δ . If a local decomposition $\mathcal{D}(\bar{l}) = \{l^{(k)} \mid k = 1, \dots, N\}$ of a logical operator \bar{l} is such that $[l^{(k)}, S(g)] = 0$ for all k and all $g \in G$, then we call $\mathcal{D}(\bar{l})$ a symmetric local decomposition of \bar{l} . We label such symmetric local decompositions with symmetry G by $\mathcal{D}_G(\bar{l})$. Then the *symmetric energy barrier* is defined as

$$\Delta_G = \min_{\bar{l}, \mathcal{D}_G(\bar{l})} \Delta_{\mathcal{D}_G(\bar{l})}. \quad (3.9)$$

Namely, it consists of the smallest energy barrier for any logical operator, where the cost is minimized over all symmetric local decompositions. For notational simplicity, we often omit the subscript G as the symmetry is clear from context.

With the abundance of no-go results for self-correction in 2D and 3D stabilizer memories, the relevant question is whether one can achieve self-correction if the system bath coupling respects a symmetry. In particular, for a given model H_S , can a symmetry $S(g)$ be imposed such that H_{sys} has a macroscopic symmetric energy barrier?

3.3 Self correction with a 1-form SPT phase

Our first example of a 3D self-correcting model in the presence of a 1-form symmetry is described by a commuting Hamiltonian based on the cluster-state model of Raussendorf, Bravyi, and Harrington (RBH) [136]. This model has been used in high-threshold schemes for fault-tolerant quantum computation [66, 136, 172]. In particular, the RBH model underpins the topological formulation of measurement-based quantum computation, where single qubit measurements are used to simulate the braiding of punctures in the 2D toric code.

The RBH model is an example of an SPT ordered system under 1-form symmetry, which is thermally stable [216]. It contains no anyonic excitations in the bulk, however when defined on a lattice with a boundary, the boundary theory can be gapped, topologically ordered, and possesses point-like anyonic excitations. In particular, the boundary can be chosen to be described by a boundary Hamiltonian equivalent to the 2D surface code. Without any symmetry, the excitations of this 2D surface code phase are deconfined, and information encoded in this surface will thermalize in constant time in the absence of error-correction. However, in the presence of symmetry, a natural question is whether the boundary code inherits any protection from the bulk SPT order. We will show that in the presence of 1-form symmetry, the bulk SPT order gives rise to confinement of boundary excitations and ultimately a macroscopic lifetime of boundary information. As such, this model provides a simple example of an anomalous SET phase on the boundary of a 3D higher-form SPT that is thermally stable, giving a self-correcting quantum memory.

We first define and present the bulk properties of this model. We then define some important boundaries of the model, including the anomalous toric code SET phase. Finally we present the global lattice and boundary conditions and discuss the resulting model as a quantum code and show that it results in a symmetry-protected SCQM.

3.3.1 The RBH model – bulk properties

The RBH bulk Hamiltonian

In this subsection, we define the RBH model in the bulk. Consider a 3D cubic lattice \mathcal{L} . Label the set of all vertices, edges, faces and volumes of \mathcal{L} by V, E, F, Q . Similarly, to prepare ourselves for boundary conditions that are to be specified later, we label the interior vertices, edges, faces and volumes by $V^\circ, E^\circ, F^\circ, Q^\circ$, and \mathcal{L}° is the collection of all interior cells. For now we ignore any boundary conditions (meaning we consider only interior cells), and one may consider periodic boundary conditions until specified otherwise. We place a qubit on every face $f \in F$ and on every edge $e \in E$. We refer to qubits on faces as primal qubits, and qubits on edges as dual qubits.

The bulk Hamiltonian is a sum of commuting cluster terms

$$H_{\mathcal{L}^\circ} = - \sum_{f \in F^\circ} K_f - \sum_{e \in E^\circ} K_e, \quad (3.10)$$

where each cluster term is a 5-body operator

$$K_f = X_f \prod_{e: e \subset f} Z_e, \quad K_e = X_e \prod_{f: e \subset f} Z_f, \quad (3.11)$$

and X_v and Z_v are the usual Pauli- X and Pauli- Z operators acting on the qubit v . These terms are depicted in Fig. 3.1

We note that the terms in the Hamiltonian can be considered ‘dressed’ terms of a simpler, trivial bulk model. In particular, we define the “trivial model” $H_{\mathcal{L}^\circ}^{(0)}$ to be a trivial paramagnet:

$$H_{\mathcal{L}^\circ}^{(0)} = - \sum_{i \in E^\circ \cup F^\circ} X_i. \quad (3.12)$$

One can see that these two models are equivalent up to a constant depth circuit

$$H_{\mathcal{L}^\circ} = U H_{\mathcal{L}^\circ}^{(0)} U^\dagger, \quad (3.13)$$

where U is a product of controlled- Z gates that act on all pairs of neighbouring qubits at sites i and j by

$$CZ_{ij} = \exp \left(\frac{i\pi}{4} (1 - Z_i)(1 - Z_j) \right). \quad (3.14)$$

Indeed, let a face f and an edge e be referred to as neighbours if the edge is contained within the face $e \subset f$. Then U is a product of controlled- Z gates over all neighbouring sites

$$U = \prod_{f \in F^\circ} \prod_{e \subset f} CZ_{fe}. \quad (3.15)$$

From this we can see that the bulk Hamiltonian $H_{\mathcal{L}^\circ}$ is non-degenerate (since $H_{\mathcal{L}^\circ}^{(0)}$ is non-degenerate).

Bulk excitations without symmetry

We now consider the excitations in the model in the absence of any symmetry considerations. In the bulk, all excitations can be created by products of Pauli- Z operators applied to the

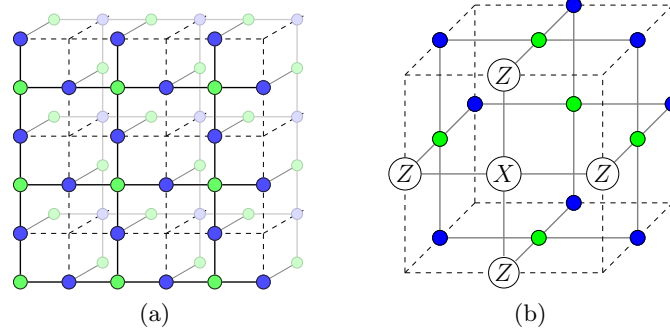


Fig. 3.1 (a) A portion of the bulk lattice. Primal qubits are depicted in green, while dual qubits are depicted in blue. (b) A bulk cluster term K_f . In both figures, bold lines indicate nearest neighbour relations between qubits, while dashed lines indicate edges of the ambient cubic lattice.

ground state. Indeed, for any subset of edges $E' \subset E^o$ or subset of faces $F' \subseteq F^o$, the operator

$$Z(E', F') = \prod_{f \in F'} Z_f \prod_{e \in E'} Z_e \quad (3.16)$$

anti-commutes with precisely the cluster terms K_e and K_f for which $e \in E'$ and $f \in F'$, and commutes with all remaining bulk terms. Moreover, all excitations can be reached in this way (as can be verified by considering the trivial model $H_{\mathcal{L}^o}^{(0)}$ and the local unitary U of Eq. (3.15)). The energy cost for creating excitations at sites in $E' \cup F'$ with the operator $Z(E', F')$ is given by

$$|E' \cup F'| \Delta_{\text{gap}} \quad (3.17)$$

where $\Delta_{\text{gap}} = 2$ is the energy gap.

The bulk model is very simple due to its low-depth equivalence with the trivial paramagnet. Excitations can be locally created on any site by flipping a spin, they have no interaction with each other, and the energy cost of a general excitation is proportional to the number of flipped spins. We refer to excitations supported on sites $F' \subseteq F^o$ as primal excitations, and excitations supported on sites $E' \subset E^o$ as dual excitations.

1-form symmetries

The model $H_{\mathcal{L}^o}$ has a \mathbb{Z}_2^2 1-form symmetry, consisting of operators supported on closed 2-dimensional surfaces on each of the primal and dual sublattices. In particular, a generating set are given by vertex and cube operators (for dual and primal qubits, respectively), for each

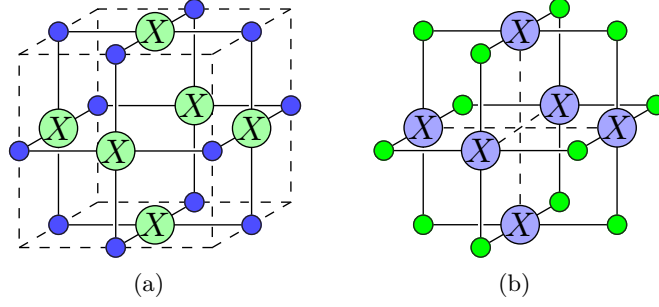


Fig. 3.2 Generators of the 1-form symmetry in the bulk. (a) A primal generator S_q . (b) A dual generator S_v . Thick lines denote neighbour relations, and dashed lines denote the cubic lattice.

$q \in Q$ and $v \in V$

$$S_q = \prod_{f: f \subset q} X_f, \quad S_v = \prod_{e: v \subset e} X_e. \quad (3.18)$$

Each of these vertex and cube operators are 6-body in the bulk. Taking products of these operators gives rise to the \mathbb{Z}_2^2 1-form symmetry

$$G = \langle S_v, S_q \mid v \in V, q \in Q \rangle. \quad (3.19)$$

One can easily check that these operators commute with both $H_{\mathcal{L}^\circ}$ and $H_{\mathcal{L}^\circ}^{(0)}$.

It has been shown that under these symmetries the bulk model $H_{\mathcal{L}^\circ}$ belongs to a nontrivial SPT phase while the trivial bulk $H_{\mathcal{L}^\circ}^{(0)}$ belongs to the trivial phase. Moreover, this distinction persists to nonzero temperature, where $H_{\mathcal{L}^\circ}$ remains SPT ordered [216].

Bulk excitations with 1-form symmetries

We now consider what excitations are possible in the presence of the 1-form symmetry G . If we consider bulk excitations, then the excitation operator $Z(E', F')$ of Eq. (3.16) is symmetric if and only if both E' is a cycle (i.e., it has no boundary) and F' is a cocycle (meaning it is dual to a cycle on the dual lattice – where vertices are replaced with cubes, edges with faces, and so on). In other words, the only symmetric bulk excitations are formed by combinations of closed loop-like (i.e., 1-dimensional) objects, and we refer to them as loop excitations. We can further refer to loop excitations as either primal or dual if they are supported on sets of faces or edges, respectively.

Both the primal and dual loop excitations have an energy cost proportional to their length, and are thus confined. This confinement leads to thermal stability of the model.

3.3.2 Boundaries

To obtain degeneracy in the ground space we must consider a lattice with boundaries. The allowable boundary Hamiltonians are dictated by the symmetry action on the boundary, which in turn is governed by the precise boundary geometry. In addition to changing the ground space degeneracy of the model, the choice of boundary Hamiltonian may allow for different types of excitations to condense on them. By condense, we mean that an excitation can be absorbed on the boundary (and the reverse process is also possible, where excitations can be emitted from a boundary). In the following, we will consider four different types of symmetric gapped boundary Hamiltonians that each allow different excitations to condense on them. These boundaries will allow us to construct the Hamiltonian with a degenerate ground space (i.e. codespace) that is self-correcting under 1-form symmetry.

We will first focus on a toric code boundary, which will be used to encode information. We will then introduce other boundary types that do not contain any degeneracy, but will allow for all logical operators to be implemented through a sequence of symmetric local moves (as required by the discussion in Sec. 3.2.3).

Boundary condensation

Throughout the remainder of this section, it will be useful to characterise the types of boundaries in terms of the types of excitations that can condense on them. By boundary, we mean a combination of the choice of how to terminate the lattice, the symmetry appropriately defined on this lattice, and a Hamiltonian that commutes with the symmetry (we will see examples of these choices in the next subsection). We define a boundary as being primal-condensing or dual-condensing as follows.

Definition 1. *We refer to a boundary as primal-condensing (dual-condensing) if any primal (dual) loop excitation can be piecewise removed near the boundary using local, symmetric operations.*

A schematic depicting a dual-condensing boundary is shown in Fig. 3.3. Importantly, for a boundary to be able to condense a general loop excitation, it must be capable of piecewise condensing it. This piecewise requirement is what makes the above definition nontrivial, as small loop excitations can always be condensed wholly, by contracting them to a point (which is not true for loop excitations with nontrivial topology). Importantly, a boundary is primal-condensing (dual-condensing) if and only if primal (dual) string excitations can terminate on them in a symmetric way. For example, Fig. 3.3 (ii) depicts a dual loop excitation terminating on a dual-condensing boundary. Therefore, symmetric excitations only need to be closed loops modulo their respective primal/dual-condensing boundaries.

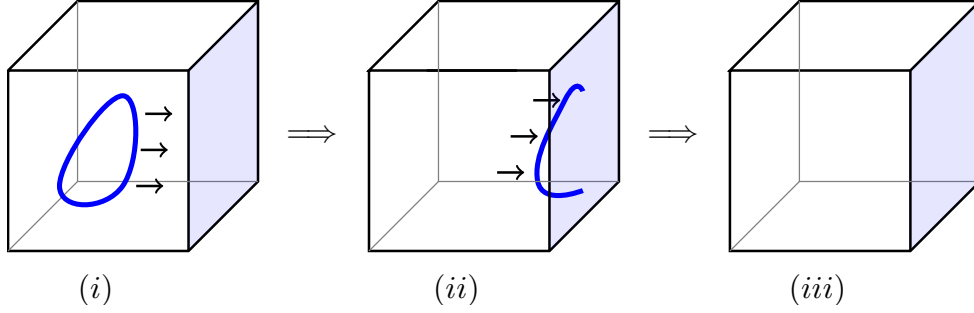


Fig. 3.3 A dual-condensing boundary can absorb a dual loop excitation. (i) A dual loop excitation in the bulk is depicted in blue, while the dual-condensing boundary is shaded light blue. (ii) The loop is moved to the boundary, where part of it is absorbed. (iii) The loop is fully absorbed.

Both the symmetry and Hamiltonian of the boundary play an important role in determining whether it is primal or dual-condensing. While a boundary may have its own set of excitations that are localised within it (and they may interact with bulk loop excitations), the definition of primal-condensing and dual-condensing are independent of this. We now look at an important boundary that is both primal-condensing and dual-condensing.

Toric code boundary conditions

As mentioned, the type of Hamiltonian that can be defined on the boundary is heavily constrained by the symmetry. We first consider boundary conditions that support a 2D toric code phase. This type of boundary will be used to encode logical information.

We consider a lattice with one boundary component which we terminate with ‘smooth’ boundary conditions (see Fig. 3.4). Namely, the cubic lattice is terminated on a smooth plane, such that there are boundary volumes, boundary faces, boundary edges, and boundary vertices, each having a lower number of incident cells (neighbours) compared to the bulk. We label the collection of all boundary volumes, faces, edges, and vertices by $\partial\mathcal{L}$. We will fix the topology and geometry more precisely later, for this section we consider a lattice supported on a 3D half space, i.e., with coordinates (x, y, z) satisfying $x \geq 0$, $-\infty < y < \infty$, $-\infty < z < \infty$, such that the boundary is on the $x = 0$ plane. On the boundary, qubits are placed only on boundary edges, and not on boundary faces, as depicted in Fig. 3.4. We refer to these qubits as boundary qubits. (Note that we have constructed this boundary using dual qubits. This choice is arbitrary, and an analogous boundary exists that is comprised of primal qubits.)

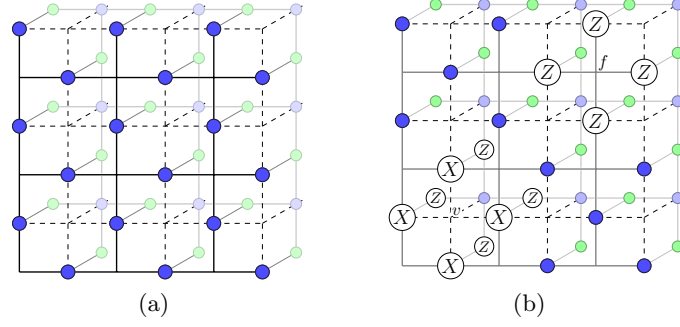


Fig. 3.4 (a) The boundary of the lattice consists only of dual qubits which are depicted in blue. Primal qubits on faces penetrating into the bulk are depicted in green. (b) The boundary terms \bar{A}_v and \bar{B}_f . In both figures, bold lines indicate nearest neighbour relations, while dashed lines indicate edges of the cubic lattice. The dashed lines on the boundary can be thought of as the edges of a toric code lattice.

For this geometry, we consider Hamiltonians of the form

$$H = H_{\mathcal{L}^\circ} + H_{\partial\mathcal{L}}, \quad (3.20)$$

where, $H_{\mathcal{L}^\circ}$ is the bulk Hamiltonian of Eq. (3.10) (which sums only over sites on the interior, meaning it contains only complete cluster terms) and $H_{\partial\mathcal{L}}$ is a boundary Hamiltonian. A boundary Hamiltonian is in general any Hamiltonian with local terms acting near the boundary of the lattice $\partial\mathcal{L}$ that commute with the symmetry (whose action we describe shortly).

Boundary degrees of freedom

To determine what types of Hamiltonians are possible on the boundary, we describe the boundary Hilbert space in terms of a more natural boundary algebra. We begin with the case $H_{\partial\mathcal{L}} = 0$ such that $H = H_{\mathcal{L}^\circ}$ consists of all 5-body cluster terms of Eq. (3.11). In this case there is an extensive degeneracy localised near the boundary: there is a qubit 'boundary degree of freedom' for every boundary edge (i.e. one for every $e \in E \cap \partial\mathcal{L}$). It is important to distinguish between the qubits that belong to the boundary, and the degrees of freedom localised near the boundary that describe the ground space. Indeed, the operators that act on these degrees of freedom within the ground space of H are not simply given by the Pauli operators acting on boundary qubits. That is, for some Pauli operator P_e acting on $e \in E \cap \partial\mathcal{L}$, we have $\Pi_0 P_e \Pi_0 \neq \Pi_0 P_e$ in general, where Π_0 is the ground space projector (in fact we have equality only if the bulk is a trivial paramagnet). The effective Pauli- X and Pauli- Z operators can be obtained by finding the dressed versions of these Pauli operators using the unitary in Eq. (3.15).

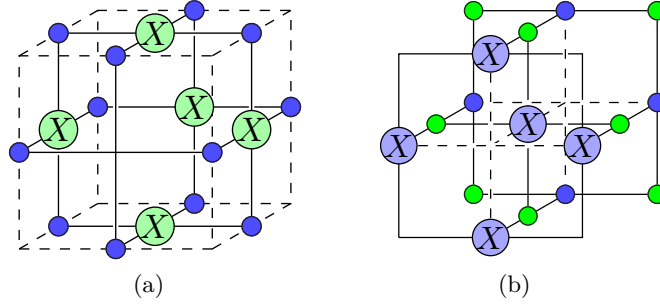


Fig. 3.5 Symmetry operators on the boundary (a) S_q with $q \in \partial\mathcal{L}$, (b) S_v with $v \in \partial\mathcal{L}$. Thick lines denote neighbour relations, and dashed lines denote the cubic lattice.

More explicitly, the effective Pauli- X and Pauli- Z operators for these boundary degrees of freedom are given by

$$\tilde{X}_e := UX_eU^\dagger = X_eZ_{f(e)}, \quad \tilde{Z}_e := UZ_eU^\dagger = Z_e, \quad (3.21)$$

where U is a product of CZ gates as in Eq (3.15) and $f(e)$ is the unique face $f \in F^\circ$ such that $e \subset f$. These operators preserve the ground space (as they commute with all bulk cluster terms) and act on the boundary degrees of freedom in the ground space as the usual Pauli spin operators. We will describe boundary degrees of freedom in terms of the boundary algebra generated by \tilde{X}_e, \tilde{Z}_e . We emphasise that the support of the boundary algebra is not strictly contained on the boundary qubits, as would be the case if the bulk Hamiltonian was trivial. This subtle difference between the boundary degrees of freedom and cut boundary qubits is important, as we will see.

Symmetry action on the boundary

The \mathbb{Z}_2^2 1-form symmetry on a lattice with a boundary is again given by the group G in Eqs. (3.18) and (3.19). On the boundary, such operators are 5-body (rather than 6-body) and are depicted in Fig. 3.5.

A general boundary Hamiltonian can be written in terms of operators from the boundary algebra. We must therefore analyse the action of the 1-form symmetry on the boundary algebra (to infer how the boundary degrees of freedom transform under the symmetry). First, we note that the operators of Eq. (3.21) are not themselves symmetric. Taking the boundary symmetry operators S_v and S_q with $v \in V \cap \partial\mathcal{L}$, $q \in Q \cap \partial\mathcal{L}$ (depicted in Fig. 3.5), for any $e \in E \cap \partial\mathcal{L}$ we

have (under conjugation)

$$S_v : \tilde{X}_e \mapsto \tilde{X}_e, \quad \tilde{Z}_e \mapsto (-1)^{\mathbb{1}_e(v)} \tilde{Z}_e \quad (3.22)$$

$$S_q : \tilde{X}_e \mapsto (-1)^{\mathbb{1}_q(e)} \tilde{X}_e, \quad \tilde{Z}_e \mapsto \tilde{Z}_e, \quad (3.23)$$

where $\mathbb{1}_e(v) = 1$ if $v \subset e$ and $\mathbb{1}_e(v) = 0$ otherwise, and similarly $\mathbb{1}_q(e) = 1$ if $e \subset q$ and $\mathbb{1}_q(e) = 0$ otherwise.

From this we can write the action of the 1-form symmetry in the ground space of H in terms of operators in the boundary algebra as follows. Define the following ‘dressed toric code’ operators for every $v \in V \cap \partial\mathcal{L}$ and every $f \in F \cap \partial\mathcal{L}$:

$$\bar{A}_v = \prod_{e \in \partial E: v \subset e} X_e \prod_{f: e \subset f} Z_f, \quad \bar{B}_f = \prod_{e: e \subset f} Z_e, \quad (3.24)$$

where $\partial E = E \cap \partial\mathcal{L}$ is the set of boundary edges. Such operators are depicted in Fig. 3.4. They are dressed versions of the usual toric code operators

$$A_v = \prod_{e \in \partial E: v \subset e} X_e \quad B_f = \prod_{e: e \subset f} Z_e, \quad (3.25)$$

and can be obtained by conjugating them by the unitary of Eq. (3.15).

Now it can be verified from the (anti)commutation relations of Eqs. (3.22-3.23) that the 1-form symmetry acts as

$$S_v \equiv \bar{A}_v \quad \forall v \in V \cap \partial\mathcal{L}, \quad (3.26)$$

$$S_q \equiv \bar{B}_{f(q)} \quad \forall q \in Q \cap \partial\mathcal{L}, \quad (3.27)$$

and as the identity otherwise. Here $f(q)$ is the unique face $f(q) = \partial q \cap \partial\mathcal{L}$, and \bar{A}_v and \bar{B}_f are defined in Eq. (3.24). The equivalence \equiv means that the two operators have the same action in the ground space. In other words, S_v and \bar{A}_v (resp. S_q and $\bar{B}_{f(q)}$) have identical commutation relations with all boundary operators \tilde{X}_e and \tilde{Z}_e of Eq. (3.21), and therefore have equivalent action on the boundary degrees of freedom.

There are two observations to make about the action of the symmetry on the boundary. Firstly, the symmetry is represented as a 1-form symmetry on the boundary degrees of freedom: i.e. \bar{A}_v and \bar{B}_f generate a symmetry group whose elements are supported on closed loops. Secondly, the supports of these symmetry operators are not strictly contained on the boundary qubits.

Toric code boundary Hamiltonian

In order to add a nontrivial Hamiltonian $H_{\partial\mathcal{L}}$ to the boundary, it must be composed of terms that commute with \bar{A}_v and \bar{B}_f from Eq. (3.24). The simplest such Hamiltonian is where the terms are given by \bar{A}_v and \bar{B}_f . This gives us the dressed toric code boundary

$$H_{\partial\mathcal{L}} = - \sum_{v \in \partial V} \bar{A}_v - \sum_{f \in \partial F} \bar{B}_f, \quad (3.28)$$

where ∂V and ∂F are the set of all boundary vertices and faces (respectively). Again, the terms of this Hamiltonian are depicted in Fig. 3.4.

Toric code boundary excitations

The toric code Hamiltonian introduces a new set of excitations on the boundary, that are interesting in themselves, but also interact nontrivially with bulk excitations.

The boundary supports anyonic excitations that are free to propagate in the absence of any symmetry. Indeed, for a string $l \subseteq \partial E$ on the boundary, we can define the string operator $Z(l) = \prod_{e \in l} Z_e$. The string operator $Z(l)$ commutes with all Hamiltonian terms, apart from vertex terms \bar{A}_v with $v \in \partial l$ for which it anti-commutes with. We define flipped \bar{A}_v terms as e -excitations, and string operators $Z(l)$ create these excitations. Similarly, we can define a dual string operator $\tilde{X}(l') = \prod_{e \in l'} X_e \prod_{f \in l'^\perp} Z_f$ for a string $l' \subset \partial E$, which when applied to the ground space, creates m -excitations on the faces at the ends of l' . Here, $l^\perp = \{f \in F^\circ : \partial f \cap l \neq \emptyset\}$ denotes the set of faces sitting just inside the boundary incident to the string l . At the endpoints of the string operator $\tilde{X}(l')$, m -excitations occur, as the plaquette operators \bar{B}_f with f on the ends of l' anti-commute with $\tilde{X}(l')$, while all remaining terms commute. Examples of such operators are depicted in Fig. 3.6

Now we consider excitations that respect the symmetry. On the boundary, we see that boundary excitations are symmetric only if they are accompanied by a bulk string excitation. In particular, a string operator $Z(l)$ creating e particles at vertices μ and ν is made symmetric by attaching a bulk string operator $Z(E')$ whose boundary is at the location of the two particles $\partial E' = \{\mu, \nu\}$ (i.e., $l \cup E'$ is a cycle). Similarly, the dual string operator $\tilde{X}(l')$ that creates m excitations at μ' and ν' can be made symmetric by attaching a bulk string operator $Z(F')$ such that the union $l'^\perp \cup F'$ is a dual cycle (i.e., has no boundary on the dual lattice). Such excitations will flip cluster stabilizers in the bulk, for all terms K_e with $e \in E'$ and K_f with $f \in F'$, but will only create a pair of e or m particles on the boundary at their endpoint.

The following two lemmas characterise the valid configurations of excitations in the presence of symmetry.

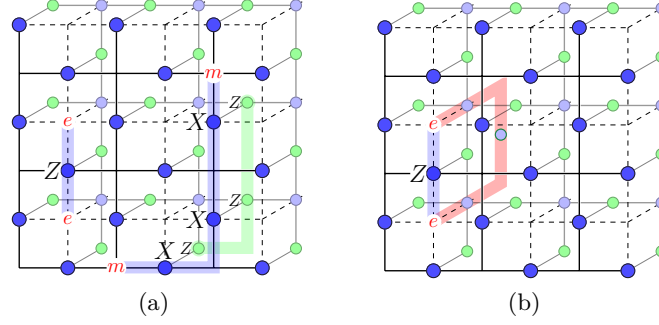


Fig. 3.6 (a) The e and m type excitations on the boundary of string and dual-string operators. For an e -excitation (m -excitation) to be symmetric they must be accompanied by a bulk dual (primal) string excitation terminating on them. (b) An example of a symmetric excitation. Two e -excitations live on the boundary of a bulk dual string excitation, depicted in red.

Lemma 1. *The toric code boundary is both primal-condensing and dual-condensing.*

Proof. We first show that it is dual-condensing. We can decompose any cycle $l \subset E$ into two components: $l = l_{\text{int}} \cup l_{\text{boun}}$ where $l_{\text{int}} = l \cap E^\circ$ is its interior component and $l_{\text{boun}} = l \cap \partial E$ is its boundary component. As we have seen, $Z(l_{\text{int}})$ anti-commutes with all terms K_e with $e \in l_{\text{int}}$ and commutes with all other terms. Also, $Z(l_{\text{boun}})$ commutes with all terms apart from \bar{A}_v with $v \in \partial l_{\text{boun}}$. Therefore any bulk dual loop excitation given by an operator $Z(l)$ may be translated to a boundary using a series of local symmetric moves (translations may be performed by sequentially applying $Z(c)$ operations for some small cycle c). The dual loop excitation can then be piecewise absorbed upon contact with the boundary.

To show primal-condensing, the argument is similar. We decompose any dual-cycle $l' \subset F$ into two components $l' = l'_{\text{int}} \cup l'_{\text{boun}}$ where $l'_{\text{boun}} = l' \cap F_{\text{boun}}$ and $l'_{\text{int}} = l' \cap (F \setminus F_{\text{boun}})$ where $F_{\text{boun}} = \{f \in F \mid \partial f \cap \partial E \neq \emptyset\}$. Intuitively, F_{boun} is the set of faces that contain one edge on the boundary of the lattice. Then $Z(l'_{\text{int}})$ anti-commutes with all terms K_f with $f \in l'_{\text{int}}$ and commutes with all other terms. Now find a string $t \subset \partial E$ on the boundary such that $t^\perp = l'_{\text{boun}}$ (recall $t^\perp = \{f \in F^\circ : \partial f \cap t \neq \emptyset\}$). Such a string can always be found. Now $Z(l'_{\text{boun}})$ itself doesn't commute with all bulk cluster terms K_f , but $Z(l'_{\text{boun}})X(t) = \tilde{X}(t)$ is a dressed string operator that commutes with all terms apart from the plaquettes \bar{B}_f with $f \in \delta t$. Then similarly to the previous case, any primal loop excitation in the bulk can be translated to the boundary where it can be piecewise absorbed by sequentially applying local Pauli X operators. \square

As we have seen, primal and dual excitations need only be closed loops modulo the toric code boundary, where they can terminate as an anyonic m or e -type excitations, respectively.

The following lemma states that in fact these anyonic excitations can only exist if they are at the end of a bulk string excitation.

In the following, for any subset of faces f , let $\delta f \subset Q$ be the set of volumes that each contain an odd number of faces of f on their boundary ($\delta f = \{q \in Q : |\partial q \cap f| \not\equiv 0 \pmod{2}\}$). have precisely one face on their boundary belonging to f .

Lemma 2. *In the 1-form symmetric sector, e -excitations can be located at sites $V_e \subset \partial V$ if and only if accompanied by a bulk string excitation supported on $l \subset E$ satisfying $\partial l = V_e$. Similarly, m -excitations can be located at sites $F_m \subset \partial F$ if and only if accompanied by a bulk string excitation supported on $l' \subset F$ satisfying $\delta F_m = \delta l'$.*

Proof. For the e -excitations, we have the following constraint: For every vertex operator \bar{A}_v , $v \in \partial V$, there exists a unique $e \in E^o$ such that $S_v = \bar{A}_v K_e$ (can be seen upon inspection of Fig. 3.5). As $S_v = +1$ in the ground space, it must also be for any excitations produced by a symmetric process. Therefore any flipped term \bar{A}_v must be accompanied by a uniquely determined flipped bulk term K_e . As every dual qubit on an edge e is in the support of two symmetry generators S_{v_1} and S_{v_2} , which also must be preserved, the flipped term K_e must be part of a string excitation can only terminate at another flipped term \bar{A}_w , $w \in \partial V$.

For the m -excitations, the argument is the same after noting the following constrain between bulk and boundary excitations: For every plaquette operator \bar{B}_f , $f \in \partial F$, there exists a unique $q \in Q$ such that $S_q = \bar{B}_f \prod_{f' \in \partial q} K_{f'}$. \square

Energetics of boundary excitations

For any two vertices $v, v' \in V$ let $d(v, v')$ denote the lattice distance between v and v' as $d(v, v') = \min_{l \subset E} \{|l| : \partial l = (v, v')\}$. Namely, it is the smallest number of edges required to connect the two vertices. Similarly, for any two faces $f, f' \in F$, $d(f, f')$ is defined to be the lattice distance between f, f' on the dual lattice (where 3-cells are replaced by vertices, faces by edges, edges by faces, and vertices by 3-cells). Also, recall $\Delta_{\text{gap}} = 2$ is the energy gap.

Lemma 3. *For the model H defined on the half Euclidean (3D) space, the minimal energy cost to symmetrically create a pair of e -excitations (m -excitations) at positions x, x' is given by $(d(x, x') + 4)\Delta_{\text{gap}}$.*

Proof. Consider the process of creating a pair e -excitations on the boundary at positions $x(i_0), x(i_0)'$ and then moving them to positions $x = x(i_k), x' = x(i_k)'$ using a sequence of moves labelled by i_1, \dots, i_k . The positions of the excitations at steps i_j are given by $x(i_j), x(i_j)'$. From Lemma 2 at every step i_j , the excitations must be accompanied by a dual string excitation in the bulk supported on $l(i_j) \subset E^o$ with $\partial l(i_j) = (x(i_j), x(i_j)')$. The energy cost of the string

$l(i_j)$ is given by its length $|l(i_j)|\Delta_{\text{gap}}$ which minimally is $(d(x(i_j), x(i_j)') + 2)\Delta_{\text{gap}}$. Adding in the energy cost $2\Delta_{\text{gap}}$ of the two e -excitations we get the result. The m -excitations follows analogously. \square

We will use this lemma in the following subsections to derive the symmetric energy barrier.

Trivial bulk and boundary

We contrast this with respect to the trivial model. Namely, consider the trivial model $H^{(0)} = H_{\mathcal{L}^o}^{(0)} + H_{\partial\mathcal{L}}^{(0)}$, with $H_{\mathcal{L}^o}^{(0)}$ defined in Eq. (3.12) and

$$H_{\partial\mathcal{L}}^{(0)} = - \sum_{v \in \partial\mathcal{L}} A_v - \sum_{f \in \partial F} B_f. \quad (3.29)$$

with A_v and B_f the undressed toric code terms of Eq. (3.25). The trivial model $H^{(0)}$ can be connected to our model H using the circuit of Eq. (3.15). Lemma 1 still holds for the trivial model, however Lemma 2 and subsequently Lemma 3 do not. Indeed one can symmetrically create a pair of flipped plaquettes B_f using a string of X operators, without creating any bulk excitation. The coupling between boundary anyons and bulk strings is crucial for self correction, as otherwise the anyons remain deconfined on the boundary. We discuss how this conditions results from the anomalous SET order of the boundary, and the SPT order of the bulk in Sec. 3.3.6.

We have now symmetry and spectral properties of the toric code boundary. We will defer the discussion of ground space degeneracy of this model until the next section where we discuss the full model and lattice topology in more detail (as the ground space degeneracy depends strongly on the boundary topology).

3.3.3 Other types of boundaries

We now define other boundary conditions that will be used in the construction of the code. These boundaries will not be used to encode logical qubits, but rather to ensure that all logical operators can be achieved using a sequence of local symmetric moves. We define three different boundary geometries that support the following types of boundary Hamiltonians:

1. the primal boundary Hamiltonian H_P , which is primal-condensing but not dual-condensing;
2. the dual boundary H_D , which is dual-condensing but not primal-condensing; and
3. the “sink” boundary H_{sink} , which is primal-condensing and dual-condensing.

The different boundaries are distinguished by what excitations can condense on them in a symmetric way; the primal boundary is chosen to allow primal string-like excitations (i.e., excitations on primal qubits) to condense, the dual boundary is chosen to allow dual string-like excitations (i.e., excitations on dual qubits) to condense, and both strings can condense on the sink boundary. There exist nondegenerate, symmetric Hamiltonians consisting of commuting Pauli terms with these properties, as we now show.

In the following, the main feature that determines the excitations that can condense is whether they support *complete* primal (S_q) or dual (S_v) 1-form symmetry generators or not. Complete 1-form generators are depicted in Fig. 3.2, and incomplete 1-form generators are depicted in Fig. 3.5. The primal boundary supports complete primal symmetry generators, and incomplete dual generators. The dual boundary supports complete dual generators and incomplete primal generators. The sink boundary supports complete primal and dual generators.

All of the Hamiltonians in this subsection are given by a sum over (potentially truncated) cluster terms

$$H_{\text{boundary}} = - \sum_{f \in \partial F} K_f - \sum_{e \in \partial E} K_e, \quad (3.30)$$

where K_e and K_f of the form of Eq. (3.11). The choice of boundary lattice geometry will dictate the precise structure of the cluster terms, and some may be lower weight than the bulk 5-body terms. The Hamiltonians are all non-degenerate as they are locally equivalent to a trivial paramagnet.

We note that similarly to the bulk case, excitations on the boundary are given by operators $Z(E', F')$ of Eq. (3.16), for $E' \subset \partial E$ and $F' \subset \partial F$. Such an operator flips precisely the terms K_e and K_f with $e \in E'$ and $f \in F'$, this can be verified by local unitary equivalence with the trivial paramagnet using Eq. (3.15). We note the usual product relation between cluster terms and symmetry operators

$$S_q = \prod_{f \in \partial q} K_f, \quad S_v = \prod_{e: v \in e} K_e, \quad \forall q \in Q, \quad \forall v \in V \quad (3.31)$$

puts nontrivial constraints on the relationship between bulk and boundary excitations, that we will now explore.

Primal boundary

For the primal boundary, we consider the ‘smooth’ boundary conditions of the previous subsection. On the boundary, qubits are placed on both boundary edges, and boundary faces, as depicted in Fig. 3.7. On this boundary, the 1-form symmetry is generated by complete (i.e. 6-body) primal symmetry operators S_q of Fig. 3.2, and incomplete (i.e. 5-body) dual symmetry

operators S_v of Fig. 3.5. The Hamiltonian terms of H_D are 4-body K_e operators and 5-body K_f operators, as depicted in Fig. 3.7. These terms all commute with the symmetry.

Lemma 4. *The primal boundary H_P is primal-condensing and not dual-condensing.*

Proof. We first show that the boundary is primal-condensing by showing that primal excitations can terminate on it. Firstly, for any pair of faces $f, f' \in \partial F$ on the boundary, any subset of faces $l' \subset F^\circ$ with $\delta l' = \delta(f \cup f')$ defines a symmetric excitation operator $Z(l')$ (i.e. $[Z(l'), S_q] = 0 \forall q \in Q$). This is due to the fact that every boundary face f belongs to a unique 3-cell q , meaning each boundary primal qubit is in the support of a unique symmetry generator S_q (as opposed to two in the bulk). As $Z(l')$ flips precisely the terms K_f with $f \in l'$ and commutes with all others, we can locally and symmetrically absorb primal loop excitations near the primal boundary.

To show that the primal boundary is not dual-condensing, we note that for every dual qubit on some boundary edge $e \in \partial$ is in the support of two symmetry generators $S_v, S_{v'}$. Therefore the only operators $Z(l), l \subset E$ that commute with the 1-form symmetry operators satisfy $\partial l = \emptyset$. This means that dual excitations must form closed loops, even on the boundary. \square

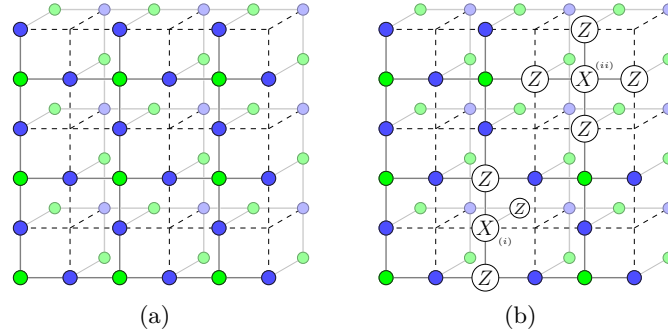


Fig. 3.7 (a) The lattice at the primal boundary. Primal qubits are depicted in green, while dual qubits are depicted in blue. (b) The primal boundary Hamiltonian H_P consists of cluster terms, as depicted by (i) and (ii). Bold lines indicate nearest neighbour relations between qubits, while dashed lines indicate edges of the ambient cubic lattice.

Dual boundary

The dual boundary is similar to the primal boundary; it can be obtained by reversing the role of primal and dual qubits on the boundary. In particular, the boundary of the lattice is depicted in Fig. 3.8. The boundary is terminated such that the 1-form symmetry is generated by complete (i.e. 6-body) dual symmetry operators S_v of Fig. 3.2, and incomplete (i.e. 5-body) primal

symmetry operators S_q of Fig. 3.5. The Hamiltonian terms of H_D are 5-body K_e operators and 4-body K_f operators, as depicted in Fig. 3.8. These terms all commute with the symmetry.

Lemma 5. *The dual boundary H_D is dual-condensing and not primal-condensing.*

Proof. The proof is the same as Lemma 4, exchanging the role of primal and dual qubits. \square

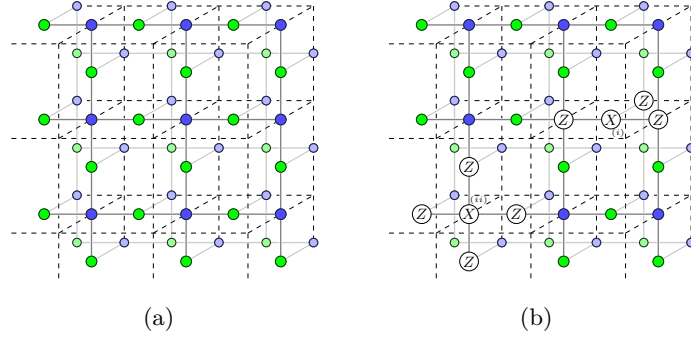


Fig. 3.8 (a) The lattice at the dual boundary. Primal qubits are depicted in green, while dual qubits are depicted in blue. (b) The dual boundary Hamiltonian H_D consists of cluster terms, as depicted by (i) and (ii). Bold lines indicate nearest neighbour relations between qubits, while dashed lines indicate edges of the ambient cubic lattice.

Sink boundary

Finally, we consider the sink boundary. This lattice boundary is again given by the ‘smooth’ boundary conditions of the previous subsection. On the boundary, qubits are placed only on boundary faces, and not boundary edges, as depicted in Fig. 3.9. On this boundary, both primal and dual 1-form symmetries are generated by complete (i.e. 6-body) operators of Fig. 3.2. The Hamiltonian terms of H_{PD} are 5-body K_e operators and 1-body or 4-body K_f operators, as depicted in Fig. 3.9. These terms all commute with the symmetry.

Lemma 6. *The sink boundary H_{PD} is both primal-condensing and dual-condensing.*

Proof. The proof is similar to the first part of Lemma 4: we observe that the boundary contains both primal and dual qubits that belong to unique 6-body symmetry generators S_q and S_v , respectively (as opposed to two). As such primal and dual excitation chains can symmetrically terminate on these qubits. \square

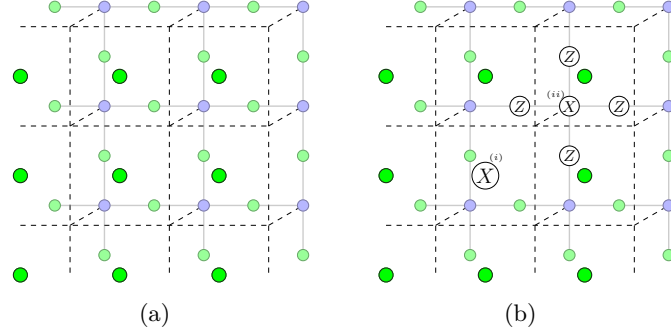


Fig. 3.9 (a) The lattice at the sink boundary. Primal qubits are depicted in green, while dual qubits are depicted in blue. (b) The dual boundary Hamiltonian H_{PD} consists of cluster terms, as depicted by (i) and (ii). The primal qubits on the boundary surface have no neighbours (meaning the corresponding cluster term is given simply by Pauli X). Bold lines indicate nearest neighbour relations between qubits, while dashed lines indicate edges of the ambient cubic lattice.

3.3.4 The cubic RBH code

We now use these various boundaries to construct a the code that is self correcting under 1-form symmetries, we call the model the cubic RBH model.

The lattice

The lattice \mathcal{L} we consider has the topology of a 3-ball. Namely, we consider cubic boundary conditions: the lattice is a cubic lattice with dimensions $d \times d \times d$, with six boundary facets, depicted in Fig. 3.10. The bulk of the model is given by the usual RBH cluster Hamiltonian, while on each of the six boundary facets we choose one of four different boundary conditions. Namely, one of the six boundary faces is chosen to support the logical information using a dressed toric code $H_{\partial\mathcal{L}}$ – which we will call the toric code boundary – and the remaining five boundary faces supports either a primal boundary, a dual boundary or a sink boundary, as depicted in Fig. 3.10.

The lattice must terminate on each of these boundary facets according to the boundary conditions outlined in the previous two subsections. In Fig. 3.10 we show a small example of the lattice when viewed from the direction of the toric code (i.e. $H_{\partial\mathcal{L}}$) boundary. Note in particular that the toric code boundary facet has planar boundary conditions due to the way it terminates on the primal and dual boundaries. Namely, the top and bottom edges of the toric code boundary facet are known as rough edges, and the left and right edges are known as smooth edges.

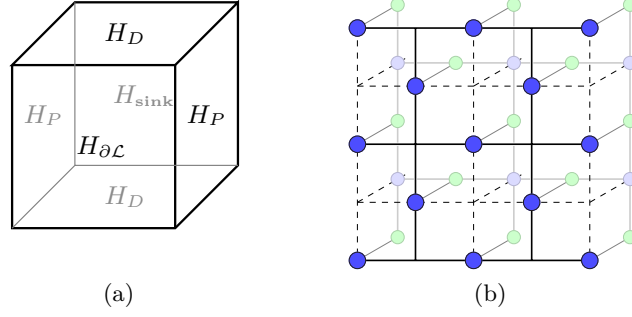


Fig. 3.10 (a) The boundaries of the cubic RBH model. $H_{\partial\mathcal{L}}$ is the toric code boundary, H_P and H_D are the primal and dual boundaries respectively, and H_{sink} is the sink boundary. (b) The lattice for the toric code boundary $H_{\partial\mathcal{L}}$. The top and bottom edges are called rough boundary conditions while the left and right edges are called smooth boundary conditions. The Hamiltonian consists of the negative sum of all star and plaquette terms \bar{A}_v, \bar{B}_f from Eq. (3.24). Dashed lines denote edges of the cubic lattice.

The Hamiltonian

The Hamiltonian decomposes into bulk and boundary components. The bulk Hamiltonian is given by the usual RBH cluster Hamiltonian $H_{\mathcal{L}^\circ}$ of Eq. (3.10). The boundary Hamiltonians come in four different types, firstly, on the toric code boundary we put the dressed toric code Hamiltonian $H_{\partial\mathcal{L}}$ of Eq. (3.28). Dressed toric code terms are truncated near the rough and smooth edges. In particular, the plaquette terms \bar{B}_f are truncated near the rough boundaries, while the star terms \bar{A}_v are truncated near the smooth boundaries. The Hamiltonians H_P, H_D , and H_{sink} on the primal, dual and sink boundaries, can all be expressed in the form H_{boundary} of Eq. (3.30). Terms in these Hamiltonians are cluster terms that are potentially truncated, depending on what boundary they reside on.

The symmetry operators are again generated by S_v and S_q of Eq. (3.18). They are 5-body or 6-body operators, depending on if they are near a particular boundary. All Hamiltonian terms are symmetric and mutually commuting.

The ground space

As discussed, the bulk Hamiltonians $H_{\mathcal{L}^\circ}$, along with the boundary Hamiltonians H_P, H_D , and H_{sink} are all non-degenerate. The overall degeneracy manifests on the toric code boundary $H_{\partial\mathcal{L}}$. In particular, for the planar boundary conditions on the toric code boundary, there is a 2-fold degeneracy. This can be easily verified by its local unitary equivalence with the planar code, which encodes one logical qubit.

Logical operators and codespace

The toric code Hamiltonian $H_{\partial\mathcal{L}}$ encodes one logical qubit, with string logical operators \bar{X} and \bar{Z} running between opposite pairs of edges of the boundary face. In particular, the logical operators are given by

$$\bar{X} = \prod_{e \in a_d} X_e \prod_{f \in a_d^\perp} Z_f, \quad \bar{Z} = \prod_{e \in b_d} Z_e, \quad (3.32)$$

where a_d is a dual-cycle on the boundary (meaning it is a cycle on the dual of the boundary lattice) that runs between the two smooth edges, b_p is a cycle on the boundary that runs between the two rough edges, and $a_d^\perp = \{f \in F^o : \partial f \cap a_d \neq \emptyset\}$. These logicals are depicted in Fig. 3.11. Note in particular, that such strings are symmetric, as the top and bottom boundary facets are dual-condensing, while the left and right are primal-condensing.

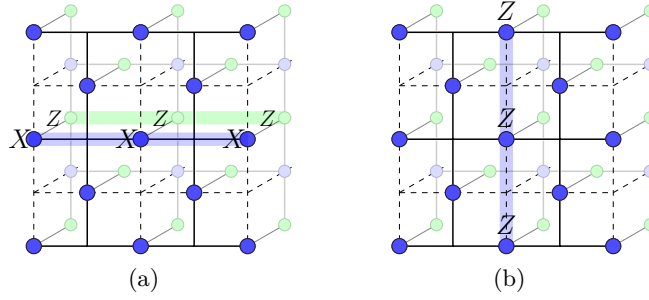


Fig. 3.11 Logical operators for the toric code boundary $H_{\partial\mathcal{L}}$. (a) Logical \bar{X} runs between the left and right smooth edges. (b) Logical \bar{Z} runs between the top and bottom rough edges. Dashed lines denote edges of the cubic lattice.

Logical operator decomposition

In this model, logical operators admit symmetric local decompositions, as we now demonstrate. The toric code Hamiltonian encodes one logical qubit, with string logical operators \bar{X} and \bar{Z} running between opposite pairs of edges of the boundary face. These logicals are given by Eq. (3.32). In order to implement either logical operators (\bar{X} or \bar{Z}) through a sequence of local moves, we will also create a large bulk excitation. (Note this is expected, as we claim the model is self-correcting, we must necessarily traverse a large energy barrier to implement a logical operator). This large bulk excitation can then be absorbed by the sink boundary in order to return to the codespace. Importantly, e -excitations (m -excitations) can be symmetrically created and destroyed at the rough edge (smooth edge) of the toric code boundary. In fact, implementing a logical \bar{Z} (\bar{X}) operator can be viewed as a process creating an e -excitation (m -excitation) from one rough (smooth) edge to the opposite rough (smooth) edge. The strategy is outlined in Fig. 3.12.

Lemma 7. *Both logical \bar{X} and \bar{Z} of the cubic RBH model admit symmetric local decompositions.*

Proof. We first consider a symmetric local decomposition of \bar{Z} . Consider a string operator $Z(c)$, $c \subset E$ supported on the dual qubits near the code boundary, as in Fig. 3.12. Grow this string operator until we achieve $Z(l + l') \equiv Z(l)Z(l')$, where $l + l'$ is a contractible loop (and therefore achievable by local symmetric moves), l is a string running between the top and bottom rough edges, and l' is a string in the bulk with the same boundaries as l . Thus $Z(l)$ is a logical \bar{Z} operator, and $Z(l')$ is an operator causing a bulk string-like excitation, anchored between the two dual boundaries. We then consider translating the bulk excitation caused by $Z(l')$ to the sink boundary, following Fig. 3.12 (which can be achieved with local symmetric moves as the two loops are homologous). This operator, and the corresponding excitations, can then be absorbed by the sink boundary as it is dual-condensing.

Logical \bar{X} operators can be decomposed in a similar way. First, consider the same process as above to produce a string operator $Z(l')$, $l \subset F$ supported on the primal qubits anchored between the opposite primal boundaries (can be achieved in the same way, as the sink boundary is primal-condensing). $Z(l')$ can be translated adjacent to the code boundary, such that $l' = a_d^\perp$ for some dual-cycle on the boundary a_d . One can then apply a sequence of Pauli- X operators along a_d , giving logical \bar{X} . \square

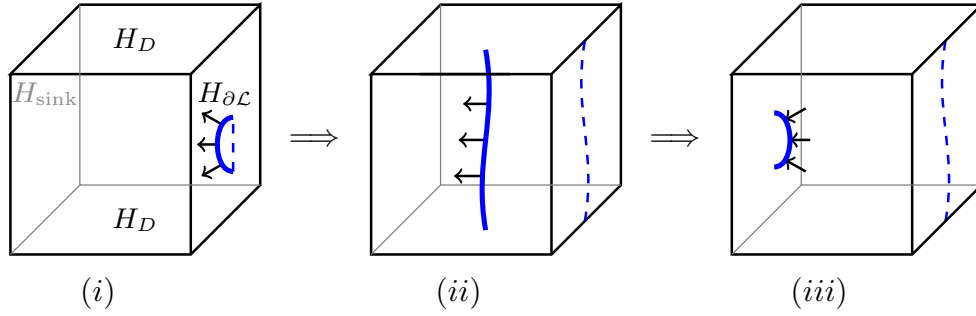


Fig. 3.12 Implementing a logical \bar{Z} operator through a sequence of local moves. (i) An error chain $Z(c)$ supported on dual qubits (the union of the solid blue and dashed blue lines) is created near the toric code boundary. This error chain creates string excitations in the bulk (solid blue), and anyonic excitations where it meets the toric code boundary. (ii) The loop is grown until it consists of a logical operator \bar{Z} (dashed blue line) along with a large bulk excitation (solid blue), anchored between the two dual boundaries. (iii) The bulk excitation is moved to the sink boundary, where it can be absorbed. The whole process results in a logical \bar{Z} . Logical \bar{X} operators can be implemented in a similar way, where an error loop on the primal lattice is grown and propagated, and an additional chain of Pauli X errors is also propagated along the toric code boundary.

The energy barrier

As we have seen, when the dynamics are restricted to the 1-form symmetric sector, bulk excitations form collections of closed loop-like objects. Secondly, boundary anyonic excitations only appear at the end of a bulk string-like excitation. This coupling of the thermal properties between bulk and boundary in the presence of symmetry, is enough to achieve a diverging symmetric energy barrier (as defined in Eq. (3.9)).

Definition 2. We define the lattice width d of the cubic RBH model as $d = \min\{d_Z, d_X, d_{\text{sink}}\}$, where d_Z is the smallest lattice distance between the two rough edges of the toric code boundary, d_X is the smallest lattice distance between the two smooth edges of the toric code boundary, and d_{sink} is the smallest lattice distance between the toric code boundary and the sink boundary.

Note that $\min\{d_Z, d_X\}$ is the usual (code) distance of the planar code on the same boundary. For any edge $e \in \partial E$ (face $f \in \partial F$) we define $d_{\text{sink}}(e)$ ($d_{\text{sink}}(f)$) as the lattice distance to the nearest dual-condensing (primal-condensing) boundary. Recall also the lattice distance $d(x, x')$ defined in Sec. 3.3.2.

Lemma 8. Let $C \subset \partial E \cup \partial F$ denote the positions of a general configuration of boundary anyons. Then the energy cost to symmetrically create this configuration is lower bounded by $(\tilde{d}_C + |C|)\Delta_{\text{gap}}$, where

$$\tilde{d}_C = \min_{P \in \hat{P}} \left\{ \sum_{\{a\}, \{b, c\} \in P} d_{\text{sink}}(a) + d(b, c) \right\} \quad (3.33)$$

where P is a partition of the elements of C into pairs $\{b, c\}$ of the same type or singletons $\{a\}$, and \hat{P} is the set of all such partitions.

Proof. This is the generalisation of Lemma 3 to the cubic RBH model. The proof follows in the same way, where we additionally note that each e (m) anyon may be connected by a bulk loop excitation to either another e (m) anyon, or to an appropriate dual-condensing (primal-condensing) boundary. As such, the smallest energy cost is obtained by finding the total length of the (shortest) perfect match for all anyons, where anyons are allowed to pair with their respective boundary. The energy cost is then obtained by scaling the length of the excitations by the gap Δ_{gap} , and adding in the contribution for each anyon. \square

Theorem 1. The symmetric energy barrier for a logical fault in the cubic RBH model is lower bounded by

$$d \cdot \frac{\Delta_{\text{gap}}}{2} - r', \quad (3.34)$$

where d is the lattice width, defined in Def. 2, and r' is constant (independent of lattice size).

Proof. Let $\{l^{(k)} \mid k = 1, \dots, N\}$ be any sequence of operators such that each $l^{(k)}$ is symmetric, $l^{(k)}$ and $l^{(k+1)}$ differ only locally, $l^{(1)} = I$ and $l^{(N)}$ is a logical operator supported on either a_d dual-cycle or the b_p cycle of Eq. (3.32). Let r be the largest range of any operator $l^{(k)}l^{(k+1)}$ for any $k \in 1, \dots, N$, which is assumed to be constant.

By locality of $l^{(k)}$, we must traverse an intermediate state that has a nonzero number of anyonic excitations on the code boundary. Moreover, since at each time step the separation between anyons can only change by a constant amount, to achieve a nontrivial logical operator, there is a time step $k' \in \{1, \dots, N\}$ with a configuration of anyons given by $C_{k'}$, such that $d_{C_{k'}} \geq \min\{\lfloor d_X/2 \rfloor, \lfloor d_Z/2 \rfloor\} - r$. Here, $d_{C_{k'}}$ is given by the (minimum length) perfect match of all anyons on ∂L , where anyons can be matched with the boundaries they can condense on. Note that $\tilde{d}_{C_{k'}} \geq \min\{d_{C_{k'}}, d_{\text{sink}}\}$, where $\tilde{d}_{C_{k'}}$ is defined in Eq. (3.33). Then by Lemma 8, we have that the energy cost of the configuration $C_{k'}$ is at least $(\tilde{d}_{C_{k'}} + |C_{k'}|)\Delta_{\text{gap}}$ which is lower bounded by $(\min\{d_{C_{k'}}, d_{\text{sink}}\} + |C_{k'}| - r)\Delta_{\text{gap}}$. Using the definition of the lattice width and letting $r' = r\Delta_{\text{gap}}$, the result follows. \square

This proof gives a conservative lower bound on the energy barrier, but it is sufficient for our purposes. In particular, as the lattice width d grows with the number of qubits, we have a macroscopic energy barrier. In other words, the energy barrier for a logical fault grows with the size of the system.

Self correction

We have shown that the 1-form symmetric cubic RBH model inherits a macroscopic energy barrier to a logical fault, due to the string-like nature of excitations resulting from the 1-form symmetry together with its coupling of bulk and boundary excitations. The question is whether this is sufficient for an unbounded memory time. In Sec. 3.9, we give an argument following the well-known Peierls argument (see also Ref. [47]) to show that this energy barrier implies self-correction of the 1-form symmetric RBH model. In brief, we estimate the probability that an excitation loop l of size w emerges within the Gibbs ensemble at inverse temperature β . We show that large loop errors are quite rare if the temperature is below a critical temperature T_c , and we give a lower bound on T_c at $2/\log(5)$. As such, if the error rate is small enough (that is, the temperature is low enough), then the logical information in the code is stable against thermal logical errors and the encoded information on the boundary will be protected for a time growing exponentially in the system size.

Along with the memory time, we have therefore met all of the requirements of a symmetry-protected, self-correcting quantum memory. In particular, we have shown that all operators

admit a symmetric, local decomposition in Lemma 7. Additionally, the ground space of this system is perturbatively stable, as it meets the TQO stability conditions of Ref. [88]. Finally, as a code, it admits an efficient decoder [47, 136]. Therefore this model meets the requirements for a self-correcting quantum memory when protected by the \mathbb{Z}_2^2 1-form symmetry.

3.3.5 Encoding in more general boundaries

One may ask what other boundary conditions can be used to construct a self-correcting code under 1-form symmetries. In this subsection we outline one other choice, along with ruling out a number of others.

In particular, note that in the previous discussion we could replace the sink Hamiltonian with another toric code Hamiltonian, as it is both primal and dual condensing. While the degeneracy of the ground space increases by another factor of two in this case, we do not get an increase in the number of qubits that we can encode. This is because the two opposite toric code boundaries must always be correlated as dictated by the symmetry: labelling the two codes as L and R , there is no local symmetric decomposition of individual logical operators \bar{Z}_L and \bar{Z}_R (\bar{X}_L and \bar{X}_R), but only of the product $\bar{Z}_L \otimes \bar{Z}_R$ ($\bar{X}_L \otimes \bar{X}_R$). This property is similar to theory of SPT phases in one dimension, where the two separate degenerate boundary modes of a 1D chain cannot be independently accessed in the presence of symmetry.

Similarly, one could remove the primal and dual boundaries, by considering the lattice \mathcal{L} with a topology of $T^2 \times I$, where T^2 is the torus and $I = [0, 1]$ is the interval. On each side, $T^2 \times \{0\}$, $T^2 \times \{1\}$ we choose toric code boundary conditions and define a toric code Hamiltonian $H_{\partial\mathcal{L}}$. With this topology, the ground space of the system is 2^4 -fold degenerate (as each boundary toric code has a degeneracy $d_g = 2^{2g}$ where g is the genus of the 2D manifold it is defined on, with $g = 1$ for the torus). For each toric code, one can define logical operators

$$\bar{X}_1 = \prod_{e \in a_d} X_e \prod_{f \in a_d^\perp} Z_f, \quad \bar{Z}_1 = \prod_{e \in b_p} Z_e, \quad (3.35)$$

and

$$\bar{X}_2 = \prod_{e \in b_d} X_e \prod_{f \in b_d^\perp} Z_f, \quad \bar{Z}_2 = \prod_{e \in a_p} Z_e, \quad (3.36)$$

for cycles a_p , b_p and dual-cycles a_d , b_d wrapping around the two nontrivial cycles of the torus labelled by a and b . Similarly, we can only make use of one of the toric codes, as the two copies are correlated under the 1-form symmetry. In other words, we do not have a symmetric decomposition of all logical operators, only a subgroup of them.

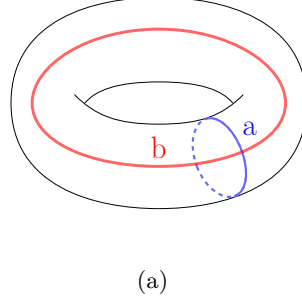


Fig. 3.13 The solid torus. The boundary of the solid torus is a torus, where two nontrivial cycles a and b are depicted. One might expect to be able to encode two logical qubits in the system, however any operator supported on the b loop does not admit a symmetric local decomposition.

Topological obstruction to logical decompositions

The issue of finding choices of boundary conditions that allow for symmetric local decompositions of logical operators is nontrivial. For example, on a solid torus $D^2 \times S^1$, with D^2 a disk and S^1 a circle (depicted in Fig. 3.13), we cannot encode any logical qubits. Although the boundary of the solid torus is a torus, there does not exist symmetric local decompositions of logical operators supported on the b cycle of Fig. 3.13). For example, logical operators \bar{Z} supported on the b cycle (in Fig. 3.13) cannot be created by a sequence of local, symmetric operators, because any such sequence results in a homologically trivial (contractible) cycle. This phenomenon will always occur for codes that live on the boundary of a 3-manifold due to the following fact: for any 2-manifold, precisely half of the noncontractible cycles (if they exist) become contractible when the manifold is realised as the boundary of a 3-manifold [228]. This justifies our consideration of the more involved boundary conditions of the previous subsection.

3.3.6 Bulk boundary correspondence at nonzero temperature

As shown above, the 1-form symmetries constrain the form of the excitations in the model and give rise to an energy barrier, and self-correction. These 1-form symmetries are a very strong constraint, and one may ask if a code is trivially guaranteed to be self-correcting whenever such symmetries are enforced. (As an example of a strong symmetry leading trivially to self-correction, consider the toric code where the symmetry of the full stabilizer group is strictly enforced.)

In this section we show that the 1-form symmetry, although strong, is itself not sufficient to lead to self-correction unless the bulk is SPT ordered (such as in the previous models). Specifically, we show that self-correction under 1-form symmetries depends on the bulk SPT order of the model, establishing a bulk-boundary correspondence for SPTs at nonzero temperature. Recall, at zero temperature, the correspondence is that a system with nontrivial SPT order in the bulk must have a protected boundary theory – meaning it is gapless or topologically ordered

– whenever the symmetry is not broken [108, 110]. Here we show that the bulk boundary correspondence holds at nonzero temperature in the RBH model; that the stability of the boundary toric code phase (i.e., whether or not we have a SCQM) depends on the bulk SPT order at nonzero temperature.

In order to make this connection, we recall a formulation of phase equivalence due to Chen *et al.* [92]. Namely, two systems belong to the same phase if they can be related by a local unitary transformation (a constant depth quantum circuit), up to the addition or removal of ancillas. Importantly, with symmetries $S(g)$ present, the local unitary transformations must commute with the symmetry and the ancillas that are added or removed must be in a symmetric state.

We now remark on the earlier claim on the necessity of the SPT nontriviality of the bulk to achieve self-correction. To do so, we first note that the symmetric energy barrier is invariant under symmetric local unitaries (that is, it is a phase invariant). Indeed consider two Hamiltonians H_A and H_B (defining quantum memories) in the same phase. Then in particular, we have $H_A + H_{\mathcal{A}}$ and H_B are related by a symmetric local unitary U , where let $H_{\mathcal{A}}$ consists of a sum of local projections on the ancillas \mathcal{A} into a symmetric state. Since H_A and $H_A + H_{\mathcal{A}}$ differ only by a sum of non-interacting terms on the ancilla, they have the same energy barrier. Let \bar{X} be a logical operator for H_A , and consider a local decomposition $\{l_X^{(k)} \mid k = 1, \dots, N\}$ of \bar{X} (recall $l_X^{(1)} = I$ and $l_X^{(N)} = \bar{X}$, and $l_X^{(k)}$ and $l_X^{(k+1)}$ differ only by a local operator). This is also a logical decomposition for $H_A + H_{\mathcal{A}}$. Then $\{Ul_X^{(k)}U^\dagger \mid k = 1, \dots, N\}$ constitutes a local decomposition for a logical operator of H_B , with the same energy barrier. This works for all choices of logical operators \bar{X} and the models have the same symmetric energy barrier.

The invariance of the energy barrier requires us to consider a SPT-nontrivial bulk to achieve self-correction in the presence of 1-form symmetries. Indeed, if we instead considered the SPT-trivial model $H_{\mathcal{L}^o}^{(0)}$ of Eq. (3.12) with undressed toric code terms of Eq. 3.25 on the boundary in the presence of 1-form symmetries, we see that there is no energy barrier, in the following way. Consider the logical \bar{X} operator, which is given by a product of Pauli X operators supported on a dual cycle on $\partial\mathcal{L}$ (it is not dressed, unlike the logical \bar{X} of the RBH model H). Then the symmetric energy barrier for this error is a constant $2\Delta_{\text{gap}}$, since the process of creating two m particles and wrapping them around a boundary cycle is symmetric, and only flips two B_f plaquettes at any given time. Therefore the trivial model is not self-correcting, even in the presence of 1-form symmetries. In particular, this also gives a simple argument for why H belongs to a distinct SPT phase to $H_{\mathcal{L}^o}^{(0)}$. Indeed, the SPT ordering in the bulk is crucial to achieving the bulk-boundary anyon coupling of Lemma 2, that leads to a confinement of anyons as in Lemma 3.

This bulk boundary correspondence (at nonzero temperature) holds for systems with onsite symmetries too; we have argued in Sec. 3.2.3 that self-correction was not possible on the 2D

boundary of a 3D SPT protected by onsite symmetry. This coincides with the lack of bulk SPT order at $T > 0$ when the protecting symmetry is onsite, as shown in Ref. [216].

Anomalies

Finally, we return to the connection between higher-form anomalies and stability of the boundary theory. Recall that anomalies arise when considering a system with a boundary and analysing the action of the symmetry on boundary degrees of freedom. Let us first clarify what we mean by a higher-form anomaly, by examining the 1-form case in 3-dimensions. Consider the bulk RBH Hamiltonian of Eq. (3.16), with the boundary conditions described in Sec. 3.3.2, which is symmetric under 1-form symmetries $S_q, S_v, q \in Q, v \in V$.

Recall the effective Pauli- X and Pauli- Z operators for these boundary degrees of freedom are given by \tilde{X}_e and \tilde{Z}_e in Eq. (3.21). As we have seen, the action of the 1-form symmetry on these boundary degrees of freedom induces a 1-form symmetry on the boundary degrees of freedom. However, this boundary 1-form symmetry cannot be strictly realised on the boundary $E \setminus E^\circ$. Indeed, from the commutation relations with 1-form symmetries, we have $S_v \equiv \bar{A}_v, S_q \equiv \bar{B}_{f(q)}$ as in Eq. (3.26). But \bar{A}_v and $\bar{B}_{f(q)}$ are not contained within $E \setminus E^\circ$.

In fact, there is no way to reduce the boundary action of Eq. (3.26) into a form that is contained entirely within the boundary, meaning that the boundary action is anomalous. Without the 1-form anomaly, there are no terms coupling the bulk and boundary, and one can choose the boundary theory to be a completely decoupled 2D theory, as in the example of $H_{\mathcal{L}^\circ}^{(0)}$. In such a theory, one can find a logical operator that has a symmetric local decomposition with constant energy cost, meaning the anomaly is necessary to have a self-correcting boundary. Such anomalies should only occur when we have a SPT ordered bulk.

3.4 The gauge color code protected by 1-form symmetry

We now turn to a model based on the gauge color code in 3 dimensions as our second example of a symmetry-protected self-correcting quantum memory. The gauge color code [75] is an example of a topological subsystem code. In this section we study a commuting Hamiltonian model with a 1-form symmetry based on the gauge color code. This model provides another example of a self-correcting quantum memory protected by a 1-form symmetry. We first give a brief overview of the gauge color code before defining the Hamiltonian model we are interested.

Subsystem codes

In addition to logical degrees of freedom, subsystem codes contain redundant ‘gauge’ degrees of freedom in the codespace that are not used to encode information. Whereas stabilizer codes are specified by a stabilizer group \mathcal{S} that is an abelian subgroup of the Pauli group, a subsystem code is specified by a (not necessarily abelian) subgroup \mathcal{G} of the Pauli group, known as the gauge group. A stabilizer group \mathcal{S} for the subsystem code can be defined by choosing any maximal subgroup of the center $\mathcal{Z}(\mathcal{G})$ of the gauge group, such that $-\mathbf{1} \notin \mathcal{S}$. In other words, $\mathcal{S} \propto \mathcal{Z}(\mathcal{G})$ (in general there are many choices for \mathcal{S} obtained by selecting different signs for generating elements). As usual, the codespace $C_{\mathcal{S}}$ is defined as the mutual $+1$ eigenspace of all elements of \mathcal{S} .

Information is only encoded into the subsystem of $C_{\mathcal{S}}$ that is invariant under all gauge operators $g \in \mathcal{G}$. More precisely, we have $C_{\mathcal{S}} = \mathcal{H}_l \otimes \mathcal{H}_g$, where \mathcal{H}_l is the state space of logical degrees of freedom (elements of \mathcal{G} act trivially on this space), and \mathcal{H}_g is that state space of the gauge degrees of freedom (elements of \mathcal{G} can act nontrivially on this space). There are two types of Pauli logical operators: bare and dressed. Bare logical operators are elements of $C(\mathcal{G})$; the centraliser of the gauge group within the Pauli group, meaning they are Pauli operators that commute with all gauge operators. Dressed logicals are elements of $C(\mathcal{S})$; the centraliser of the stabilizer group within the Pauli group (meaning they are Pauli operators that commute with all stabilizer operators). Bare logicals act exclusively on logical degrees of freedom and act trivially on the gauge degrees of freedom, while dressed logicals can act nontrivially on gauge degrees of freedom, too. Both types of logicals are identified up to stabilizers (as stabilizers act trivially on the codespace).

3.4.1 The gauge color code lattice

Gauge color codes are defined on lattices known as 3-colexes [55]. In particular, a 3-colex is the result of gluing together 3-cells (polyhedra) such that each vertex is 4-valent (meaning each vertex belongs to 4 edges) and 4-colorable (meaning each polyhedral 3-cell can be given one of four colors such that neighbouring 3-cells are differently colored). Let these four colors be labelled \mathbf{r} , \mathbf{b} , \mathbf{g} , and \mathbf{y} (for red, blue, green, and yellow).

We note that, similar to the RBH model, the gauge color code must have boundaries in order to possess a nontrivial codespace. For concreteness, we consider the tetrahedral boundary conditions of Ref. [76], but one could also consider more general boundary conditions. In the following, we label the Tetrahedral 3-colex by \mathcal{C}_3 , which is a set of vertices, edges, faces and 3-cells. Tetrahedral 3-colexes \mathcal{C}_3 are given by cellulations of the 3-ball, whose boundary consists of four facets, each of which must satisfy a certain coloring requirement. To describe this requirement, we first note that each non-boundary edge can be given a single color label, where

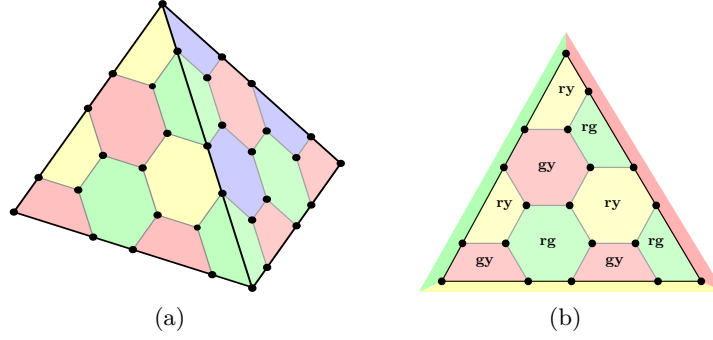


Fig. 3.14 (a) The tetrahedral 3-colex. (b) The \mathbf{b} boundary of the tetrahedral lattice consists of faces that are colored \mathbf{uv} with $\mathbf{u}, \mathbf{v} \neq \mathbf{b}$, which are then relabelled according to $\mathbf{gy} \leftrightarrow \mathbf{A}$, $\mathbf{ry} \leftrightarrow \mathbf{B}$, and $\mathbf{rg} \leftrightarrow \mathbf{C}$.

the color is determined by that of the two 3-cells that it connects. If an edge terminates on a boundary (meaning precisely one of its vertices belongs to the boundary) then its color is determined by unique bulk 3-cell on its other endpoint. Then the boundary coloring requirement is as follows: for each boundary facet, only edges of one color can terminate on the boundary and this color is unique for each facet. We therefore color each boundary facet by the color of the edges that terminate on it.

Similarly, each face f in \mathcal{C}_3 can be labelled by pairs of colors $\mathbf{uv} \equiv \mathbf{vu}$, inherited from the two neighbouring 3-cells that it belongs to. Namely, each non-boundary face is colored by the complement of the two colors on the 3-cells the face is incident to (e.g., a face belonging to a \mathbf{r} and \mathbf{b} 3-cell is colored \mathbf{gy}). Faces on the boundary are colored by the opposite of the color of the boundary and the color of the unique 3-cell they belong to. As such, the boundary of color \mathbf{k} consists of plaquettes of all colors \mathbf{uv} such that $\mathbf{u}, \mathbf{v} \neq \mathbf{k}$. We arbitrarily choose one of the boundary facets, the \mathbf{b} facet, and call this the outer colex \mathcal{C}_{out} , which consists of the vertices, edges and plaquettes strictly contained on the boundary. This outer colex is therefore a 2-colex (a trivalent and 3-colorable two-dimensional lattice), and can be used to define a 2-dimensional color code. The remainder of the lattice $\mathcal{C}_3 \setminus \mathcal{C}_{\text{out}}$ is called the inner colex.

On the outer colex, each plaquette has one of three possible color pairs $\{\mathbf{gy}, \mathbf{ry}, \mathbf{rg}\}$, which we relabel for simplicity according to $\mathbf{gy} \leftrightarrow \mathbf{A}$, $\mathbf{ry} \leftrightarrow \mathbf{B}$, $\mathbf{rg} \leftrightarrow \mathbf{C}$ as in Fig. 3.14. Each edge of the outer colex neighbours two plaquettes of distinct colors, we color each edge the third remaining color. Moreover, each of the three boundaries of the outer colex can be given a single color according to what color edges can terminate on them, as depicted in Fig. 3.14.

3.4.2 The 3D gauge color code

To each vertex of the lattice \mathcal{C}_3 we place a qubit. The gauge color code is specified by the gauge group \mathcal{G} , which is a subgroup of the Pauli group on n qubits (where n is the number of vertices).

The stabilizer group \mathcal{S} is in the center of the gauge group, consisting of elements of the gauge group that commute with every other element and where the signs are chosen such that $-1 \notin \mathcal{S}$. For the gauge color code, we have an X and Z gauge generator for each face of the lattice,

$$\mathcal{G} = \{G_f^X, G_f^Z \mid f \text{ a face of } \mathcal{C}_3\}, \quad (3.37)$$

where $G_f^X = \prod_{v \in f} X_v$ and $G_f^Z = \prod_{v \in f} Z_v$ are Pauli operators supported on the face f . The stabilizers of the code are given by X and Z on the 3-cells of the lattice

$$\mathcal{S} = \{S_q^X, S_q^Z \mid q \text{ a 3-cell of } \mathcal{C}_3\}, \quad (3.38)$$

where $S_q^X = \prod_{v \in q} X_v$ and $S_q^Z = \prod_{v \in q} Z_v$ are Pauli operators supported on 3-cells. Codestates of the gauge color code are the states that are in the +1 eigenspace of all elements of the stabilizer group. With the aforementioned boundary conditions, the code encodes one logical qubit, and bare logical operators can be taken to be $\bar{X} = \prod_{v \in \mathcal{C}_3} X_v$ and $\bar{Z} = \prod_{v \in \mathcal{C}_3} Z_v$, where the products are over all vertices of the lattice. Importantly, note that equivalent logical operators (i.e., up to products of stabilizers) can be found on the outer colex, namely $\bar{X} \sim \prod_{v \in \mathcal{C}_{\text{out}}} X_v$ and $\bar{Z} \sim \prod_{v \in \mathcal{C}_{\text{out}}} Z_v$ are valid representatives. One can find dressed versions of these logicals on the outer colex that are stringlike – we will discuss this in the following subsection. Similarly to the RBH model, we are therefore justified in viewing the logical information as being encoded on the boundary.

There are many different Hamiltonians whose ground space contains a representation of the logical degrees of freedom of the gauge color code (here representation means that one can find dressed logicals of the gauge color code that are logical operators for the ground space of a given model). One possible choice of Hamiltonian that represents the GCC logical degrees of freedom in its ground space is given by the sum of all local gauge terms,

$$H_{\mathcal{G}} = - \sum_f G_f^X - \sum_f G_f^Z, \quad (3.39)$$

which we refer to as the *full GCC Hamiltonian*. This Hamiltonian is frustrated, meaning one cannot exactly satisfy all of the constraints G_f^X and G_f^Z simultaneously, making it difficult to study. There are many different Hamiltonians whose ground spaces contain the codespace of the gauge color code, and in the next subsection we introduce a solvable model, consisting of mutually commuting terms.

3.4.3 A commuting model

Here we define an exactly solvable model for the gauge color code. The Hamiltonian is given by a sum of gauge terms that belong to 3-cells of a single color. Without loss of generality, fix

this color to be **b** (blue), and take all faces X_f and Z_f belonging to the blue 3-cells or blue boundary facet. That is, all faces f that have color \mathbf{uv} with $\mathbf{u}, \mathbf{v} \neq \mathbf{b}$. Label the set of these faces by

$$\mathcal{G}_{\mathbf{b}} = \{G_f^X, G_f^Z \mid \mathcal{K}(f) \in \{\mathbf{gr}, \mathbf{gy}, \mathbf{ry}\}\}, \quad (3.40)$$

where $\mathcal{K}(f)$ denotes the color of f . Note that $\mathcal{G}_{\mathbf{b}}$ consists of commuting terms, as all terms are supported on either a bulk 3-cell or the **b** boundary (which are both 3-colorable and 3-valent sublattices). Or equivalently, if two faces share a common color then the terms commute. We can define an exactly solvable Hamiltonian by

$$H_{\mathcal{G}_{\mathbf{b}}} = - \sum_{G \in \mathcal{G}_{\mathbf{b}}} G. \quad (3.41)$$

This Hamiltonian decomposes into a number of decoupled 2D color codes, one on the **b** boundary, and one for each bulk 3-cell of color **b**. Additionally, every qubit is in the support of at least one $G \in \mathcal{G}_{\mathbf{b}}$.

With the above choice of boundary conditions, the outer colex (the **b** boundary) encodes one logical qubit, while the bulk 2D color codes are non-degenerate (as they are each supported on closed 2-cells). The ground space of the model is the joint +1 eigenspace of all terms $G \in \mathcal{G}_{\mathbf{b}}$, and the ground space degeneracy is two-fold. This choice of Hamiltonian explicitly represents the gauge color code codespace on the outer colex. This situation is reminiscent of the RBH model, where quantum information is encoded on the boundary of the 3D bulk. We remark that the ground state of $H_{\mathcal{G}_{\mathbf{b}}}$ can be thought of as a gauge fixed version of the gauge color code \mathcal{G} .

Logical operators can be chosen to be string-like operators supported entirely on the outer colex (the **b** boundary facet). Recall that edges and plaquettes on the outer colex has one of three possible colors, **A**, **B**, or **C**, as defined in Fig. 3.14, and the boundaries are given a single color according to what color edges can terminate on them, as depicted in Fig. 3.15. The logical operators take the form of strings that connect all three boundaries of the triangular facet as in Fig. 3.15. Logical Pauli operators are supported on at least d qubits, where d is the smallest side length of the boundary facet and referred to as the distance of the code.

On the outer colex, a string operator with color $\mathbf{k} \in \{\mathbf{A}, \mathbf{B}, \mathbf{C}\}$ will flip the two **k** coloured plaquettes on the boundary of the string. In particular, a **k**-colored X -string will create $m_{\mathbf{k}}$ excitations on its boundary (corresponding to the flipped G_f^Z plaquettes). Similarly, a **k**-colored Z -string will create $e_{\mathbf{k}}$ excitations on its boundary (corresponding to the flipped G_f^X plaquettes). These are depicted in Fig. 3.15. On a **k** colored boundary, both $e_{\mathbf{k}}$ and $m_{\mathbf{k}}$ particles can condense, meaning they can be locally created or destroyed at the boundary as in Fig. 3.15.

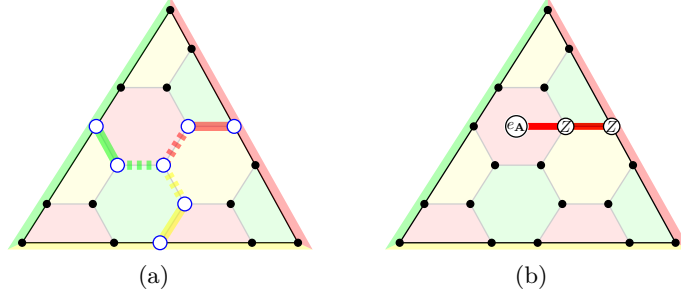


Fig. 3.15 (a) A logical string consists of three colored strings extending from their respective boundary and meeting at a point. The support of the logical X or Z is indicated by the larger white nodes. (b) $e_{\mathbf{A}}$ excitations appear at the ends of a \mathbf{A} -colored Z -string. Both $e_{\mathbf{A}}$ and $m_{\mathbf{A}}$ excitations can condense on the \mathbf{A} -colored boundary (and analogously for other boundaries).

As such, the action of logical \bar{X} (\bar{Z}) can then be interpreted as creating three m -type (e -type) quasiparticles of each color from the vacuum at a point, then moving each colored excitation to its like-colored boundary where it is destroyed.

Relation to the RBH model

To motivate how the model $H_{\mathcal{G}_b}$ was constructed, we draw a comparison to the RBH model of the previous section. In particular, the RBH also has the structure of a subsystem code, that on a certain lattice is dual to the gauge color code. For the RBH model, one can consider the gauge group \mathcal{G}_C is given by

$$\mathcal{G}_C = \langle K_p, X_p \mid p \in E \cup F \rangle, \quad (3.42)$$

where K_p are the cluster state stabilizers of Eq. (3.11) and X_p are single qubit Pauli X operators. The corresponding stabilizer group \mathcal{S}_C is given by

$$\mathcal{S}_C = \langle S_p \mid p \in Q \cup V \rangle, \quad (3.43)$$

where S_p are the 1-form symmetry generators of the RBH model, given by Eq. (3.18). (The choice of gauge generators X_p stems from the application of the RBH model to fault-tolerant measurement-based quantum computing, where X -measurements are used to propagate information.)

The commuting model describing the RBH model was chosen by selecting a subset \mathcal{G}' of local, commuting elements of \mathcal{G}_C to define the Hamiltonian, and imposing symmetries given by the stabilizer \mathcal{S}_C . This choice is non-unique, as there are many other subsets \mathcal{G}' of \mathcal{G} that could be used to construct a commuting model. Additionally, to avoid spontaneous symmetry breaking we choose \mathcal{G}' such that the stabilizer is a subgroup of the group generated by \mathcal{G}' , that

is, $\mathcal{S}_C \leq \langle \mathcal{G}' \rangle$. The same construction was also used to generate the commuting GCC model, and can be used more generally for subsystem codes with a stabilizer group that has the structure of a \mathbb{Z}_2^k 1-form symmetry for some k . We note however there are many distinct ways generating such Hamiltonians, and not all of them will be self-correcting under the 1-form symmetry.

3.4.4 1-form symmetry and color flux conservation

The commuting model $H_{\mathcal{G}_b}$ without any symmetry constraints is easily shown to be disordered at any non-zero temperature. (It is a collection of uncoupled 2D color codes.) In this section, we identify a 1-form symmetry of this model that, when enforced, leads to a diverging energy barrier and therefore self-correction on the boundary code.

The Hamiltonian $H_{\mathcal{G}_b}$ has a \mathbb{Z}_2^2 1-form symmetry given by the stabilizer group \mathcal{S} of Eq. (3.38). Recall that \mathcal{S} is generated by the stabilizers S_q^X and S_q^Z on the 3-cells q of the lattice, and consists of operators supported on closed codimension-1 (contractible) surfaces. The two copies of \mathbb{Z}_2 1-form symmetry come from the independent X -type and Z -type operators. The symmetry \mathcal{S} give strong constraints (conservation laws) on the possible excitations in the model: this is the color flux conservation of Bombin [75]. To discuss the color flux conservation that arises from the \mathbb{Z}_2^2 1-form symmetry, let us assume that the system $H_{\mathcal{G}_b}$ is coupled to a thermal bath (as in Eq. (3.1)) such that the whole system respects the symmetry \mathcal{S} , and discuss what type of excitations are possible in the model.

The model $H_{\mathcal{G}_b}$ is a stabilizer Hamiltonian, and so excitations are labelled in the standard way. Specifically, excited states can be labelled by the set of ‘flipped terms’ $\mathcal{G}_{\text{ex}} \subseteq \mathcal{G}_b$. Not all sets \mathcal{G}_{ex} can be reached from the ground space in the presence of the symmetry \mathcal{S} . Since the ground space of $H_{\mathcal{G}_b}$ consists of the states in the +1 eigenspace of all terms in \mathcal{G}_b , it follows that the ground space is also the +1 eigenspace of all operators in \mathcal{S} , and since they are conserved, only the excited states that satisfy color flux conservation on each cell (as we will describe) can be reached.

In particular, note that for any 3-cell q of color $\mathbf{k} \neq \mathbf{b}$, there is precisely one way of obtaining the stabilizers S_q^X and S_q^Z from terms in \mathcal{G}_b , while for a 3-cell of color \mathbf{b} there are three ways of obtaining the stabilizers. More precisely, for the X -type stabilizers we have

$$S_q^X = \prod_{\substack{f \subset q \\ \mathcal{K}(f) = \mathbf{ub}}} G_f^X, \quad (3.44)$$

where

$$\mathbf{uv} \in \begin{cases} \{\mathbf{gy}\} & \text{if } \mathcal{K}(q) = \mathbf{r} \\ \{\mathbf{ry}\} & \text{if } \mathcal{K}(q) = \mathbf{g} \\ \{\mathbf{rg}\} & \text{if } \mathcal{K}(q) = \mathbf{y} \\ \{\mathbf{gy}, \mathbf{ry}, \mathbf{rg}\} & \text{if } \mathcal{K}(q) = \mathbf{b}. \end{cases} \quad (3.45)$$

The above expression holds similarly for the stabilizer S_q^Z . This can be seen as any plaquette that neighbours a 3-cell of color \mathbf{k} must be of color \mathbf{uv} with $\mathbf{u}, \mathbf{v} \neq \mathbf{k}$, for which there is only one choice within $\mathcal{G}_{\mathbf{b}}$ for $\mathbf{k} \neq \mathbf{b}$, and three choices when $\mathbf{k} = \mathbf{b}$. Note that the multiple ways of forming S_q^X and S_q^Z on blue 3-cells as per Eq. (3.45) leads to local product constraints on these blue 3-cells (further constraining the excitations) however this is not important for the present discussion.

To ensure that an excitation \mathcal{G}_{ex} is valid, we must remain in the +1-eigenspace of \mathcal{S} . From Eq. (3.44) we see that every 3-cell q must have an even number of flipped plaquettes belonging to its boundary. Indeed, a single flipped plaquette G_f^X of color \mathbf{uv} would violate the two stabilizer operators S_q^X and $S_{q'}^X$ on the neighbouring \mathbf{u} and \mathbf{v} colored 3-cells q and q' . This constraint implies that symmetric excitation configurations consist of collections of closed loop-like sets of flipped plaquettes.

This can be more easily visualised on the dual lattice, where where 3-cells are replaced by vertices, faces by edges, edges by faces, and vertices by 3-cells. On the dual lattice, vertices carry a single color, edges are labelled by pairs of colors, and excitations are therefore given by sets of edges. We call the edges on the dual lattice that define an excitation a flux string. The color flux conservation on these closed flux strings is as follows.

To satisfy the constraints of Eqs. (3.44), and (3.45), for each vertex v of color $\mathbf{k} \in \{\mathbf{b}, \mathbf{r}, \mathbf{g}, \mathbf{y}\}$ the number of edges in a flux string incident to v must be even. Since the vertices of color $\mathbf{k} \in \{\mathbf{r}, \mathbf{g}, \mathbf{y}\}$ only support terms in $\mathcal{G}_{\mathbf{b}}$ on neighbouring edges of a single color type (e.g. a \mathbf{r} vertex only supports terms on its neighbouring \mathbf{gy} -colored edges), then the color of the excitation is conserved at each one of these vertices. Similarly on a \mathbf{b} vertex, all pairs of colors are separately conserved. This means if a \mathbf{uv} colored edge excitation enters a vertex, there must be a \mathbf{uv} colored edge excitation leaving the vertex. In summary, bulk excitations must form closed loops, where the color is conserved at every vertex, and this is illustrated in Fig. 3.16.

Flux loops may terminate on the outer colex. Recall that for a boundary facet of color \mathbf{k} , there are no faces of color \mathbf{uk} for any \mathbf{u} . In particular, for $\mathbf{k} \neq \mathbf{b}$, there is a unique color \mathbf{u} such that there are terms G_f^X and G_f^Z of color \mathbf{uk} in $\mathcal{G}_{\mathbf{b}}$. Flux loops of color \mathbf{uk} can terminate on this \mathbf{k} -colored boundary facet. For the \mathbf{b} colored boundary facet (the outer colex), all three color pairs of flux loops can terminate on the outer colex. Flux loops terminating on the \mathbf{b} -facet

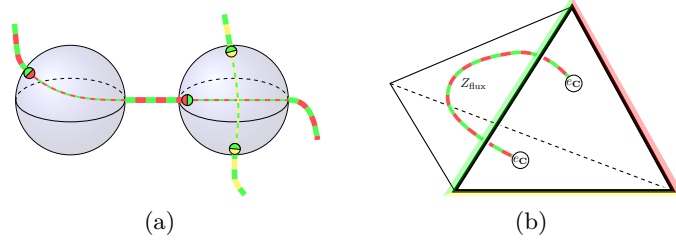


Fig. 3.16 (a) An example of a flux loop, where the corresponding colored strings on the dual lattice are depicted, the shaded blue spheres represent \mathbf{b} colored 3-cells. (The constraint from Eq. (3.44) requires an even number of flipped \mathbf{rg} plaquettes on a \mathbf{y} colored 3-cell). (b) A \mathbf{rg} colored flux loop of flipped G_f^Z terms (coming from a string of X operators) terminating with a pair of e_C anyons on the outer colex.

can be viewed as ending in a $e_{\mathbf{k}}$ or $m_{\mathbf{k}}$ anyonic excitation on the boundary for $\mathbf{k} \in \{\mathbf{A}, \mathbf{B}, \mathbf{C}\}$ as in Fig. 3.16 (recall the colors are relabelled on the outer colex according to $\mathbf{gy} \leftrightarrow \mathbf{A}$, $\mathbf{ry} \leftrightarrow \mathbf{B}$, $\mathbf{rg} \leftrightarrow \mathbf{C}$). Moreover, in the same way, the only way anyons can exist on the outer colex is at the ends of a flux loop on the bulk, as stand-alone boundary anyonic excitations violate the symmetry.

3.4.5 Energy barrier

We are now equipped to calculate the symmetric energy barrier for $H_{\mathcal{G}_b}$ in the presence of the symmetry \mathcal{S} . Recall that a logical error occurs when a triple of excitations $\alpha_{\mathbf{A}}, \alpha_{\mathbf{B}}, \alpha_{\mathbf{C}}$, where $\alpha = e$ or m , are created at a point, and each anyon travels to its like-colored boundary. Put another way, a logical error occurs if an anyonic excitations $\alpha_{\mathbf{k}}$ is created at each boundary, and the three anyons move and fuse back to the vacuum in the bulk of the outer colex. In any case, the only way to achieve a logical Pauli error is to create a number of anyonic excitations, which must move a combined distance of at least d , the side length of the outer colex. In the symmetric sector, anyonic excitations can only exist on the boundary if they are accompanied by a bulk flux loop, and so the above creation, movement and fusion process can only occur when accompanied by bulk flux loops.

Since boundary excitations $\alpha_{\mathbf{k}}$ with $\alpha \in \{e, m\}$ and $\mathbf{k} \in \{\mathbf{A}, \mathbf{B}, \mathbf{C}\}$ appear on the end of flux loops (each of which can only terminate on its like-colored boundary) to calculate the energy barrier we need only track the smallest length flux loops required to move the boundary anyons to create a logical error. From any point v on the outer colex, let $l_{\mathbf{A}}(v)$, $l_{\mathbf{B}}(v)$, $l_{\mathbf{C}}(v)$ be the shortest flux loops from a face f on the outer colex containing v , to a face on the \mathbf{A} , \mathbf{B} , and \mathbf{C} facets, respectively (these flux loops are dual to a closed path on the dual lattice). Let $|l_{\mathbf{A}}(v)|$, $|l_{\mathbf{B}}(v)|$, $|l_{\mathbf{C}}(v)|$ be the lengths of these flux loops (i.e., the number of edges on the dual

path) and define

$$d_{\perp} := \min_{v \in \mathcal{C}_{\text{out}}} (|l_{\mathbf{A}}(v)| + |l_{\mathbf{B}}(v)| + |l_{\mathbf{C}}(v)|) \quad (3.46)$$

to be the shortest combined distance from any point on the outer colex to all three other facets. Note that d_{\perp} grows as all side lengths of the tetrahedral 3-colex are increased.

Then during any anyon creation, movement and annihilation process resulting in a logical error, the bulk flux loops which accompany the boundary anyons must have a combined length of at least d_{\perp} . This will incur an energy penalty of $\Delta_E = 2d_{\perp}$ since each flux loop consists of a path of flipped terms $G_f^{\alpha} \in \mathcal{G}_{\mathbf{b}}$. As such the energy is proportional to d_{\perp} which scales linearly with the minimum side length of the tetrahedral 3-colex. In particular, the model H' with symmetry \mathcal{S} has a macroscopic energy barrier, and the boundary information is protected in the presence of a 3D bulk and symmetry constraint.

We make two remarks. First, the energy barrier and conservation laws in this section were presented in terms of excitations rather than error operators (as opposed to the operator approach for the RBH model). For the purposes of calculating the energy barrier these two pictures are equivalent, since the sequence of local (symmetric) excitations corresponds to a sequence of local (symmetric) operators, and vice-versa. Second, we remark that a tri-string logical operator of the above form can be pushed onto a single boundary of the outer colex, giving rise to a string-like representative. As such, a logical error can arise from a pair of anyons of the same color being created and moved along the boundary of the outer colex. Such a process also has an energy lower bounded by $\Delta_E = 2d_{\perp}$ since a \mathbf{k} -colored string on the boundary of the outer colex is never adjacent to a boundary where its \mathbf{k} -flux loops can terminate.

The argument from the symmetric energy barrier to self-correction follows identically to that of the RBH model. That is, provided the temperature is sufficiently low, information can be stored for a time that grows exponentially with the system size. (Note that the critical temperature will depend on the specific choice of 3-colex.) As a result, our stabilizer model based on the 3D gauge color code protected by \mathbb{Z}_2^2 1-form symmetry provides another example of a self-correcting quantum memory.

In the RBH model, the fact that the boundary was self-correcting in the presence of 1-form symmetries could be interpreted as directly resulting from the thermally stable bulk SPT order. In this stabilizer model of the gauge color code, the boundary stability and bulk SPT (at nonzero temperature) are also related [229].

3.5 Emergent 1-form symmetries

As we have shown, SET models protected by a 1-form symmetry can be self-correcting. However, enforcing such 1-form symmetries is a very strong constraint, and in addition these symmetries are unusual in physics compared with the more prevalent onsite (0-form) symmetries. Here we explore the idea that 1-form symmetries may actually appear naturally in 3D topological models, and not require any sort of external enforcement. We refer to such a symmetry as *emergent*. It sounds too good to be true, but note that emergent symmetries in 2D topological models are ubiquitous (while perhaps poorly understood). In this section, we review emergent (0-form) symmetries in 2D topological models, as first highlighted by Kitaev [193]; here we will focus on the 2D color code. We then show that 3D models may possess emergent 1-form symmetries associated with such emergent 0-form symmetries on closed 2D submanifolds of the 3D model. We revisit the 3D gauge color code in light of these observations. Finally, we demonstrate the stability of emergent 1-form symmetries in topologically ordered models, and discuss the implications for self-correction.

3.5.1 Emergent 0-form symmetries in 2D

Kitaev observed the emergence of symmetry in 2D topological models such as the toric code and referred to this as a ‘miracle’ [193]. As we now know, emergent symmetries are a generic property of 2D topologically ordered models. We begin this section by reviewing an instructive first example: the 2D color code. We demonstrate the emergence of a \mathbb{Z}_2^4 0-form symmetry in this 2D code, and how this gives rise to the well known anyonic color conservation (see for example Ref. [119]). Although we will focus on how global product constraints are helpful to expose global conservation laws, we emphasise that the more important physical property is the local conservation law (associated with a 0-form symmetry) that arises in relation to the modular Gauss law.

We first consider a 2D color code defined on the surface of a sphere (one can equivalently consider any closed surface for the discussion that follows). Recall, a 2D color code is defined on a lattice known as a 2-colex, which is a 3-colorable, 3-valent cellulation Λ of a 2-dimensional surface, which in this case is a sphere. We place a qubit on each vertex of Λ , and define the familiar X -type and Z -type face operators $G_f^X = \prod_{v \in f} X_v$ and $G_f^Z = \prod_{v \in f} Z_v$ for each face $f \subset \Lambda$. In particular, since the lattice is 3-colorable and 3-valent, these face operators G_f^X and G_f^Z all commute. These operators generate the 2D color code stabilizer group $\mathcal{S}_{cc} = \langle G_f^X, G_f^Z \mid f \text{ a face of } \Lambda \rangle$, and define a corresponding Hamiltonian H_{2D-cc} by

$$H_{2D-cc} = - \sum_{\text{faces } f} (G_f^X + G_f^Z). \quad (3.47)$$

This 2D color code differs only from that defined on the outer colex (considered in Sec. 3.4, Fig. 3.14) by a choice of boundary conditions.

Recall, a generating set for the anyonic excitations of this model can be labelled by $m_{\mathbf{k}}$, and $e_{\mathbf{k}}$, where $\mathbf{k} \in \{\mathbf{A}, \mathbf{B}\}$ labels a color, e -type anyons corresponds to flipped X -type plaquettes, and m -type anyons correspond to flipped Z -plaquettes. One can obtain \mathbf{C} colored anyons as the fusion of an \mathbf{A} and \mathbf{B} colored anyon of the same type. This set of anyons forms a group under fusion $\mathcal{A}_{2D\text{-cc}} \cong \mathbb{Z}_2^4$, with the above choice of generators.

However, not all anyonic excitation configurations are possible as there are global constraints that need to be satisfied in this model. In particular, since our model is defined on a closed surface, we have the following identities for each $\alpha \in \{X, Z\}$

$$\prod_{\substack{f \subset \Lambda \\ \mathcal{K}(f)=\mathbf{A}}} G_f^\alpha = \prod_{\substack{f \subset \Lambda \\ \mathcal{K}(f)=\mathbf{B}}} G_f^\alpha = \prod_{\substack{f \subset \Lambda \\ \mathcal{K}(f)=\mathbf{C}}} G_f^\alpha = \prod_{v \in \Lambda} \alpha_v. \quad (3.48)$$

Letting $N_{\mathbf{k}}^e$ and $N_{\mathbf{k}}^m$ be the number of $e_{\mathbf{k}}$ and $m_{\mathbf{k}}$ anyonic excitations respectively, then the above equation implies the following relation

$$N_{\mathbf{A}}^e = N_{\mathbf{B}}^e = N_{\mathbf{C}}^e \quad \text{mod } 2, \quad (3.49)$$

and similarly for $N_{\mathbf{k}}^m$. In particular this means that the number of $e_{\mathbf{A}}$, $e_{\mathbf{B}}$ and $e_{\mathbf{C}}$ anyons is conserved mod 2 (and similarly for $m_{\mathbf{A}}$, $m_{\mathbf{B}}$, and $m_{\mathbf{C}}$).

If we regard anyons of color \mathbf{C} as being comprised of an \mathbf{A} color and a \mathbf{B} color anyon, we can obtain further constraints. Namely, for any two colors, $\mathbf{u}, \mathbf{v} \in \{\mathbf{A}, \mathbf{B}, \mathbf{C}\}$, we have a product constraint

$$\prod_{\substack{f \subset \Lambda \\ \mathcal{K}(f)=\mathbf{u}}} G_f^\alpha \prod_{\substack{f \subset \Lambda \\ \mathcal{K}(f)=\mathbf{v}}} G_f^\alpha = I. \quad (3.50)$$

This implies a constraint on the parity of anyons

$$N_{\mathbf{u}}^e + N_{\mathbf{v}}^e = 0 \quad \text{mod } 2, \quad (3.51)$$

which along with the fact that we are regarding $N_{\mathbf{C}}^e = N_{\mathbf{A}}^e + N_{\mathbf{B}}^e$, means that $N_{\mathbf{A}}^e = N_{\mathbf{B}}^e = 0 \text{ mod } 2$ (and similarly for m -type anyons). The product constraint of Eq. (3.50) exists on the whole 2-dimensional lattice (that is, a codimension-0 surface), and gives rise to 4 independent anyonic constraints: that the number of $e_{\mathbf{A}}$ anyons must be created or destroyed in pairs, and similarly for $e_{\mathbf{B}}$, $m_{\mathbf{A}}$, and $m_{\mathbf{B}}$. Thus, we refer to it as an emergent \mathbb{Z}_2^4 0-form symmetry.

The identities of Eq. (3.50) make this emergent symmetry look like a global constraint, however it is in fact a 0-form symmetry. That is, we can identify an action of this symmetry on any submanifold, not just the whole lattice. This structure to the symmetry is best seen by

reformulating it as a type of Gauss' law for anyonic excitations, detecting the total topological charge in a region through an observable localized to the boundary of the region. Specifically, consider submanifolds that are not closed. Let \mathcal{M} be a codimension-0 submanifold of the 2-colex (that is, a subset of faces), with boundary. Then for $\alpha \in \{X, Z\}$ it holds that

$$\prod_{\substack{f \subset \mathcal{M} \\ \mathcal{K}(f)=\mathbf{u}}} G_f^\alpha \prod_{\substack{f \subset \mathcal{M} \\ \mathcal{K}(f)=\mathbf{v}}} G_f^\alpha = h_{\partial \mathcal{M}}, \quad (3.52)$$

where $h_{\partial \mathcal{M}} = \prod_{v \in \partial \mathcal{M}} \alpha_v$ is supported on the boundary of \mathcal{M} . (Note that we have assumed the 2-colex is closed, however the above equation also holds when \mathcal{M} is disjoint from the boundary of the 2-colex). Now instead of the global constraint of Eq. (3.51), we get a constraint for every submanifold \mathcal{M} . Namely, the charge within the region \mathcal{M} is equal (mod 2) to the eigenvalue of on the operator $h_{\partial \mathcal{M}}$

$$N_{\mathbf{u}}^e + N_{\mathbf{v}}^e = \langle h_{\partial \mathcal{M}} \rangle \quad \text{mod } 2, \quad (3.53)$$

for any excited state (provided, as is true with this model, that anyons are well-localized). Choosing $\mathbf{v} = \mathbf{C}$ lets us determine $N_{\mathbf{A}}^e$ and $N_{\mathbf{B}}^e$ independently, and similarly for $N_{\mathbf{k}}^m$. In other words, one can detect the topological charge within the region \mathcal{M} using operators on the boundary of the region, giving rise to the well-known topological charge conservation law for anyons in the color code. Thus we have seen that the conservation law applies locally as well (provided that the length scale is such that anyons remain well-localized), and is not just a global constraint on the entire manifold.

Importantly, in the above considerations, emergent symmetries were revealed not by elements of a symmetry group, but rather product constraints amongst the Hamiltonian terms. This is a result of the stabilizer Hamiltonian models that we have considered as examples. We can now turn to higher-dimensional examples, again of stabilizer Hamiltonians, where this holds true for higher-form symmetries, i.e., where emergent q -form symmetries are associated with product constraints on closed codimension- q submanifolds of the lattice. Ultimately, however, we expect the symmetry considerations rather than the product constraints to be more fundamental, and we return to this issue in Sec. 3.5.3. However, first, we will examine the underlying emergent 1-form symmetries in the gauge color code in the next section.

3.5.2 Emergent 1-form symmetries in 3D

Here we demonstrate how emergent 1-form symmetries can arise in a 3D model, in a sense by bootstrapping from the 2D case.

Single-sector 3D gauge color code

For illustrative purposes, we first consider a single charge sector of the 3D gauge color code H_G . This single-sector model is not topologically ordered, and so does not possess emergent symmetries; nonetheless it will be useful to illustrate the connection between 1-form symmetries in a 3D model and 0-form symmetries in associated 2D models existing across all codimension-1 submanifolds of the 3D model. The 1-form symmetries fix excitations to be 1-dimensional objects that conserve color flux.

Recall, the gauge color code is defined on a 3-colex \mathcal{C}_3 (a 4-colorable, 4-valent cellulation) with a qubit on each vertex. For concreteness, we restrict our discussion to the X -sector of the gauge color code (the Z -sector follows similarly). That is, we consider the Hamiltonian

$$H_X = - \sum_f G_f^X, \quad (3.54)$$

consisting of the sum of all face terms over a 3-colex. The ground space of H_X is the mutual $+1$ eigenspace of all terms G_f^X , and excitations are eigenstates of the Hamiltonian in the -1 eigenspace of some terms (we say these terms are $G_f^X = -1$). We can label excited states uniquely by specifying which terms are $G_f^X = -1$, but importantly not all configurations are allowed, as there are algebraic constraints amongst terms.

Consider any closed codimension-1 submanifold \mathcal{M} of the 3-colex that is also a 2-colex, with the color-pairs $\mathbf{A}_\mathcal{M}$, $\mathbf{B}_\mathcal{M}$, and $\mathbf{C}_\mathcal{M}$ selected from the 6 possible color-pairs of faces in \mathcal{C}_3 . On this sub-2-colex, we have the familiar constraints. Namely, for any 2 color-pairs $\mathbf{u}, \mathbf{v} \in \{\mathbf{A}_\mathcal{M}, \mathbf{B}_\mathcal{M}, \mathbf{C}_\mathcal{M}\}$, we have

$$\prod_{\substack{f \subset \mathcal{M} \\ \mathcal{K}(f)=\mathbf{u}}} G_f^X \prod_{\substack{f \subset \mathcal{M} \\ \mathcal{K}(f)=\mathbf{v}}} G_f^X = I, \quad (3.55)$$

mirroring the constraints of Eq. (3.50). In particular, this relation holds in the smallest instance when \mathcal{M} is the boundary of a 3-cell.

The product relations of Eq. (3.55) lead to constraints on excitations. Namely, for each codimension-1 submanifold (that is a 2-colex), the number of faces $f \subset q$ with $G_f^X = -1$ carrying a color \mathbf{k} must sum to $(0 \bmod 2)$, and this holds for each (single) color \mathbf{k} . This in turn requires excitations (which carry pairs of colors) to form closed loop-like objects that conserve color. The dual lattice again provides the visualization, where excitations correspond to sets of edges and edges carry a pair of colors. At each vertex v of the dual lattice, let $N_{\mathbf{k}}^v$ be the number of loop excitations carrying the (single) color \mathbf{k} that contain v . Then the constraints of Eq. (3.55) mean that

$$N_{\mathbf{k}}^v = 0, \quad \forall \mathbf{k}, v, \quad (3.56)$$

which is precisely the color flux conservation discussed in Sec. 3.4.4. In particular, this implies that excitations must form closed loop-like objects.

Not all excitations are independent. A string excitation of a color \mathbf{xz} may branch into a pair of strings with colors \mathbf{xk} and \mathbf{kz} for $\mathbf{k} \neq \mathbf{x}, \mathbf{z}$. This then means there are three independent color pairs, such that all loop excitations can be regarded as the fusion of these loops. The flux conservation can be regarded as three independent constraints on loop-like excitations.

Similar to the 0-form case, 1-form symmetries also imply a constraint (conservation law) for the loop-like excitations. We can infer a generalization of the law for detecting topological charge, which in this case applies to color flux, by considering codimension-1 submanifolds that are not closed. In particular, let \mathcal{M}' be a codimension-1 submanifold with a boundary. Then it holds that

$$\prod_{\substack{f \subset \mathcal{M}' \\ \mathcal{K}(f)=\mathbf{u}}} G_f^X \prod_{\substack{f \subset \mathcal{M}' \\ \mathcal{K}(f)=\mathbf{v}}} G_f^X = h_{\partial \mathcal{M}'}, \quad (3.57)$$

where $h_{\partial \mathcal{M}'}$ is an operator supported on the (1-dimensional) boundary of \mathcal{M} (again we are assuming that \mathcal{M} is supported away from any boundary of the 3-colex). This means that the number (mod 2) of \mathbf{u} colored and \mathbf{v} colored excitations that thread the region \mathcal{M}' is detected by an operator $h_{\partial \mathcal{M}'}$ on the boundary of that region. Again, we can use the constraints to determine this number on each independent color pair.

In summary, we have seen that this model supports three independent types of excitations, each constrained to form closed loops (with the possibility of branching and fusion). This 3D example, then, gives the appearance of an emergent \mathbb{Z}_2^3 1-form symmetry arising from a 0-form symmetry on codimension-1 submanifolds (where the rank of the 1-form symmetry group is due to the number of independent excitations that are conserved). We note, however, that by restricting to the X -sector, we do not have a topologically ordered model; the codimension-1 submanifolds do not have an *emergent* 0-form symmetry without both sectors, and so an emergent 1-form symmetry does not appear in the 3D model. Both electric and magnetic sectors are required simultaneously in order to have the emergent symmetry associated with either [193]. Regardless, our purpose here was simply illustrative—we are not fundamentally interested in this single-sector model, but rather a topologically-ordered 3D model with both sectors such as the gauge color code. We turn to that model now.

The gauge color code and color flux conservation

Does the topologically-ordered 3D gauge color code have an emergent 1-form symmetry associated with color flux conservation? Each sector of the gauge color code on its own, H_X and H_Z , has loop-like, color-flux-conserving excitations. Proliferation of such excitations is therefore

suppressed, as they are energetically confined. For the full gauge color code Hamiltonian,

$$H_G = - \sum_f G_f^X - \sum_f G_f^Z, \quad (3.58)$$

it is tempting to conclude that a \mathbb{Z}_2^6 1-form symmetry will emerge, and lead to confined errors and suppression of logical faults. However, the terms of H_G are not mutually commuting (and indeed frustrated), and therefore we cannot immediately label excited states by specifying terms $G_f^X, G_f^Z = \pm 1$. In other words, this frustrated model's excitations are not guaranteed to be well-defined extended objects with well-defined color flux as appear in each sector separately. If they were, then this would be strong evidence that the model was self-correcting.

Unfortunately, there are few tools available to understand the spectrum of a frustrated Hamiltonian such as H_G , and without such information it is a very difficult task to analyse the thermal stability and memory time of the code. In this sense, one can view the exactly solvable model H_{G_b} as the result of removing terms from the Hamiltonian until it is commuting, in the process losing its emergent 1-form symmetries and supplementing them with enforced 1-form symmetries. Understanding the excitations in H_G remains an important problem, to determine if it is self-correcting.

Higher-dimensional generalizations and emergent q -form symmetries

We briefly generalize the discussion to emergent q -form symmetries in d -dimensional systems that arise from (product) constraints residing on codimension- q submanifolds. In particular, a commuting Hamiltonian $H = \sum_{X \subset \Lambda} h_X$ in d -dimensions has an emergent \mathbb{Z}_2 q -form symmetry if for all closed codimension- q submanifolds \mathcal{M} , there exists a constraint

$$\prod_{X \subset \mathcal{M}} h_X = I. \quad (3.59)$$

If there are multiple independent such constraints on the submanifolds, then there are multiple copies of emergent \mathbb{Z}_2 q -form symmetries. Importantly, we note that these constraints all look like emergent \mathbb{Z}_2 0-form symmetries on codimension- q submanifolds. The generalized conservation law states that the number (mod 2) of excitations (which must be q -dimensional objects) threading the codimension- q region \mathcal{M}' can be measured by the operator $H_{\partial \mathcal{M}'}$ on the codimension- $(q+1)$ boundary of the region. In particular, if H has a q -form emergent symmetry, let \mathcal{M}' be a codimension- q submanifold with a boundary, then it holds that

$$\prod_{i \in \mathcal{M}'} h_i = h_{\partial \mathcal{M}'} , \quad (3.60)$$

where $h_{\partial M'}$ is an operator supported on a small neighbourhood of the boundary of \mathcal{M} . (This is because if we chose a complementary codimension- q submanifold \mathcal{M}'' such that $\partial M' = \partial M''$, then if \mathcal{M} is the result of gluing \mathcal{M} and \mathcal{M}' along their boundary, we would have the usual constraint of Eq. (3.59). Thus $\prod_{i \in \mathcal{M}'} h_i$ can only differ from the identity by an operator supported on a small neighbourhood of $\partial \mathcal{M}'$.)

Examples of models with emergent higher-form symmetries include toric codes in various dimensions. For dimensions $d \geq 2$, there are $d-1$ distinct ways of defining a toric code. Namely, for each $k \in \{1, \dots, d-1\}$, we define the $(k, d-k)$ toric code that has k -dimensional logical X operators, and $(d-k)$ -dimensional logical Z operators. One can confirm that these models have emergent \mathbb{Z}_2 $(k-1)$ -form and \mathbb{Z}_2 $(d-k-1)$ -form symmetries. The smallest dimension that allows for a toric code with emergent \mathbb{Z}_2^2 1-form symmetries is $d = 4$, with the $(2, 2)$ toric code, which is a self-correcting quantum memory.

3.5.3 Stability of emergent symmetries

Our discussion of emergent symmetries has focussed on Hamiltonians with commuting terms. This property allowed for the simple identification of product constraints. One can ask if the resulting emergent symmetries are a property of a finely tuned system alone, or if they hold more generally. In this section, we show that these symmetries are robust features of phases of matter, that they cannot be broken by local perturbations, *irrespective of any symmetry considerations*, provided they are sufficiently small. The argument uses the idea of quasi adiabatic continuation, following Ref. [93].

Consider a family of local Hamiltonians H_s , labelled by a continuous parameter $s \in [0, 1]$, such that $H_0 = H$ is the original Hamiltonian, and H_s remains gapped for all $s \in [0, 1]$. This family of Hamiltonians can be used to describe the situation where a perturbation is added to H . We label ground states of H by $|\psi_i\rangle$, and groundstates of H_s by $|\psi_i^s\rangle$. Note that the ground states can be unitarily related by an adiabatic continuation. Then, following Ref. [93], there exists a unitary $U(s)$ corresponding to a quasi-adiabatic change of the Hamiltonian with the following properties. For any operator O , one can find a dressed operator $O_s = U(s)OU(s)^\dagger$, such that O_s has approximately the same expectation value in $|\psi_{\text{ex}}^s\rangle$ as O does in $|\psi_i\rangle$ (and similarly for low-energy states). Moreover, if O is local, then O_s is local too. (The support of the dressed operators increases by a size determined by the choice of quasi-adiabatic continuation unitary $U(s)$. The approximate ground state expectation values improve exponentially in the range of increased support of dressed operators.)

Importantly, one can use quasiadiabatic continuation to find dressed versions $h_X(s) = U(s)h_X U(s)^\dagger$ of the Hamiltonian terms that have approximately the same low-energy expectation values as those in the unperturbed Hamiltonian. These Hamiltonian terms will also

have the same constraints. In particular, if H had an emergent q -form symmetry arising from some product constraints amongst Hamiltonian terms, then the dressed Hamiltonian also has the same local conservation laws. To see this, note that local conservation laws can always be inferred at low energies, as they involve only Hamiltonian terms in a small neighbourhood. We needn't be concerned with the high energy sector as by checking all local conservation laws, one can establish that the model has an emergent q -form symmetry. Note that the dressed terms will in general be supported in a larger region, meaning one may need to rescale the lattice to resolve excitations and faithfully capture the generalized conservation law in the perturbed Hamiltonian. For example, consider the color code in the presence of perturbations, then one can renormalize the lattice such that individual excitations are well defined. Then in the renormalized lattice, these excitations still conserve anyon parity, and they still obey a conservation law for topological charge.

We remark that we required the gap to remain open in the presence of the perturbations. This can be guaranteed for any local perturbation (provided it is sufficiently weak), if H satisfies the conditions of TQO-1 and TQO-2 of Ref. [88]. In particular, the example models we have considered in Sec. 3.3 and Sec. 3.4 satisfy the conditions.

3.5.4 Duality between emergent and enforceable symmetries

For emergent symmetries, we are faced with the puzzle that we have a conservation law without any symmetry operator. What is the origin of this symmetry? As pointed out by Kitaev in the case of the 2D toric code [193], we can always recover symmetry operators by introducing redundant “unphysical” degrees of freedom, viewed as gauge degrees of freedom. Here we briefly consider how Kitaev's approach can be applied to higher-form symmetries. In particular, for systems with emergent symmetries, we will construct symmetry operators on an enlarged Hilbert space. This construction provides a duality between systems where the q -form symmetry is emergent and systems where it is enforced.

We will begin with the color code in 2D, and then show how to lift the construction to the 1-form case in 3D. We start by introducing new ancillary degrees of freedom—one ancilla for each term in the Hamiltonian. Label these ancilla by $a_X(f)$ and $a_Z(f)$ corresponding to the terms G_f^X and G_f^Z and fixed them in the $+1$ eigenspace of Pauli operators X and Z , respectively. We can now regard the new Hilbert space as $\mathcal{H} \otimes \mathcal{A}$, and states in \mathcal{H} are embedded according to the isometry $|\psi\rangle \mapsto |\psi\rangle \otimes |a\rangle$, where $|a\rangle = (\otimes_{a_X(f)} |+\rangle)(\otimes_{a_Z(f)} |0\rangle)$. We refer to the (original) degrees of freedom in \mathcal{H} as matter, and those in \mathcal{A} as gauge. Importantly, not all states $|\varphi\rangle \in \mathcal{H} \otimes \mathcal{A}$ are physical, only the subspace of states satisfying $X_{a_X(f)} |\varphi\rangle = |\varphi\rangle$ and $Z_{a_Z(f)} |\varphi\rangle = |\varphi\rangle$ are physical. At this point, it is clear from the embedding that the physical state space is the same as the original state space.

We now couple the matter and gauge degrees of freedom with an entangling unitary. Consider the mapping of gauge terms and matter Hamiltonian terms

$$X_{a_X(f)} \mapsto S_f^X, \quad G_f^X \mapsto G_f^X, \quad (3.61)$$

$$Z_{a_Z(f)} \mapsto S_f^Z, \quad G_f^Z \mapsto G_f^Z, \quad (3.62)$$

where $S_f^X = X_{a_X(f)} G_f^X$ and $S_f^Z = Z_{a_Z(f)} G_f^Z$. Such a mapping can be achieved with a unitary U as we show below. In this new Hilbert space, which we label $U(\mathcal{H} \otimes \mathcal{A})U^\dagger$, the physical state space is the subspace satisfying

$$S_f^X |\varphi\rangle = S_f^Z |\varphi\rangle = |\varphi\rangle. \quad (3.63)$$

The symmetry operators S_f^X and S_f^Z are known as gauge transformations, and states and operators that are related by them are thought of as equivalent.

The entangling unitary U that will result in the above mapping can be constructed out of 2-qubit CNOT gates, $A_{i,j}$, which act by conjugation on Pauli operators as follows

$$X_i \mapsto X_i X_j, \quad Z_i \mapsto Z_i \quad (3.64)$$

$$X_j \mapsto X_j, \quad Z_j \mapsto Z_i Z_j. \quad (3.65)$$

Then for each face f , we define the following unitaries

$$U_f^X = \prod_{v \in f} A_{a_X(f),v}, \quad U_f^Z = \prod_{v \in f} A_{v,a_Z(f)}. \quad (3.66)$$

Note that U_f^X has the following action:

$$U_{f'}^X X_{a_X(f)} U_{f'}^{X\dagger} = \begin{cases} S_f^X & \text{if } f = f' \\ X_{a_X(f)} & \text{otherwise.} \end{cases} \quad (3.67)$$

Moreover, $U_{f'}^X$ commutes with all Hamiltonian terms G_f^X and $G_f^Z \forall f$ (this statement only needs to be verified for terms G_f^Z where f' and f are neighbours, where it holds because neighbouring terms intersect an even number of times – as is always the case for commuting CSS stabilizer Hamiltonians). A similar calculation gives the action of U_f^Z

$$U_{f'}^Z Z_{a_Z(f)} U_{f'}^{Z\dagger} = \begin{cases} S_f^Z & \text{if } f = f' \\ Z_{a_Z(f)} & \text{otherwise} \end{cases} \quad (3.68)$$

where again $U_{f'}^Z$ commutes with all Hamiltonian terms G_f^X and $G_f^Z \forall f$. Then the desired unitary U is given by $U = \prod_f U_f^X U_f^Z$.

Since the Hamiltonian is unchanged by U , one can ask what the excitations in the physical space of $U(\mathcal{H} \otimes \mathcal{A})U^\dagger$ look like. Namely, for each flipped term G_f^X (G_f^Z) we must also flip the ancilla $a_X(f)$ ($a_Z(f)$). Thus one can equally label excitations by the terms G_f^X and G_f^Z , or the terms $X_{a_X(f)}$ and $Z_{a_Z(f)}$, as the two sets are gauge equivalent. The emergent 0-form symmetry manifests itself as product constraints amongst Hamiltonian terms (following Eq. (3.50)). Specifically, it is equivalent to the following constraints, for any color $\mathbf{u} \neq \mathbf{v}$

$$\prod_{f|\mathcal{K}(f)=\mathbf{u}} S_f^X \prod_{f|\mathcal{K}(f)=\mathbf{v}} S_f^X = \prod_{a_X(f)} X_{a_X(f)}, \quad (3.69)$$

and similarly for the Z -terms. Here, we see that the operator $\prod_{a_X(f)} X_{a_X(f)}$ (which is gauge equivalent to a product of color code terms G_f^X) counts the number of excitations mod 2. As it is a product of symmetry operators, any physical state must lie in its $+1$ eigenspace. That is, we have found a symmetry operator that determines the parity conservation of anyons, by introducing gauge degrees of freedom.

In the same way, we can perform an analogous procedure for each sector in the 3D gauge color code. Again, we associate ancilla to each term in the Hamiltonian, and then apply the unitary U that entangles gauge and matter degrees of freedom. Much like the 2D case, this leads to symmetry operators constructed on all codimension-1 submanifolds (out of products of S_f^X and S_f^Z on these surfaces) and a requirement that the physical states must live in their common $+1$ eigenspace (the enforced 1-form symmetry). These symmetry operators mirror the 1-form operators that we have seen in sections 3.3 and 3.4. In fact, this construction works for any CSS stabilizer code (in any dimension), where the product over $v \in f$ in Eq. (3.66) is replaced by product over the qubits in the support of the stabilizer term.

By introducing redundant degrees of freedom, we have related a model with an emergent symmetry to one with an enforced symmetry. The duality mapping known as *gauging* [109, 118, 156, 230–232] formalizes this relationship. Gauging a model with an onsite (0-form) symmetry produces a model with an emergent 0-form symmetry. Gauging also provides a potential direction for identifying models with emergent 1-form symmetries. We note that formalisms for gauging/ungauging more general types of symmetries have been explored by Vijay, Haah, and Fu [233], Williamson [234], as well as Kubica and Yoshida [229]; these approaches provide potentially powerful tools to identify self-correcting quantum memories protected by emergent 1-form symmetries.

We also remark on the parallels between this simple duality mapping and error correction. In fact, the coupling of gauge degrees of freedom is similar to many schemes of syndrome extraction, where measurement of ancillas is used to infer the eigenvalues of stabilizer terms. Measurement errors can break this correspondence, however, and result in a misidentification of errors. This is typically accommodated by requiring many rounds of measurements. For

single shot error correction (such as in the GCC [48]), only a single round of measurements is needed, owing to the extensive number of symmetry constraints present, whose violation indicates a measurement error. In the case of emergent 0-form symmetries, the global constraint alone cannot provide sufficient information to correct for measurement errors. In a similar vein to self-correction in 3D, it would be interesting find 2D topological codes (if they exist) with emergent \mathbb{Z}_2^2 1-form symmetries, as such codes could in principle admit single-shot error correction.

3.6 Discussion

We have shown that spin lattice models corresponding to 2D SET ordered boundaries of thermally-stable 3D SPT ordered phases protected by a suitable 1-form symmetry can be self-correcting quantum memories. The key features of these 1-form symmetric models are that the bulk excitations are string-like and confined, and that the symmetry naturally couples bulk and boundary excitations to confine the later as well.

We have presented two explicit examples of 3D self-correcting quantum memories protected by 1-form symmetries. The understanding and classification of such 3D models remains largely unexplored. A natural class of candidates are the (modular) Walker-Wang models [209, 235–238], which possess many of the desirable properties we seek. In particular, if the input anyon theory to the Walker-Wang construction is modular, then all bulk excitations are confined, while the 2D boundary contains a copy of the input anyon theory. One can consider building 1-form symmetries into these types of models, as has been done by Williamson and Wang [239] for a class of models based on the state sum TQFTs of Ref. [240]. (We note this is similar to the way that Ref. [209] ‘decorates’ a Walker-Wang model with a 0-form symmetry.) The 2-group construction of Ref. [153] presents another interesting family of models that warrants further investigation. In the stabilizer case, another possible approach to construct 3D models with 1-form symmetries is to “foliate” [241, 242] a topological stabilizer code with emergent 0-form symmetries. As an example, foliation of a d -dimensional topological CSS code with emergent q -form symmetry generates a $(d+1)$ -dimensional generalized RBH-type model with a $(q+1)$ -form symmetry.

In the examples we have explored, we have seen the necessity of the bulk SPT-ordering in order to have a self-correcting boundary, and for the bulk SPT-ordering of these models to be thermally stable. A common viewpoint is that a self-correcting quantum memory should be topologically ordered at nonzero temperature. While this has not been proven to be strictly necessary, it has been observed to be true for many examples under Hastings’ definition for topological order at $T \geq 0$ [123]. (For example, 2D commuting projector Hamiltonian models

and the 3D toric code all lack topological order at $T > 0$, corresponding to the absence of self-correction.) Our examples provide further support to this perspective.

We briefly consider what our results imply for self-correction in the 3D gauge color code. As we have shown in Sec. 3.4, the 3D gauge color code realized as commuting Hamiltonians protected by an (enforced) 1-form symmetry is self-correcting. If we consider the full Hamiltonian of Eq. (3.58), the model is frustrated and it is difficult to prove that it possesses the string-like excitations with well-defined topological charge required for our arguments. We have also argued that the full model possesses an emergent 1-form symmetry: the color flux conservation as previously identified by Bombin [75]. This emergent symmetry gives strong supporting evidence that proving self-correction for the full Hamiltonian of Eq. (3.58) (without enforcing any symmetry requirement) may be possible. What remains is to understand the spectrum of the model, and in particular verify whether the energy cost of a loop excitation grows with its length.

The idea that 1-form symmetries may be emergent in 3D topological models is extremely intriguing, both from the perspective of self-correction and more generally. We have argued that 1-form symmetries may emerge in 3D models that possess emergent 0-form symmetries on all codimension-1 submanifolds, which in turn can be guaranteed by topological ordering of these submanifolds. We can ask whether the 1-form symmetries of the RBH model or commuting GCC model can be realised in an emergent fashion in a 3D commuting, frustration-free Hamiltonian. It is not clear if this is possible. The key goal here is to identify models that possess well-defined bulk excitations together with sufficient emergent 1-form symmetries to guarantee confinement for all of such excitations. This is in contrast to the 3D toric code, where only one sector has an emergent 1-form symmetry, and correspondingly only one type of logical operator is thermally stable (giving rise to a self-correcting classical memory). Topological subsystem codes, such as the gauge color code, are natural candidates. Along with obviating the need to enforce symmetries, another advantage of emergent symmetries is that the conservation laws are manifestly true, without putting any restrictions on the system-bath coupling.

A key open question is how to construct more general families of models with emergent higher-form symmetries. We have discussed a simple duality between emergent and enforceable symmetries, that symmetries can be introduced by adding gauge degrees of freedom in systems with emergent symmetries. In the case of 0-form symmetries, a simple well-known gauging map [109, 118, 156, 230–232] can be used to obtain a model with emergent \mathbb{Z}_2 0-form symmetry from a model with an enforced \mathbb{Z}_2 0-form symmetry. Investigating this more generally in the presence of both enforced and emergent higher-form symmetries may lead to interesting new models, and here we point the interested reader to new results by Kubica and Yoshida on generalized gauging and ungauging maps [229].

We have not considered the issue of efficient decoding for these self-correcting quantum memories. We note that our two examples, the RBH model and the gauge color code, have efficient decoders with the additional feature of being single-shot [136, 216, 243]. In general, we note that the string-like nature of the excitations (errors) in these 1-form symmetric self-correcting quantum memories ensure that efficient decoders exist in general [244].

Finally, there are many avenues for further investigation into the role of symmetry in self-correcting quantum memories. In particular, one can consider the stability and feasibility of self-correction in defect-based encodings, for example in twist defects [67, 214] or the “Cheshire charge” loops of Refs. [140, 245]. Such defects have a rich connection with SPT order, as well as with both enforced and emergent symmetries. Namely, as shown in Ref. [119], one can view topological phases with nontrivial domain walls as having SPT ground states protected by 0-form symmetries, where the protecting symmetry comes from the emergent 0-form symmetries of the topological model. It would be interesting to see if SPTs protected by higher-form symmetries also arise in this way, that is, from domain walls of topological models with emergent higher-form symmetries, and whether these associated domain walls (and symmetry defects that live on their boundaries) can be thermally stable. For example, the SPT order (at temperature $T \geq 0$) in the RBH model manifests as a thermally stable domain wall in the 4D toric code [216]. Whether one can construct similarly stable domain walls in 3D or less is an open problem. Another direction is to consider more general subsystem symmetries, where the dimension need not be an integer. For example, fracton topological orders (which can be partially self-correcting [12]) have been of great interest recently [233, 234, 246].

3.7 Davies Formalism

In this section we briefly review the Davies formalism. Recall the system-bath coupling

$$H_{\text{full}} = H_{\text{sys}} + H_{\text{bath}} + \lambda \sum_{\alpha} S_{\alpha} \otimes B_{\alpha}, \quad (3.70)$$

where $S_{\alpha} \otimes B_{\alpha}$ describe the system-bath interaction for S_{α} a local operator acting on the system side, B_{α} is an operator acting on the bath side, and α is an arbitrary index. It is assumed that the coupling parameter is small, $|\lambda| \ll 1$. Suppose that the state is initialized in a ground state $\rho(0)$ of H_{sys} , then the state evolves under a Markovian master equation

$$\dot{\rho}(t) = -i[H_{\text{sys}}, \rho(t)] + \mathcal{L}(\rho(t)), \quad (3.71)$$

where \mathcal{L} is the Lindblad generator. Then the initial ground state $\rho(0)$ evolves under this master equation according to

$$\rho(t) = e^{t\mathcal{L}}(\rho(0)). \quad (3.72)$$

Here, the Lindblad generator is given by

$$\mathcal{L}(\rho) = \sum_{\alpha, \omega} h(\alpha, \omega) \left(A_{\alpha, \omega} \rho A_{\alpha, \omega}^\dagger - \frac{1}{2} \{ \rho, A_{\alpha, \omega}^\dagger A_{\alpha, \omega} \} \right) \quad (3.73)$$

In the above, $A_{\alpha, \omega}$ are the Fourier components of $A_\alpha(t) = e^{iH_{\text{sys}}t} A_\alpha e^{-iH_{\text{sys}}t}$, meaning they satisfy

$$\sum_{\omega} e^{-i\omega t} A_{\alpha, \omega} = e^{iH_{\text{sys}}t} A_\alpha e^{-iH_{\text{sys}}t}. \quad (3.74)$$

One can think of $A_{\alpha, \omega}$ as the component of A_α that transfers energy ω from the system to the bath. Note that when the Hamiltonian H_{sys} is comprised of commuting terms, the terms $A_\alpha(t)$ and therefore also $A_{\alpha, \omega}$ are local operators. The function $h(\alpha, \omega)$ can be thought of as determining the rate of quantum jumps induced by A_α that transfer energy ω from the system to the bath, and is the only part that depends on the bath temperature. It must satisfy the detailed balance condition $h(\alpha, -\omega) = e^{-\beta\omega} h(\alpha, \omega)$, which ensures that the Gibbs state

$$\rho_\beta = e^{-\beta H_{\text{sys}}} / \text{Tr}(e^{-\beta H_{\text{sys}}}), \quad (3.75)$$

at inverse temperature β is a fixed point of the dynamics of Eq. (3.73). That is, $\rho_\beta = \lim_{t \rightarrow \infty} \rho(t)$. Moreover, under natural ergodicity conditions (see [165, 166] for more details), it is the unique fixed point.

In the case that we have a symmetry ,

$$[H_{\text{full}}, S(g)] = 0, \quad (3.76)$$

then all of the errors that are introduced due to interactions with the bath must be from processes that conserve $S(g)$. In particular, only excitations that can be created by symmetric thermal errors will be allowed. Indeed, in the case that Eq. (3.76) holds, we will have that

$$e^{\mathcal{L}t} (S(g)^\dagger \rho_0 S(g)) = S(g)^\dagger e^{\mathcal{L}t} (\rho_0) S(g) \quad (3.77)$$

which justifies the consideration of the symmetric energy barrier in Eq. (3.9).

We note that the assumptions of this formalism are satisfied for systems where the terms are comprised of commuting Paulis, as in this case the system Hamiltonian has a discrete spectrum with well separated eigenvalues. However the formalism will not necessarily work beyond this exact case, for instance, when perturbations are added and small energy splittings are introduced between previously degenerate eigenvalues. The study of thermalization times for many body stabilizer Hamiltonians in the presence of perturbations is an interesting problem.

3.8 Thermal instability of 0-form SPT ordered memories

In this section we argue that onsite symmetries are insufficient to promote a 2D topological quantum memory to be self-correcting, even if such a phase lives on the boundary of a 3D SPT model. We restrict our discussion to the case where the boundary Hamiltonian is an abelian twisted quantum double. The interesting case is where the boundary symmetry action is anomalous. (However we don't allow this boundary symmetry action to permute the anyon types.)

We will argue that the boundary theory of a 3D SPT ordered bulk phase, if topologically ordered, will necessarily possess deconfined anyons. That is, the boundary string operators corresponding to error chains can be deformed while still respecting the symmetry, even with anomaly. We focus on (twisted) quantum doubles on the boundary of 3D group cohomology SPTs, and rather than going into the details of their construction, we focus on the key features. In particular, local degrees of freedom (of both bulk and boundary) for these models are labelled by group elements, as $|g\rangle$, $g \in G$. The symmetry action of these 2D (boundary) systems takes the form $S(g) = R(g)N(g)$, where $R(g) = \otimes_i u(g)$, with $u(g) = \sum_{h \in G} |gh\rangle \langle h|$ and $N(g)$ is diagonal in the $|g\rangle$ basis and can be represented as a constant depth quantum circuit. One can think of $R(g)$ as the onsite action, and $N(g)$ as an anomaly. This anomaly must be trivial in a strictly 2D system, or equivalently if the system is at the boundary of a trivial SPT phase.

There are two types of excitation operators in the (twisted) quantum doubles. One type of excitation string operator for the boundary system is diagonal in the $|g\rangle$ basis (i.e., it is the same as in the untwisted theory), so it commutes with $N(g)$. This excitation string operator commutes with $u(g)$, up to a phase (that is a k th root of unity for some $k \in \mathbb{N}$), so to commute with $R(g)$ we need to consider excitation string operators of certain lengths. In particular, the process of creating an anyonic excitation at one boundary and dragging it to another boundary (or creating an anyon pair and dragging one around a nontrivial cycle before annihilating them again) can be done in a symmetric way. Since such an operation results in a logical error and only costs a constant amount of energy, we see that the boundary theory is unstable.

Thus we see that the anomaly affords no extra stability, and the model has the same stability as a topological model with an extra onsite symmetry on top. That is, like genuine 2D topological models of this type, the model has a constant symmetric energy barrier. Note that this argument can break down in 4D, where the boundary is a 3D twisted quantum double.

Therefore we see that in the case of onsite (0-form) symmetries, the SPT ordered bulk offers no additional stability to the boundary theory. Indeed, the symmetric energy barrier for the abelian twisted quantum double remains the same as the energy barrier without symmetry: constant in the size of the system. This motivates us to consider the boundaries of SPTs protected by 1-form (or other higher-form) symmetries.

3.9 Energy barrier is sufficient

In this section, we consider the timescale for logical faults in the 1-form symmetric RBH model. We estimate the probability that an excitation loop l of size w emerges within the Gibbs ensemble at inverse temperature β . We show that large loop errors are quite rare if the temperature is below a critical temperature T_c , which we lower bound by $2/\log(5)$.

Recall the symmetric excitations are given by applying operators $Z(E', F') = \prod_{f \in F'} Z_f \prod_{e \in E'} Z_e$, where E' is a cycle (i.e., has no boundary) and F' is dual to a cycle on the dual lattice. We will refer to both such subsets E' and F' as cycles, $l = E' \cup F'$, and the resulting excitation $|\psi(l)\rangle$ as an excitation loop configuration. Moreover, we will refer to each connected component of l as a loop (intuitively loops are minimal in that no proper subset of a loop can be a cycle). The energy $E(\gamma)$ of such an excitation configuration is given by $2|(E' \cup F') \cap \mathcal{L}^o| + 2|\partial(E' \cup F') \cap \partial\mathcal{L}|$, i.e., it is proportional to the length of the bulk cycle plus the number of times a bulk cycle touches the boundary. Then the Gibbs state ρ_β is given by the weighted mixture of all symmetric excitations, where the weights are given by

$$P_\beta(\gamma) = \frac{1}{\mathcal{Z}} e^{-\beta E(\gamma)}, \quad \mathcal{Z} = \sum_{\gamma} P_\beta(\gamma), \quad (3.78)$$

and $\gamma = (E', F')$ represents a valid (i.e., symmetric) excitation.

Define $d = \min\{d_Z, d_X, d_{\text{sink}}\}$ from Def. 2. For a logical error to have occurred during the system-bath interaction, we must pass through an excited state $|\psi(c)\rangle$ such that c contains a bulk loop with length $w \geq d - r$, for some constant r independent of system size. (Here a bulk loop is one where at least half of its support is away from the boundary). Let us bound the probability that configurations containing such a loop occurs. Define \mathcal{B}_w to be the set of cycles containing a bulk loop with size at least w . Then

$$\sum_{c \in \mathcal{B}_w} P_\beta(c) \leq \sum_{\substack{\text{loops } l \\ |l| \geq w}} \sum_{\substack{\text{cycles } c \\ l \subset c}} P_\beta(c) \quad (3.79)$$

$$\leq \sum_{\substack{\text{loops } l \\ |l| \geq w}} e^{-\beta E(l)} \sum_{\substack{\text{cycles } c \\ l \not\subset c}} P_\beta(c) \quad (3.80)$$

$$\leq \sum_{\substack{\text{loops } l \\ |l| \geq w}} e^{-\beta E(l)}, \quad (3.81)$$

where from the first to the second line we have used that a configuration c containing a loop l differs in energy from the configuration $c \setminus l$ by $E(c) = e^{-\beta E(l)} E(c \setminus l)$. Now the last line can be rewritten to give

$$\sum_{c \in \mathcal{B}_w} P_\beta(c) \leq \sum_{k \geq w} N(k) e^{-2\beta k}, \quad (3.82)$$

where we have ignored contributions to $E(l)$ due to the boundary (these will only decrease the right hand side of Eq. (3.81)) and $N(k)$ counts the number of loops of size k . Since a loop l resides on either the primal or dual sublattice, each of which has the structure of a cubic lattice, we can obtain a crude upper bound on $N(k)$ by considering a loop as a non-backtracking walk, where at each step one can move in 5 independent directions. This gives the bound $N(k) \leq p(d)5^m = k$, where $p(d)$ is a polynomial in d , and is in particular proportional to the number of qubits.

Then, provided $T \leq 2/\log(5)$, we have

$$\sum_{c \in \mathcal{B}_w} P_\beta(c) \leq p(d) \sum_{k \geq w} e^{k(\log(5)-2\beta)} \quad (3.83)$$

$$= p(d) \frac{e^{k(\log(5)-2\beta)}}{(1 - e^{\log(5)-2\beta})} \quad (3.84)$$

which is exponentially decaying in k (again provided $T \leq 2/\log(5)$). Since errors can be achieved only if we pass through a configuration with a bulk loop of length $d - r$, we have the contribution of configurations that can cause a logical error is bounded by

$$\text{poly}(d) \frac{e^{-\alpha d}}{(1 - e^{-\alpha})} \quad (3.85)$$

where $\alpha = 2\beta - \log(5) > 0$ is satisfied when the temperature is small enough. One can show that the decay rate of the logical operators is exponentially long, and therefore the fidelity of the logical information is exponentially long in the system size (see Proposition 1 of Ref. [62]). One could perform a more detailed calculation to show that, with a suitable decoder, error correction succeeds after an evolution time that grows exponentially in the system size (i.e., that logical faults are also not introduced during the decoding).

We also note that a similar argument can be made for the commuting gauge color code model of Sec. 3.4. A different critical temperature will be observed that depends on the choice of 3-colex.

4 | Universal fault-tolerant measurement-based quantum computation

Abstract

Certain physical systems that one might consider for fault-tolerant quantum computing where qubits do not readily interact, for instance photons, are better suited for measurement-based quantum-computational protocols. We develop a framework to map fault-tolerant procedures for quantum computation that have been natively designed for use with stabilizer codes onto a measurement-based protocol, allowing us to take advantage of the wealth of recent developments from the field of circuit-based fault-tolerant quantum computation with promising alternative architectures. We derive our framework by regarding measurement-based quantum computation as a specific case of gauge fixing where the gauge group of the underlying subsystem code is the union of the stabilizer group of a resource state and a single-qubit measurement pattern. To demonstrate our new framework we construct a new model of universal quantum computation based on the braiding and fusion of foliated topological defects that are akin to Majorana modes.

4.1 Introduction

Candidate quantum computational architectures must be capable of encoding and manipulating quantum information with its available qubits, while simultaneously identifying errors that may be introduced to the system as data is processed. The most suitable approach to perform these tasks should account for the shortcomings of the qubits of the system. Certain architectures where measurements are most readily performed destructively, for instance linear-optical quantum systems, are more amenable to measurement-based models of fault-tolerant quantum computation [26, 247–250]. It is important to support the experimental progress that is being

made with photonic systems [22, 251–258] by discovering new models of quantum computation that are suitable for this architecture.

The three-dimensional topological cluster-state model [136] is the prototypical design for fault-tolerant measurement-based quantum computation [66]. With this model high-threshold universal quantum computation is achieved [172, 259] by supplementing fault-tolerant Clifford gates with magic state distillation [260, 261]. In the original proposal [66], which is often likened to the surface code in a 2+1 dimensional spacetime manifold, logical Clifford operations are realised by braiding tube-like defects that lie within the cluster-state lattice. Braiding these defects realise non-trivial topologies in the manifold which correspond to different logical operations. Notably, photonic implementations of the fault-tolerant cluster-state model are discussed in Refs. [21, 262–264]. Since the work of Raussendorf *et al.* it has since been shown [241], that we can transmit any Calderbank-Shor Steane (CSS) stabilizer code [46, 265] through a specially chosen resource state using single-qubit measurements and classical post processing, and, recently, it was shown that sparse codes generated by this method can be decoded in Ref. [266]. In Ref. [267] it was shown that lattice surgery [70, 71, 73] can be mapped onto a measurement-based computational model, thus offering an alternative to computation by braiding defects. See also recent work in Ref. [268] where the topological cluster-state model is generalised to find robust codes, and Ref. [269] where a new scheme for universal fault-tolerant measurement-based quantum computation is proposed based on the three-dimensional color code [56].

Owing to its high threshold error rates [172, 259, 270] and its experimental amenability the surface code [11, 47] has become the cornerstone of modern designs for fault-tolerant quantum computation. Recently, there have been a number of proposals [214, 271–273] in the quantum error-correction literature that show how to deterministically perform the complete set of Clifford operations with the surface code. However, such schemes make use of twist defects [67], and to the best of our knowledge, there are no CSS variants of the surface code where the lattice supports a twist away from the boundary. This motivates the generalisation of code foliation [241], namely the process of mapping quantum-error correction schemes onto measurement-based computational models.

In the present work, we show how to propagate an arbitrary stabilizer [42] code through a resource state onto an output system via a measurement-based scheme. In addition to this we show how we can compose multiple foliated channels to implement fault-tolerant gates on an input system. We show that this enables us to realise the full Clifford group via fault-tolerant measurement-based quantum computation based on the surface code model. Together with state initialisation that we also discuss, we recover a universal set of quantum computational operations through magic state distillation.

Advantageous to our framework for foliation is that we can show that the output system, which takes the form of a stabilizer code, is determined simply from the input code and a second stabilizer code upon which we base the resource state we use to propagate the input system. Our model significantly simplifies the development of fault-tolerant measurement-based schemes for quantum computation, as we are able to overlook the intricate microscopic details to find the function of a given channel. Instead, we need only consider two codes that we are free to draw from the wealth of well-studied models in the quantum error-correction literature that has accumulated over the last two decades [137, 274, 275] to design new fault-tolerant measurement-based channels. With this simplification, not only can we show how to foliate general stabilizer codes, but we can also compose many foliated channels to realise non-trivial computational operations.

The remainder of this article is organised as follows. We begin by reviewing notation we use to describe quantum error-correcting codes in Sec. 4.2. After introducing some basic notation we summarise the results of this Chapter and give a guide to the reader to parse the different aspects of our model in Sec. 4.3. Then, in Sec. 4.4 develop a microscopic model for the one-dimensional cluster state model as a simple instance of foliation, and we consider parity measurements between separate foliated qubits. In Sec. 4.5 we use the microscopic framework we build to show how a channel system can propagate an input stabilizer code unchanged. We explicitly demonstrate this by foliating the twisted surface code model. In Sec. 4.7 we go on to show that we can manipulate input states with a careful choice of channel systems. We demonstrate this by showing we can perform Clifford gates and prepare noisy magic states with the foliated surface code before offering some concluding remarks.

4.2 Quantum error correction

Here we introduce the notion of a subsystem code [49] that we use to describe the foliated systems of interest. A subsystem code is a generalisation of a stabilizer code [42, 276] where not all of the logical operators of the code are used to encode logical information. The disregarded logical Pauli operators for each gauge qubit are known as gauge operators which have been shown to be useful for a number of other purposes [51, 74, 137, 274, 275].

A subsystem code is specified by its gauge group, $\mathcal{G} \subseteq \mathcal{P}_n$; a subgroup of the Pauli group acting on n qubits. The Pauli group is generated by Pauli operators X_j and Z_j , together with the phase i , where the index $1 \leq j \leq n$ denotes the code qubit the operator acts on. More precisely we have

$$P_j = \underbrace{\mathbb{1} \otimes \mathbb{1} \otimes \cdots \otimes \mathbb{1}}_{j-1} \otimes P \otimes \underbrace{\mathbb{1} \otimes \cdots \otimes \mathbb{1}}_{n-j}, \quad (4.1)$$

where $\mathbb{1}$ is the two-by-two identity matrix and $P = X, Y, Z$ is a Pauli matrix.

The gauge group describes a code space specified by its stabilizer group

$$\mathcal{S} \propto \mathcal{C}(\mathcal{G}) \cap \mathcal{G}, \quad (4.2)$$

where $\mathcal{C}(\mathcal{G})$ denotes the centralizer of a group \mathcal{G} within \mathcal{P}_n which consists of all elements of \mathcal{P}_n that commute with all elements of \mathcal{G} . With the stabilizer group defined we specify the code space as the subspace spanned by a basis of state vectors $|\psi\rangle$ where

$$S|\psi\rangle = (+1)|\psi\rangle. \quad (4.3)$$

By definition, the stabilizer group must satisfy $-1 \notin \mathcal{S}$.

We also consider a generating set of logical operators $\mathcal{L} = \mathcal{C}(\mathcal{G}) \setminus \mathcal{G}$. The group \mathcal{L} is generated by the logical Pauli operators \bar{X}_j, \bar{Z}_j with $1 \leq j \leq k$, such that \bar{X}_j anti-commutes with \bar{Z}_k if and only if $j = k$. Otherwise all logical operators commute with one another.

The logical operators generate rotations within the code space of the stabilizer code. We will frequently make use of the fact that logical operators $L, L' \in \mathcal{L}$ such that $L' = sL$ with $s \in \mathcal{S}$ have an equivalent action on the code space. This follows from the definitions given above. We thus use the symbol ' \sim ' to denote that two operators are equivalent up to multiplication by a stabilizer operator. For instance, with the given example we can write $L' \sim L$.

It is finally worth noting that the special Abelian subclass of subsystem codes, namely stabilizer codes [42, 276], are such that $\mathcal{S} = \mathcal{G}$ up to phases.

4.2.1 Transformations and compositions of codes

It will be important to make unitary maps between subsystem codes. Given the generating set of two different stabilizer codes \mathcal{R} and \mathcal{S} with elements $r \in \mathcal{R}$ and $s \in \mathcal{S}$, the stabilizer group $\mathcal{T} = \mathcal{R} \otimes \mathcal{S}$ is generated by elements $r \otimes 1, 1 \otimes s \in \mathcal{T}$. We also use the shorthand $\mathcal{T} = U\mathcal{S}$ to define the stabilizer group

$$\mathcal{T} = \{UsU^\dagger : s \in \mathcal{S}\}, \quad (4.4)$$

where U is a Clifford operator. Of course, the commutation relations between two operators are invariant under conjugation by a unitary operator.

4.2.2 Expressing Pauli operators as vectors

For situations where one is willing to neglect the phases of elements of the stabilizer group, it is common to write elements of the Pauli group as vectors of a $2n$ -dimensional vector space over a binary field with a symplectic form that captures the commutation relations of the different

elements of the Pauli group [276, 60]. We express Pauli operators in vector notation such that $p = (p^X p^Z)^T$ where $p^X(p^Z)$ are vectors from the n -dimensional vector space over the binary field \mathbb{Z}_2 and the superscript T denotes the transpose of the vector such that, up to phases, the Pauli operator $P \in \mathcal{P}_n$ is expressed $P = \prod_{j=1}^n X_j^{p_j^X} Z_j^{p_j^Z}$.

We will frequently move between Pauli operators and the vectorised notation. It is thus helpful to define the function $v : \mathcal{P}_n \rightarrow \mathbb{Z}_2^{2n}$ such that

$$v(P) \equiv (p^X p^Z)^T, \quad (4.5)$$

where vectors $p^X, p^Z \in \mathbb{Z}_2^n$ are such that

$$P \propto \prod_{j \in |p^X|} X_j \prod_{j \in |p^Z|} Z_j, \quad (4.6)$$

up to a phase factor and we have defined the support of vector p , denoted $|p|$, as the set of elements of p that are non-zero.

Using this notation, we additionally have the symplectic form where, for two vectors p and q specifying two elements of the stabilizer group, we have

$$\Upsilon(p, q) \equiv p^T \lambda_n q, \text{ with } \lambda_n = \begin{pmatrix} 0 & \mathbb{1}_n \\ \mathbb{1}_n & 0 \end{pmatrix}, \quad (4.7)$$

where the summation is taken modulo 2 and $\mathbb{1}_n$ is the $n \times n$ identity matrix such that $\Upsilon(p, q) = 0$ if and only if Pauli operators p and q commute. We also define the inner product

$$p \cdot q \equiv \sum_j p_j q_j, \quad (4.8)$$

where addition is taken modulo 2.

4.3 Foliation

Quantum computation proceeds by using a series of channels where each channel maps its input nontrivially onto some output state [20]. These channels are commonly known as gates, and with an appropriate composition of said channels we can realise non-trivial quantum algorithms. In this work we build a generic model that takes an arbitrary scheme of fault-tolerant quantum computation based on stabilizer codes, and provides a measurement-based protocol that performs the same function.

Channels are readily composed by unifying the output of the last with the input of the next, so here we focus on developing a model of a single channel with an input and an output and a single designated function. Most important is that the channel is tolerant to errors, and as such we show that we can propagate quantum error-correcting codes through a channel in a fault-tolerant manner. While a foliated system is relatively straight forward to understand in comparison to its analogous circuit-based counterpart, its microscopic details can become quite obtuse without subdividing the system into constituent parts that depend on their function. In what follows is a macroscopic overview for the model of foliation we consider with some description of the function of each part. We conclude our overview with a reader's guide which outlines which subdivisions of the total system each section addresses. Nonetheless, the reader should bare the macroscopic structure presented in this section in mind throughout our exposition.

4.3.1 The model

We look to build a foliated system, denoted \mathcal{F} . The channel consists of two components; a resource state, \mathcal{R} , and a measurement pattern, \mathcal{M} , that propagates the input state that is encoded within \mathcal{R} onto the output system. The union of both \mathcal{M} and \mathcal{R} can be regarded as the generating set for subsystem codes.

The resource state is a specially-prepared many-body entangled state known as a graph-state that we describe in more detail shortly. The measurement pattern is a list of single-qubit measurements that are performed on the physical qubits not included in the output system. The measurement pattern is chosen specifically to move the input state through the resource onto the output system up to the data collected from the single-qubit measurements. In addition to this, the data obtained from the measurements is used to determine physical qubits that have experienced errors during the preparation of the resource state or during the readout process.

Abstractly, we can regard the foliation as a gauge-fixing procedure where the foliated system is described by the gauge group

$$\mathcal{F} = \mathcal{R} \cup \mathcal{M}, \tag{4.9}$$

where we use the symbol $\cdot \cup \cdot$ to denote the group generated by elements of both \mathcal{R} and \mathcal{M} . Foliation then is the procedure of preparing system the system \mathcal{R} and subsequently fixing the gauge of \mathcal{F} by measuring \mathcal{M} . The preparation of \mathcal{R} and choice of \mathcal{M} determines the action of the channel, and the data we obtain to identify the locations of errors.

Advantageous to the model we present here is that, provided we choose a channel that is consistent with some stabilizer code in a sense we make precise shortly, and that we choose the graph state of the channel such that it respects some well-motivated symmetry, we need only regard the input and the subsystem code implemented by the channel to understand the logical

effect of the channel on the input system. The microscopic model we build on the other hand will indeed become helpful for the development of numerical simulations to test and compare different foliated systems.

We next briefly elaborate on the resource state \mathcal{R} . The resource state can be decomposed into an entangled channel system \mathcal{K} and ancilla qubits \mathcal{A} together with a unitary operator U^A which couples the ancilla qubits to the channel

$$\mathcal{R} = U^A (\mathcal{K} \otimes \mathcal{A}). \quad (4.10)$$

Supposing that $\mathcal{R} = \mathcal{K}$, the resource state will propagate the input system onto the output system provided no errors occur once the measurements are performed and interpreted. Once coupled to the channel, the ancilla qubits perform two roles upon measurement. First of all they are included to perform check measurements on the channel system to identify errors that may be introduced to the physical system. Their second role is to modify the input system through the channel as it progresses to the output system. This modification is analogous to code deformation in the more familiar circuit-based model of quantum computation [68, 148, 214, 270]. Later we will investigate how different choices of channel affect the transformation made on the input state.

The microscopic details of the channel system require careful bookkeeping; a system for which we introduce below, but broadly speaking, the channel system is a series of one-dimensional cluster states that propagates the input quantum error-correcting code. The one-dimensional cluster state can be used as a channel for a single physical qubit where a qubit is encoded on the first site of the system and measurements are performed to move the encoded qubit onto the last qubit of the chain. The channel system then uses a single one-dimensional cluster state for each qubit of the input code to move each of the code qubits onto the output system of each chain. Using a single chain to move each qubit of the input code thus provides a measurement-based channel for an entire quantum error-correcting code that may consist of many qubits. We discuss different approaches to for moving information through individual chains as this determines different ways we might choose to couple ancilla to the different chains to perform different functions throughout the channel.

4.3.2 A guide for the reader

The following exposition follows a number of avenues to help better understand foliated systems both at the microscopic and the macroscopic level, but ultimately all the sections have the model presented above in common. We thus provide a guide to help explain the aspects of the fault-tolerant measurement-based model we build over the course of this article.

The main results are stated most abstractly in Sec. 4.5. This section states the general results we obtain, namely, we describe the action a given foliated system will have on an input code which is manifest at the output system once the data from the single-qubit measurement pattern has been collected and processed. The section also describes the check observables that are collected at the microscopic level of the foliated system that are used to identify the locations of errors. This will become important when discussing the error-correction procedure for the foliated system.

In order to understand the details of Sec. 4.5 we must first examine closely the one-dimensional cluster state that propagates qubits through an entangled system of physical qubits by means of single-qubit measurements. In Sec. 4.4 we study the one-dimensional system and we build notation to describe parity measurements between qubits propagated through a series of one-dimensional cluster-states that make up the measurement-based channel for a quantum error-correcting code. The details presented in this section are necessary to understand the technical aspects of the proof we give in Sec. 4.5.

Beyond Sec. 4.5 we look at specific instances of the general theory we develop. Indeed, in Sec. 4.6 we examine the microscopic details of the foliated variant of the twisted surface code. This presents a non-trivial generalisation of the foliated models considered in Ref. [241] since there exists no CSS representation of this model. In Sec. 4.7 we show at a logical level how we can compose different channels to realise fault-tolerant measurement-based quantum computation. We consider a model based on surface code quantum computation using code deformations as an example of our framework.

In Fig. 4.1 we show a schematic diagram of how fault-tolerant measurement-based quantum computation will proceed. The figure shows the composition of three channels, each of which perform a different operation. The system is measured such that the logical data is mapped from the input system to the output system, under an operation that is determined by the choice of different resource states. Each of the sections describe how to produce different channels that can be composed to realise measurement-based quantum-computational protocols.

4.4 Foliated qubits

Measurement-based quantum computation proceeds by performing single-qubit measurements on a specially prepared many-body entangled state. We begin by focusing on a one-dimensional cluster state which propagates a single-qubit along a line.

To foliate a quantum error-correcting code we first encode each of the code qubits of a quantum error-correcting code onto a separate one-dimensional cluster state. We can propagate the quantum error-correcting code through this collection of one-dimensional chains from one end

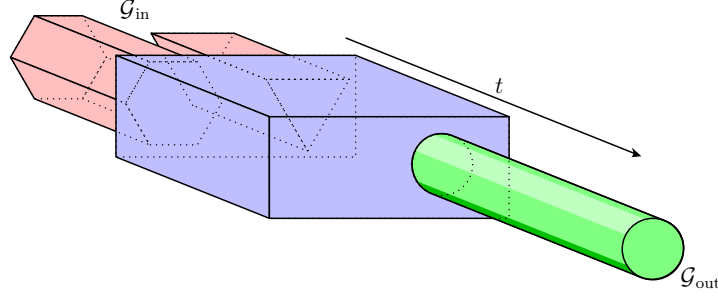


Fig. 4.1 Three resource states shown in red, blue and green are composed to map an input state onto the output state under a mapping determined by the different resource states. A temporal direction can be assigned such that the input system is input at the initial time and the output system emerges at the final instance.

to the other via single-qubit measurements. To this end we examine here the one-dimensional cluster state and show how to move quantum information along the chain by making different types of single-qubit measurements on the physical qubits of the system. We additionally show how to perform parity measurements between several chains using additional ancilla qubits.

4.4.1 The one-dimensional cluster state

The cluster state is readily described using the stabilizer formalism introduced above. However, while discussing the cluster-state wire we will denote Pauli matrices acting on the physical qubit indexed μ with operators $\sigma^X[\mu]$, $\sigma^Y[\mu]$ and $\sigma^Z[\mu]$ to discriminate them from Pauli matrices that act on the code qubits of the input and output quantum error-correcting code. Similarly, the logical operators of the cluster state are denoted X , Y and Z without the bar notation for the same reason. The logical qubits of the one-dimensional cluster-state wire will become the code qubits of foliated stabilizer codes as this discussion progresses. To this end, wherever there is ambiguity, we will refer to the qubits that lie in a cluster state as ‘physical qubits’. These qubits are not to be confused with the ‘code qubits’ of a quantum error-correcting code.

To describe the cluster state we first consider the initial product state $|\psi\rangle_1|+\rangle_2|+\rangle_3\ldots|+\rangle_N$ where $|\psi\rangle$ is an arbitrary single-qubit state, the states $|\pm\rangle$ are eigenstates of the Pauli-X matrix, i.e., $\sigma^X|\pm\rangle = (\pm 1)|\pm\rangle$. We can express this state with the stabilizer group $\mathcal{I} = \langle \sigma^X[\mu] \rangle_{\mu=2}^N$ whose logical operators are $X = \sigma^X[1]$ and $Z = \sigma^Z[1]$. The cluster state, whose stabilizer group we denote as $\mathcal{K} = U\mathcal{I}$, with U defined as

$$U = \prod_{\mu=1}^{N-1} U^Z[\mu, \mu+1], \quad (4.11)$$

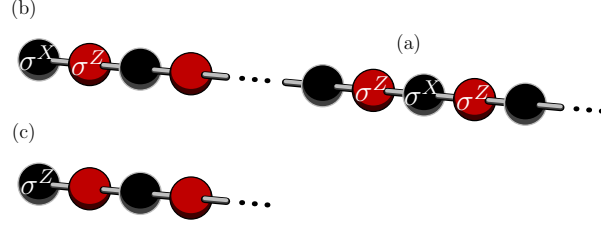


Fig. 4.2 The one-dimensional cluster state. Physical qubits are shown as vertices ordered along a line where the left-most vertex represents the first qubit of the system and edges indicated pairs of vertices that are entangled via a controlled-phase gate. (a) A stabilizer operator denoted C_μ shown at an arbitrary point along the lattice. (b) and (c) show, respectively the logical Pauli-X and Pauli-Z operators once the cluster state is initialised.

where $U^Z[\mu, \nu] = (1 + \sigma^Z[\mu] + \sigma^Z[\nu] - \sigma^Z[\mu] \sigma^Z[\nu])/2$ is the controlled-phase gate. The unitary operator U couples nearest-neighbour pairs of physical qubits along the open chain.

The following facts about the controlled-phase gate are helpful throughout our exposition. We firstly note that operators $U^Z[\mu, \nu]$ and $\sigma^Z[\rho]$ commute for an arbitrary choice of μ, ν and ρ . Moreover, $U^Z[\mu, \nu]$ and $U^Z[\rho, \lambda]$ commute for any μ, ν, ρ and λ . Further, the Hermitian entangling gate satisfies the relationship

$$U^Z[\mu, \nu] \sigma^X[\mu] U^Z[\mu, \nu] = \sigma^X[\mu] \sigma^Z[\nu]. \quad (4.12)$$

We also have that $U^Z[\mu, \nu] = U^Z[\nu, \mu]$ by definition.

With the above definitions it is readily checked that \mathcal{K} is generated by operators

$$C[\mu] = \sigma^Z[\mu - 1] \sigma^X[\mu] \sigma^Z[\mu + 1], \quad (4.13)$$

for $2 \leq \mu \leq N - 1$ and the stabilizer

$$C[N] = \sigma^Z[N - 1] \sigma^X[N]. \quad (4.14)$$

The logical operators that act on the encoded qubit are

$$X = \sigma^X[1] \sigma^Z[2], \quad Z = \sigma^Z[1]. \quad (4.15)$$

We show examples of a stabilizer operator, and the logical Pauli-X and Pauli-Z operator in Fig. 4.2. We point out that, as is common when describing cluster states, we use a graphical notation to describe states of interest. In particular, pairs of qubits that are coupled via a controlled-phase gate are connected by an edge of a graph where each qubit is represented by vertex.

The goal of the one-dimensional cluster state is to transport the logical information along the chain onto the last qubit, indexed N . To do so we make single qubit measurements on all of the qubits except qubit N . We study two different types of foliated qubits. The first, which is already well understood in the literature, transmits information by measuring the physical qubits in the Pauli-X basis, and the second, which does not appear in the literature to the best of our knowledge, moves information using Pauli-Y measurements. We refer to these two foliated qubits as type-I and type-II foliated qubits respectively. While we find that using type-I qubits is sufficient to realise any foliated system of interest within the scope we set here, we believe that there may be practical advantages to be gleaned using type-II qubits in a foliated scheme. As such we dedicate a later section to the type-II foliated qubits in Sec. 4.9.1 and we discuss their potential applications throughout our exposition. For simplicity though we focus only on type-I foliated qubits in the main text.

4.4.2 Measurement-based qubit transmission

We review here a foliated qubit where the physical qubits of the entangled chain are measured in the Pauli-X basis whose stabilizer group is \mathcal{K} as defined above. We first look at the action of measuring the first physical qubit of the system. In particular we are interested in the action of the measurement on the logical operators. This action is easily understood by finding logical operators that commute with the measurement. We find logical operators that commute with the measurement operator $M_1 = \sigma^X [1]$ by multiplying the logical operators by stabilizer operators. We find that the logical operator

$$Z \sim \sigma^X [2] \sigma^Z [3], \quad (4.16)$$

commutes with $\sigma^X [1]$. Similarly X , as defined above, commutes with the measurement operator M_1 . After making the measurement we project the code such that we have a new stabilizer $C[1] \in \mathcal{K}$ where $C[1] \equiv x_1 M_1 = x_1 \sigma^X [1]$. Multiplying X by C_1 we have

$$X \sim x_1 \sigma^Z [2]. \quad (4.17)$$

The stabilizer $C[2]$ is removed from \mathcal{K} . Having accounted for the measurement outcome we can also disregard the first qubit of the chain since the projective measurement has disentangled it from the rest of the system.

It is important to note that the logical operator X , up to the sign determined by the measurement outcome, is now a single-qubit Pauli-Z operator acting on the second qubit. In contrast, before the measurement, the logical operator Z that was a single-qubit Pauli-Z operator acting on the first qubit has now become a weight-two operator acting on the second and third physical qubits along the chain. We show the logical Pauli-X and Pauli-Z operators

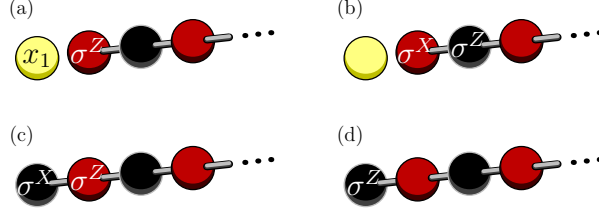


Fig. 4.3 The logical operators of the one-dimensional cluster state after and before the first qubit is measured in the Pauli-X basis. In (a) we show the logical Pauli-X operator and in (b) we show the logical Pauli-Z operator after the first qubit is measured, and the measurement outcome x_1 is returned. Importantly, after the measurement the logical Pauli-X operator is a single-qubit Pauli-Z operator on the second qubit, whereas the logical Pauli-Z operator is supported on two physical qubits. In contrast, before the measurement the logical Pauli-Z operator is supported on a single qubit, whereas the logical Pauli-X operator is a weight-two operator. We show the logical Pauli-X and logical Pauli-Z operator in (c) and (d), respectively.

after the first qubit has been measured in Figs. 4.3(a) and (b). We compare these logical operators with the same logical operators before the measurement has taken place in Figs. 4.3(c) and (d), respectively.

The advantage of measurement-based quantum computation lies in the fact that once the resource state is prepared, quantum information can be transmitted and processed by performing single-qubit measurements on qubits of the resource state. Supposing then that we can only make single-qubit measurements, we see that we can measure the logical operator Z with the single-qubit measurement σ^Z [1] on the first qubit. Conversely, to infer the value of X , we measure the first qubit in the Pauli-X basis, and the second qubit in the computational basis. We thus see that we can learn either the logical Pauli-X or Pauli-Z information from the cluster state by measuring the appropriate physical qubit in the Pauli-Z basis, and the qubits that preceded it in the Pauli-X basis. Alternatively, were we to measure both qubit 1 and qubit 2 in the Pauli-X basis, we would have moved the logical information along the chain without having inferred any logical data.

To find a general expression for the logical operators, suppose we have measured the first $\tau - 1$ physical qubits in the Pauli-X basis which returned outcomes $x_\mu = \pm 1$ for $\mu < \tau$. We then have that

$$X \sim \left(\prod_{\mu=1}^{\tau/2} x_{2\mu-1} \right) \sigma^Z [\tau], \quad (4.18)$$

$$Z \sim \left(\prod_{\mu=1}^{\tau/2} x_{2\mu} \right) \sigma^X [\tau] \sigma^Z [\tau + 1], \quad (4.19)$$

for even τ and

$$X \sim \left(\prod_{\mu=1}^{(\tau-1)/2} x_{2\mu-1} \right) \sigma^X [\tau] \sigma^Z [\tau + 1], \quad (4.20)$$

$$Z \sim \left(\prod_{\mu=1}^{(\tau-1)/2} x_{2\mu} \right) \sigma^Z [\tau], \quad (4.21)$$

where τ is odd. With this, we see that we can learn the logical Pauli-X information using single-qubit measurements on sites where τ is even and logical Pauli-Z information on sites where τ is odd, given that we have outcomes for the physical Pauli-X measurements made on the first $\tau - 1$ qubits. To this end, we find that it is particularly convenient to use a new notation to index the qubits of the chain. We define

$$X(t) = 2t, \quad Z(t) = 2t - 1, \quad (4.22)$$

such that now we can rewrite the logical operators of the system such that

$$X \sim \Sigma^X(t) \sigma^Z [X(t)], \quad Z \sim \Sigma^Z(t) \sigma^Z [Z(t)], \quad (4.23)$$

for any t , where the operators

$$\Sigma^X(t) \equiv \prod_{\mu=1}^t \sigma^X [Z(\mu)], \quad \Sigma^Z(t) \equiv \prod_{\mu=1}^{t-1} \sigma^X [X(\mu)]. \quad (4.24)$$

Importantly, the operators $\Sigma^X(t)$ and $\Sigma^Z(t)$ are the tensor product of the Pauli-X matrix. This means these operators are inferred from the single-qubit measurement pattern if all the qubits along the chain are measured in the Pauli-X basis as is the case for type-I foliated qubits.

The above redefinition of indices is such that at each ‘time’ interval, indexed by t , we can recover either the logical Pauli-X or Pauli-Z information from the chain with a single-qubit Pauli-Z measurement provided the previous qubits along the chain have been measured in the Pauli-X basis. Specifically, each interval contains two adjacent qubits of the chain, the first, which lies at site $\tau = 2t - 1$, gives access to the Pauli-Z information via a single-qubit measurement, and at every second site, $\tau = 2t$, we can learn logical Pauli-X information with a single-qubit Pauli-Z measurement. We show the logical operators at a given time interval in Fig. 4.4.

4.4.3 Measurements using ancilla

We have thus far imagined replacing the single-qubit Pauli-X measurement on some appropriately chosen qubit with a Pauli-Z measurement to perform logical measurements on the propagated information. To develop foliated codes further we will require the ability to perform logical measurements without adapting the measurement pattern of the foliated qubits. Instead we couple extra ancilla qubits to the system to learn logical information at a given time interval.

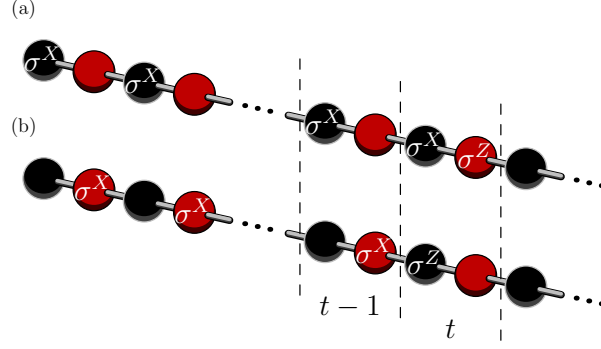


Fig. 4.4 (a) Logical Pauli-X and (b) logical Pauli-Z operators at time interval t . Each time interval contains one black vertex and one red vertex. Local to each time interval we can adjust our single-qubit measurement pattern by measuring the appropriate qubit in the Pauli-Z operator to measure either the logical Pauli-X or Pauli-Z operator given that the preceding qubits of the system are measured in the Pauli-X basis.

To show how to make a logical measurement of a one-dimensional cluster state with an ancilla we consider the resource state $\mathcal{R} = U^A (\mathcal{K} \otimes \mathcal{A})$, as we have introduced in Eqn. (4.10), where the channel \mathcal{K} is the one-dimensional cluster state described above and $\mathcal{A} = \langle \sigma^X [a] \rangle$ describes the stabilizer group of a single ancilla qubit we couple to \mathcal{K} with unitary U^A which we specify shortly. We use the elements of \mathcal{A} to measure logical information from \mathcal{K} .

We must specify a measurement pattern to carry out the propagation of information, as well as the single-qubit measurement we make on the ancilla to learn logical information from the resource state. We write the pattern of measurements

$$\mathcal{M} = \mathcal{M}^C \cup \mathcal{M}^A, \quad (4.25)$$

where $\mathcal{M}^C(\mathcal{M}^A)$ describes the measurements made on subsystem $\mathcal{K}(\mathcal{A})$. For the case of type-I foliated qubits discussed previously we have $\mathcal{M}^C = \langle \{ \sigma^X [\mu] \}_{\mu=1}^{N-1} \rangle$. After the measurements are performed the resulting quantum information is maintained on the output qubit which is the last qubit of the chain.

Logical operators of the resource state, $P \in \mathcal{L} = \mathcal{C}(\mathcal{R}) \setminus \mathcal{R}$, are measured if $P \sim P' \in \mathcal{M}$. For now we choose $\mathcal{M}^A = \langle \sigma^X [a] \rangle$ to this end. In this example we couple the ancilla to the target qubit indexed $T = P(t)$ with unitary $U^A = U^Z[T, a]$ to perform a logical measurement $P \in \mathcal{L}$ where $P = X, Z$ is a logical Pauli operator.

We check that $P' \in \mathcal{M}$ by studying the stabilizer group of the resource state \mathcal{R} . The state has stabilizers

$$C[a] = \sigma^X [a] \sigma^Z [T], \quad (4.26)$$

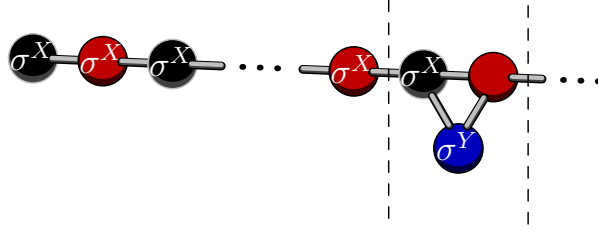


Fig. 4.5 The logical Pauli-Y operator on a type-I foliated qubit where the blue ancilla qubit is coupled both to qubits $Z(t)$ and $X(t)$ of the chain. The logical operator commutes with the measurement pattern where all of the qubits along the chain are measured in the Pauli-X basis, and the ancilla qubit is measured in the Pauli-Y basis, thus allowing us to recover Pauli-Y data from the foliated qubit.

and

$$C[T] = \sigma^Z [T-1] \sigma^X [T] \sigma^Z [T+1] \sigma^Z [a]. \quad (4.27)$$

Now, using that $P \sim P' = \Sigma^P(t) \sigma^Z [P(t)]$ we have

$$P \sim P' C[a] = \Sigma^P(t) \sigma^X [a] \in \mathcal{M}, \quad (4.28)$$

provided $\mathcal{M}^A = \langle \sigma^X [a] \rangle$ as prescribed, thus giving the desired logical measurement at time interval t once the resource state is measured with measurement pattern \mathcal{M} .

We additionally find that we can measure the logical Pauli-Y information from a type-I foliated qubit using an ancilla-assisted measurement. We achieve this by coupling the ancilla to multiple target qubits. To show this we continue with the resource state model \mathcal{R} given in Eqn. (4.10) where again we have $\mathcal{A} = \langle \sigma^X [a] \rangle$ and \mathcal{K} is a one-dimensional cluster state. The chain is measured as a type-I foliated qubit such that $\mathcal{M}^C = \langle \left\{ \sigma^X [\mu] \right\}_{\mu=1}^{N-1} \rangle$, and we couple the ancilla to the chain with the unitary $U^A = U^Z[Z(t), a] \times U^Z[X(t), a]$. We find that $Y \sim Y' \in \mathcal{M}$ provided $\mathcal{M}^A = \langle \sigma^Y [a] \rangle$ as we show below.

From the discussion given, we have that the operator $i \left(\Sigma^X(t) \sigma^Z [X(t)] \right) \left(\Sigma^Z(t) \sigma^Z [Z(t)] \right)$ is a representative of the logical Pauli-Y operator for \mathcal{K} . It is then readily checked then that

$$iXZ \sim Y' = i \left(\Sigma^X(t) \sigma^Z [X(t)] \right) \left(\Sigma^Z(t) \sigma^Z [Z(t)] \right) \sigma^Z [a], \quad (4.29)$$

is a representative of the logical Pauli-Y operator of \mathcal{R} using the expressions given in Eqns. (4.12) and (4.24). Then using the stabilizer $C[a] \in \mathcal{R}$ where,

$$C[a] = \sigma^X [a] \sigma^Z [Z(t)] \sigma^Z [X(t)], \quad (4.30)$$

we find that $iXZ \sim Y'C[a] \in \mathcal{M}$ provided $\mathcal{M}^A = \langle \sigma^Y[a] \rangle$ which is depicted in Fig. 4.5, thus showing we can infer the logical Pauli-Y data of a type-I foliated qubit from \mathcal{M} by coupling to multiple targets. We finally remark that one can show that the resource state with $U^A = U^Z[T_1, a] \times U^Z[T_2, a]$ where $T_1 = X(t_1)$ and $T_2 = Z(t_2)$ such that $t_1 \neq t_2$, we also recover encoded Pauli-Y information. We do not require this degree of generality here so we leave the proof of this fact as an exercise to the reader.

We conclude this subsection by summarising the differences between type-I foliated qubits considered here and the type-II qubits discussed in Sec. 4.9.1. Indeed, here we have shown that we can make a Pauli-Y measurement with a foliated qubit by coupling an ancilla to two target qubits. In contrast, following an argument similar to that given above, by measuring the physical qubits of a foliated chain in the Pauli-Y basis instead of the Pauli-X basis we find that we can measure the Pauli-Y operator by coupling an ancilla to a single qubit. This comes at the expense of including three qubits at each time interval instead of two, as is the case with type-I foliated qubits. As such, the physicist that is looking to perform a measurement-based experiment that demands a significant number of Pauli-Y measurements should decide carefully whether type-I or type-II foliated qubits are the most appropriate depending on whether the number of physical qubits or generating interactions between pairs of physical qubits is the most precious commodity of a given laboratory.

4.4.4 Parity measurements with foliated qubits

In general it will be necessary to make parity measurements between several foliated qubits that are encoded on different chains. We now specify the channel of a resource state consisting of several foliated qubits, together with its ancilla system to which it is entangled that affects the obtained logical measurements. More precisely we consider the resource state $\mathcal{R} = U^A(\mathcal{K} \otimes \mathcal{A})$, of n foliated qubits. As in the previous section, for now we consider a single ancilla prepared in a known eigenstate of the Pauli-X basis. The channel of the resource state is such that

$$\mathcal{K} = \bigotimes_{j=1}^n \mathcal{K}_j, \quad (4.31)$$

and $\mathcal{K}_j = U_j \mathcal{I}_j$ is the stabilizer group of the j -th one-dimensional cluster state of length N_j as defined in Subsec. 4.4.1. It will also become helpful later on to define the unitary operator that entangles the initial state to give the channel system, namely

$$U^C = \bigotimes_{j=1}^n U_j, \quad (4.32)$$

where $U_j = \prod_{\mu=1}^{N-1} U_j^Z[\mu, \mu+1]$. This will be helpful where we consider variations on the initial state $\mathcal{I} = \bigotimes_{j=1}^n \mathcal{I}_j$. One could choose the length of each cluster arbitrarily but for simplicity we suppose that all the type-I chains have an equal length $N_j = 2D + 1$ where D is the number of time intervals and we include an additional qubit at the end of the chain to support the output of each foliated qubit.

The logical operators of \mathcal{K}_j are denoted X_j and Z_j , and its physical qubits are indexed $X_j(t)$ and $Z_j(t)$ according to Eqn. (4.22) where indices have been appended. Again, we have for logical operators $P_j = X_j, Z_j$ such that

$$P_j \sim \Sigma_j^P(t) \sigma^Z[P_j(t)]. \quad (4.33)$$

with respect to the stabilizer group \mathcal{K} . For now we consider the ancilla system that includes only a single ancilla qubit, i.e., $\mathcal{A} = \langle \sigma^X[a] \rangle$.

The measurement pattern for the foliated system $\mathcal{M} = \mathcal{M}^C \otimes \mathcal{M}^A$ is specified

$$\mathcal{M}^C = \bigotimes_{j=1}^n \mathcal{M}_j^C, \quad (4.34)$$

where \mathcal{M}_j^C is the set of single-qubit measurements acting for the cluster \mathcal{K}_j . We have that $\mathcal{M}_j^C = \langle \{ \sigma^X[\mu] \}_{\mu=1}^{N_j-1} \rangle$ for type-I foliated qubits. We determine the measurements we make on the ancilla system, \mathcal{M}^A , depending on the choice of parity measurement.

We look to prepare \mathcal{R} such that we measure the logical Pauli operator $P \in \mathcal{P}_n$ by measuring the ancilla qubit in an appropriate basis. We thus couple the ancilla to the channel to construct \mathcal{R} as such with unitary

$$U^A = \prod_{j \in |p^X|} U^Z[X_j(t), a] \prod_{j \in |p^Z|} U^Z[Z_j(t), a], \quad (4.35)$$

where $p = (p^X p^Z)^T$ such that $p = v(P)$ as defined in Eqn. (4.5). Again, for simplicity, we have coupled the ancilla to the physical qubits of a common time interval t , but showing our construction is general beyond this constraint is straight forward. In fact, as we will observe, we find practical benefits from coupling an ancilla to physical qubits in different time intervals later in Sec. 4.6.

Upon coupling the ancilla to the channel system to form the resource state will include the stabilizer $C[a] = U^A \sigma^X[a] U^{A\dagger} \in \mathcal{R}$ such that

$$C[a] = \sigma^X[a] \prod_{j \in |p^X|} \sigma^Z[X_j(t)] \prod_{j \in |p^Z|} \sigma^Z[Z_j(t)]. \quad (4.36)$$

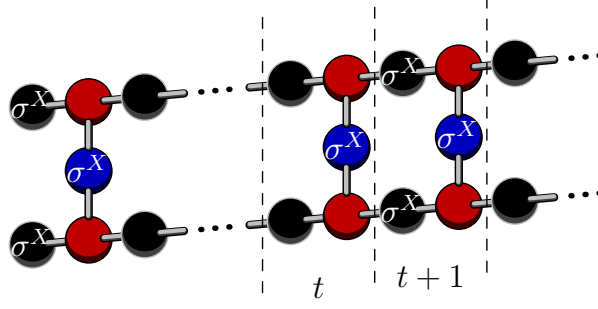


Fig. 4.6 Two type-I foliated qubits where ancillas are coupled to perform X_1X_2 parity measurements. To the left of the figure we show a logical operator $\sim X_1X_2$ by coupling an ancilla, shown in blue, to qubits $X_1(1)$ and $X_2(t)$. To the right of the figure we show an element of the measurement pattern that is generated by two parity measurements that are made at different time intervals.

We additionally have logical operators of the resource state

$$X_j \sim \sigma^Z[a]^{p_j^Z} \Sigma_j^X(t) \sigma^Z[X_j(t)], \quad (4.37)$$

and

$$Z_j \sim \Sigma_j^Z(t) \sigma^Z[Z_j(t)]. \quad (4.38)$$

which follows from Eqn. (4.12) and the definition of the logical operators of the channel system \mathcal{K} shown in Eqn. (4.33) where p_j^Z is the j -th element of the vector p^Z . Combining the above expressions we find $P' \sim P$ such that

$$\begin{aligned} P' &= \sigma^Z[a]^{p^X \cdot p^Z} \prod_{j \in |p^X|} \Sigma_j^X(t) \sigma^Z[X_j(t)] \\ &\times \prod_{j \in |p^Z|} \Sigma_j^Z(t) \sigma^Z[Z_j(t)]. \end{aligned} \quad (4.39)$$

It follows then that $P \sim P'C[a]$ such that

$$P'C[a] = \sigma^X[a] \sigma^Z[a]^{p^X \cdot p^Z} \prod_{j \in |p^X|} \Sigma_j^X(t) \prod_{j \in |p^Z|} \Sigma_j^Z(t). \quad (4.40)$$

We therefore have that $P \sim C[a]P' \in \mathcal{M}$ provided we choose $\sigma^X[a] \sigma^Z[a]^{p^X \cdot p^Z} \in \mathcal{M}^A$, thus showing we can infer the logical operator P from the measurement data given an appropriate choice of measurements \mathcal{M} . To the left of Fig. 4.6 we show the element $P' \in \mathcal{M}$ with $P' \sim P = X_1X_2$ measured from a pair of type-I foliated qubits. We also show a parity check $P' \in \mathcal{M}$ in Fig. 4.7 such that we measure $P' \sim P = Y_1Y_2$. In this case the ancilla qubit couples with each foliated qubit twice to include Pauli-Y terms in the check.

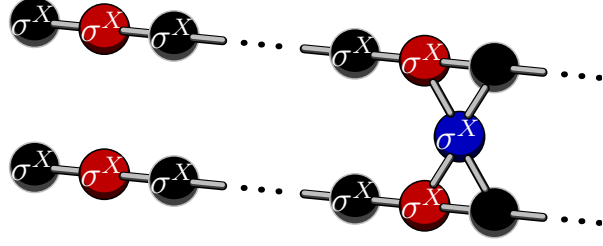


Fig. 4.7 Two type-I foliated qubits where we use the ancilla to measure the parity of the two foliated qubits in the Pauli-Y basis. The ancilla is coupled to an $X(t)$ and a $Z(t)$ target for each qubit. We measure the ancilla in the Pauli-X basis, since there are an even number of Pauli-Y terms in the parity measurement.

4.4.5 The compatibility of parity measurements

Having now discussed how to include a single logical measurement in the foliated system, we next investigate the conditions under which we can simultaneously measure two degrees of freedom of the input system, P and Q where $P, Q \in \mathcal{P}_n$.

We now consider a resource state \mathcal{R} with two ancillas $\mathcal{A} = \langle \sigma^X[a], \sigma^X[b] \rangle$ that are coupled to the channel $\mathcal{K} = \bigotimes_j \mathcal{K}_j$ at time intervals t and t' , respectively, via unitary $U^A = U_a U_b$ where

$$U_a = \prod_{j \in |p^X|} U^Z[X_j(t), a] \prod_{j \in |p^Z|} U^Z[Z_j(t), a], \quad (4.41)$$

and

$$U_b = \prod_{j \in |q^X|} U^Z[X_j(t'), b] \prod_{j \in |q^Z|} U^Z[Z_j(t'), b]. \quad (4.42)$$

where $p = v(P)$ and $q = v(Q)$. The measurement pattern is chosen according to the rules above such that the chosen parity measurements are made correctly. In any case ancillas a and b are measured in either the Pauli-X or Pauli-Y basis. We first suppose that $t' \neq t$, and afterwards we look at the more complicated case where $t = t'$. As we will show, we find that we can measure both P and Q simultaneously from the logical space of the channel provided P and Q commute. While the setup presented above is sufficient if both U_a and U_b are coupled to the channel at two different time intervals, we find that in certain situations it is necessary to modify U^A in order to measure both P and Q with a coupling at a common time interval.

Without loss of generality we begin with the case where $t < t'$ such that P' as in Eqn.(4.40) is an element of \mathcal{R} since this operator shares no common support with U_b . The resource state additionally includes the representation of the logical operator $Q' \sim Q$ such that

$$Q' = U_a \left(M[b] \prod_{j \in |q^X|} \Sigma_j^X(t') \prod_{j \in |q^Z|} \Sigma_j^Z(t') \right) U_a^\dagger \quad (4.43)$$

where we take $M[b] = \sigma^X[b] \sigma^Z[b]^{q^X \cdot q^Z}$ which follows from the inclusion of the term $C[b] = U_b \sigma^Z[b] U_b^\dagger \in \mathcal{R}$. To determine the value of Q' we are interested in the commutation relations between the operator U_a and the operators $\Sigma_j^X(t')$ and $\Sigma_j^Z(t')$ which share mutual support on the physical system. Using Eqns. (4.12) and (4.33) it follows that

$$U_a \Sigma_j^X(t') U_a^\dagger = \Sigma_j^X(t') \sigma^Z[a]^{p_j^Z}, \quad (4.44)$$

and

$$U_a \Sigma_j^Z(t') U_a^\dagger = \Sigma_j^Z(t') \sigma^Z[a]^{p_j^X}. \quad (4.45)$$

Given that $U_b M[a] U_b^\dagger = M[b]$ we thus have that

$$Q' = M[b] \sigma^Z[a]^{\Upsilon(p,q)} \prod_{j \in |q^X|} \Sigma_j^X(t') \prod_{j \in |q^Z|} \Sigma_j^Z(t'), \quad (4.46)$$

where $\Upsilon(p, q)$ is given in Eqn. (4.7). In this case, for $\Upsilon(p, q) \neq 0$ we must measure ancilla a in the Pauli-Z basis in order to infer the value of Q from the measurement pattern. On the other hand, to measure P we must measure ancilla a in either the Pauli-X basis or the Pauli-Y basis to infer its value from \mathcal{M} . The conclusion of this discussion is that we cannot infer both measurements P and Q from \mathcal{M} unless $\Upsilon(p, q) = 0$ in order for them to be measured simultaneously from the logical space of the channel. This is consistent with the standard postulates of quantum mechanics which only permits the simultaneous measurement of both P and Q provided the operators commute.

We next consider the case that $t = t'$. In this case we have that

$$U_a \Sigma_j^X(t) U_a^\dagger = \Sigma_j^X(t) \sigma^Z[a]^{p_j^Z}, \quad (4.47)$$

and

$$U_b \Sigma_j^X(t) U_b^\dagger = \Sigma_j^X(t) \sigma^Z[b]^{q_j^Z}. \quad (4.48)$$

Unlike the previous case though, U_a and U_b commute with $\Sigma_j^Z(t)$ terms. To this end we find that

$$P \sim M[a] \sigma^Z[b]^{p^X \cdot q^Z} \prod_{j \in |p^X|} \Sigma_j^X(t) \prod_{j \in |p^Z|} \Sigma_j^Z(t), \quad (4.49)$$

and

$$Q \sim M[b] \sigma^Z[a]^{p^Z \cdot q^X} \prod_{j \in |q^X|} \Sigma_j^X(t') \prod_{j \in |q^Z|} \Sigma_j^Z(t'), \quad (4.50)$$

where $M[a]$ and $M[b]$ are either Pauli-X or Pauli-Y measurements. We thus see that with the current choice of U^A the measurements of both P and Q are incompatible unless both $p^X \cdot q^Z = 0$ and $p^Z \cdot q^X = 0$; conditions which ensures that P and Q commute. Indeed, if $PQ = QP$ then $p^X \cdot q^Z = p^Z \cdot q^X$.

We also find that it is possible to modify the channel to measure two commuting operators, P and Q . One approach to deal with this issue, as we have already discovered, is to measure the two operators at different time intervals. A smaller modification may simply be to change only a subset of the target qubits of either U_a or U_b onto a different time interval. We present an example where we use this method to good effect in the following Section. Alternatively, we can include an additional controlled-phase gate, $U^Z[a, b]$, in the entangling circuit U^A which also recovers the compatibility of the two commuting measurements.

4.5 The foliated system

Having discussed how to propagate logical information along a one-dimensional cluster state, and how to make parity measurements between the logical qubits encoded over several chains, we are now ready to define the foliated channel; the system that will propagate an input quantum error-correcting code onto an output state. Further, we will also see that with a suitable choice of resource state we are able to measure the input state in such a way to deform the code with the foliated system. In what follows we sketch out the different components we use to make up a foliated system before presenting two theorems that describe its function. Specifically, we will require definitions of the initial system, the channel system, the resource state and the system after the prescribed pattern of measurements is made. Theorem. 1 then explains the action of the foliated system on the logical input state, and Theorem. 2 describes stabilizer checks we can use to identify errors that act on the physical qubits of the foliated system. See Ref. [72] for a related discussion from the perspective of code deformations with stabilizer codes. The construction is summarised in Fig. 4.8.

As described in Sec. 4.3, the foliated system is defined as

$$\mathcal{F} = \mathcal{R} \cup \mathcal{M}, \quad (4.51)$$

where \mathcal{R} is the resource state, and \mathcal{M} is the measurement pattern. The system \mathcal{F} is jointly determined by an input code \mathcal{G}_{in} and a channel code \mathcal{G}_{ch} . Also to be determined is the length of the channel D , which, unless otherwise stated, we suppose is large, i.e. comparable to the distance of the code \mathcal{G}_{ch} . We assume that both codes \mathcal{G}_{in} and \mathcal{G}_{ch} are stabilizer codes and, moreover, are supported on the same set of qubits that we index $1 \leq j \leq n$.

The resource state is of the form $\mathcal{R} = U^A(\mathcal{K} \otimes \mathcal{A})$ where \mathcal{K} is the channel system and \mathcal{A} is a set of ancilla qubits prepared in a product state that we couple to the channel with unitary operator U^A . The channel \mathcal{K} is specified by \mathcal{G}_{in} . The ancilla system \mathcal{A} and the entangling unitary U^A are determined by a generating set of \mathcal{G}_{ch} .

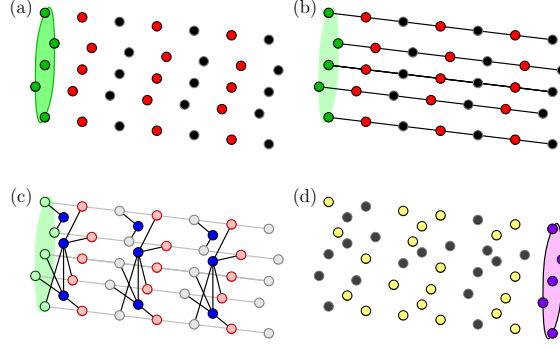


Fig. 4.8 Sketch of the foliation process and construction of the system. Time moves from left to right across the page in each figure. (a) The initial system, \mathcal{I} , consists of an input code, \mathcal{G}_{in} , shown with green qubits to the left of the figure, and other qubits, shown in black and red in the figure, prepared in the $|+\rangle$ state. (b) The channel system \mathcal{K} is produced by applying unitary U^C to \mathcal{I} . The edges in the figure represent controlled phase gates prepared between pairs of qubits. Effectively, we have concatenated each of the qubits of \mathcal{G}_{in} into the code space of a one-dimensional cluster state. (c) We produce \mathcal{R} by entangling ancilla qubits of the ancilla system, \mathcal{A} , to the channel system. The coupling is specified by the choice of \mathcal{G}_{ch} , which determines the check operators of the foliated system, and the deformation on the input qubit. (d) The qubits of \mathcal{R} are measured according to \mathcal{M} . This propagates the input system onto the output system, \mathcal{G}_{ch} , shown in purple to the right of the figure. The measurement pattern determines the value of stabilizer checks, and in turn the correction that must be applied to the output system.

We remind the reader that we index the qubits of each chain in terms of time intervals, indexed $1 \leq t \leq D$, such that the qubit at the $2\tau - 1$ -th site (2τ -th site) of the j -th chain is indexed $Z_j(t)$ ($X_j(t)$) and we have that the last qubit of each chain is indexed $Z_j(D+1) = 2D+1$ in the Pauli coordinate system which supports the output state.

Previously we have considered the tensor product of n one-dimensional cluster states, $\bigotimes_{j=1}^n \mathcal{K}_j$, where $\mathcal{K}_j = U_j \mathcal{I}_j$, to propagate n individual qubits described by logical operators X_j and Z_j for $1 \leq j \leq n$. In the following definition of the channel system we encode the input code \mathcal{G}_{in} onto the logical qubits of the n foliated qubits.

Definition 1 (Channel system). *The channel system $\mathcal{K} = U^C \mathcal{I}$ is produced by applying unitary operator U^C as defined in Eqn. (4.32) to the initial state \mathcal{I} . The stabilizer group \mathcal{I} is such that the stabilizers of \mathcal{G}_{in} are encoded on the qubits indexed $Z_j(1)$, and the other qubits are prepared in a product state. Explicitly, for each $G \in \mathcal{G}_{\text{in}}$ we have $G_{\text{in}} \in \mathcal{I}$ with*

$$G_{\text{in}} \equiv \prod_{j \in |g^X|} \sigma^X [Z_j(1)] \prod_{j \in |g^Z|} \sigma^Z [Z_j(1)], \quad (4.52)$$

where $(g^X g^Z)^T = v(G)$. The other qubits of \mathcal{I} are encoded in the +1 eigenvalue eigenstate of the Pauli-X matrix, such that we have

$$\sigma^X [X_j(t)] \in \mathcal{I} \quad \forall j, t \leq D, \quad (4.53)$$

and

$$\sigma^X [Z_j(t)] \in \mathcal{I} \quad \forall j, 2 \leq t \leq D + 1. \quad (4.54)$$

The resource state is generated by coupling ancilla qubits to the channel. Measuring these qubits in the appropriate basis provides data to identify qubits that have experienced errors. We couple ancilla to the resource state in a fashion according to a particular generating set $\mathcal{G}_{\mathcal{R}}$ of some gauge group $\mathcal{G}_{\text{ch.}}$. The generating set $\mathcal{G}_{\mathcal{R}}$ may be an over complete generating set of $\mathcal{G}_{\text{ch.}}$.

Definition 2 (Resource state). *For a choice of input code \mathcal{G}_{in} that is implicit in the channel system \mathcal{K} , see Def. 1, and channel code $\mathcal{G}_{\text{ch.}}$ with a specified generating set $\mathcal{G}_{\mathcal{R}}$, we define the stabilizer group of the resource state by*

$$\mathcal{R} = U^A (\mathcal{K} \otimes \mathcal{A}), \quad (4.55)$$

where the ancilla system \mathcal{A} and entangling unitary U^A are defined as follows. The ancilla system is in the product state

$$\mathcal{A} = \left\{ \sigma^X [G(t)] : \forall t, G \in \mathcal{G}_{\mathcal{R}} \right\}, \quad (4.56)$$

where the coordinates $G(t)$ uniquely index all the ancillae in the ancilla system at a given time interval t . The entangling unitary U^A is given by

$$U^A = V \prod_{G \in \mathcal{G}_{\mathcal{R}}, t} U[G(t)], \quad (4.57)$$

where

$$U[G(t)] = \prod_{j \in |g^X|} U^Z [X_j(t), G(t)] \prod_{j \in |g^Z|} U^Z [Z_j(t), G(t)], \quad (4.58)$$

for $(g^X g^Z)^T = v(G)$ and $V = \prod_t V(t)$ with

$$V(t) = \prod_{\substack{G, H \in \mathcal{G}_{\mathcal{R}} \\ G \neq H}} U^Z [G(t), H(t)]^{g^X \cdot h^Z}, \quad (4.59)$$

where $(g^X g^Z)^T = v(G)$ and $(h^X h^Z)^T = v(H)$.

We remark that in the above, the unitary U^A couples the ancilla qubits to the channel system along with each other. The component V enables the simultaneous measurement of all commuting measurements of $G \in \mathcal{G}_{\mathcal{R}}$ at common time intervals (as per the discussion in Sec. 4.4.5).

We specify a measurement pattern that propagates information through the resource state onto the output system while additionally acquiring data that enables us to identify the locations of errors.

Definition 3 (Measurement pattern). *The measurement pattern is such that*

$$\mathcal{M} = \mathcal{M}^C \cup \mathcal{M}^A, \quad (4.60)$$

where \mathcal{M}^C and \mathcal{M}^A denote the measurements on the channel and ancilla system, respectively, given by

$$\mathcal{M}^C = \left\{ \sigma^X[Z_j(t)], \sigma^X[X_j(t)] \in \mathcal{M}^C : 1 \leq t \leq D \right\}, \quad (4.61)$$

and

$$\mathcal{M}^A = \left\{ M[G(t)] \in \mathcal{M}^A : G \in \mathcal{G}_{\mathcal{R}}, 1 \leq t \leq D \right\}, \quad (4.62)$$

where $(g^X g^Z)^T = v(G)$ and we have

$$M[G(t)] = \sigma^X[G(t)] \left(i\sigma^Z[G(t)] \right)^{g^X \cdot g^Z}. \quad (4.63)$$

It may be helpful to expand Eqn. (4.63) such that

$$M[G(t)] = \begin{cases} \sigma^X[G(t)] & \text{if } g^X \cdot g^Z = 0, \\ \sigma^Y[G(t)] & \text{if } g^X \cdot g^Z = 1, \end{cases} \quad (4.64)$$

and we remember the inner product is taken modulo 2.

4.5.1 Foliation

With the resource state and measurement pattern defined above we now turn our attention to the foliated system \mathcal{F} . Important properties of the system will be determined from elements in $\mathcal{C}(\mathcal{F})$. While we have introduced the foliated model as a subsystem code, we have included additional structure to capture the process of foliation, namely, we prepare the system in a fixed gauge of the resource state, \mathcal{R} and we project the system onto a gauge of \mathcal{M} . As such, elements of $\mathcal{C}(\mathcal{F})$ have a different role depending on their inclusion in \mathcal{R} and \mathcal{M} .

Elements $\mathcal{C}(\mathcal{F}) \cap \mathcal{M}$ are observable degrees of freedom that are measured under projection by the single-qubit measurement pattern. Among these include stabilizer operators and

logical operators of the input state that are measured by the resource. On the other hand elements $\mathcal{C}(\mathcal{F}) \setminus \mathcal{M}$ give rise to the stabilizers and logical operators of the output state which are propagated or inferred at a later point by taking the output as the input of another channel. Further, we can also look at elements of $\mathcal{C}(\mathcal{F})$ with respect to their membership of \mathcal{R} . Indeed, elements $\mathcal{C}(\mathcal{F}) \cap \mathcal{R}$ are stabilizers whereas elements $\mathcal{C}(\mathcal{F}) \setminus \mathcal{R}$ are logical degrees of freedom that are either propagated through the resource state or measured under the projection.

Remarkably, due to the decomposition of the foliated system we have presented here we can separate error correction, determined by stabilizer group \mathcal{S} , and the logical function of a given channel, \mathcal{G}_{out} , into two separate parts. Let us now characterize the output state of the foliated system after measurements have been performed, as well as the stabilizers of the channel responsible for detecting errors.

The output of the channel consists of an encoding, determined by \mathcal{G}_{out} , and a set of logical operators \mathcal{L}_{out} . The logical function of the channel can be summarised by how it maps input logical operators to output logical operators. The following theorem describes the output encoding and logical degrees of freedom.

Theorem 1. *For any foliated channel \mathcal{F} determined by input code \mathcal{G}_{in} , channel code $\mathcal{G}_{\text{ch.}}$, the output state is a codeword of the output code \mathcal{G}_{out} , with*

$$\mathcal{G}_{\text{out}} = \mathcal{G}_{\text{ch.}} \cup (\mathcal{G}_{\text{in}} \cap \mathcal{C}(\mathcal{G}_{\text{ch.}})). \quad (4.65)$$

The logical operators of \mathcal{G}_{out} are given by

$$\mathcal{L}_{\text{out}} = (\mathcal{C}(\mathcal{G}_{\text{in}}) \cap \mathcal{C}(\mathcal{G}_{\text{ch.}})) \setminus (\mathcal{G}_{\text{in}} \cup \mathcal{G}_{\text{ch.}}). \quad (4.66)$$

Further, elements of $(\mathcal{C}(\mathcal{G}_{\text{in}}) \setminus \mathcal{G}_{\text{in}}) \cap \mathcal{G}_{\text{ch.}}$ are measured.

The two equations given above specify precisely the function of a channel at a macroscopic level, independent of the foliated system that performs the manipulation of the input state.

For the channel to be fault-tolerant, we need the channel to contain stabilizers that can check for errors, and these stabilizers need to be able to be inferred from measurements. Recall the stabilizer of the foliated system is given by

$$\mathcal{S} = \mathcal{C}(\mathcal{F}) \cap \mathcal{R} \cap \mathcal{M}. \quad (4.67)$$

The following theorem identifies two types of important operators that we call bulk stabilizers and boundary stabilizers.

Theorem 2. *For any foliated channel \mathcal{F} specified by input code \mathcal{G}_{in} and $\mathcal{G}_{\mathcal{R}}$ which generates $\mathcal{G}_{\text{ch.}}$, we have*

$$1. S_{bulk}[G(t)] \in \mathcal{S} \quad \forall G \in \mathcal{G}_{ch.}, 2 \leq t \leq D,$$

$$2. S_{bdry.}[G(t)] \in \mathcal{S} \quad \forall G \in \mathcal{G}_{ch.} \cap \mathcal{G}_{in}, t \leq D,$$

where for $v(G) = (g^X g^Z)^T$ we have

$$S_{bulk}[G(t)] = M[G(t)]M[G(t-1)] \prod_{j \in |g^X|} \Sigma_j^X(t) \Sigma_j^X(t-1) \prod_{j \in |g^Z|} \Sigma_j^Z(t) \Sigma_j^Z(t-1), \quad (4.68)$$

and

$$S_{bdry.}[G(t)] = \prod_{\tilde{G} \in \xi(G)} M[\tilde{G}(t)] \prod_{j \in |g^X|} \Sigma_j^X(t) \prod_{j \in |g^Z|} \Sigma_j^Z(t), \quad (4.69)$$

where $\xi(G) \subseteq \mathcal{G}_{\mathcal{R}}$ is defined such that the product of all the terms of $\xi(G)$ give $G \in \mathcal{G}_{ch.}$.

We remark that the set $\xi(G)$ necessarily exists by definition, since we construct the resource state with terms $\mathcal{G}_{\mathcal{R}}$ which generates $\mathcal{G}_{ch.}$. However, $\xi(G)$ is not necessarily unique, in which case any choice will suffice. We defer the proofs of the above Theorems to Sec. 4.9.2.

It is also worth pointing out that Theorem 2 may not necessarily describe the stabilizer group of \mathcal{F} exhaustively. Indeed, with certain choices of $\mathcal{G}_{\mathcal{R}}$ we can obtain additional elements of $\mathcal{C}(\mathcal{F}) \cap \mathcal{F}$. For instance, we may choose to foliate a self-correcting stabilizer model [137] such as the four-dimensional toric code [47]. In which case we have additional checks that are local to a given time interval due to constraints among the stabilizer group. It is precisely the constraints that these models present that give rise to single-shot error correction [75, 243, 277–279] which enable us to identify errors on the ancillary qubits we use to make checks, see also Sec. 4.9.4 for a discussion on single-shot error correction by foliation of the gauge color code. The stabilizers we have described in Theorem 2 are generic to all foliated models using the construction we have presented.

In the following section we apply the above theorems to the twisted surface code model. This provides an illustrative example that we later use in our model of fault-tolerant quantum computation. We note that the above construction and theorems are readily generalised to include other methods of foliation including foliation using type-II qubits as we will see in the next section and Sec. 4.9.1, and compressed foliation, Sec. 4.9.3. Our scheme for foliation and related results also generalise to subsystem codes provided they are generated by a group with particular properties. For instance, our results apply to all CSS subsystem codes. We give a discussion of this extension in Sec. 4.9.4.

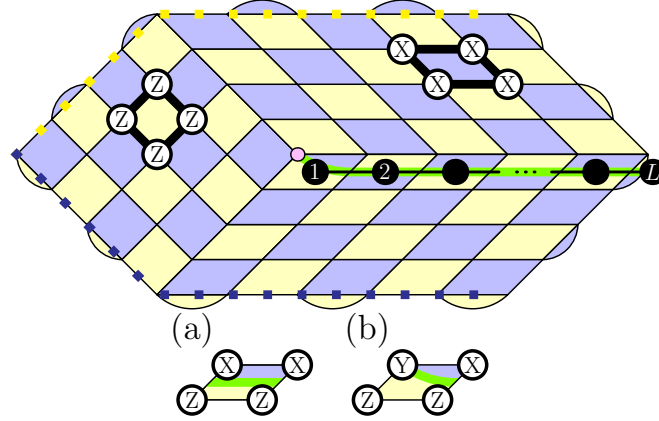


Fig. 4.9 The twisted surface code model. Examples of star and plaquette operators are shown explicitly on thick outlined plaquettes on a blue and yellow face respectively. Logical operators are supported on the qubits followed by the yellow and blue dotted lines. A defect line runs from the right-hand side of the lattice to its centre. An example of the modified stabilizers that support the defect line is shown at (a). The green line terminates at the centre of the lattice. We write the stabilizer where the defect line terminates below the lattice at part (b). We focus on foliating the stabilizers that lie on the defect line, as such we number them explicitly with indices shown in black circles on the figure.

4.6 The twisted surface code

The twisted surface code [272] provides an interesting example of a stabilizer code that cannot be foliated using existing constructions [241]. Moreover this example will be helpful later on when we consider different schemes for fault-tolerant measurement-based quantum computation. We will briefly review the stabilizer model before showing resource states for the foliated model.

The stabilizer group for the twisted surface code are closely related to those of the surface code. However the model has an impressive encoding rate due to a twist defect [67] lying in the centre of the lattice [214, 272]. Nonetheless, due to the central twist defect we cannot find a CSS representation of the model, and as such, we require the generalised construction for foliation given above. We will mostly focus on these stabilizers.

The stabilizer group for twisted surface code $\mathcal{G}_{\text{twisted}}$ is represented on the lattice in Fig. 4.9 where qubits lie on the vertices of the lattice and stabilizers are associated to the faces, indexed f . On blue(yellow) faces we have the well-known star(plaquette) operators which are the tensor product of Pauli-X(Pauli-Z) operators lying on the vertices on the corners of their respective face. The twisted surface code additionally has a defect line running from the right-hand side of the lattice to the centre, along which, stabilizers are modified. The stabilizers lying along the defect line, which is marked green in the figure, are weight-four terms that are the tensor product of Pauli-X(Pauli-Z) stabilizers on the blue(yellow) part of the face. An example of a modified stabilizer is shown in Fig. 4.9(a). The stabilizer where the defect line terminates also

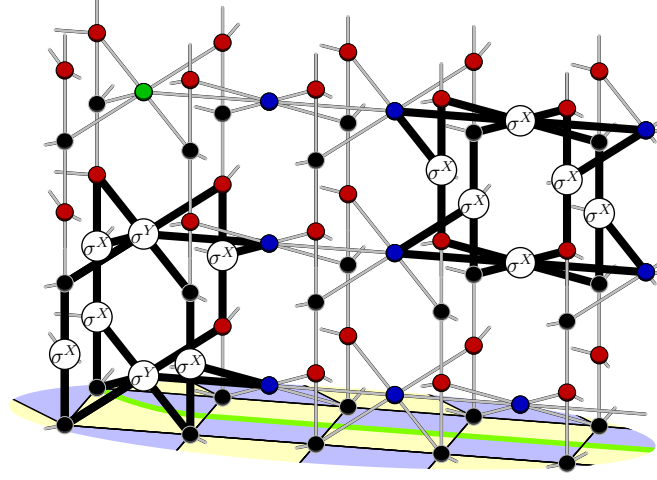


Fig. 4.10 A foliation pattern for the defect line of the twisted surface code. The code is initialised at the bottom of the figure where the lattice that describes the stabilizers of the code are shown. Qubits that are coupled with a controlled-phase gate are connected by an edge. Qubits indexed $Z_j(t)(X_j(t))$ are coloured black(red), and ancilla qubits are coloured in blue(green), depending on whether they are measured in the Pauli-X(Pauli-Y) basis. Example elements S_{bulk} (as in Theorem 2) which belong to $\mathcal{C}(\mathcal{F}) \cap \mathcal{R} \cap \mathcal{M}$ are also shown.

includes a Pauli-Y term as shown in Fig. 4.9(b). Representations of logical operators $\bar{X}(\bar{Z})$ that act on the one encoded qubit are the tensor product of Pauli-X(Pauli-Z) operators supported on the dotted blue (yellow) lines on the lattice.

We now consider foliating the twisted surface code with the prescription given in the previous section where $\mathcal{G}_{\text{ch.}} = \mathcal{G}_{\text{twisted}}$. Stabilizers of the form of a CSS code, i.e. stabilizers where either g^X or g^Z are the null vector where $(g^X g^Z)^T = v(G)$ for $G \in \mathcal{G}_{\text{twisted}}$, are foliated using the methods of Ref. [241] and take the form of those in the original works [66, 172, 259], as such we focus on the terms that lie along the defect line. In Fig. 4.10 we show the resulting graph where physical qubits indexed $Z_j(t)(X_j(t))$ are coloured black(red) in the figure and time runs vertically up the page.

We denote the stabilizers lying along the defect line $G_f \in \mathcal{G}_{\text{twisted}}$ where we index face terms $1 \leq f \leq L$ as shown in Fig. 4.9. We consider vectors $v(G_f) = (g_f^X g_f^Z)^T$. Notably, the stabilizers that lie along the defect line all have $g_f^X \cdot g_{f+1}^Z = 1$. As such the operator

$$V = \prod_{f,t} U^Z[S_f(t), S_{f+1}(t)], \quad (4.70)$$

couples adjacent ancilla qubits. These bonds are shown as horizontal edges connecting adjacent blue ancilla qubits in Fig. 4.10. Further, the stabilizer G_1 is such that $g_1^X \cdot g_1^Z = 1$, we therefore measure these ancillas in the Pauli-Y basis, i.e., $\sigma^Y[G_1(t)] \in \mathcal{M}$. We color these ancilla qubits in green in Fig. 4.10.

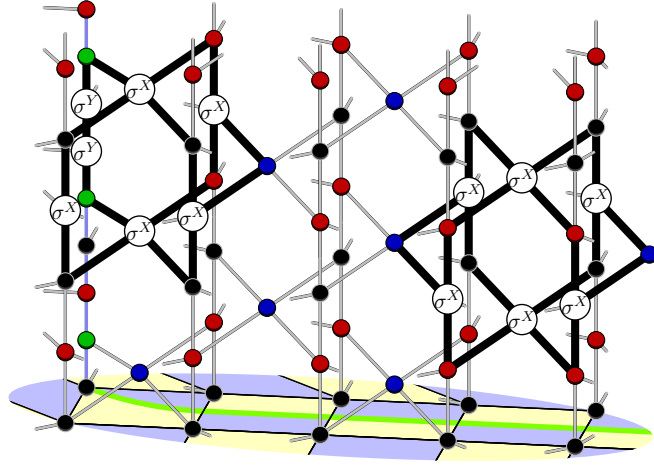


Fig. 4.11 Resource state where we change the time interval of some of the targets of certain ancilla qubits as is described in the main text. Qubits indexed $X_j(t)$, $Y_j(t)$ and $Z_j(t)$ are coloured red, green and black, respectively, and ancilla qubits are shown in blue. We also show the type-II foliated qubit in blue. No physical qubit has more than four incident edges. Two elements of $\mathcal{C}(\mathcal{F}) \cap \mathcal{R} \cap \mathcal{M}$ are shown.

The figure also shows two stabilizers, i.e., elements of $\mathcal{S} = \mathcal{C}(\mathcal{F}) \cap \mathcal{R} \cap \mathcal{M}$ of the form shown in Eqn. (4.68). The stabilizers are weight six, except the stabilizer at the centre of the lattice which includes a Pauli-Y term. This operator is weight seven.

We finally remark that the resource state we have thus far considered is by no means unique, and using the foliation techniques considered in the previous section we can devise other, arguably favourable, resource states. In Fig 4.11 we show one such alternative. In this figure, for even values of f we replace the coupling operators with

$$U[G_f(t)] = \prod_{j \in |g_f^X|} U^Z[X_j(t), G_f(t)] \times \prod_{j \in |s_f^Z|} U^Z[Z_j(t+1), G_f(t)], \quad (4.71)$$

where now the check couples to targets $Z_j(t+1)$ instead of $Z_j(t)$. With this modification all the checks are compatible where we set $V = 1$, thus reducing the valency of the ancilla qubits. We additionally replace the foliated qubit where the defect terminates with a type-II foliated qubit, which is coloured by blue edges. This further reduces the valency of ancillas used to measure operators $S_1(t)$ as we need only couple to a single target to measure the Pauli-Y component of this check. This also reduces the valency of the physical qubits of the type-II foliated chain. However, this comes at the expense of including an additional physical qubit per time interval to include a type-II foliated qubit in the system.

To summarise the present discussion we have seen that we can introduce Pauli-Y terms in stabilizer measurements either by using type-II foliated qubits or by coupling an ancilla to multiple targets of the same foliated qubit, and we have seen that in general we can

periodically measure a full set of check measurements by either lifting the targets of selected check measurements to higher time intervals or by coupling pairs of ancillas where it is appropriate. The examples of resource states we have considered here are by no means exhaustive and other variations can be made following the general principles of foliation given in the previous section, but given the multitude of variations one could come up with we leave further experimentation to the reader. One variation we have considered [280] is where checks are made at intermediate time intervals where we couple additional ancilla to physical qubits at layers indexed $X_j(t)$ and $Z_j(t+1)$. This increases the number of ancilla qubits required along the defect line, and increases the valency of the physical qubits along each foliated wire, but in return we reduce the weight of the check operators and increase the number of available check operators. We summarise this compressed construction in Sec. 4.9.3.

4.7 Quantum computation with the foliated surface code

In what follows we explore the general theory we have established here by following the example of the foliated surface code. This model is a CSS stabilizer code and is thus foliated using the methods in Ref. [241] and has been studied from the perspective of computation in Refs. [172, 259, 267]. Beyond the work in the literature, using the generalised framework for foliation we have presented, we can additionally realise a phase gate deterministically in the foliated picture using ideas from Refs. [214, 272]. In particular, in Ref. [214] it was shown that the corners of the planar code where two distinct types of boundary meet can be regarded as a Majorana mode. Throughout the discussion we give here we extend this analogy [15, 67, 281–283] further.

We see that, in the spacetime picture provided by a foliation, that the corners of the planar code extend to world lines of Majorana modes. We find that the worldlines of the Majorana modes that live at the interface of different boundaries follow the trajectories we would expect if we were to realise fault-tolerant topological quantum computation by braiding Ising anyons [15, 284–289]. We show this analogy in a macroscopic picture in Fig. 4.12 where we show the foliated planar code [47, 241]. The planar code has rough boundaries and smooth boundaries, that appear as faces of the foliated system as they are extended along the time axis. The figure shows the different boundaries in blue and yellow. At the interface of the different boundary types we see the world line of a Majorana mode. In this picture the modes move vertically upwards with no horizontal motion. This is because with this channel we execute an identity gate. In what follows we show that generalising the picture of foliation allows us to braid and fuse Majorana modes in the spacetime model. We see this by explicitly considering the initialisation of arbitrary states, with lattice surgery by foliation, and by performing a fault-tolerant phase gate.

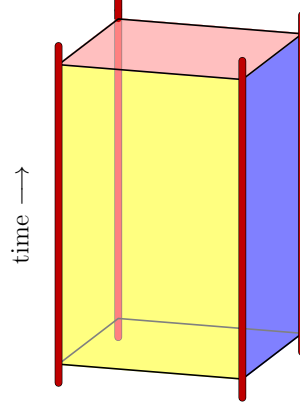


Fig. 4.12 The foliated planar code. The code is extended through spacetime where the rough and smooth boundaries are shown in yellow and blue, and the output is shown in red. At the interface between the rough and smooth boundaries we see the world lines of Majorana modes, depicted by thick red lines. The four modes that encode the qubit move directly along the temporal axis, and as such do not nontrivially manipulate the encoded state over the channel.

Initialisation

In order to realise fault-tolerant universal quantum computation with the surface code we require the ability to generate eigenstates of non-Pauli matrices for magic state distillation [260]. This is similarly true for computation with the fault-tolerant cluster state model [172, 259]. State initialisation by measurements with the surface code has been considered in Refs. [73, 290, 291]. The work on initialisation is readily adapted for the input-output model of fault-tolerant measurement-based quantum computation we have developed above.

Common to all of the references on initialisation, the qubits that go on to form the surface code begin in some easily prepared state, such as a product state, which are then measured with the stabilizers of the desired code. In Fig. 4.13(a) we show the initial state we prepare in order to initialise the surface code in an arbitrary state as given in Ref. [290]. Qubits in the green(blue) boxes are initialised in known eigenstates of the Pauli-X(Pauli-Z) basis, and the central red qubit is prepared in an arbitrary state.

By including this state as the stabilizer group \mathcal{S}_I of the initial state \mathcal{I} , and the stabilizers of the surface code as the stabilizers measured through the channel, \mathcal{S}_C , we recover the graph state shown in Fig. 4.13(b). The figure shows the input state on the layer closest to the reader and the time axis of the foliated model extends into the page. The qubits are coloured using the convention in earlier sections where black(red) vertices mark qubits with indices $Z_j(t)(X_j(t))$ and the blue vertices show ancilla qubits. The central green qubit is prepared in an arbitrary

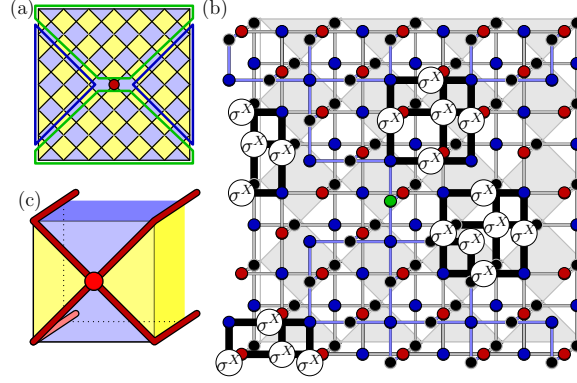


Fig. 4.13 Preparing an arbitrary state. (a) The initial product state used to initialise the surface code from Ref. [290]. Qubits lie on the vertices of the graph, and star(plaquette) operators lie on the blue(yellow) faces of the lattice. The system is initialised in a product state where all the qubits within the dark green(blue) boxes begin in the $+1$ eigenvalue eigenstate of the Pauli-X(Pauli-Z) operator, and the central red qubit is prepared in an arbitrary state. Measuring the stabilizers shown on the lattice initialise the code in the state of the central qubit. (b) The graph state showing initialisation where the initial state shown in (a) lies at the front of the figure, and the time axis of the foliated system extends into the page. Qubits initialised in an eigenstate of the Pauli-Z operator are not drawn, as these qubits do not entangle with the resource state. Examples of check operators are shown on the graph. (c) Macroscopic depiction of the initialisation, showing the creation of two pairs of Majorana modes at the center whose worldlines extend to the outer edges of the lattice, in between different boundaries.

state. All of the qubits are measured in the Pauli-X basis¹. To help the qubits of the input system stand out we colour the edges that connect them in light blue.

All of the qubits support check operators except the central qubit that is prepared in an initial state, we show examples of elements of $\mathcal{C}(\mathcal{G})$ in the figure. We do not draw qubits that were initialised in an eigenstate of the Pauli-Z operator. Indeed, these states respond trivially to the action of the operator U which is diagonal in the computational basis, and as such these qubits do not entangle nontrivially with the resource state. We are therefore free to neglect them.

It is interesting to view initialisation from the macroscopic viewpoint. The initial state shown in Fig. 4.13(a) are chosen such that both a logical Pauli-X and a logical Pauli-Z operator are supported on the physical qubits initialised in the Pauli-X(Pauli-Z) basis, where both operators intersect at the central qubit. Both of these logical operators extend along the surface where the input state is initialised onto the distinct boundaries where the logical operators terminate. Once the surface code is foliated the respective boundaries of the surface code extend along the temporal axis of the foliated system, and together with the boundaries extend the

¹One could alternatively prepare the green qubit in a known eigenstate of Pauli-X and measure the green qubit in an arbitrary basis, the output will be the same.

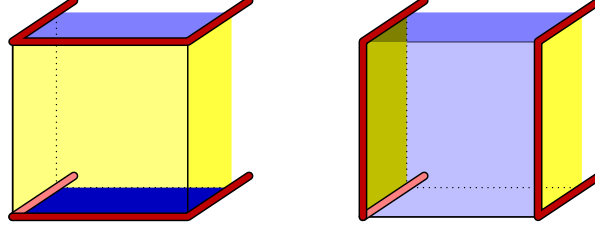


Fig. 4.14 Macroscopic picture with time moving into the page showing preparation such that the output is state is a logical Pauli-Z(Pauli-X) state on the left(right) of the figure where the input system are prepared with the physical qubits rotated into eigenstates of the Pauli-Z(Pauli-X) basis. The world lines of the Majorana modes that move between the distinct boundaries emerge in two distinct pair creation operations, which is true to the analogy with fault-tolerant quantum computation with Ising anyons.

logical operators of the system. In this way we can regard the logical operators that extend to the output system as two-dimensional surfaces. Logical operators propagated along a boundary in this way are commonly known as correlation surfaces [66].

In the same way that the different logical operators of the surface code terminate at their distinct respective boundaries, so too do the correlation surfaces of the foliated surface code terminate exclusively at their respective boundary. This is similarly true at the different regions of the surface where the qubits of the input state is initialised differently. In this sense we can regard the different regions where qubits are prepared in eigenstates of the Pauli-X or Pauli-Z basis extensions of the other boundaries of the system. In Fig. 4.13(c) we colour code the boundaries of the foliated lattice according to the correlation surfaces that can terminate at them. In particular, correlation surfaces corresponding to the propagation of logical Pauli-X(Pauli-Z) operators of the surface code terminate at the blue(yellow) boundaries of the figure, respectively.

As discussed, we can regard the interface between the two different boundary types as worldlines of the Majorana modes. As Fig. 4.13(c) shows, the four red lines meet at the single point where the nontrivial state is initialised. We thus see that the analogy between the boundaries of the foliated system and Majorana-based fault-tolerant quantum computation holds, as in such a system, to prepare an arbitrary state, two pairs of Majorana modes would need to be prepared simultaneously at a common location and noisily rotated into a desired state before the modes are separated such that the encoded information is topologically protected [292, 293].

We can similarly explore this analogy by preparing logical qubits in eigenstates of Pauli operators. With the surface code, we can prepare a logical qubit in an eigenstate of the Pauli-X(Pauli-Z) by initialising all of the physical qubits in the Pauli-X(Pauli-Z) basis. Using these product states at the input states, we can show the boundaries of the system macroscopically

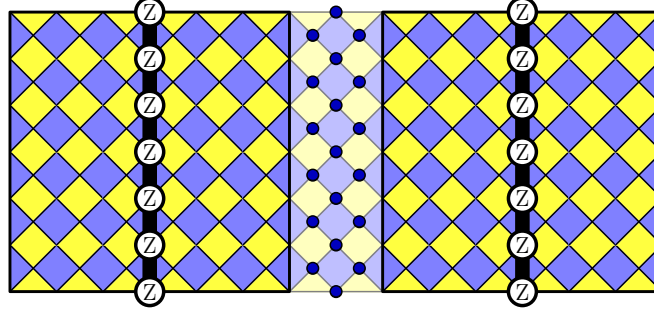


Fig. 4.15 Two surface code lattices are shown in bold colours to the left and the right of the figure. To measure the parity of these two logical qubits, we initialise the qubits that separate the two lattices in known eigenstates of the Pauli-X operator and then begin measuring the stabilizers of the extended rectangular stabilizers which includes the pale-coloured stabilizers in between the two lattices.

in Fig. 4.14 where the input state is shown by the boundary on the input face shown closest to the reader. In this instance, the figure shows two pairs of Majorana modes are prepared a macroscopic distance from one another. This is similarly true with fault-tolerant quantum computation with anyons, as these logical states are also prepared robustly in this way.

Fault-tolerant parity measurements

We next investigate the how lattice surgery [70, 71, 73, 214] maps into the measurement-based picture. Lattice surgery offers a route to performing entangling gates between qubits encoded with topological codes via fault-tolerant parity measurements. Foliated lattice surgery with the surface code has already been considered in Ref. [267] but here we revisit this example within the more general framework we have developed for fault-tolerant measurement-based quantum computation. We will also witness nontrivial dynamics between the world lines of the Majorana modes that are present in the foliated surface code.

We briefly review lattice surgery with the surface code before examining it at the macroscopic level of foliation. To the left and right of Fig. 4.15 we see two surface code lattices in bold colours. Each of these encodes a single logical qubit. The goal is to make the logical parity measurement $\bar{Z}_1 \bar{Z}_2$ of these two encoded qubits. The support of the operator we aim to measure is shown in the figure. To make this logical measurement fault-tolerantly, we begin measuring the stabilizers of a single extended rectangular surface code, which includes the pale-coloured stabilizers in between the two codes. Importantly, the logical operator of the two codes we intended to measure is a member of the stabilizer group of the extended code. As such, by measuring the stabilizers of the code we additionally recover the value of the parity measurement.

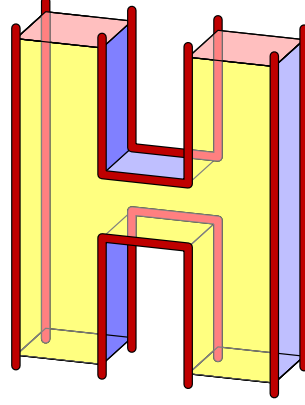


Fig. 4.16 Lattice surgery for the parity measurement $\bar{Z}_1\bar{Z}_2$ in the foliated surface code where the time axis runs from the bottom of the page to the top. We show two distinct surface codes at the bottom of the page. At the point where we begin the parity measurement the two foliated qubits are connected through an extended piece of foliated surface code. We show the trajectories of the foliated Majorana modes in red. We see that at the connection point two pairs of Majorana modes are fused, where one mode from each pair are taken from the two different foliated codes. Once the parity data is collected the connection is broken by inputting the rectangular lattice into a new channel to separate the two encoded qubits. This is shown at the top of the figure.

To initialise the extended surface code, each of the physical qubits that lie in between the two encoded qubits are prepared in a known eigenstate of the Pauli-X operator and we then measure the stabilizers of the rectangular code. To the best of our knowledge, the literature thus far has only considered a very narrow separation between the two encoded lattices such that the number of qubits involved in the procedure is minimal. We know of no practical advantage of widening this gap but for the purposes of our exposition we find that the wider gap helps elucidate some of the topological features of lattice surgery.

We now consider lattice surgery within a measurement-based framework. We consider as an input state included in \mathcal{I} two surface code lattices together with some ancillary physical qubits prepared in the $+1$ eigenvalue eigenstate of the Pauli-X matrix as shown in bold in Fig. 4.15, where we might imagine that the two surface code lattices have emerged as the output of two foliated surface codes. We then append to the resource state the check measurements of the larger rectangular surface code such that the logical parity measurement is read from the resource state once the single-qubit measurement outcomes have been collected.

We show this foliated picture macroscopically in Fig. 4.16. The figure shows two foliated surface codes entering the surgery channel where the two lattices are connected make the parity check. Once the parity check is completed, we take as an input the output of the channel of the rectangular code and input it back into the original channel where the two lattices are separated

and the qubits that connect the two lattices are measured transversally in the Pauli-X basis which completes the operation.

We next study the trajectories of the Majorana modes while the parity measurement takes place. Given that the qubits that form the connection between the two codes are initialised in the Pauli-X basis, the boundary where the connection is formed terminates the correlation surface that propagates the logical Pauli-X data of the channel. As such, we regard this boundary as an extension of the blue boundaries in the figure where the correlation surfaces for the logical Pauli-X operators can terminate. An equivalent argument holds at the moment the connection is broken. From this we can infer the trajectories of the Majorana modes.

At the point the two codes are connected we observe the world lines of the Majorana modes that mark the interface between the distinct boundaries fuse. Two pairs of Majorana modes fuse where each pair takes a single mode from each of the two input codes. The product of these two fusion operations gives the parity of the two encoded qubits which is consistent with the topological interpretation of lattice surgery given in Ref. [214].

More precisely, if we consider a system where two qubits are encoded over eight Majorana modes, γ_j with $1 \leq j \leq 8$, and $\bar{X}_1 = i\gamma_1\gamma_3$, $\bar{Z}_1 = i\gamma_3\gamma_4$, $\bar{X}_2 = i\gamma_6\gamma_8$ and $\bar{Z}_2 = i\gamma_5\gamma_6$, and we make measurements $M_1 = i\gamma_3\gamma_5$ and $M_2 = i\gamma_4\gamma_6$ we have that $\bar{Z}_1\bar{Z}_2 = M_1M_2$. One may worry that the logical measurement of M_1 and M_2 may affect encoded information, but in fact this measurement only disturbs the global charge conservation of the two encoded qubits, $\gamma_1\gamma_2\gamma_3\gamma_4$ and $\gamma_5\gamma_6\gamma_7\gamma_8$, which could be regarded as gauge degrees of freedom. It is clear from Fig. 4.16 that lattice surgery is performing an analogous operation with the foliated Majorana modes.

A phase gate

We finally show how to perform a phase gate with a surface code that is propagated through a resource state. This presents an interesting example as we require the composition of several channels to complete this operation. Moreover, we will observe a braid in the trajectories of the foliated Majorana modes which is true to the analogy we have painted alongside fault-tolerant quantum computation with anyons. The gate we use is based on a method presented with stabilizer codes in Ref. [272], but we point out that the general theory of foliated quantum computation is readily adapted to other proposals to realise Clifford gates [271, 214] including other schemes presented in Ref. [272]. See also recent work in Ref. [73, 294]. As in the previous Subsection we will present the scheme at the level of stabilizer codes before discussing the foliated variant of the logical gate.

We first summarise the execution of a phase gate abstractly at the logical level. A phase gate maps logical operators such that $\bar{X} \rightarrow \bar{Y}$ and $\bar{Y} \rightarrow \bar{X}$ where phases are neglected, and the logical Pauli-Z operator is invariant under a phase rotation. Using an additional ancillary qubit

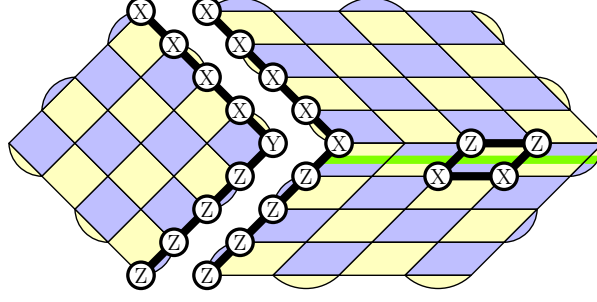


Fig. 4.17 Two surface codes where Pauli-X type stabilizers lie on blue faces and Pauli-Z stabilizers on yellow faces. A dislocation is shown in green running through the middle of the right surface code which are the product of two Pauli-X terms and two Pauli-Z terms. An example of such a stabilizer is shown. The left qubit, qubit 1, is initially encoded in an arbitrary state, and the right qubit, qubit 2, is prepared in an eigenstate of the logical Pauli-Z operator. The logical operator whose measurement outcome is inferred from the stabilizer measurements during lattice surgery with support running from the top to the bottom of the figure is shown explicitly.

we can achieve this operation by code deformation. If we encode the logical information on the first logical qubit, and we prepare the second qubit in an eigenstate of the logical Pauli-Z operator, then one can check that performing the following sequence of measurements; $\bar{Y}_1 \bar{X}_2$, \bar{Z}_1 , $\bar{X}_1 \bar{X}_2$, \bar{Z}_2 will complete a phase gate up to phases which are determined by the outcomes of the measurements. In what follows we show how these measurements can be achieved fault-tolerantly using two surface code models.

We must first measure $\bar{Y}_1 \bar{X}_2$ where the ancilla qubit is prepared in an eigenstate of the Pauli-Z operator. We consider the initial system shown in Fig. 4.17 where logical information is encoded on the lattice shown to the left and the surface code to the right is initialised in an eigenstate of the logical Pauli-Z operator. An important feature of the surface code at the right of the figure is that it has a continuous defect line running through the middle of the lattice, but we remark that the model is locally equivalent to the well-known CSS variant of the surface code on a rectangular lattice. Once the system is prepared in this state, by measuring this system with the stabilizers of the twisted surface code as shown in Fig. 4.9, we recover the value of the desired logical parity measurement. This is because the operator of the initial system, $\bar{Y}_1 \bar{X}_2$, is an element of the stabilizer group of the twisted surface code. To make this clear we show the operator $\bar{Y}_1 \bar{X}_2$ explicitly on Fig. 4.17.

It is worth pointing out that, similar to the standard surface code which, as explained above, can be fault-tolerantly initialised in an eigenstate of the Pauli-Z basis, the lattice to the right is readily initialised in an eigenstate of the Pauli-Z operator by initialising the physical qubits above(below) the defect line in a known eigenstate of the Pauli-Z(Pauli-X) basis before measuring the stabilizers of the model to complete the preparation.

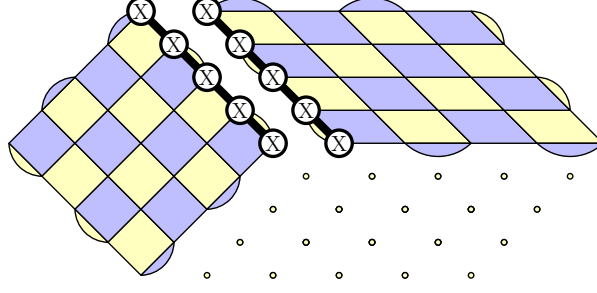


Fig. 4.18 After transversally measuring the qubits below the defect line of the lattice to the right transversally in the computational basis the right qubit is reduced to a smaller square lattice. The system to the left is initialised in a logical eigenstate of the Pauli-Z operator. The support of the logical parity measurement that is made under the surgery is shown.

Once we have performed the first parity measurement the remaining steps to complete the phase gate have already been well described in the literature, we thus only briefly summarise the remaining technical steps. We must first measure the first system in the logical Pauli-Z basis. This is achieved by measuring all of the physical qubits transversally in the Pauli-Z basis, the outcome of the measurement can be inferred from the single-qubit measurement outcomes. This leaves the logical information encoded on the second logical qubit on the rectangular lattice.

To make the final parity measurement, we additionally require that we reduce the length of the rectangular lattice. This is also achieved by transversally measuring the qubits below the defect line on the rectangular lattice transversally in the Pauli-Z basis. After we have completed all of the transversal measurements we reinitialise the first system in an eigenstate of the logical Pauli-Z operator which is carried out by preparing all of the physical qubits in the Pauli-Z basis and subsequently measuring standard surface code stabilizers.

Upon completing these three operations, the first two of which could be carried out simultaneously, we end with the system shown in Fig. 4.18. Finally, to transfer the rotated logical information back to the first lattice, we perform another logical parity measurement, $\bar{X}_1\bar{X}_2$ which is carried out using standard lattice surgery that we discussed in the previous subsection before finally measuring the remaining qubits of the second ancillary system transversally in the Pauli-Z basis which completes the final logical measurement \bar{Z}_2 .

As in the case of lattice surgery, the steps of the code deformation procedure outlined above are readily mapped onto a foliated system by using each new deformation as the stabilizers of the channel system of a resource state such that the output is the deformed variant of the initial state. The phase gate we have presented provides a particularly interesting example as it shows that certain gates are achieved using several different channels where the input of the j -th channel is the output of the $j - 1$ -th channel. We also remark that several of these channels require the general methods of code foliation that we have developed in the earlier

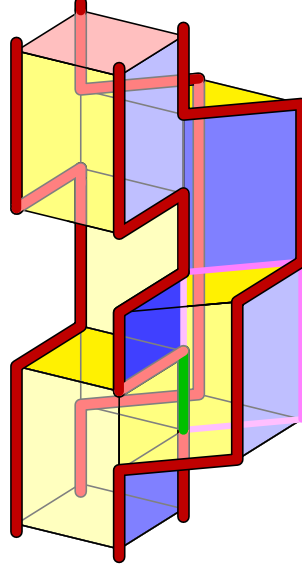


Fig. 4.19 The sequence of foliated channels that execute a phase gate on a qubit transmitted with a foliated surface code where time increases up the page. The worldlines of the Majorana modes are shown in red(green) if they run through the exterior boundary(bulk) of the foliated system and the boundary of the dislocation of the foliated surface code is shown in pink. One can track the world lines of the modes from the bottom to the top of the page to see the two right most world lines exchange.

sections of this work. The channel where we measure the stabilizers of the twisted surface code for instance can be foliated using the graph states proposed in Sec. 4.6.

We show the series of channels in Fig. 4.19 where the temporal axis increases up the page. Interestingly, we observe that the two right-most Majorana modes at the bottom of the figure are exchanged over time, where the right-most mode moves through the interior of the resource state through the channel that measures the stabilizers of the twisted surface code. The point where the world line of this mode moves through the interior is highlighted in green. To the best of our knowledge, this presents the first example of a foliated system where a defect is moved through the interior of a resource state. While this defect is in the interior of the system, the other mode involved in the exchange is braided around the exterior of the system before the exchange is completed thus executing a phase gate. Once again, the analogy with Majorana modes holds in the model we consider here as, indeed, exchanging a pair of Majorana modes executes phase gate. This can be seen by considering a qubit encoded with four Majorana modes such that $\bar{X} = i\gamma_1\gamma_3$, $\bar{Y} = i\gamma_2\gamma_3$ and $\bar{Z} = i\gamma_1\gamma_2$. One can see that up to phases \bar{X} and \bar{Y} differ by the exchange of indices 1 and 2 whereas \bar{Z} is invariant under the exchange modulo a negative phase which is equivalent to the exchange of the modes in the foliated channel.

4.8 Concluding remarks

We have presented a framework that allows us to map quantum computational schemes that use code deformations on stabilizer codes to schemes of fault-tolerant measurement-based quantum computation. We have shown how to view each component of the computation as a ‘foliated channel’ as a gauge-fixing process of a subsystem code, from which all properties of the computation can be inferred. We have used this framework to show we can initialise, fuse and braid foliated Majorana defects in a three-dimensional fault-tolerant cluster-state model to carry out universal quantum computation with Clifford operations and magic state distillation.

It remains an important problem to find the most resource efficient models of fault-tolerant quantum computation, as such it will be fruitful to study the robustness of other foliated stabilizer codes to experimentally relevant sources of noise. In particular, it will be valuable to study the tolerance of different models to loss, as foliated models are most applicable to photonic architectures where this is a dominant source of error [264]. From a condensed matter perspective, the models we have constructed can be viewed as symmetry-protected topological phases [119, 134, 135, 156, 216, 295]. Further study of these models may therefore lead to new phases of matter that are robust resources for quantum information tasks. Finally, one can readily check that we can foliate the canonical examples of subsystem codes [50–52, 75] within our framework, by replacing the channel stabilizer group by a generating set of the gauge group, whereby the foliated system inherits many of the desirable features of the subsystem code. While the general theory of subsystem code foliation remains to be described explicitly, we find it exciting to map the advantageous characteristics of these models such as gauge fixing [74, 75, 296] and single-shot error-correction [48, 243, 278, 279] into foliated systems in the future.

4.9 Proofs and generalisations

The following sections are dedicated to proving the main Theorems in this chapter, as well as discussing several generalisations, including type-II foliation, subsystem code foliation and compressed foliation.

4.9.1 Type-II foliated qubits

In this section we consider a variation of the foliated qubit where we perform single-qubit Pauli-Y measurements instead of Pauli-X measurements to move information along a one-dimensional cluster state. We refer to these as type-II foliated qubits. Qubit foliation by this method offers a natural way to measure the encoded Pauli-Y information by coupling an ancilla to just one

single qubit of the chain. This may be of practical benefit as it reduces the valency of the graph of a resource state at the expense of including three qubits in each time interval of the foliated qubit instead of two in the case of a type-I foliated qubit.

One can produce a foliated system \mathcal{F} based on type-II qubits, by following the prescription in Sec. 4.5 where some or all of the foliated qubits in the channel \mathcal{K} are replaced by type-II foliated qubits, and producing a new resource \mathcal{R} and measurement pattern \mathcal{M} to perform the required parity measurements. Theorem 1 and Theorem 2 follow analogously.

We begin with the cluster state of length $N = 3D + 1$ with stabilizer group defined in Eqns. (4.13) and (4.14) and logical operators defined in Eqn. (4.15) such that we can measure the logical Pauli-Z information with a single-qubit Pauli-Z measurement on the first qubit.

We notice the difference between type-I and type-II foliated qubits by first looking at what happens if we make a Pauli-Y measurement instead of a Pauli-X measurement on the first qubit. We first multiply both logical operators by the stabilizer $C_2 = \sigma^Z [1] \sigma^X [2] \sigma^Z [3]$ such that both logical operators commute with $M_1 = \sigma^Y [1]$. We have

$$X \sim \sigma^Y [1] \sigma^Y [2] \sigma^Z [3], \quad Z \sim \sigma^X [2] \sigma^Z [3], \quad (4.72)$$

With these logical operators it is easily checked that measuring $M_1 = \sigma^Y [1]$, which becomes the stabilizer $C_1 = y_1 \sigma^Y [1]$, where $y_1 = \pm 1$ is the random measurement outcome, that after the measurement we have the logical operators

$$X \sim y_1 \sigma^Y [2] \sigma^Z [3], \quad Z \sim \sigma^X [2] \sigma^Z [3]. \quad (4.73)$$

Notably, we also have that

$$Y = iXZ \sim y_1 \sigma^Z [2], \quad (4.74)$$

using the logical operator expressions given in Eqn. (4.73). From this equation it is easily seen that logical Pauli-Y information can be accessed by making a single-qubit Pauli-Z measurement on the second qubit provided the first qubit is measured in the Pauli-Y basis.

One can then check that measuring the second qubit in the Pauli-Y basis, whose measurement outcome is $y_2 = \pm 1$, we obtain

$$X \sim y_1 y_2 \sigma^Z [3], \quad Z \sim y_2 \sigma^Y [3] \sigma^Z [4], \quad (4.75)$$

and in turn $Y \sim y_1 \sigma^X [3] \sigma^Z [4]$. With the example of measuring the first two qubits along the cluster state in the Pauli-Y basis, we see that we cyclicly permute the logical operator that can be accessed with a single-qubit Pauli-Z measurement as we progress along the chain. In contrast, the type-I foliated exchanges the information that is accessible by single-qubit measurements between logical Pauli-X and Pauli-Z data.

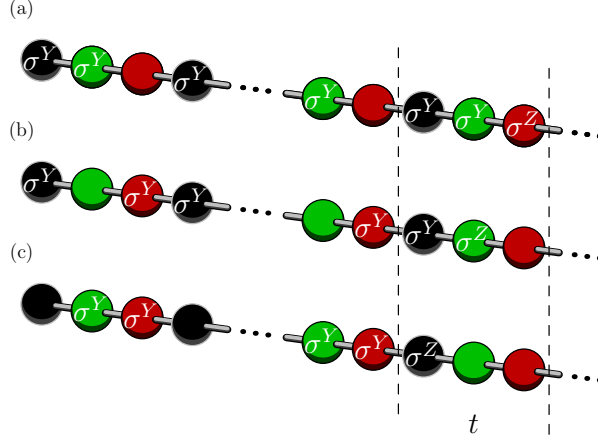


Fig. 4.20 We show the logical Pauli-X, Pauli-Y and Pauli-Z operators in (a), (b) and (c) respectively. From these diagrams we see that by measuring the appropriate qubit within the time interval in Pauli-Z basis, and otherwise measuring the other qubits of the system in the Pauli-Y basis, we can measure the logical information of the chain in an arbitrary Pauli basis.

As in the case of the type-I foliated qubit, it is convenient to redefine the indices of the system in terms of intervals, indexed by t . For type-II foliated qubits we define

$$X(t) = 3t, \quad Y(t) = 3t - 1, \quad Z(t) = 3t - 2 \quad (4.76)$$

In this case we have intervals of three adjacent qubits where either the logical Pauli-X, Pauli-Y, or Pauli-Z measurement information can be accessed via single qubit measurements. Specifically, we have that

$$X \sim \Sigma^X(t) \sigma^Z [X(t)], \quad Y \sim \Sigma^Y(t) \sigma^Z [Y(t)], \quad (4.77)$$

and

$$Z \sim \Sigma^Z(t) \sigma^Z [Z(t)], \quad (4.78)$$

where we have defined

$$\Sigma^X(t) = \prod_{\mu=1}^t \sigma^Y [Y(\mu)] \sigma^Y [Z(\mu)], \quad (4.79)$$

$$\Sigma^Y(t) = \sigma^Y [Z(t)] \prod_{\mu=1}^{t-1} \sigma^Y [X(\mu)] \sigma^Y [Z(\mu)], \quad (4.80)$$

and

$$\Sigma^Z(t) = \prod_{\mu=1}^{t-1} \sigma^Y [X(\mu)] \sigma^Y [Y(\mu)]. \quad (4.81)$$

which commute with the measurement pattern of type-II foliated qubits. We show a time interval for a type-II foliated qubit in Fig. 4.20.

We will frequently consider the action of operators R_P and $R'_P(t)$ on the resource state where these operators are defined as follows

$$\begin{aligned} R_P &= \prod_{G \in \mathcal{G}_R} \prod_{t \leq D} \sigma^Z [G(t)]^{\Upsilon(p,g)} \\ &\times \prod_{j \in |p^X|} \Sigma_j^X(D) \sigma^X [Z_j(D+1)] \\ &\times \prod_{j \in |p^Z|} \Sigma_j^Z(D+1) \sigma^Z [Z_j(D+1)], \end{aligned} \quad (4.83)$$

and

$$\begin{aligned} R'_P(t) &= \prod_{G \in \mathcal{G}_R} \left(\sigma^Z [G(t)]^{p^X \cdot g^Z} \prod_{t' < t} \sigma^Z [G(t')]^{\Upsilon(p,g)} \right) \\ &\times \prod_{j \in |p^X|} \Sigma_j^X(t) \sigma^Z [X_j(t)] \\ &\times \prod_{j \in |p^Z|} \Sigma_j^Z(t) \sigma^Z [Z_j(t)], \end{aligned} \quad (4.84)$$

where P is a Pauli operator with corresponding vector representation $(p^X p^Z)^T = v(P)$ and $(g^X g^Z) = v(G)$ for each $G \in \mathcal{G}_R$.

Lemma 1. *Operators R_P and $R'_P(t)$ act on code states of the resource state, \mathcal{R} , denoted $|\psi\rangle$, such that*

$$R_P |\psi\rangle = R'_P(t) |\psi\rangle = U^A U^C I_P |\varphi\rangle \quad (4.85)$$

for code states $|\varphi\rangle = (U^A U^C)^\dagger |\psi\rangle$ of the initial stabilizer code $\mathcal{I} \otimes \mathcal{A}$ where

$$I_P = \prod_{j \in |p^X|} \sigma^X [Z_j(1)] \prod_{j \in |p^Z|} \sigma^Z [Z_j(1)]. \quad (4.86)$$

Proof. The action of unitary operator U^C on $I_P |\varphi\rangle$ gives $(U^C I_P U^{C\dagger}) U^C |\varphi\rangle = U^C I_P |\varphi\rangle$ where, written explicitly, we have

$$U^C I_P U^{C\dagger} = \prod_{j \in |p^X|} \sigma^X [Z_j(1)] \sigma^Z [X_j(1)] \prod_{j \in |p^Z|} \sigma^Z [Z_j(1)], \quad (4.87)$$

and $U^C |\varphi\rangle$ is a codestate of \mathcal{K} . Multiplying by elements of the stabilizer group \mathcal{K} we have $K_P, K'_P(t) \sim U^C I_P U^{C\dagger}$ such that

$$K_P = \prod_{j \in |p^X|} \Sigma_j^X(D) \sigma^X [Z_j(D+1)] \prod_{j \in |p^Z|} \Sigma_j^Z(D+1) \sigma^Z [Z_j(D+1)]. \quad (4.88)$$

and

$$K'_P(t) = \prod_{j \in |p^X|} \Sigma_j^X(t) \sigma^Z[X_j(t)] \prod_{j \in |p^Z|} \Sigma_j^Z(t) \sigma^Z[Z_j(t)]. \quad (4.89)$$

By the definition of stabilizer operators, both K_P and $K'_P(t)$ of Eqns. (4.88) and (4.89) acts equivalently on the codespace of \mathcal{K} to $U^C I_P U^{C\dagger}$ Eqn. (4.87).

We obtain Eqns. (4.83) and (4.84) by conjugating K_P and $K'_P(t)$ with U^A such that $R_P = U^A K_P U^{A\dagger}$ and $R'_P(t) = U^A K'_P(t) U^{A\dagger}$. Lemma 1 holds by the unitarity of U^A . \square

Lemma 2. *The stabilizer group of the resource state includes terms $C[G(t)] \in \mathcal{R}$ for $G \in \mathcal{G}_{\mathcal{R}}$ such that*

$$C[G(t)] = \sigma^X[G(t)] \prod_{\substack{\tilde{G} \in \mathcal{G}_{\mathcal{R}}, \\ \tilde{G} \neq G}} \sigma^Z[\tilde{G}(t)]^{g^X \cdot \tilde{g}^Z} \prod_{j \in g^X} \sigma^Z[X_j(t)] \prod_{j \in g^Z} \sigma^Z[Z_j(t)], \quad (4.90)$$

where $(g^X g^Z)^T = v(G)$ and $(\tilde{g}^X \tilde{g}^Z)^T = v(\tilde{G})$.

Proof. By Def. 2 we have $\mathcal{R} = U^A(\mathcal{K} \otimes \mathcal{A})$ and $\sigma^X[G(t)] \in \mathcal{K} \otimes \mathcal{A}$ since $\sigma^X[G(t)] \in \mathcal{A}$. We obtain Eqn. (4.90) using that $C[G(t)] = U^A \sigma^X[G(t)] U^{A\dagger}$ which follows from U^A given explicitly in Eqn. (4.57) of Def. 2. \square

We are also interested in the measurement outcomes of terms $P \in \mathcal{G}_{\text{ch.}}$ of the input data that are not necessarily included $\mathcal{G}_{\mathcal{R}}$. It will be helpful to define the subset $\xi(P) \subseteq \mathcal{G}_{\mathcal{R}}$ such that $P = \prod_{G \in \xi(P)} G$. The subset $\xi(P)$ must exist for any $P \in \mathcal{G}_{\text{ch.}}$ by the definition of $\mathcal{G}_{\mathcal{R}}$, i.e., $\mathcal{G}_{\mathcal{R}}$ is a generating set of $\mathcal{G}_{\text{ch.}}$.

Corollary. *The term $C[\xi(P)(t)] \equiv \prod_{G \in \xi(P)} C[G(t)] \in \mathcal{R}$ where*

$$\begin{aligned} C[\xi(P)(t)] &= \prod_{\tilde{G} \in \mathcal{G}_{\mathcal{R}}} \sigma^Z[\tilde{G}(t)]^{p^X \cdot \tilde{g}^Z} \\ &\times \prod_{G \in \xi(P)} \sigma^X[G(t)] \sigma^Z[G(t)]^{g^X \cdot g^Z} \\ &\times \prod_{j \in |p^X|} \sigma^Z[X_j(t)] \prod_{j \in |p^Z|} \sigma^Z[Z_j(t)]. \end{aligned} \quad (4.91)$$

where $(p^X p^Z)^T = v(P)$.

The above corollary is obtained as follows. We have

$$\begin{aligned}
C[\xi(P)(t)] &= \prod_{G \in \xi(P)} \sigma^X[G(t)] \\
&\times \prod_{G \in \xi(P)} \left(\prod_{\substack{\tilde{G} \in \mathcal{G}_{\mathcal{R}}, \\ \tilde{G} \neq G}} \sigma^Z[\tilde{G}(t)]^{g^X \cdot \tilde{g}^Z} \right) \\
&\times \prod_{j \in |p^X|} \sigma^Z[X_j(t)] \prod_{j \in |p^Z|} \sigma^Z[Z_j(t)],
\end{aligned} \tag{4.92}$$

using that $C[\xi(P)(t)] = \prod_{G \in \xi(P)} C[G(t)]$ and the expression for $C[G(t)]$ given in Eqn. (4.90) in Lemma 2. We obtain the above expression for $C[\xi(P)(t)]$ then using the following identity

$$\begin{aligned}
\prod_{G \in \xi(P)} \left(\prod_{\substack{\tilde{G} \in \mathcal{G}_{\mathcal{R}}, \\ \tilde{G} \neq G}} \sigma^Z[\tilde{G}(t)]^{g^X \cdot \tilde{g}^Z} \right) &= \prod_{G \in \xi(P)} \left(\sigma^Z[G(t)]^{g^X \cdot g^Z} \prod_{\tilde{G} \in \mathcal{G}_{\mathcal{R}}} \sigma^Z[\tilde{G}(t)]^{g^X \cdot \tilde{g}^Z} \right) \\
&= \prod_{\tilde{G} \in \mathcal{G}_{\mathcal{R}}} \sigma^Z[\tilde{G}(t)]^{\tilde{g}^Z \cdot \sum_{G \in \xi(P)} g^X} \prod_{G \in \xi(P)} \sigma^Z[G(t)]^{g^X \cdot g^Z} \\
&= \prod_{\tilde{G} \in \mathcal{G}_{\mathcal{R}}} \sigma^Z[\tilde{G}(t)]^{p^X \cdot \tilde{g}^Z} \prod_{G \in \xi(P)} \sigma^Z[G(t)]^{g^X \cdot g^Z}.
\end{aligned}$$

We are now in a position to prove Theorem 1 and 2.

Proof of Theorem 1. We deal with Eqns. (4.65) and (4.66) separately before finally examining elements of $\mathcal{C}(\mathcal{G}_{\text{in}}) \setminus \mathcal{G}_{\text{in}}$ that are measured by the foliated system. We begin by determining \mathcal{G}_{out} .

Proof of Eqn. (4.65). For any element of $P \in \mathcal{G}_{\text{in}}$ with $(p^X p^Z)^T = v(P)$ we have a stabilizer of the initial state $I_P \in \mathcal{I} \otimes \mathcal{A}$ of the form Eqn. (4.86) such that we have $R_P \in \mathcal{R}$ defined according to Eqn. (4.83) by Lemma 1. Then, provided $P \in \mathcal{C}(\mathcal{G}_{\text{ch.}})$ we have that $\Upsilon(p, g) = 0$ for all $g = v(G)$ with $G \in \mathcal{G}_{\mathcal{R}}$. Therefore, we have

$$R_P = \prod_{j \in |p^X|} \Sigma_j^X(D) \sigma^X[Z_j(D+1)] \prod_{j \in |p^Z|} \Sigma_j^Z(D+1) \sigma^Z[Z_j(D+1)], \tag{4.93}$$

for $P \in \mathcal{G}_{\text{in}} \cap \mathcal{C}(\mathcal{G}_{\text{ch.}})$. Given that $\Sigma_j^X(D), \Sigma_j^Z(D+1) \in \mathcal{M}$ we have that

$$\prod_{j \in |p^X|} \sigma^X[Z_j(D+1)] \prod_{j \in |p^Z|} \sigma^Z[Z_j(D+1)] \in \mathcal{G}_{\text{out}}, \tag{4.94}$$

up to the measurement outcomes inferred from \mathcal{M} .

We next show elements $P \in \mathcal{G}_{\text{ch.}}$ are elements of $\mathcal{G}_{\text{out.}}$. We note that $P^2 = 1 \in \mathcal{G}_{\text{in.}}$. Likewise, $I_P^2 \in \mathcal{I} \otimes \mathcal{A}$ by unitarity of U^C . Therefore, by Lemma 1 we have $R'_P(t)R_P \in \mathcal{R}$. We write this explicitly

$$\begin{aligned}
 R'_P(t)R_P &= \prod_{G \in \mathcal{G}_{\mathcal{R}}} \sigma^Z [G(t)]^{p^X \cdot g^Z} \\
 &\times \prod_{j \in |p^X|} \sigma^Z [X_j(t)] \prod_{j \in |p^Z|} \sigma^Z [Z_j(t)] \\
 &\times \prod_{j \in |p^X|} \Sigma_j^X(t) \Sigma_j^X(D) \sigma^X [Z_j(D+1)] \\
 &\times \prod_{j \in |p^Z|} \Sigma_j^Z(t) \Sigma_j^Z(D+1) \sigma^Z [Z_j(D+1)],
 \end{aligned} \tag{4.95}$$

where $\Upsilon(p, g) = 0$ since $\mathcal{G}_{\text{ch.}}$ is Abelian. Now, given that $P \in \mathcal{G}_{\text{ch.}}$ there exists some $\xi(P)$ such that we have $C[\xi(P)(t)] \in \mathcal{R}$ as shown in Eqn. (4.91).

The product of Eqn. (4.91) and (4.95) then gives

$$\begin{aligned}
 C[\xi(P)(t)]R'_P(t)R_P &= \prod_{G \in \xi(P)} \sigma^X [G(t)] \sigma^Z [G(t)]^{p^X \cdot g^Z} \\
 &\times \prod_{j \in |p^X|} \Sigma_j^X(t) \Sigma_j^X(D) \\
 &\times \prod_{j \in |p^Z|} \Sigma_j^Z(t) \Sigma_j^Z(D+1) \\
 &\times \prod_{j \in |p^X|} \sigma^X [Z_j(D+1)] \\
 &\times \prod_{j \in |p^Z|} \sigma^Z [Z_j(D+1)].
 \end{aligned} \tag{4.96}$$

Since $M[G(t)] = \sigma^X [G(t)] \sigma^Z [G(t)]^{g^X \cdot g^Z} \in \mathcal{M}^A$ and $\Sigma_j^X(t), \Sigma_j^Z(t) \in \mathcal{M}^C$ we find that their values are inferred from \mathcal{M} . We therefore find the term

$$\prod_{j \in |p^X|} \sigma^X [Z_j(D+1)] \prod_{j \in |p^Z|} \sigma^Z [Z_j(D+1)] \in \mathcal{G}_{\text{out}}, \tag{4.97}$$

for $P \in \mathcal{G}_{\text{ch.}}$ up to the measurement outcomes of \mathcal{M} . The results of Eqn. (4.94) and Eqn. (4.97) thus verify Eqn. (4.65). \square

Proof of Eqn. (4.66). We now turn to the logical operators as determined by $\mathcal{L}_{\text{out}} = \mathcal{C}(\mathcal{G}_{\text{out}}) \setminus \mathcal{G}_{\text{out}}$. We require that

$$P \in \mathcal{C}(\mathcal{G}_{\text{in}}) \setminus \mathcal{G}_{\text{in}}, \tag{4.98}$$

such that $R_P \in \mathcal{C}(\mathcal{R}) \setminus \mathcal{R}$ by Lemma 1.

We also require that operator R_P in Eqn. (4.83) is such that $P \in \mathcal{C}(\mathcal{G}_{\text{ch.}})$ such that $\Upsilon(p, g) = 0$. Otherwise, $R_P \notin \mathcal{C}(\mathcal{M})$ and is therefore not a logical operator of \mathcal{F} by the definition of a subsystem code.

Finally, elements $R \in \mathcal{G}_{\text{ch.}}$ are elements of \mathcal{G}_{out} as we showed above, and are thus not logical operators. We therefore see that

$$P \in \mathcal{C}(\mathcal{G}_{\text{ch.}}) \setminus \mathcal{G}_{\text{ch.}}. \quad (4.99)$$

Combining Eqns. (4.98) and (4.99) verify Eqn. (4.66). \square

We also have that $P \in (\mathcal{C}(\mathcal{G}_{\text{in}}) \setminus \mathcal{G}_{\text{in}}) \cap \mathcal{G}_{\text{ch.}}$ are elements of \mathcal{M} , and are therefore measured under the foliation process. We see this by considering $R'_P(t)$ as in Eqn. (4.84). For elements $P \in \mathcal{G}_{\text{ch.}}$ there exists a $\xi(P)$ such that $R'_P(t)C[\xi(P)(t)] \in \mathcal{M}$. \square

We require a representative operator $R_Q \in (\mathcal{C}(\mathcal{R}) \setminus \mathcal{R}) \cap \mathcal{C}(\mathcal{M})$ of the form of Eqn. (4.83) to propagate the logical information to the output state. It is worthwhile writing this explicitly as its value needs to be inferred from \mathcal{M} at the point of readout. In some cases, it may be possible to choose

$$R_Q = \prod_{j \in |q^X|} \Sigma_j^X(D) \sigma^X [Z_j(D+1)] \prod_{j \in |q^Z|} \Sigma_j^Z(D+1) \sigma^Z [Z_j(D+1)], \quad (4.100)$$

where, by definition, $\Upsilon(q, g) = 0$ for all $G \in \mathcal{G}_{\mathcal{R}}$ with $(g^X g^Z)^T = v(G)$. Since $\Sigma_j^X(D), \Sigma_j^Z(D+1) \in \mathcal{M}$ we have

$$R_Q \sim \prod_{j \in |q^X|} \sigma^X [Z_j(D+1)] \prod_{j \in |q^Z|} \sigma^Z [Z_j(D+1)], \quad (4.101)$$

supported on the output system. Sometimes, however, this operator is not suitable because, perhaps, some of the qubits that support R_Q are not available due to loss, or because we require the evaluation of an alternative representative at the output system for later information processing. In which case, we are free to multiply R_Q by stabilizer operators of the form of Eqn. (4.96), $C[\xi(P)(t)]R'_P(t)R_P \in (\mathcal{C}(\mathcal{R}) \cap \mathcal{R}) \cap \mathcal{C}(\mathcal{M})$, for an arbitrary choice of t , to change the support of the surface. We are also, of course, free to multiply the logical operators by any stabilizers of the foliated system, such as those described in Theorem 2.

Proof of Theorem 2. We next verify the elements of the stabilizer group. We consider the term $R'_P(t)$ and $R'_P(t-1)$ in Eqn. (4.84) where $P \in \mathcal{G}_{\mathcal{R}}$ such that $\Upsilon(p, g) = 0$. We take the product

of the two terms to give

$$\begin{aligned}
R'_p(t)R'_p(t-1) &= \prod_{G \in \mathcal{G}_{\mathcal{R}}} \left(\sigma^Z[G(t-1)] \sigma^Z[G(t)] \right)^{p^X \cdot g^Z} \\
&\times \prod_{j \in |p^X|} \Sigma_j^X(t-1) \Sigma_j^X(t) \\
&\times \prod_{j \in |p^Z|} \Sigma_j^Z(t-1) \Sigma_j^Z(t) \\
&\times \prod_{j \in |p^X|} \sigma^Z[X_j(t-1)] \sigma^Z[X_j(t)] \\
&\times \prod_{j \in |p^Z|} \sigma^Z[Z_j(t-1)] \sigma^Z[Z_j(t)],
\end{aligned} \tag{4.102}$$

where $R'_p(t)R'_p(t-1) \in \mathcal{R}$. The product of this term with $C[P(t)]C[P(t-1)] \in \mathcal{R}$ where $C[P(t)]$ is defined in Eqn. (4.90) gives $S_{\text{bulk}}[G(t)] \in \mathcal{R} \cap \mathcal{M}$ of Eqn. (4.68).

We finally show that $S_{\text{bdry.}}[G(t)]$ of Eqn. (4.69) belongs to \mathcal{S} . This is shown by considering again Eqn. (4.83) where $P \in \mathcal{G}_{\text{in}}$ such that $R'_p(t) \in \mathcal{R}$. Then, taking the product of $R'_p(t)$ and $C[\xi(P)(t)] \in \mathcal{R}$ as defined in Eqn. (4.91) gives the desired operator which is included in \mathcal{M} . \square

4.9.3 Compressed foliation

In this section we discuss compressed foliation. This method includes additional check measurements of elements of $\mathcal{G}_{\mathcal{R}}$ in addition to those defined in \mathcal{F} in the main text. The construction is similar to that described in Sec. 4.5, but where additional ancillae and entangling unitaries are added, as we now describe.

In the construction of the new resource state, \mathcal{R} , one begins with a channel system \mathcal{K} according to Def. 1. The ancilla system \mathcal{A} is constructed by using two ancillae for each element of $\mathcal{G}_{\mathcal{R}}$ and t , giving

$$\mathcal{A} = \left\{ \sigma^X[G(t)], \sigma^X[G^C(t)] : \forall t, G \in \mathcal{G}_{\mathcal{R}} \right\}, \tag{4.103}$$

where $G(t)$ and $G^C(t)$ label the coordinates of ancillae and the superscript C denotes the additional ancilla for each G and t .

One entangles the ancillae to the channel using the unitary

$$U^A = V \prod_{G \in \mathcal{G}_{\mathcal{R}}, t} U[G(t)]U[G^C(t)], \tag{4.104}$$

where $U[G(t)]$ is defined in the main text and

$$U[G^C(t)] = \prod_{j \in |g^X|} U^Z[X_j(t), G^C(t)] \prod_{j \in |g^Z|} U^Z[Z_j(t+1), G^C(t)], \quad (4.105)$$

for $(g^X g^Z)^T = v(G)$. Moreover, we update the operator V with $V = \prod_t V(t) V^C(t)$ such that

$$V^C(t) = \prod_{\substack{G, H \in \mathcal{G}_{\mathcal{R}} \\ G \neq H}} U^Z \left[G^C(t, a), H^C(t, a) \right]^{g^X \cdot h^Z} \quad (4.106)$$

with $(g^X g^Z)^T = v(G)$ and $(h^X h^Z)^T = v(H)$, and $V(t)$ is also defined in the main text.

In the case of CSS codes, compressing the foliation does not lead to any novel channels – in essence, each $G \in \mathcal{G}_{\mathcal{R}}$ is measured twice per time interval. In the non-CSS codes compressed foliation leads to qualitatively different channels. In particular, compressed foliation results in resource states with higher degree, but can result in lower weight stabilizers. With a local basis change, one can always take a CSS code to a non-CSS code [297–299], and foliation of the two can lead to drastically different resource states. One needs to assess which channel is more suitable for a given purpose.

4.9.4 Foliating subsystem codes

In the main text we focused on the foliation of stabilizer codes. In fact, we find that our method for foliation extends to certain classes of subsystem codes as well with minor modifications to the scheme we have given above.

We consider a foliated channel where $\mathcal{G}_{\mathcal{R}}$ is a non-Abelian generating set for subsystem code \mathcal{G}_{ch} . The input code \mathcal{G}_{in} may also be a subsystem code. However, we will not be interested in its gauge degrees of freedom, only its logical operators and its stabilizers. As such, without loss of generality, we will continue to denote the stabilizers of this system as \mathcal{G}_{in} as before to maintain consistency with the theorems given above. The gauge and logical degrees of freedom can both be regarded as logical operators. This simplification allows us to keep our definition of the channel system, Def. 1, unchanged in our generalisation to subsystem codes.

Further, we keep the ancilla system and the measurement pattern the same following the prescription set by $\mathcal{G}_{\mathcal{R}}$. We index elements of the ancilla system with labels $G(t)$ where G denotes an element of the non-Abelian generating set $\mathcal{G}_{\mathcal{R}}$ and t denotes a time interval. We then define elements of the stabilizer group of the ancilla system such that we have $\sigma^X[G(t)] \in \mathcal{A}$ for all t and gauge generators $G \in \mathcal{G}_{\mathcal{R}}$. Likewise, we keep our definition of the measurement pattern, Def. 3, where we use only type I foliated qubits in the channel system². Explicitly, we

²Though we remark that generalising to make use of type II foliated qubits is straight forward.

measure all the qubits of the channel system in the Pauli-X basis. Ancilla qubits are measured in the basis $\sigma^X [G(t)] \sigma^Z [G(t)]^{g^X \cdot g^Z} \in \mathcal{M}$ where $(g^X g^Z)^T = v(G)$ for all $G \in \mathcal{G}_{\mathcal{R}}$.

We modify the definition of the resource state. We modify Def. 2 such that $V = 1$. We find that this modification is suitable for a large class of subsystem codes which, among others, includes CSS subsystem codes such as the Bacon-Shor code [51], the subsystem surface code [50], the gauge color code [75] and variations of these models [300–304]. Written explicitly, for a given $\mathcal{G}_{\mathcal{R}}$ we have

$$\mathcal{R} = U^A (\mathcal{K} \otimes \mathcal{A}), \quad (4.107)$$

where the ancilla system is in the product state

$$\mathcal{A} = \left\{ \sigma^X [G(t)] : \forall t, G \in \mathcal{G}_{\mathcal{R}} \right\}, \quad (4.108)$$

and the entangling unitary U^A is given by

$$U^A = V \prod_{G \in \mathcal{G}_{\mathcal{R}}, t} U[G(t)], \quad (4.109)$$

where now $V = 1$ and

$$U[G(t)] = \prod_{j \in |g^X|} U^Z[X_j(t), G(t)] \prod_{j \in |g^Z|} U^Z[Z_j(t), G(t)], \quad (4.110)$$

with $(g^X g^Z)^T = v(G)$ for each $G \in \mathcal{G}_{\mathcal{R}}$. We leave the $V = 1$ term in Eqn. (4.109) for a discussion we give later to generalise beyond the class of subsystem codes we can foliate easily.

Using the definitions given above, we state some facts about elements of \mathcal{F} and their inclusion in \mathcal{R} and \mathcal{M} without proof. Instead, we only remark that the following statements are proven using the methodology given above where $\mathcal{G}_{\text{ch.}}$ is replaced with a non-Abelian group. To approach this discussion, we consider the following operators for arbitrary Pauli operators $P \in \mathcal{C}(\mathcal{G}_{\text{ch.}})$ with $(p^X p^Z)^T = v(P)$. We consider

$$\begin{aligned} R'_P(t) &= \prod_{j \in |p^X|} \Sigma_j^X(t) \sigma^Z [X_j(t)] \prod_{j \in |p^Z|} \Sigma_j^Z(t) \sigma^Z [Z_j(t)] \\ &\quad \times \prod_{G \in \mathcal{G}_{\mathcal{R}}} \sigma^Z [G(t)]^{p^X \cdot g^Z} \prod_{t' < t} \sigma^Z [G(t')]^{\Upsilon(p, g)} \end{aligned} \quad (4.111)$$

and

$$\begin{aligned}
R_P &= \prod_{j \in |p^X|} \Sigma_j^X(D) \sigma^X [Z_j(D+1)] \\
&\times \prod_{j \in |p^Z|} \Sigma_j^Z(D+1) \sigma^Z [Z_j(D+1)] \prod_{\substack{G \in \mathcal{G}_{\mathcal{R}}, \\ t \neq D+1}} \sigma^Z [G(t)]^{\Upsilon(p,g)}
\end{aligned} \tag{4.112}$$

While we have written the term explicitly here, for $P \in \mathcal{C}(\mathcal{G}_{\text{ch.}})$ we have $\Upsilon(p, g) = 0$ for all $g = v(G)$ and $G \in \mathcal{G}_{\mathcal{R}}$ by the definition of a subsystem code. We therefore neglect terms with exponents of $\Upsilon(p, q)$ from the above two equations hereon. We also consider the operator

$$\begin{aligned}
C[\xi(P)(t)] &= \prod_{G \in \xi(P)} C[G(t)] \\
&= \prod_{G \in \xi(P)} \sigma^X [G(t)] \sigma^Z [G(t)]^{g^X \cdot g^Z} \\
&\times \prod_{j \in |p^X|} \sigma^Z [X_j(t)] \prod_{j \in |p^Z|} \sigma^Z [Z_j(t)]
\end{aligned} \tag{4.113}$$

which exists only for elements $P \in \mathcal{G}_{\text{ch.}}$.

The product of these two terms gives us a stabilizer element of \mathcal{R}

$$\begin{aligned}
C[\xi(P)(t)] R'_P(t) &= \prod_{\tilde{G} \in \xi(P)} \sigma^X [\tilde{G}(t)] \sigma^Z [\tilde{G}(t)]^{\tilde{g}^X \cdot \tilde{g}^Z} \\
&\times \prod_{j \in |p^X|} \Sigma_j^X(t) \prod_{j \in |p^Z|} \Sigma_j^Z(t) \\
&\times \prod_{G \in \mathcal{G}_{\mathcal{R}}} \sigma^Z [G(t)]^{p^X \cdot g^Z}.
\end{aligned} \tag{4.114}$$

Likewise, for $P \in \mathcal{C}(\mathcal{G}_{\text{ch.}}) \cap \mathcal{G}_{\text{ch.}} \setminus \mathcal{G}_{\text{in}}$ we have stabilizer generators

$$C[\xi(P)(t-1)] R'_P(t-1) C[\xi(P)(t)] R'_P(t) \in \mathcal{R}. \tag{4.115}$$

In Eqn. (4.114) lies the issue with the foliation of general subsystem codes. In particular, it is not clear in general if $C[\xi(P)(t)] R'_P(t)$ lies in \mathcal{M} due to the term on the third line of Eqn. (4.114)

$$\prod_{G \in \mathcal{G}_{\mathcal{R}}} \sigma^Z [G(t)]^{p^X \cdot g^Z} = \sigma^Z [G(t)]^{p^X \cdot \sum_{G \in \mathcal{G}_{\mathcal{R}}} g^Z}. \tag{4.116}$$

Since $\sigma^Z [G(t)] \notin \mathcal{M}$ for any G or t , we rely on $p^X \cdot \sum_{G \in \mathcal{G}_{\mathcal{R}}} g^Z = 0$ for all $P \in \mathcal{C}(\mathcal{G}_{\mathcal{R}}) \cap \mathcal{G}_{\mathcal{R}}$ and $G \in \mathcal{G}_{\mathcal{R}}$.

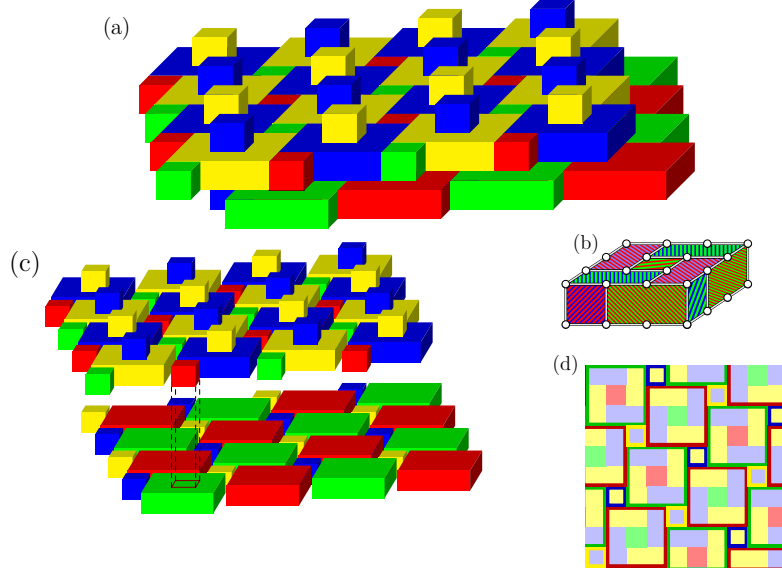


Fig. 4.22 The gauge color code lattice arranged with the qubits lying on the vertices of a cubic lattice. (a) The stabilizers are supported on cells of the lattice which are eight and thirty-two body terms living on the cuboidal cells of the lattice. (b) The cells are separated to better reveal the structure of the lattice. The gauge terms lie on faces where pairs of cells share common support. (c) A two dimensional representation of how cells lying on the layer above, marked with bold outlines, lie atop the layer below, where the cells are filled with pale colors.

This issue was easily dealt with in the case of stabilizer codes with inclusion of the V operator. Indeed, for the case where $\mathcal{G}_{\mathcal{R}}$ is Abelian we had that $\xi(P) = \{P\}$ for all stabilizers $P \in \mathcal{G}_{\mathcal{R}}$, and P and $Q \in \mathcal{G}_{\mathcal{R}}$ commuted such that $p^X \cdot q^Z = q^X \cdot p^Z$. We were therefore able to eliminate all the spurious Pauli-Z terms in the stabilizer group of \mathcal{R} by simply coupling the ancillas with the controlled phase gate $U^Z[P(t), Q(t)]$ for all $P, Q \in \mathcal{G}_{\mathcal{R}}$ such that $p^X \cdot q^Z = 1$. However, in the case of subsystem codes, where we use multiple ancilla qubits to infer the value of a stabilizer, so it is not clear which ancilla qubits we should couple to nullify the spurious Pauli-Z terms. We leave the general solution to this problem to future work.

Provided the Pauli-Z terms of the resource state can be cancelled out we can use the operators in Eqns. (4.112) and (4.114) to infer the stabilizers of the foliated system, as in Theorem 2, and we can determine the output stabilizer group as in Theorem 1. We finally remark that the logical degrees of freedom, $P \in (\mathcal{C}(\mathcal{G}_{\text{in}}) \setminus \mathcal{G}_{\text{in}}) \cap (\mathcal{C}(\mathcal{G}_{\text{ch.}}) \setminus \mathcal{G}_{\text{ch.}})$, propagate through the foliated channel, and elements $P \in (\mathcal{C}(\mathcal{G}_{\text{in}}) \setminus \mathcal{G}_{\text{in}})$ can be measured by the channel using the operator shown in Eqn. (4.114), again, provided $\sigma^Z[G(t)]^{p^X \cdot \sum_{G \in \mathcal{G}_{\mathcal{R}}} g^Z} = 0$. This allows us to generalise Theorem 1 for subsystem codes where $\sigma^Z[G(t)]^{p^X \cdot \sum_{G \in \mathcal{G}_{\mathcal{R}}} g^Z} = 0$ for all P .

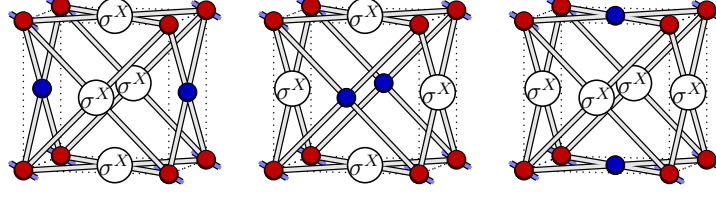


Fig. 4.23 The stabilizers of a single cell of the resource state for the gauge color code on qubits indexed $X(t)$. Measuring the face terms of the gauge color code infers the value of the stabilizer three times. Taking the product of pairs of these measurements gives additional stabilizer data.

There are many subsystem codes that can be foliated without choosing a nontrivial V operator. The CSS codes are natural candidates since

$$\sigma^Z [G(t)]^{p^X \cdot \sum_{G \in \mathcal{G}_R} g^Z} = \sigma^Z [G(t)]^{p \cdot \sum_{G \in \mathcal{G}_R} g} = 0, \quad (4.117)$$

by the definition of a CSS code. We therefore find that $V = 1$ is suitable to learn stabilizer data. We also find that the subsystem color code [52] can be foliated with our prescription.

It is interesting to study subsystem codes that we can foliate, as they give us another perspective on fault-tolerant quantum error correction. As an example, we consider single-shot error correction with the gauge color code [75, 48, 243]. We give an alternative representation of the lattice of the gauge color code in Fig. 4.22 where the qubits lie on the vertices of a cubic lattice.

The gauge group of the gauge color code has elements $B_f^X = \prod_{j \in \partial f} X_j$ and $B_f^Z = \prod_{j \in \partial f} Z_j$ for all the faces of the lattice f , where ∂f are the set of qubits that touch the face, and the product of a subset of the faces living on the boundary of a cell give a cell stabilizer. Specifically, the faces surrounding the cube are three-coloured, see Fig. 4.22(b). The product of the face terms of all of the faces of one particular colour of a cells gives the value of a stabilizer for the corresponding cell. However, as we measure all of the faces, we redundantly learn the value of cell stabilizers three times. This redundancy enables us to predict the locations of measurement errors more reliably as each stabilizer is constrained to give the same value.

We now briefly look at these constraints from the perspective of foliation. In Fig. 4.23 we show a single cubic cell of the gauge color code on the qubits indexed $X(t)$. It is readily checked that the operators shown in the figure that are the product of the face operators on two of the different colours of each cell are stabilizers of the foliated system. These stabilizers are unlike the stabilizers discussed in the main text where, if we exclude boundary stabilizers, we require measurements from qubits in different time intervals to learn the value of a stabilizer. We therefore find we have additional stabilizer data for error correction with foliated single-shot codes within each time interval. Indeed, a natural extension of our model of quantum

computation is to perform gauge fixing between the three-dimensional color code and the gauge color code [74, 75] via foliated channels. Moreover, unlike many of the examples we have considered where we have assumed a large number of time intervals, due to its single-shot nature [48] this can be achieved with just a single time interval.

5 | Conclusion

In this thesis we investigated the role of symmetry-protected topological phases in quantum computation. We focussed on the question of how topological phases with symmetry can be utilised for storage, error correction and robust processing of quantum information. An important component of this question was to characterise what types of quantum phases can exist in equilibrium, and in particular, at nonzero temperature.

The first question that was addressed was whether SPT phases can persist at nonzero temperature. We formalised a definition for symmetry-protected topological order at nonzero temperature, determined by the circuit depth required to prepare the Gibbs ensemble from a classical ensemble. It was then proven that many models describing nontrivial SPT orders with onsite symmetries are thermally fragile, meaning their Gibbs states can be prepared by low depth (symmetric) circuits. We discovered that nontrivial SPT phases can exist at nonzero temperature, when protected by more general symmetries. In particular, the three-dimensional cluster state model of Raussendorf, Bravyi and Harrington [136] retains nontrivial SPT order at nonzero temperature when protected by a \mathbb{Z}_2^2 1-form symmetry. This thermally-stable SPT order is fundamentally connected to fault-tolerance in the scheme of topological MBQC based on the 3D cluster state.

We then considered the feasibility of symmetry-protected topological phases as self-correcting quantum memories – where quantum information can be stored and protected for arbitrarily long times, without the need for resource-expensive error correction schemes. We found that 3D SPT phases protected by 1-form symmetries can be self-correcting. These phases are also thermally stable, in that their bulk SPT order persists at nonzero temperature (in terms of circuit complexity). This connection between thermal stability (an equilibrium property of a system) and self-correction (a dynamic property) is perhaps fundamental, and we hope that it provides a principle for investigating further candidate self-correcting quantum memories.

Finally, we developed new protocols to achieve fault-tolerant universality within measurement-based quantum computation. Motivated by recent advances fault-tolerance, we constructed a framework that allows computational protocols designed in the circuit model to be implemented within the setting of MBQC (with single qubit measurements on a cluster state). By expressing

MBQC as gauge fixing of a particular subsystem code, we highlighted the similarities between MBQC and more traditional approaches to quantum computing. As a concrete example, we focussed on constructing a MBQC scheme based on the braiding and fusion of symmetry defects (twists) in the surface code – the basis of many of the most promising and low-overhead approaches to quantum computation. These protocols are well-suited for optical architectures that are currently being actively perused.

Looking forward, there are a number of open directions to investigate.

Quantum computation in thermal equilibrium.

Is quantum computation possible in thermal equilibrium? The conventional model of quantum computation requires systems that are approximately in their ground space, maintained by frequent rounds of error-correction. If thermal computation were possible, it would profoundly impact the way we think about quantum computing. A first feasible step toward answering this question is to establish whether perturbatively stable quantum wires can exist at nonzero temperature (in the context of computational phases). Due to the fault-tolerance of models presented in Chapter 4, we expect their corresponding Hamiltonian realisations to be thermally stable, in terms of SPT-order, for sufficiently low temperatures. Perhaps these models, along with the machinery of code deformation, lattice surgery and gauge fixing can then be utilized to find universal computational phases that are thermally robust (while avoiding the Eastin and Knill [63] result). Obtaining a more precise understanding of this thermal stability for various parts of the computation, particularly for the magic state distillation protocols is an interesting facet of this broader goal.

As a complementary goal, understanding if thermally stable, universal computational phases of matter can exist would also sharpen our understanding of single-shot error-correction. Is single shot error correction possible in 2D topological codes, and can thermally stable SPT phases exist in 2D? Such questions are deeply related to the potential for quantum computation in thermal equilibrium.

Self-correction and quantum phases beyond commuting projector models.

Whether self-correcting quantum memories can exist in three-dimensions or less is one of the central unsolved questions in quantum information theory. One direction is to utilize the symmetry-first approach and search for models that exhibit emergent 1-form symmetries. A tantalising hint is provided by the existence of emergent symmetries in several well studied topological models, including the toric code and color codes. If one is to find a self-correcting phase in 3D, it is clear that we must move beyond local commuting projector Hamiltonians.

A promising direction is to analyse the potential of subsystem code Hamiltonians in 3D [51, 49]. These models are highly symmetric and enjoy many of the nice properties of commuting stabilizer models, but exhibit substantially richer physics and importantly can lie outside the assumptions of the many no-go theorems. The difficulty in studying these models comes from the lack of general tools to solve Hamiltonians with non-commuting terms to obtain their spectrum. A notable model in this class is the gauge-color code, which exhibits many promising features for self-correction, including single-shot error-correction (a necessary condition for self-correction [48]). Very little is known about the possible quantum phases of the gauge color code – as unlike stabilizer codes, for subsystem codes there is no ‘preferred’ choice of Hamiltonian¹. Indeed there are a wide variety of inequivalent choices of Hamiltonians that contain the codespace as their groundspace, and there is no guarantee that distinct Hamiltonians will belong to the same phase.

Complementary to this, is the question of whether self-correcting classical memories can exist in 2D or less. The 2D Ising model does not meet the conditions of a self-correcting classical memory due to its lack of perturbative stability. It has recently been shown that classical self-correction is possible in 3D with a classical Hamiltonian [305]. Previously, the 3D toric code, a quantum model, was the canonical example of a self-correcting classical memory. Perhaps self correcting classical memories are possible in 2D using a quantum Hamiltonian.

Improving resource overheads for quantum computation.

A crucial problem in the field of quantum information is to improve resource overheads of quantum computation, and finding more efficient avenues to fault-tolerance. Recently, novel computational protocols have come from the utilization of defects in topological phases. While in 2D, these defects have been systematically understood [112, 113, 118, 306], they are substantially richer in three dimensions and higher. In particular, symmetry defects in 3D phases can form codimension 1 or 2 objects, with interesting interplay [119, 245]. What are the logical gates that can be realised by their braiding and fusion? In order to understand the computational utility of these defects, one can use the theory of symmetry-protected topological (SPT) phases and their boundaries, along with the duality known as gauging to study these defects. For example, braiding processes in 3D can be very complicated, but can be captured by the more amenable three-loop braiding statistics which, in turn are inferable from an underlying SPT phase. By understanding defects in this way, we can discover new routes to fault-tolerant logical gates, with the potential to improve (or even transcend) magic state distillation schemes – whose resource costs dominate all other in quantum computation.

¹Recall for stabilizer codes, the Hamiltonian is given by the negative sum of a local, generating set of the stabilizer group. Different local generating sets do not lead to different physics as they can be adiabatically connected.

Contextuality of computational phases of matter.

An important goal is to understand the structures that underpin quantum computation, and the resource that powers it. One interesting aspect of this would be to investigate the role of contextuality [307–310] (a proposed resource for quantum computation [311–315]) in the context of computational phases of matter. That is, whether there is a relationship between contextuality and SPT order, both having been shown to be resources for MBQC. A tantalising hint comes from the perspective that (group) cohomology has been used to classify both contextuality [316–319] and SPT phases [111, 129, 116].

Concluding remark

The exciting field of quantum information is rapidly changing. Initially propelled by the challenges posed by decoherence, the tools of quantum error-correction and fault-tolerance are now being used to refine our approach to fundamental physics. The application of these tools in foreign contexts, such as high-energy physics, have already led to profound physical insights. It is an inspiring time to be working in this field, and I look forward to its promising and diverse future.

Bibliography

- [1] R. P. Feynman, International journal of theoretical physics **21**, 467 (1982).
- [2] P. W. Shor, SIAM review **41**, 303 (1999).
- [3] L. K. Grover, in *Proceedings of the twenty-eighth annual ACM symposium on Theory of computing* (ACM, 1996) pp. 212–219.
- [4] D. R. Simon, SIAM journal on computing **26**, 1474 (1997).
- [5] A. W. Harrow, A. Hassidim, and S. Lloyd, Phys. Rev. Lett. **103**, 150502 (2009).
- [6] D. Aharonov and M. Ben-Or, SIAM Journal on Computing **38**, 1207 (2008).
- [7] A. Y. Kitaev, Russian Mathematical Surveys **52**, 1191 (1997).
- [8] E. Knill, R. Laflamme, and W. H. Zurek, in *Proceedings of the Royal Society of London A: Mathematical, Physical and Engineering Sciences*, Vol. 454 (The Royal Society, 1998) pp. 365–384.
- [9] P. Aliferis, Quantum Inf. Comput. **6**, 97 (2006).
- [10] B. W. Reichardt, in *International Colloquium on Automata, Languages, and Programming* (Springer, 2006) pp. 50–61.
- [11] A. Y. Kitaev, Annals of Physics **303**, 2 (2003).
- [12] J. Haah, Physical Review A **83**, 042330 (2011).
- [13] D. E. Deutsch, Proc. R. Soc. Lond. A **425**, 73 (1989).
- [14] E. Farhi, J. Goldstone, S. Gutmann, and M. Sipser, arXiv preprint arXiv:quant-ph/0001106 (2000).
- [15] A. Kitaev, Ann. Phys. **321**, 2 (2006).
- [16] R. Raussendorf and H. J. Briegel, Physical Review Letters **86**, 5188 (2001).
- [17] D. Aharonov, W. Van Dam, J. Kempe, Z. Landau, S. Lloyd, and O. Regev, SIAM review **50**, 755 (2008).
- [18] M. H. Freedman, A. Kitaev, and Z. Wang, Communications in Mathematical Physics **227**, 587 (2002).
- [19] M. H. Freedman, M. Larsen, and Z. Wang, Communications in Mathematical Physics **227**, 605 (2002).

- [20] R. Raussendorf, D. E. Browne, and H. J. Briegel, Phys. Rev. A **68**, 022312 (2003).
- [21] M. Gimeno-Segovia, P. Shadbolt, D. E. Browne, and T. Rudolph, Phys. Rev. Lett. **115**, 020502 (2015).
- [22] P. Walther, K. J. Resch, T. Rudolph, E. Schenck, H. Weinfurter, V. Vedral, M. Aspelmeyer, and A. Zeilinger, Nature **434**, 169 (2005).
- [23] R. Stock and D. F. V. James, Phys. Rev. Lett. **102**, 170501 (2009).
- [24] B. P. Lanyon, P. Jurcevic, M. Zwerger, C. Hempel, E. A. Martinez, W. Dür, H. J. Briegel, R. Blatt, and C. F. Roos, Phys. Rev. Lett. **111**, 210501 (2013).
- [25] Y. Shi, arXiv preprint arXiv:quant-ph/0205115 (2002).
- [26] R. Raussendorf and H. J. Briegel, Phys. Rev. Lett. **86**, 5188 (2001).
- [27] D. E. Browne and H. J. Briegel, arXiv preprint arXiv:quant-ph/0603226 (2006).
- [28] D. Gross, S. T. Flammia, and J. Eisert, Physical review letters **102**, 190501 (2009).
- [29] M. Van den Nest, A. Miyake, W. Dür, and H. J. Briegel, Physical review letters **97**, 150504 (2006).
- [30] D. Gross, J. Eisert, N. Schuch, and D. Perez-Garcia, Physical Review A **76**, 052315 (2007).
- [31] J. Cai, A. Miyake, W. Dür, and H. J. Briegel, Physical Review A **82**, 052309 (2010).
- [32] T.-C. Wei, I. Affleck, and R. Raussendorf, Physical review letters **106**, 070501 (2011).
- [33] A. Miyake, Annals of Physics **326**, 1656 (2011).
- [34] A. S. Darmawan, G. K. Brennen, and S. D. Bartlett, New Journal of Physics **14**, 013023 (2012).
- [35] J. Miller and A. Miyake, npj Quantum Information **2**, 16036 (2016).
- [36] Y. Takeuchi, T. Morimae, and M. Hayashi, arXiv preprint arXiv:1809.07552 (2018).
- [37] D. Gross and J. Eisert, Physical review letters **98**, 220503 (2007).
- [38] S. D. Bartlett and T. Rudolph, Physical Review A **74**, 040302 (2006).
- [39] X. Chen, B. Zeng, Z.-C. Gu, B. Yoshida, and I. L. Chuang, Physical review letters **102**, 220501 (2009).
- [40] Y. Li, D. E. Browne, L. C. Kwek, R. Raussendorf, and T.-C. Wei, Phys. Rev. Lett. **107**, 060501 (2011).
- [41] W. K. Wootters and W. H. Zurek, Nature **299**, 802 (1982).
- [42] D. Gottesman, *Stabilizer Codes and Quantum Error Correction*, Ph.D. thesis, California Institute of Technology (2001).
- [43] P. W. Shor, Physical review A **52**, R2493 (1995).
- [44] F. J. MacWilliams and N. J. A. Sloane, *The theory of error-correcting codes*, Vol. 16 (Elsevier, 1977).

- [45] A. M. Steane, IEEE Transactions on Information Theory **45**, 1701 (1999).
- [46] A. R. Calderbank and P. W. Shor, Phys. Rev. A **54**, 1098 (1996).
- [47] E. Dennis, A. Kitaev, A. Landahl, and J. Preskill, Journal of Mathematical Physics **43**, 4452 (2002).
- [48] H. Bombín, Physical Review X **5**, 031043 (2015).
- [49] D. Poulin, Physical Review Letters **95**, 230504 (2005).
- [50] S. Bravyi, G. Duclos-Cianci, D. Poulin, and M. Suchara, Quant. Inf. Comp. **13**, 0963 (2013).
- [51] D. Bacon, Physical Review A **73**, 012340 (2006).
- [52] H. Bombin, Phys. Rev. A **81**, 032301 (2010).
- [53] M. Vasmer and D. E. Browne, arXiv preprint arXiv:1801.04255 (2018).
- [54] H. Bombín and M. A. Martin-Delgado, Phys. Rev. Lett. **97**, 180501 (2006).
- [55] H. Bombin and M. Martin-Delgado, Physical Review B **75**, 075103 (2007).
- [56] H. Bombin and M. Martin-Delgado, Physical Review Letters **98**, 160502 (2007).
- [57] S. Bravyi, D. Poulin, and B. Terhal, Physical review letters **104**, 050503 (2010).
- [58] S. Bravyi, Physical Review A **83**, 012320 (2011).
- [59] T. J. Yoder, arXiv preprint arXiv:1901.06319 (2019).
- [60] J. Haah and J. Preskill, Phys. Rev. A **86**, 032308 (2012).
- [61] S. Bravyi and B. Terhal, New Journal of Physics **11**, 043029 (2009).
- [62] R. Alicki, M. Horodecki, P. Horodecki, and R. Horodecki, Open Systems & Information Dynamics **17**, 1 (2010).
- [63] B. Eastin and E. Knill, Physical review letters **102**, 110502 (2009).
- [64] S. Bravyi and R. König, Physical review letters **110**, 170503 (2013).
- [65] F. Pastawski and B. Yoshida, Physical Review A **91**, 012305 (2015).
- [66] R. Raussendorf, J. Harrington, and K. Goyal, Annals of Physics **321**, 2242 (2006).
- [67] H. Bombin, Physical Review Letters **105**, 030403 (2010).
- [68] H. Bombin and M. A. Martin-Delgado, J. Phys. A: Math. Theor. **42**, 095302 (2009).
- [69] H. Bombin, New Journal of Physics **13**, 043005 (2011).
- [70] C. Horsman, A. G. Fowler, S. Devitt, and R. V. Meter, New J. Phys. **14**, 123011 (2012).
- [71] H. P. Nautrup, N. Friis, and H. J. Briegel, Nat. Commun. **8**, 1231 (2017).
- [72] C. Vuillot, L. Lao, B. Criger, C. G. Almudéver, K. Bertels, and B. M. Terhal, arXiv preprint arXiv:1810.10037 (2018).

- [73] A. J. Landahl and C. Ryan-Anderson, arXiv preprint arXiv:1407.5103 (2014).
- [74] A. Paetznick and B. W. Reichardt, Phys. Rev. Lett. **111**, 090505 (2013).
- [75] H. Bombín, New Journal of Physics **17**, 083002 (2015).
- [76] H. Bombín, New Journal of Physics **18**, 043038 (2016).
- [77] L. D. Landau, Ukr. J. Phys. **11**, 19 (1937).
- [78] X.-G. Wen, Physical Review B **44**, 2664 (1991).
- [79] V. Kalmeyer and R. Laughlin, Physical review letters **59**, 2095 (1987).
- [80] I. Affleck and J. B. Marston, Physical Review B **37**, 3774 (1988).
- [81] G. Baskaran and Z. Zou, Solid State Commun. **63**, 973 (1987).
- [82] R. B. Laughlin, Physical Review Letters **50**, 1395 (1983).
- [83] X.-G. Wen and Q. Niu, Physical Review B **41**, 9377 (1990).
- [84] A. Auerbach, *Interacting electrons and quantum magnetism* (Springer Science & Business Media, 2012).
- [85] K. v. Klitzing, G. Dorda, and M. Pepper, Physical Review Letters **45**, 494 (1980).
- [86] D. C. Tsui, H. L. Stormer, and A. C. Gossard, Physical Review Letters **48**, 1559 (1982).
- [87] P. W. Anderson, Materials Research Bulletin **8**, 153 (1973).
- [88] S. Bravyi, M. B. Hastings, and S. Michalakis, Journal of Mathematical Physics **51**, 093512 (2010).
- [89] S. Bravyi and M. B. Hastings, Communications in mathematical physics **307**, 609 (2011).
- [90] S. Michalakis and J. P. Zwolak, Communications in Mathematical Physics **322**, 277 (2013).
- [91] M. B. Hastings, Quantum Theory from Small to Large Scales **95**, 171 (2010).
- [92] X. Chen, Z.-C. Gu, and X.-G. Wen, Physical Review B **82**, 155138 (2010).
- [93] M. B. Hastings and X.-G. Wen, Physical Review B **72**, 045141 (2005).
- [94] T. J. Osborne, Physical review a **75**, 032321 (2007).
- [95] A. Kitaev and J. Preskill, Physical review letters **96**, 110404 (2006).
- [96] M. M. Wolf, F. Verstraete, M. B. Hastings, and J. I. Cirac, Physical review letters **100**, 070502 (2008).
- [97] J. Eisert, M. Cramer, and M. B. Plenio, arXiv preprint arXiv:0808.3773 (2008).
- [98] A. Hamma, R. Ionicioiu, and P. Zanardi, Physical Review A **71**, 022315 (2005).
- [99] S. Bravyi, (2008), unpublished.
- [100] L. Zou and J. Haah, Physical Review B **94**, 075151 (2016).

-
- [101] D. J. Williamson, A. Dua, and M. Cheng, arXiv preprint arXiv:1808.05221 (2018).
 - [102] C. G. Brell, New Journal of Physics **17**, 023029 (2015).
 - [103] D. Bacon and S. T. Flammia, Phys. Rev. A **82**, 030303 (2010).
 - [104] C. L. Kane and E. J. Mele, Phys. Rev. Lett. **95**, 226801 (2005).
 - [105] M. König, S. Wiedmann, C. Brüne, A. Roth, H. Buhmann, L. W. Molenkamp, X.-L. Qi, and S.-C. Zhang, Science **318**, 766 (2007).
 - [106] M. Z. Hasan and C. L. Kane, Rev. Mod. Phys. **82**, 3045 (2010).
 - [107] F. Haldane, Physics Letters A **93**, 464 (1983).
 - [108] X. Chen, Z.-X. Liu, and X.-G. Wen, Physical Review B **84**, 235141 (2011).
 - [109] M. Levin and Z.-C. Gu, Physical Review B **86**, 115109 (2012).
 - [110] C. Wang, C.-H. Lin, and M. Levin, Physical Review X **6**, 021015 (2016).
 - [111] X. Chen, Z.-C. Gu, Z.-X. Liu, and X.-G. Wen, Physical Review B **87**, 155114 (2013).
 - [112] J. Wang, X.-G. Wen, and E. Witten, Phys. Rev. X **8**, 031048 (2018).
 - [113] M. Barkeshli, P. Bonderson, M. Cheng, and Z. Wang, arXiv preprint arXiv:1410.4540 (2014).
 - [114] C. Heinrich, F. Burnell, L. Fidkowski, and M. Levin, Physical Review B **94**, 235136 (2016).
 - [115] M. Cheng, Z.-C. Gu, S. Jiang, and Y. Qi, Physical Review B **96**, 115107 (2017).
 - [116] D. V. Else and C. Nayak, Physical Review B **90**, 235137 (2014).
 - [117] L. Fidkowski and A. Vishwanath, Physical Review B **96**, 045131 (2017).
 - [118] D. J. Williamson, N. Bultinck, and F. Verstraete, arXiv preprint arXiv:1711.07982 (2017).
 - [119] B. Yoshida, Physical Review B **91**, 245131 (2015).
 - [120] C. Castelnovo and C. Chamon, Phys. Rev. B **76**, 184442 (2007).
 - [121] C. Castelnovo and C. Chamon, Physical Review B **78**, 155120 (2008).
 - [122] S. Iblisdir, D. Pérez-García, M. Aguado, and J. Pachos, Phys. Rev. B **79**, 134303 (2009).
 - [123] M. B. Hastings, Physical Review Letters **107**, 210501 (2011).
 - [124] B. Yoshida, Annals of Physics **326**, 2566 (2011).
 - [125] A. C. Doherty and S. D. Bartlett, Physical Review Letters **103**, 020506 (2009).
 - [126] A. Miyake, Physical Review Letters **105**, 040501 (2010).
 - [127] D. V. Else, I. Schwarz, S. D. Bartlett, and A. C. Doherty, Physical Review Letters **108**, 240505 (2012).

- [128] R. Raussendorf, D.-S. Wang, A. Prakash, T.-C. Wei, and D. T. Stephen, *Physical Review A* **96**, 012302 (2017).
- [129] X. Chen, Z.-C. Gu, and X.-G. Wen, *Physical Review B* **83**, 035107 (2011).
- [130] X. Chen, Z.-C. Gu, and X.-G. Wen, *Physical Review B* **84**, 235128 (2011).
- [131] N. Schuch, D. Pérez-García, and I. Cirac, *Physical Review B* **84**, 165139 (2011).
- [132] D. V. Else, S. D. Bartlett, and A. C. Doherty, *New Journal of Physics* **14**, 113016 (2012).
- [133] T.-C. Wei and C.-Y. Huang, *Physical Review A* **96**, 032317 (2017).
- [134] R. Raussendorf, C. Okay, D.-S. Wang, D. T. Stephen, and H. P. Nautrup, *arXiv preprint arXiv:1803.00095* (2018).
- [135] T. Devakul and D. J. Williamson, *Phys. Rev. A* **98**, 022332 (2018).
- [136] R. Raussendorf, S. Bravyi, and J. Harrington, *Physical Review A* **71**, 062313 (2005).
- [137] B. J. Brown, D. Loss, J. K. Pachos, C. N. Self, and J. R. Wootton, *Reviews of Modern Physics* **88**, 045005 (2016).
- [138] N. D. Mermin and H. Wagner, *Physical Review Letters* **17**, 1133 (1966).
- [139] S. Elitzur, *Physical Review D* **12**, 3978 (1975).
- [140] D. V. Else, P. Fendley, J. Kemp, and C. Nayak, *Physical Review X* **7**, 041062 (2017).
- [141] A. C. Potter, *Phys. Rev. X* **6**, 041001 (2016).
- [142] S. D. Bartlett, G. K. Brennen, A. Miyake, and J. M. Renes, *Physical Review Letters* **105**, 110502 (2010).
- [143] J. M. Renes, A. Miyake, G. K. Brennen, and S. D. Bartlett, *New Journal of Physics* **15**, 025020 (2013).
- [144] J. Miller and A. Miyake, *Physical Review Letters* **114**, 120506 (2015).
- [145] B. Yoshida, *Annals of Physics* **377**, 387 (2017).
- [146] Y. Bahri, R. Vosk, E. Altman, and A. Vishwanath, *Nature communications* **6**, 7341 (2015).
- [147] N. Y. Yao, C. R. Laumann, and A. Vishwanath, *arXiv preprint arXiv:1508.06995* (2015).
- [148] A. G. Fowler, M. Mariantoni, J. M. Martinis, and A. N. Cleland, *Phys. Rev. A* **86**, 032324 (2012).
- [149] K. Fujii and T. Morimae, *Phys. Rev. A* **85**, 010304 (2012).
- [150] K. Fujii, Y. Nakata, M. Ohzeki, and M. Mura, *Phys. Rev. Lett.* **110**, 120502 (2013).
- [151] J. Baez and U. Shreiber, *arXiv preprint arXiv:hep-th/0412325* (2004).
- [152] J. C. Baez and J. Huerta, *General Relativity and Gravitation* **43**, 2335 (2011).
- [153] A. Kapustin and R. Thorngren, in *Algebra, Geometry, and Physics in the 21st Century* (Springer, 2017) pp. 177–202.

-
- [154] A. Kapustin and R. Thorngren, *Phys. Rev. Lett.* **112**, 231602 (2014).
 - [155] D. Gaiotto, A. Kapustin, N. Seiberg, and B. Willett, *Journal of High Energy Physics* **2015**, 172 (2015).
 - [156] B. Yoshida, *Physical Review B* **93**, 155131 (2016).
 - [157] E. B. Davies, *Quantum theory of open systems* (London: Academic Press, 1976).
 - [158] E. B. Davies, *Journal of Functional Analysis* **34**, 421 (1979).
 - [159] M. Cheng, M. Zaletel, M. Barkeshli, A. Vishwanath, and P. Bonderson, *Phys. Rev. X* **6**, 041068 (2016).
 - [160] Y. Huang and X. Chen, *Phys. Rev. B* **91**, 195143 (2015).
 - [161] A. Vishwanath and T. Senthil, *Physical Review X* **3**, 011016 (2013).
 - [162] M. A. Metlitski, C. L. Kane, and M. P. A. Fisher, *Phys. Rev. B* **88**, 035131 (2013).
 - [163] C. Wang and T. Senthil, *Physical Review B* **87**, 235122 (2013).
 - [164] F. J. Burnell, X. Chen, L. Fidkowski, and A. Vishwanath, *Physical Review B* **90**, 245122 (2014).
 - [165] H. Spohn, *Letters in Mathematical Physics* **2**, 33 (1977).
 - [166] A. Frigerio, *Communications in Mathematical Physics* **63**, 269 (1978).
 - [167] L. Kong and X.-G. Wen, arXiv preprint arXiv:1405.5858 (2014).
 - [168] K. Siva and B. Yoshida, *Phys. Rev. A* **95**, 032324 (2017).
 - [169] D. Gross and J. Eisert, *Phys. Rev. A* **82**, 040303 (2010).
 - [170] W. Son, L. Amico, and V. Vedral, *Quantum Information Processing* **11**, 1961 (2012).
 - [171] H. P. Nautrup and T.-C. Wei, *Physical Review A* **92**, 052309 (2015).
 - [172] R. Raussendorf, J. Harrington, and K. Goyal, *New Journal of Physics* **9**, 199 (2007).
 - [173] L.-Y. Hung and Y. Wan, *Phys. Rev. B* **86**, 235132 (2012).
 - [174] J. Haegeman, K. Van Acoleyen, N. Schuch, J. I. Cirac, and F. Verstraete, *Phys. Rev. X* **5**, 011024 (2015).
 - [175] D. J. Williamson, N. Bultinck, M. Mariën, M. B. Sahinoglu, J. Haegeman, and F. Verstraete, arXiv preprint arXiv:1412.5604 (2014).
 - [176] A. Kubica, B. Yoshida, and F. Pastawski, *New Journal of Physics* **17**, 083026 (2015).
 - [177] T. Kennedy and H. Tasaki, *Phys. Rev. B* **45**, 304 (1992).
 - [178] T. Kennedy and H. Tasaki, *Communications in Mathematical Physics* **147**, 431 (1992).
 - [179] D. V. Else, S. D. Bartlett, and A. C. Doherty, *Phys. Rev. B* **88**, 085114 (2013).
 - [180] P. Kurzyński, T. Paterek, R. Ramanathan, W. Laskowski, and D. Kaszlikowski, *Phys. Rev. Lett.* **106**, 180402 (2011).

- [181] R. Peierls, Mathematical Proceedings of the Cambridge Philosophical Society **32**, 477–481 (1936).
- [182] J. B. Kogut, Reviews of Modern Physics **51**, 659 (1979).
- [183] E. Fradkin and L. Susskind, Physical Review D **17**, 2637 (1978).
- [184] M. Caselle, M. Hasenbusch, and M. Panero, Journal of High Energy Physics **2003**, 057 (2003).
- [185] F. Verstraete, M. Popp, and J. I. Cirac, Phys. Rev. Lett. **92**, 027901 (2004).
- [186] L. C. Venuti and M. Roncaglia, Phys. Rev. Lett. **94**, 207207 (2005).
- [187] I. Marvian, Phys. Rev. B **95**, 045111 (2017).
- [188] C. Wang, J. Harrington, and J. Preskill, Annals of Physics **303**, 31 (2003).
- [189] A. Kubica and M. E. Beverland, Physical Review A **91**, 032330 (2015).
- [190] J. C. Teo, T. L. Hughes, and E. Fradkin, Annals of Physics **360**, 349 (2015).
- [191] F. L. Pedrocchi and D. P. DiVincenzo, Physical review letters **115**, 120402 (2015).
- [192] E. Campbell, arXiv preprint arXiv:1502.05626 (2015).
- [193] A. Y. Kitaev, Annals of Physics **303**, 2 (2003).
- [194] S. Bravyi and J. Haah, Physical Review Letters **111**, 200501 (2013).
- [195] O. Landon-Cardinal and D. Poulin, Physical Review Letters **110**, 090502 (2013).
- [196] O. Landon-Cardinal, B. Yoshida, D. Poulin, and J. Preskill, Physical Review A **91**, 032303 (2015).
- [197] A. Kómar, O. Landon-Cardinal, and K. Temme, Physical Review A **93**, 052337 (2016).
- [198] K. P. Michnicki, Physical Review Letters **113**, 130501 (2014).
- [199] K. Michnicki, arXiv preprint arXiv:1208.3496 .
- [200] A. Hamma, C. Castelnovo, and C. Chamon, Physical Review B **79**, 245122 (2009).
- [201] F. L. Pedrocchi, A. Hutter, J. R. Wootton, and D. Loss, Physical Review A **88**, 062313 (2013).
- [202] C. G. Brell, New Journal of Physics **18**, 013050 (2016).
- [203] B. J. Brown, A. Al-Shimary, and J. K. Pachos, Physical Review Letters **112**, 120503 (2014).
- [204] Y. You, T. Devakul, F. Burnell, and S. Sondhi, arXiv preprint arXiv:1803.02369 (2018).
- [205] A. Mesaros and Y. Ran, Physical Review B **87**, 155115 (2013).
- [206] M. Hermele, Physical Review B **90**, 184418 (2014).
- [207] N. Tarantino, N. H. Lindner, and L. Fidkowski, New Journal of Physics **18**, 035006 (2016).

-
- [208] A. Vishwanath and T. Senthil, *Physical Review X* **3**, 011016 (2013).
- [209] X. Chen, F. J. Burnell, A. Vishwanath, and L. Fidkowski, *Physical Review X* **5**, 041013 (2015).
- [210] C. Wang, C.-H. Lin, and M. Levin, *Physical Review X* **6**, 021015 (2016).
- [211] D. J. Williamson and S. D. Bartlett, *New Journal of Physics* **17**, 053019 (2015).
- [212] M. Barkeshli, C.-M. Jian, and X.-L. Qi, *Physical Review B* **87**, 045130 (2013).
- [213] P. Webster and S. D. Bartlett, *Physical Review A* **97**, 012330 (2018).
- [214] B. J. Brown, K. Laubscher, M. S. Kesselring, and J. R. Wootton, *Physical Review X* **7**, 021029 (2017).
- [215] I. Cong, M. Cheng, and Z. Wang, *Physical Review Letters* **119**, 170504 (2017).
- [216] S. Roberts, B. Yoshida, A. Kubica, and S. D. Bartlett, *Physical Review A* **96**, 022306 (2017).
- [217] G. Zhu, M. Hafezi, and M. Barkeshli, *Bulletin of the American Physical Society* (2018).
- [218] S. D. Bartlett, G. K. Brennen, and A. Miyake, *Quantum Science and Technology* **3**, 014010 (2018).
- [219] K. Temme, *Communications in Mathematical Physics* **350**, 603 (2017).
- [220] K. Temme and M. J. Kastoryano, *arXiv preprint arXiv:1505.07811* (2015).
- [221] R. Thorngren and C. von Keyserlingk, *arXiv preprint arXiv:1511.02929* (2015).
- [222] E. Lake, *arXiv preprint arXiv:1802.07747* (2018).
- [223] C. Wang and T. Senthil, *Physical Review B* **87**, 235122 (2013).
- [224] F. J. Burnell, X. Chen, L. Fidkowski, and A. Vishwanath, *Physical Review B* **90**, 245122 (2014).
- [225] A. Kapustin, *arXiv preprint arXiv:1403.1467* (2014).
- [226] P. Etingof, D. Nikshych, V. Ostrik, and E. Meir, *arXiv preprint arXiv:0909.3140* (2009).
- [227] M. B. Hastings, G. H. Watson, and R. G. Melko, *Physical review letters* **112**, 070501 (2014).
- [228] A. Hatcher, “Notes on basic 3-manifold topology,” (2000).
- [229] A. K. Kubica and B. Yoshida, *arXiv preprint arXiv:1805.01836* (2018).
- [230] J. Haegeman, K. Van Acoleyen, N. Schuch, J. I. Cirac, and F. Verstraete, *Physical Review X* **5**, 011024 (2015).
- [231] L.-Y. Hung and Y. Wan, *Physical Review B* **86**, 235132 (2012).
- [232] D. J. Williamson, N. Bultinck, M. Mariën, M. B. Şahinoğlu, J. Haegeman, and F. Verstraete, *Physical Review B* **94**, 205150 (2016).
- [233] S. Vijay, J. Haah, and L. Fu, *Physical Review B* **94**, 235157 (2016).

- [234] D. J. Williamson, Physical Review B **94**, 155128 (2016).
- [235] K. Walker and Z. Wang, Frontiers of Physics **7**, 150 (2012).
- [236] C. W. von Keyserlingk, F. J. Burnell, and S. H. Simon, Phys. Rev. B **87**, 045107 (2013).
- [237] F. J. Burnell, C. W. von Keyserlingk, and S. H. Simon, Phys. Rev. B **88**, 235120 (2013).
- [238] Z. Wang and X. Chen, Phys. Rev. B **95**, 115142 (2017).
- [239] D. J. Williamson and Z. Wang, Annals of Physics **377**, 311 (2017).
- [240] S. X. Cui, arXiv preprint arXiv:1610.07628 (2016).
- [241] A. Bolt, G. Duclos-Cianci, D. Poulin, and T. Stace, Physical Review Letters **117**, 070501 (2016).
- [242] B. J. Brown and S. Roberts, arXiv preprint arXiv:1811.11780 (2018).
- [243] B. J. Brown, N. H. Nickerson, and D. E. Browne, Nature Communications **7**, 12302 (2016).
- [244] A. Kubica, N. Delfosse, M. Beverland, F. Brandao, J. Preskill, and K. Svore, Unpublished.
- [245] D. V. Else and C. Nayak, arXiv preprint arXiv:1702.02148 (2017).
- [246] H. Ma, E. Lake, X. Chen, and M. Hermele, Physical Review B **95**, 245126 (2017).
- [247] H. J. Briegel and R. Raussendorf, Phys. Rev. Lett. **86**, 910 (2001).
- [248] R. Raussendorf, D. E. Browne, and H. J. Briegel, J. Mod. Opt. **49**, 1299 (2002).
- [249] H. J. Briegel, D. E. Browne, W. Dür, R. Raussendorf, and M. V. den Nest, Nat. Phys. **5**, 19 (2009).
- [250] M. A. Nielsen and C. M. Dawson, Physical Review A **71**, 042323 (2005).
- [251] R. Prevedel, P. Walther, F. Tiefenbacher, P. Böhi, R. Kaltenbaek, T. Jennewein, and A. Zeilinger, Nature **445**, 65 (2007).
- [252] M. S. Tame, R. Prevedel, M. Paternostro, P. Bohi, M. S. Kim, and A. Zeilinger, Phys. Rev. Lett. **98**, 140501 (2007).
- [253] X.-C. Yao, T.-X. Wang, H.-Z. Chen, W.-B. Gao, A. G. Fowler, R. Raussendorf, Z.-B. Chen, N.-L. Liu, C.-Y. Lu, You-JinDeng, Y.-A. Chen, and J.-W. Pan, Nature **482**, 489 (2012).
- [254] S. Barz, R. Vasconcelos, C. Greganti, M. Zwerger, W. Dür, H. J. Briegel, and P. Walther, Physical Review A **90**, 042302 (2014).
- [255] X.-D. Cai, D. Wu, Z.-E. Su, M.-C. Chen, X.-L. Wang, L. Li, N.-L. Liu, C.-Y. Lu, and J.-W. Pan, Physical review letters **114**, 110504 (2015).
- [256] N. Spagnolo, C. Vitelli, M. Bentivegna, D. J. Brod, A. Crespi, F. Flamini, S. Giacomini, G. Milani, R. Ramponi, P. Mataloni, *et al.*, Nature Photonics **8**, 615 (2014).
- [257] J. W. Silverstone, R. Santagati, D. Bonneau, M. J. Strain, M. Sorel, J. L. O'Brien, and M. G. Thompson, Nature communications **6**, 7948 (2015).

-
- [258] J. Carolan, J. D. Meinecke, P. J. Shadbolt, N. J. Russell, N. Ismail, K. Wörhoff, T. Rudolph, M. G. Thompson, J. L. O’Brien, J. C. Matthews, *et al.*, *Nature Photonics* **8**, 621 (2014).
- [259] R. Raussendorf and J. Harrington, *Phys. Rev. Lett.* **98**, 190504 (2007).
- [260] S. Bravyi and A. Kitaev, *Phys. Rev. A* **71**, 022316 (2005).
- [261] E. T. Campbell, B. M. Terhal, and C. Vuillot, *arXiv preprint arXiv:1612.07330* (2016).
- [262] S. J. Devitt, A. G. Fowler, A. M. Stephens, A. D. Greentree, L. C. L. Hollenberg, W. J. Munro, and K. Nemoto, *New J. Phys.* **11**, 083032 (2009).
- [263] D. A. Herrera-Martí, A. G. Fowler, D. Jennings, and T. Rudolph, *Phys. Rev. A* **82**, 032332 (2010).
- [264] T. Rudolph, *APL Photonics* **2**, 030901 (2017).
- [265] A. Steane, *Proc. R. Soc. A* **452**, 2551 (1996).
- [266] A. Bolt, D. Poulin, and T. M. Stace, *arXiv preprint arXiv:1810.11572* (2018).
- [267] D. Herr, A. Paler, S. J. Devitt, and F. Nori, *arXiv preprint arXiv:1711.04921* (2017).
- [268] N. H. Nickerson and H. Bombín, *1810.0962* (2018).
- [269] H. Bombin, *arXiv preprint arXiv:1810.0957* (2018).
- [270] A. G. Fowler, A. M. Stephens, and P. Groszkowski, *Phys. Rev. A* **80**, 052312 (2009).
- [271] M. B. Hastings and A. Geller, *Quant. Inf. Comp.* **15**, 0962 (2015).
- [272] T. J. Yoder and I. H. Kim, *Quantum* **1**, 2 (2017).
- [273] D. Litinski and F. von Oppen, *Quantum* **2**, 62 (2018).
- [274] B. M. Terhal, *Rev. Mod. Phys.* **87**, 307 (2015).
- [275] E. T. Campbell, B. M. Terhal, and C. Vuillot, *Nature* **549**, 172 (2017).
- [276] A. R. Calderbank, E. M. Rains, P. W. Shor, and N. J. A. Sloane, *Phys. Rev. Lett.* **78**, 405 (1997).
- [277] K. Duivenvoorden, N. P. Breuckmann, and B. M. Terhal, *arXiv preprint arXiv:1708.09286* (2017).
- [278] E. T. Campbell, *arXiv preprint arXiv:1805.09271* (2018).
- [279] O. Fawzi, A. Grospellier, and A. Leverrier, *arXiv preprint arXiv:1808.03821* (2018).
- [280] H. Bombín, (2017), private communication.
- [281] B. J. Brown, S. D. Bartlett, A. C. Doherty, and S. D. Barrett, *Phys. Rev. Lett.* **111**, 220402 (2013).
- [282] J. R. Wootton, *J. Phys. A: Math. Theor.* **48**, 215302 (2015).
- [283] H. Zheng, A. Dua, and L. Jiang, *Phys. Rev. B* **92**, 245139 (2015).
- [284] G. Moore and N. Read, *Nucl. Phys. B* **360**, 362 (1991).

- [285] G. K. Brennen and J. K. Pachos, *Proc. R. Soc. A* **464**, 1 (2007).
- [286] C. Nayak, S. H. Simon, A. Stern, M. Freedman, and S. D. Sarma, *Rev. Mod. Phys.* **80**, 1083 (2008).
- [287] J. Preskill, *Caltech Lecture Notes* (1999).
- [288] J. K. Pachos, *Introduction to Topological Quantum Computation* (Cambridge University Press, 2012).
- [289] V. Lahtinen and J. K. Pachos, *SciPost Phys.* **3**, 021 (2017).
- [290] J. Łodyga, Paweł, A. Grudka, and M. Horodecki, *Sci. Rep.* **5**, 8975 (2015).
- [291] Y. Li, *New J. Phys.* **17**, 023037 (2015).
- [292] S. Bravyi, *Phys. Rev. A* **73**, 042313 (2006).
- [293] T. Karzig, Y. Oreg, G. Refael, and M. H. Freedman, *Phys. Rev. X* **6**, 031019 (2016).
- [294] M. S. Kesselring, F. Pastawski, J. Eisert, and B. J. Brown, *Quantum* **2**, 101 (2018).
- [295] S. Roberts and S. D. Bartlett, *arXiv preprint arXiv:1805.01474* (2018).
- [296] T. J. Yoder, *arXiv preprint arXiv:1705.01686* (2017).
- [297] X.-G. Wen, *Phys. Rev. Lett.* **90**, 016803 (2003).
- [298] Z. Nussinov and G. Ortiz, *Ann. Phys.* **324**, 977 (2009).
- [299] B. J. Brown, W. Son, C. V. Kraus, R. Fazio, and V. Vedral, *New J. Phys.* **13**, 065010 (2011).
- [300] D. Bacon and A. Casaccino, *arXiv preprint arXiv:quant-ph/0610088* (2006).
- [301] S. Bravyi, *Phys. Rev. A* **83**, 012320 (2011).
- [302] S. Bravyi and A. Cross, *arXiv preprint arXiv:1509.03239* (2015).
- [303] T. Jochym-O'Connor and S. D. Bartlett, *Phys. Rev. A* **93**, 022323 (2016).
- [304] C. Jones, P. Brooks, and J. Harrington, *Phys. Rev. A* **93**, 052332 (2016).
- [305] D. Poulin, R. G. Melko, and M. B. Hastings, *arXiv preprint arXiv:1812.03936* (2018).
- [306] M. Barkeshli, C.-M. Jian, and X.-L. Qi, *Physical Review B* **88**, 241103 (2013).
- [307] J. S. Bell, in *John S Bell On The Foundations Of Quantum Mechanics* (World Scientific, 2001) pp. 1–6.
- [308] S. Kochen and E. P. Specker, in *The logico-algebraic approach to quantum mechanics* (Springer, 1975) pp. 293–328.
- [309] N. D. Mermin, *Reviews of Modern Physics* **65**, 803 (1993).
- [310] A. Peres, *Journal of Physics A: Mathematical and General* **24**, L175 (1991).
- [311] R. Raussendorf, D. E. Browne, N. Delfosse, C. Okay, and J. Bermejo-Vega, *Physical Review A* **95**, 052334 (2017).

- [312] J. Bermejo-Vega, N. Delfosse, D. E. Browne, C. Okay, and R. Raussendorf, *Physical Review Letters* **119**, 120505 (2017).
- [313] M. Frembs, S. Roberts, and S. D. Bartlett, *New Journal of Physics* **20**, 103011 (2018).
- [314] J. Anders and D. E. Browne, *Physical Review Letters* **102**, 050502 (2009).
- [315] R. Raussendorf, *Physical Review A* **88**, 022322 (2013).
- [316] S. Abramsky, S. Mansfield, and R. S. Barbosa, *arXiv preprint arXiv:1111.3620* (2011).
- [317] R. Raussendorf, *arXiv preprint arXiv:1602.04155* (2016).
- [318] C. Okay, S. Roberts, S. D. Bartlett, and R. Raussendorf, *Quantum Information & Computation* **17**, 1135 (2017).
- [319] C. Okay, E. Tyhurst, and R. Raussendorf, *arXiv preprint arXiv:1806.04657* (2018).

